# THERMO-MECHANICAL CHARACTERISATION OF CARBON FOAMS AND COMPOSITE MATERIALS FOR THE ATLAS UPGRADE

**Isaac Bonad**


University
*of*
Glasgow

September, 2011

Thesis submitted for the degree of Doctor of Philosophy
at the University of Glasgow

# Acknowledgements

I would firstly like to thank my supervisor, Richard Bates for his invaluable help and guidance over the years of my PhD. I appreciate greatly the friendship that we have developed during the last few years. Craig Buttar, my back up supervisor deserves a big thanks for his advices. I would also like to acknowledge Calum Torrie and Liam Cunningham who helped me out at the beginning of my PhD. Liam has been there for me when I needed him, even to the end of the studies.

John Malone, Fiona McEwan, Raymond DiMattia and Frederick Doherty helped me with their technical expertise over the years. Their willingness to assist me over the years has been invaluable. Cheers to Fiona for being there for me when I was finishing this thing off.

My CASE sponsors Rutherford Appleton Laboratory (RAL) helped support these studies and for that I am very grateful, especially to Simon Canfer at the Advanced Materials Technology group, Ian Wilmut the ATLAS project engineer and Andy Nichols who supervised me at RAL. Their help and advice are greatly appreciated. Cyrill Locket was also a great help, not only by building mechanical devices but by patiently being with me to make them work. Thanks to Stephanie Jones who helped me out when I was finishing my work at RAL.

I also like to thank Aaron MacRaighne for his help and guidance. Aaron, together with Dima Maneuski and Kenny Wraight, provided much entertainment on the football front.

Thanks to Valerie Flood for helping me with all the travel arrangements, administration and many other things. Always made sure that things went smoothly, well done.

Cheers to all the guys I had good times with at the department other the years, Nacho, Christina, Michael, big Russell, Andy Blue, Jack, Lars etc. Thanks also to my Pastors and church friends, Professor Abraham Ogwu, Abu, Ambakissye, Mugi, Kaifalas, Tulibako, Lucas, Francis, Gabriel, Eugene, David-West, Mary Bundu, Blessing, Faith, Judy, Dunnors, Veronica Zuma, Florence kanu etc. for their help and spiritual advices. To all the lads in Glasgow - Silvester, Jean Michel, Christopher, Charlortte, Adelaide, Jose etc.

I would also like to thank of my family - Sahoua Monique nee Bonao, James Amwayi, Rachelle Lund Bonad, Bente Lund Bente, Sarah E. Bonad, Jacob J. Bonad, Rebecca Bonao nee Dion, Rachel Bonao, Gedeon Bonao, Eliezer Bonao, Dion Edmond, Tanoh Guillaume, Marie Claude, Germain Bagou, Sophie Bagou, the late John Cole, Judy Amwayi, Anitta Amwayi, Totto Amwayi, Evelin Amwayi - for the family support over the years. A big thank to my late father who taught me that this was all worthwhile. Biggest thank to Veronica Bonad for supporting, encouraging and being with me over the years.

I cannot forget the source of my strength. ”The joy of the Almighty GOD is my strength”.

Thank you Lord for good health and divine wisdom from above.

# Declaration

The research results presented in this thesis are the product of my own work. Appropriate references are provided when results of third parties are mentioned. The research presented here was not submitted for another degree in any other department or university.

Isaac Bonad

# Abstract

As a result of the need to increase the luminosity of the Large Hadron Collider (LHC) at CERN-Geneva by 2020, the ATLAS detector requires an upgraded inner tracker. Upgrading the ATLAS experiment is essential due to higher radiation levels and high particle occupancies. The design of this improved inner tracker detector involves development of silicon sensors and their support structures. These support structures need to have well understood thermal properties and be dimensionally stable in order to allow efficient cooling of the silicon and accurate track reconstruction. The work presented in this thesis is an investigation which aims to qualitatively characterise the thermal and mechanical properties of the materials involved in the design of the inner tracker of the ATLAS upgrade. These materials are silicon carbide foam (SiC foam), low density carbon foams such as PocoFoam and Allcomp foam, Thermal Pyrolytic Graphite (TPG), carbon/carbon and Carbon Fibre Reinforced Polymer (CFRP). The work involves the design of a steady state in-plane and a steady state transverse thermal conductivity measurement systems and the design of a mechanical system capable of accurately measuring material stress-strain characteristics. The in-plane measurement system is used in a vacuum vessel, with a vacuum of approximately $10^{-5}$ mbar, and over a temperature range from -30°C to 20°C. The transverse and mechanical systems are used at room pressure and temperature. The mechanical system is designed so that it measures mechanical properties at low stress below 30MPa. The basic concepts used to design these measurement systems and all the details concerning their operations and implementations are described. The thermal measurements were performed at the Physics and Astronomy department of the University of Glasgow while the mechanical measurements were performed at the Advanced Materials Technology department, at the Rutherford Appleton Laboratory (RAL). Essential considerations about the measurement capabilities and experimental issues are presented together with experimental results. The values obtained for the materials with well understood properties agree well with the values available in the literature, confirming the reliability of the measurement systems. Additionally, a Finite Element Analysis (FEA) is performed to predict the thermal and mechanical properties of PocoFoam. The foam is created by generating spherical bubbles randomly in the computational tool MatLab according to the topology of PocoFoam. The model is transferred to the CAD program Solid works to be extruded and be transformed into PocoFoam. It is later on transferred to the FEA tool ANSYS to be analysed. Simulations of a specimen of density equal to 0.60g/c$m^3$ are performed and the results are compared with the values measured for a specimen of density equal to 0.56g/c$m^3$. The simulated results agree within 32$\%$ with the experimental values. The experimental results achieved in the studies undertaken in thesis have made a considerable contribution to the R$\&$D of the stave design by helping to understand and optimise the current stave design and explore new design possibilities. The stave is a mechanical support with integrated cooling onto which the silicon sensors are directly glued.

# Contents

# List of Tables

# List of Figures

# Chapter 1

# Introduction

The Large Hadron Collider (LHC) is the world's largest and most powerful particle accelerator and is located at the European Organisation for Nuclear Research (CERN). The LHC consists of a 27 km ring of superconducting magnets and a number of accelerating structures, which accelerate the particles around the ring. Inside the accelerator, two beams of protons travel at a speed close to the speed of light before being brought together at four collision points around the ring. The beams travel in opposite directions in separate beam pipes, which are kept at ultrahigh vacuum. The protons are guided along the accelerator ring with a strong magnetic field, achieved by the use of superconducting electromagnets. They are built from coils of special electrical cable that operate in a superconducting state, efficiently conducting electricity without resistance or loss of energy. This requires chilling the magnets to around -271°C [1]. Many magnets of different varieties and sizes are used to guide the beams along the ring. These include magnets of 15 m in length, which are used to bend the beams and quadrupole magnets of 5 to 7 m of length to focus the beams. Prior to the collision points, another set of quadrupole magnets are used to focus the particles to come close to each other in order to increase the chances of collision.

Six experiments are currently running at the LHC by international collaboration bringing together scientists from institutes all over the world. The ToTal Elastic and diffractive cross section Measurement (TOTEM) [2], [3] and the Large hadron Collider forward (LHCf) [4], [5] are the smallest in size. The LHCf uses forward particles created inside the LHC as a source to simulate cosmic rays in laboratory conditions and TOTEM studies forward particles to focus on physics that is not accessible to general purpose experiments such as the size of the proton as well as the accurate monitoring of the LHC's luminosity. The Large Hadron Collider beauty (LHCb) [6] and A Large Ion Collider Experiment (ALICE) [7], [8] are the two medium size experiments. The LHCb experiment focuses in investigating the slight difference between matter and antimatter by studying a type of particle called the "beauty quark" or "b quark". ALICE collides lead ions to recreate the conditions just after the big bang under laboratory conditions. The data obtained should allow physicists to study a state of matter known as quark-gluon plasma. The Compact Muon Solenoid (CMS) [9] and A Toroidal LHC Apparatus (ATLAS) [10] are the largest experiments in CERN. They are based on general purpose detectors to investigate a wide range of physics including the

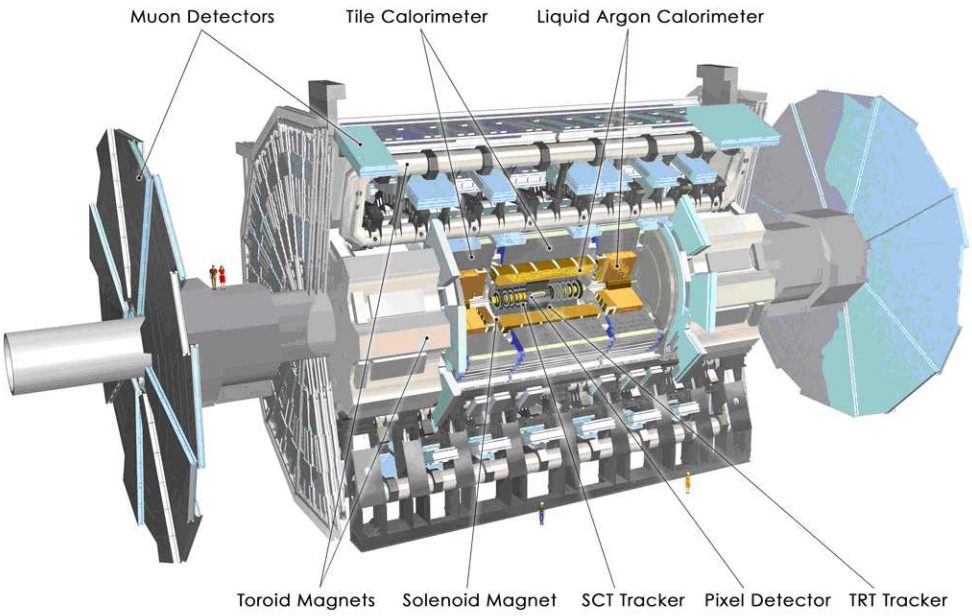


Figure 1.1: Overview of ATLAS [1]

search for Higgs bosons. Although they have the same scientific goals, they use different technical solutions and design, which are vital for cross confirmation of any new discovery made. The ATLAS experiment is the focus of this thesis because the technical solutions and detector designs considered in this study are only applicable to it. The ATLAS experiment is 44m long, 25m high with a weight of about 7000 tonnes. It comprises an inner detector system immersed in a 2 Tesla solenoidal magnetic field, an electromagnetic and a hadronic calorimetry, and an outermost muon spectrometer embedded in three superconducting air-core toroids with a typical field of 0.5T in the barrel and 1T in the end-caps [11]. The layout of ATLAS is illustrated in figure 1.1.

## 1.1 Motivation

ATLAS is a general purpose detector for the study of proton-proton (p-p) interactions [12]. At the centre of ATLAS, inside a solenoid magnet, the inner tracking detector is located. The inner detector consists of the Transition Radiation Tracker (TRT) [13], the Silicon Central Tracker (SCT) [14] and the innermost part, the Pixel detector [13] [14]. The inner detector is designed to provide hermetic and robust pattern recognition, excellent momentum resolution and both primary and secondary vertex measurements for charged tracks above a given threshold, nominally 0.5GeV [15], [16], [17]. The layout of the inner detector is shown in figure 1.2. The pixel detector provides critical tracking information for pattern recognition near the interaction point and contributes significantly to the reconstruction of secondary vertices. Furthermore, it provides good spatial resolution for the reconstruction of primary vertices.

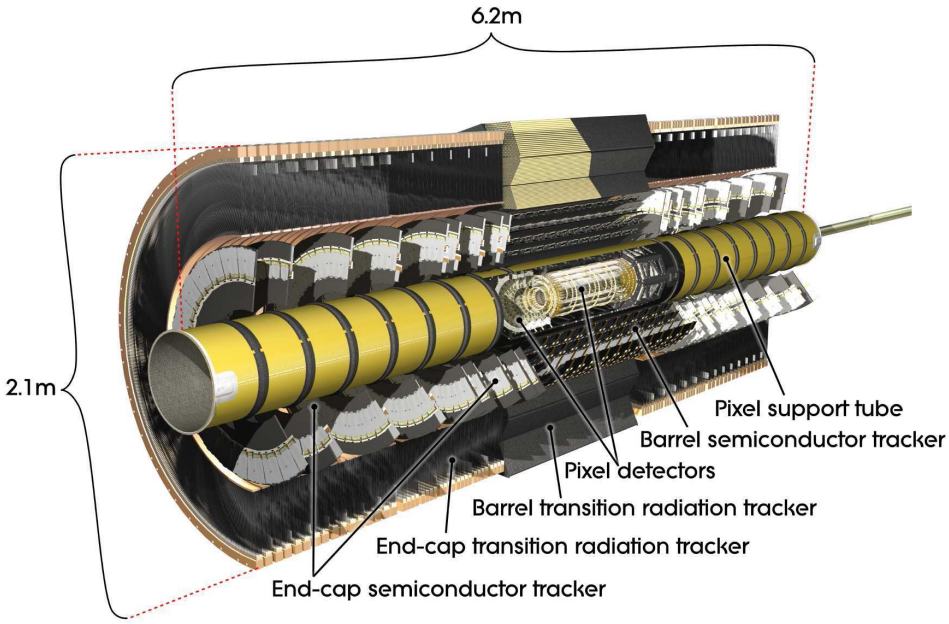


Figure 1.2: Structural cut along the ATLAS inner detector [18]

The design beam energy of the accelerator is 7 TeV with a luminosity of $10^{34}/cm^2s$. Radiation from the LHC beam will damage the magnets of the LHC accelerator as the luminosity is accumulated. The quadrupole magnets at the interaction points may end their lives around an integrated luminosity of $700/fb$. With constant design luminosity of $10^{34}/cm^2s$, this may occur at the end of 2016 [10]. This date was reviewed recently and postponed to 2022. Replacement of the quadrupole magnets have been discussed. The upgrading of the accelerator to the super LHC (SLHC) and the accompanying upgrade of the ATLAS experiment are being investigated. The upgrade should provide an opportunity to extend the LHC physics program by extending the mass reach in the search for new particles predicted by many theories, or by allowing high-precision measurements including the couplings of the Higgs boson to various other particles. The first stage is to increase the luminosity by a factor 10, to $10^{35}/cm^2s$ resulting in an integrated luminosity of $3000/fb$ [10]. The increase of luminosity has two direct consequences in an experiment. The first is the increase of pileup events per beam crossing, from 20 to 200, and the second is the increase of the total fluence of particles inside the tracker corresponding to the increase in the integrated luminosity; that is a factor 4 for a luminosity increase from 700 to $3000/fb$ [10].

For the ATLAS upgrade the minimal requirement for the beam crossing rate is that the detector keeps the same readout interval of 25ns, as in the muon and calorimeter systems, enabling the use of the same electronics. The basic requirements in terms of design is radiation hardness and efficient tracking capabilities with detector occupancies under control [19].

The inner detector system of the ATLAS upgrade has to keep the same performance that it achieved for the current tracker operation. The main challenges are the increased occupancy resulting from the instantaneous increase in event rate and the radiation damage resulting from the fluence of particles. Because of high occupancy, the TRT system will cease to work and will be replaced with silicon microstrip sensors. The SCT system has to have finer

granularity to keep the occupancy acceptably low. The SCT and the pixel systems need to have radiation tolerance in their silicon microstrip and pixel sensors, which are a factor ten higher than that of the LHC operation.

In the light of these LHC upgrade considerations, it is evident that the ATLAS experiment will be exposed to significant challenges. Its entire tracking system needs to be replaced. The expected high radiation level as well as the large increase in occupancy impose very strict requirements on the inner tracker system. R&D is well advanced and prototypes are being constructed and tested in order to take SLHC data around the year 2020. The increased occupancy is dealt with by replacing the trackers with higher granularity ones, which implies an additional 2-3 times increase in channels. The increased channel number imposes strict constraints for the power consumption as well as for the material budget. Additionally, very radiation-hard techniques will be needed for the "hottest" region within 20 cm from the beam pipe [20]. Such an environment is demanding fundamental R&D for new detector materials and concepts. The efforts of this thesis go towards coping with these challenges. The thesis contributes to an international collaboration, whose objective is to design a mechanical support with integrated cooling supporting the strip sensors in the tracker detector, which structure is commonly called "stave". This includes understanding the thermal and mechanical properties of the stave, benchmarking these properties with finite element analysis, understanding the sensitivity of the design to material change and the ways to improve it.

## 1.2 Stave Design

The design work of the stave is well advanced in the collaboration. In order to examine the magnitude of work already done by the ATLAS upgrade collaboration, this section presents the progress of the work done by the American collaborators and reported by M. Gilchriese et al. in [21]. At the present stage, the UK and US collaborators are working on a similar design but with some difference in the details. The USA collaborators use aluminium for the cooling pipes while the UK collaborators use stainless steel. In this thesis, the US work is presented because considerable advances have been made in this group and documentation is easily available. The design challenges presented here are similar to the other collaboration groups. The proposed layout for the ATLAS inner detector for the SLHC is shown on figure 1.3. The pixel layers are in green, the short-strips in blue, the long strips in red, and the forward disks in purple.

The objectives of this layout is first to produce a robust design that can withstand ten times the projected dose of the current detector (the specification for the upgrade tracker is survival to an integrated luminosity of $2x3000/fb$, 2 being the safety margin), secondly to cope with an instantaneous luminosity increase to $10^{35}/cm^2s$. The requirements on the absolute value of the stiffness of the stave depends upon the overall stiffness of the stave and the CFRP barrel structure that it is mounted on. In the UK/US design, the silicon strip detectors will be mounted directly on the stave, which will supply all the necessary services and mechanical support. The stave is meant to be mounted on the barrel semiconductor

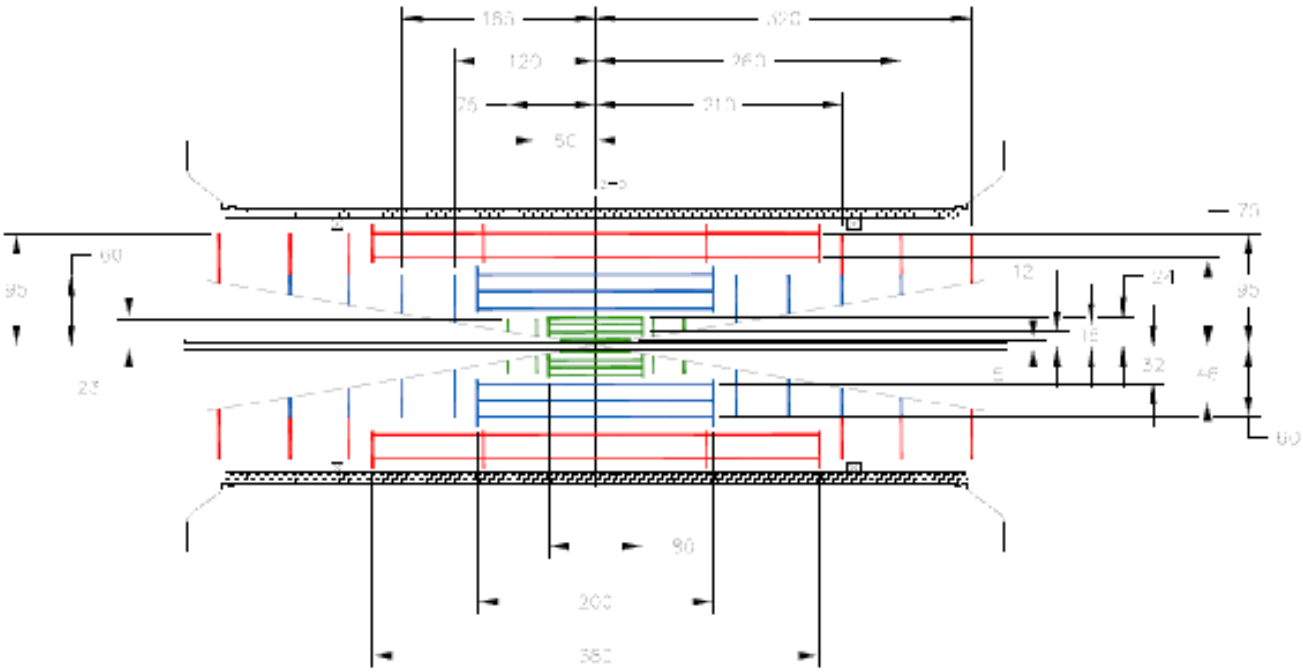

Figure 1.3: Proposed all-silicon layout of the inner detector for the ATLAS upgrade [22]]

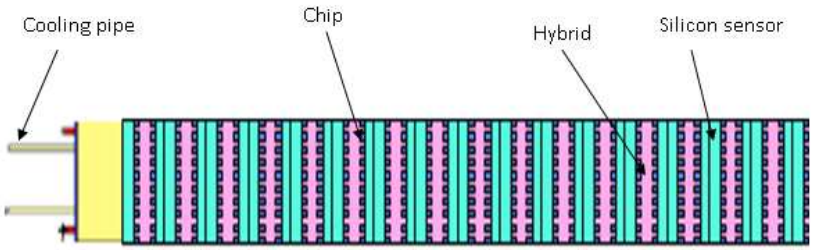


Figure 1.4: Illustration of the stave with short-strip silicon detectors. Modules are mounted on both sides of the stave [21]

tracker, shown in figure 1.2. The proposed US stave for the barrel region of the tracker is illustrated in figure 1.4.

The stave consists of [21], [22]:

- A mechanical support with integrated cooling - the mechanical core of the stave
- A bus cable (copper-aluminium-kapton flex-circuit to distribute electrical signals, power and high voltage). The bus cable is directly glued to the mechanical core (one on each side of the core)
- Single-sided silicon detector modules glued onto the bus cables. Each single-sided module consists of four rows of 10 read out chips (each of 128 channels) arranged on two hybrids and glued directly to the sensitive surface of the sensor. A total of 10

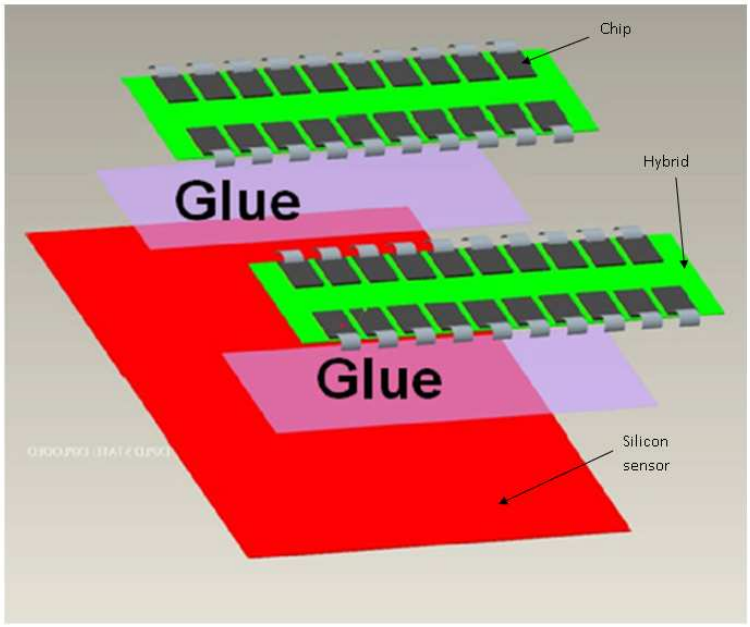


Figure 1.5: Overview of a single sided-module [22]. The red component is the silicon and the green component is the hybrid.

modules cover each side of the stave. An exploded view of a single-sided module is shown on figure 1.5.

- an end-of-stave card for stave readout and control (yellow region) in figure1.4.

The mechanical core of the US stave is made of aluminium cooling pipes embedded inside a sandwich consisting of carbon fibre reinforced polymer, PocoFoam and a carbon fibre honeycomb. A side view of the stave is illustrated on figure 1.6 and shows the different components inside the mechanical core. These components are mounted as follows:

- Facings (carbon fibre) on both sides of the stave on which the bus cable is glued. The facings are to provide stiffness to the stave.
- Core material (honeycomb), between the facings and glued to them to provide stiffness to the overall structure.
- Aluminium cooling tubes embedded and glued onto PocoFoam. The PocoFoam is also glued onto the carbon fibre. The PocoFoam forms a high thermally conductive path between the pipe and the stave facing.

The stave is designed with silicon sensors directly glued on the bus cable. These silicon sensors cover both sides of the stave and are about 10cm x 10cm each in all regions. The length of the short strip is set to 1 m, while that of the long strip is set to 2 m. Apart from the

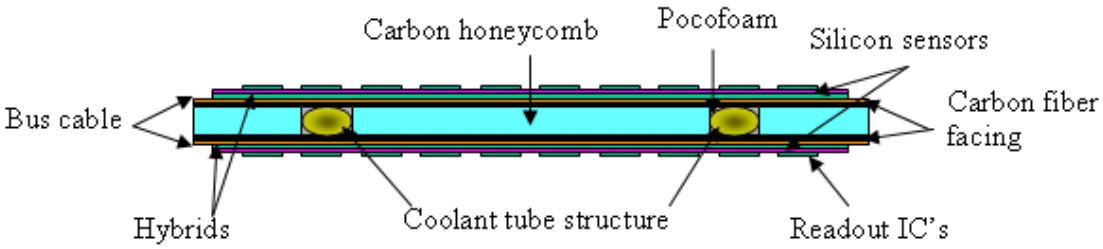


Figure 1.6: Cross section view of the stave [21]

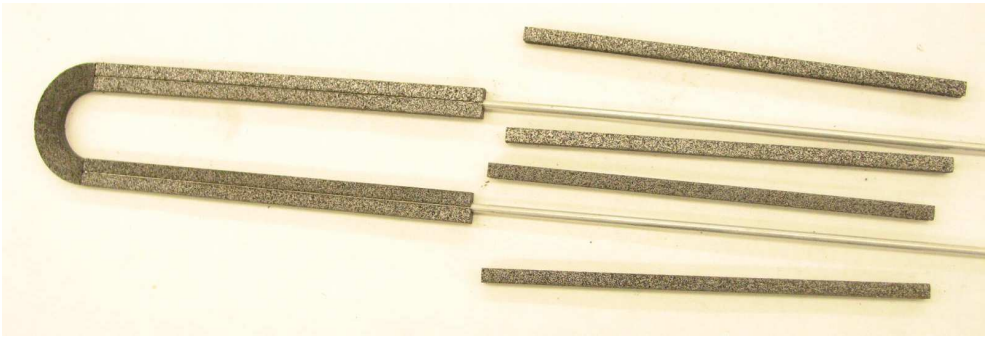

Figure 1.7: The round aluminium tube surrounding by PocoFaom pieces

aluminium tubes and adhesives, the design of the mechanical core utilises only carbon based materials.

## 1.3 Stave prototype

M. Gilchriese et al. prototyped for their studies a series of staves with different shapes of cooling tubes and different coolants. However, presented in this thesis is only the prototype considered qualified for further study. The reasons for the fabrication of the staves are to gain experience with the fabrication techniques of the stave and explore a range of potential coolants and measure their thermal performance

The prototype retained for further studies and improvement is the one illustrated via its fabrication stages, in figure 1.7, figure 1.8 and figure 1.9. PocoFoam pieces are first glued onto a round (outer diameter equal to 4.8mm) and bent aluminium tube with CGL 7018 from AI Technology [23]. The PocoFoam was machined to the required thickness and shape. It originates from POCO graphite foam [24] and has a nominal density of about 0.55g/c$m^3$. The carbon fibre facing material is a K13D2U Graphite Toughened Cyanate Ester Unitape, 80g/c$m^2$, 6" width and cured at 250 °F with EX 1515 resin.

The assembly is then glued directly onto one of the carbon fibre facings with Hysol 9396, figure 1.8 (right). Onto the other carbon fibre facing, the pre-cut honeycomb is glued with the same adhesive, figure 1.8 (left).

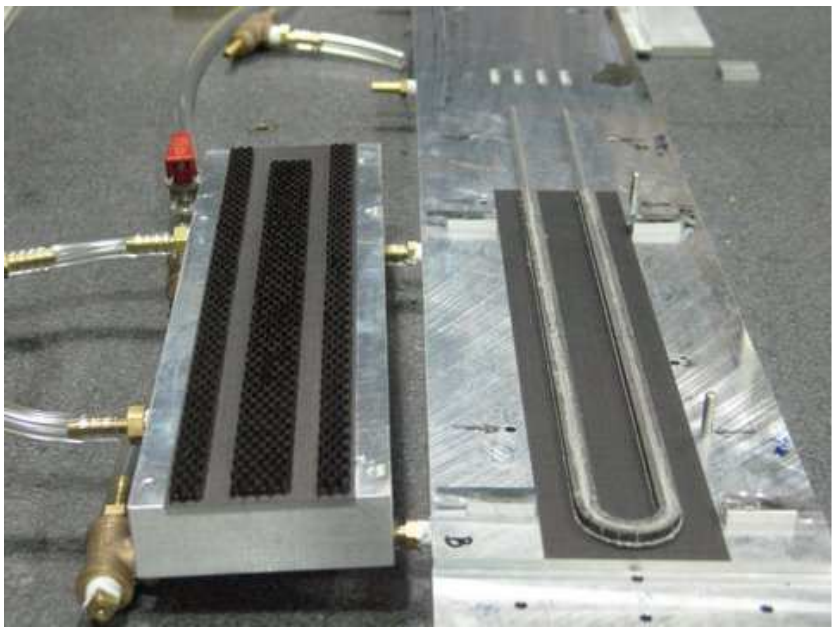

Figure 1.8: Gluing of honeycomb to facing (left). Gluing of round aluminium tube to facing (right)

The two half assemblies are glued together and constitute the mechanical core of the stave. The sides are closed with carbon fibre facing material and the ends with aluminium pieces, see figure 1.9.

## 1.4 Thermal Performance

To evaluate the thermal performance of the stave, heaters, dummy hybrids and dummy silicon detectors were utilised in the following experiment. They were mounted on the bus cable which was glued directly onto the facing material as shown in figure 1.10. This arrangement was made in order to create the expected operational conditions of the stave in the SLHC. In this section only the experimental thermal measurements performed on the prototype consisting of the aluminium cooling pipes with outer diameter equal to 4.8mm and entirely surrounded by PocoFoam are shown. One surface of the PocoFoam was bonded to the facing with CGL-7018 adhesive and the other surface with EG7658[1]. The results of the measurements will be compared with a thermal FEA analysis in order to assist in the validation of the stave modeling process and design improvement.

In normal operation and conditions of the stave in the SLHC, the heat load on the stave will arise from the electronics glued onto the hybrids, the silicon detector heating (leakage current that varies with the amount of radiation damage and voltage), resistive heating in the bus cable and heat loads from the ambient environment of the stave. The heat arising from the electronics contributes significantly more than the other heat sources. Its contribution is

[1] also from www.aitechnology.com

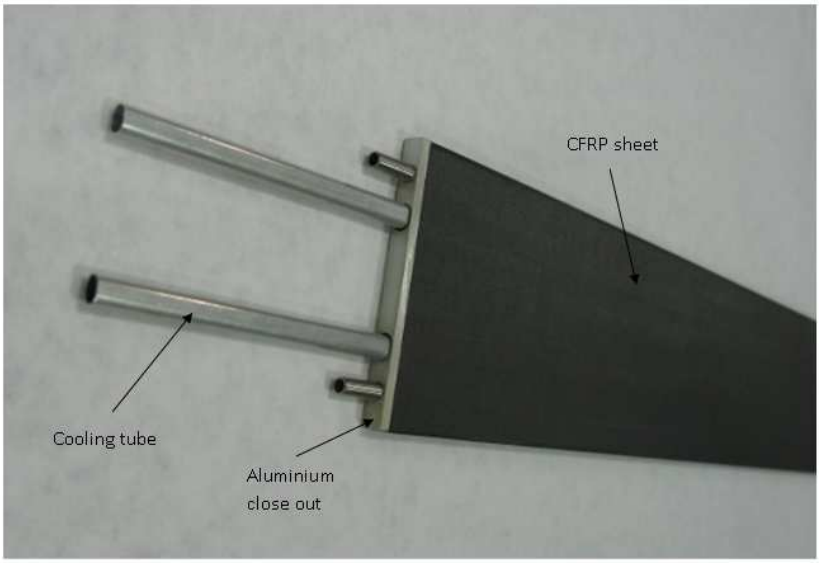


Figure 1.9: Overview of the mechanical core of the stave

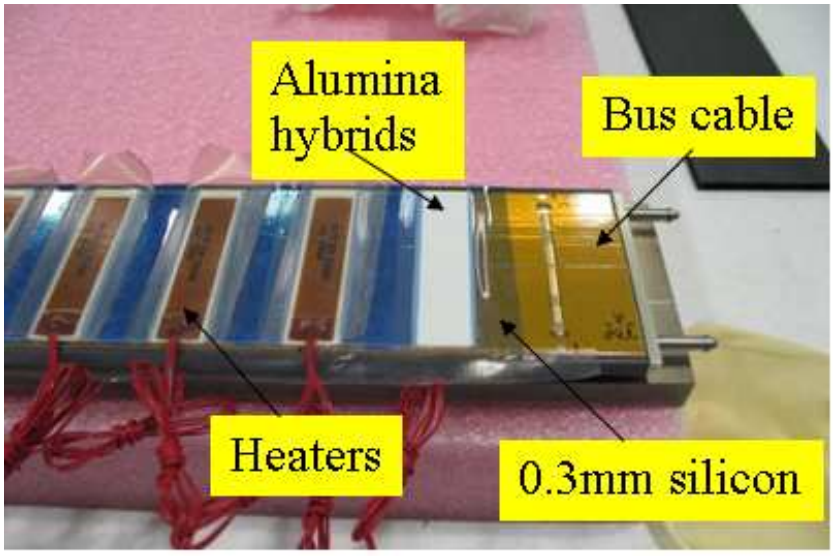


Figure 1.10: Overview of stave attached with bus cable, heaters, dummy hybrids and dummy silicon [21]

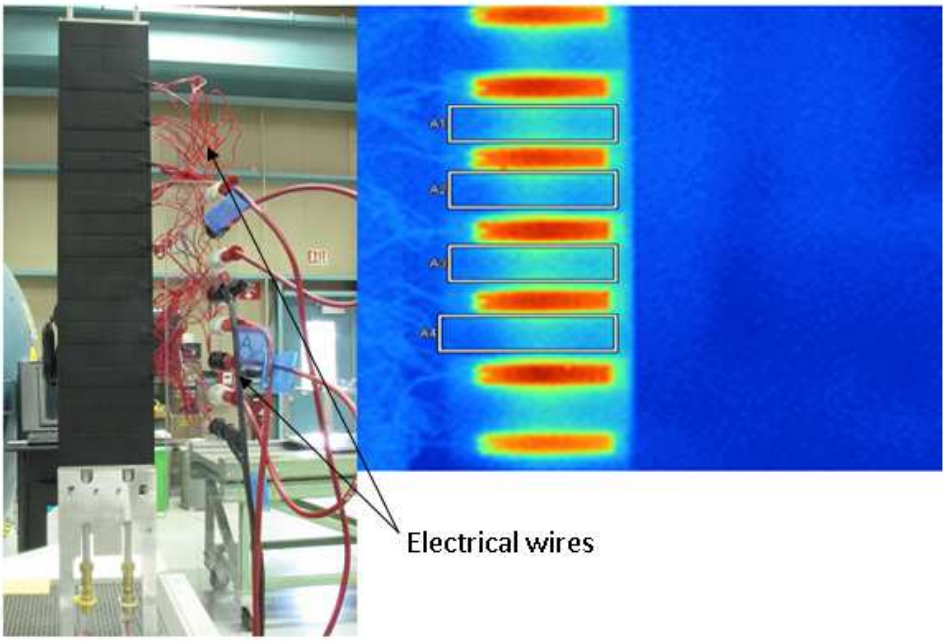


Figure 1.11: Overview of stave under thermal test with an IR camera [21]

estimated to be around 0.3W per chip. The contribution of the other sources is assumed to be 10% of this. Therefore 3.3W (0.33W x 10 chips) is applied onto the heaters representing the total heat load transferred from all heat sources onto half a hybrid (10 chips). Figure 1.11 shows power connections, connections to water cooling at the bottom of the stave and a typical IR image of the stave. Water at approximately room temperature was used for cooling.

It is worth noting that, during the experiment heat was applied on one surface of the stave only. The water inlet and outlet temperatures were measured with sensors placed directly in the water flow and their average measured temperatures were around 20.1°C and 20.3°C for the water inlet and the water outlet, respectively. The experiment was performed with eight heaters powering the side of the stave. An Infra-red (IR) camera was used to measure the temperature of the surface. The temperature measured when no intentional heat was applied was equal to 20.6°C. The difference between the inlet water temperature and the measured temperature on the surface of the stave was, according to M. Gilchriese et al., due to the calibration of the sensors and the IR camera or from a small heat exchange with the ambient environment. The temperature gradient through the stave (between the surface of the stave and the cooling water) was determined using the average temperature of the cooling water (20.2°C). The minimum and maximum temperature raises, when no intentional heat is applied were $\Delta T_{min}$=2.3°C and $\Delta T_{max}$=5.8°C. Heat of 3.3W was applied on the heaters and the maximum and minimum temperatures measured on the surfaces were $T_{max}$=26.4°C and $T_{min}$=22.9°C. The minimum and maximum temperature gradients were calculated to be $\Delta T_{min}$=2.7°C and $\Delta T_{max}$=6.2°C. The results of the measurements are summarised in table 1.1. The measured temperature drops are useful as a comparison to results from a simulation of the stave.

Table 1.1: Measurements of the thermal performance of the retained stave prototype with 3.3W applied per hybrid

| | IR reading | | | Relative to Ave. water temperature | | | Relative to 0W | | |
|---|---|---|---|---|---|---|---|---|---|
| | T min | T max | T ave | $\Delta T$min | $\Delta T$max | $\Delta T$ave | $\Delta T$min | $\Delta T$max | $\Delta T$ave |
| PocoFoam with 4.8mm OD tube | 22.9 | 26.4 | 24.61 | 2.7 | 6.2 | 4.4 | 2.3 | 5.8 | 4.0 |

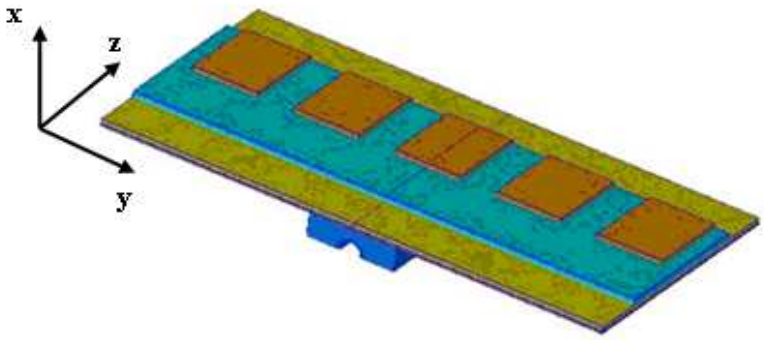


Figure 1.12: CAD simulation of 1/4 of the module. The x-axis goes through the thickness of the stave, y-axis runs parallel to the width of the stave and the z-axis runs parallel to the length of the stave [21]

## 1.5 FEA Thermal Performance

This subsection reports a brief description of the FEA thermal model constructed and compared with the thermal prototype previously discussed. A detailed explanation of the heating parameters is given together with an estimation of the stave thermal runaway power.

### 1.5.1 Thermal Modeling

A 10 cm wide module consists of 10 electronic chips per hybrid with 4 hybrids per module. The total number of chips per module in the US model is then 40. The U-cooling tube runs in the stave's axial direction with a symmetrical transverse spacing, see figure 1.8. In this study, an 1/8th size of the module was used where the stave lateral dimension was divided into two equal transverse thermal zones with respect to the chips, see figure 1.12. The cooling tube was therefore placed 1/4 of the distance from the outboard stave edge.

The finite element baseline parameters used in this model are summarised in table 1.2. Coordinates are $x$ (normal to stave surface) , $y$ (stave's long axis) and $z$ (transverse to stave's long axis), see figure 1.12. The properties of the materials are considered isotropic if nothing else is mentioned.

Table 1.2: Baseline properties used in finite element model

| Item | Thickness (mm) | Thermal Conductivity (W/mK) x/y/z |
|---|---|---|
| Solid Elements | | |
| Al tube OD(2.8mm) ID(2.1mm) | | 200 |
| CFRP (K13D2U) | 0.21 | 1.3/294/148 |
| Cable | 0.125 | 0.12 |
| Silicon sensor | 0.28 | 148 |
| BeO | 0.38 | 210 |
| Hybrid | 0.23 | 5 |
| Chip | 0.38 | 148 |
| PocoFoam (0.9 mm min) | varies | 125/50/50 |
| Adhesives | | |
| Foam to Tube (CGL) | 0.1 | 1 |
| Foam to CFRP facing (CGL) | 0.1 | 1 |
| CFRP facing to cable (ME7863) | 0.05 | 0.8 |
| Cable to silicon sensor (ME7863) | 0.05 | 0.8 |
| Silicon sensor to BeO (ME7863) | 0.05 | 0.8 |
| BeO to hybrid (ME7835-RC) | 0.05 | 1.55 |
| Hybrid to chip (ME7835-RC) | 0.05 | 1.55 |

### 1.5.2 FEA Thermal Model Compared with the Prototype

A Finite Element Analysis was performed in ANSYS on the model and a maximum silicon temperature of 5-6°C (depending on different assumptions about thermal conductivity of facing, foam and bus cable) was observed. This calculated value is the temperature gradient established between the stave surface and the cooling pipe. The value agrees well within around 1° with the maximum gradient temperatures $\Delta T$max=6.2°C and $\Delta T$max=5.8°C relative to the average water temperature and relative to the 0W condition, respectively, see table 1.1. However, the authors point out that the absolute error in the measurements is about 1°C and also the thermal conductivities of the stave components are not well known in order to predict temperatures to an accuracy better than 2°C. In conclusion, despite the agreement between the model and the measurement results, one should bear in mind that uncertainties in the range of 1-2°C exist.

### 1.5.3 Heating Parameters

On one side of a short strip detector, the total heat load is 120 watts, which is equivalent to 40 (number of chips per module) x 0.3W (each front chip) x 10 (modules per stave). As mentioned earlier, the heat load on the stave will arise from the electronics glued onto the hybrids, the silicon detector heating, resistive heating in the bus cable and heat loads from the ambient environment of the stave. The heat load from the environment is considered negligible and not included. The detector self heating is taken from an integrated luminosity of $6000/fb$ [22]. This luminosity roughly corresponds to six years at an average luminosity of $10^{35}/cm^2sec$ with a safety factor of 2. The self heating is numerically equal to $1mW/mm^2$ at 0°C. The power dissipation in the bus cable depends significantly on the details of the implementation of the module powering scheme. It is assumed that the design of the bus cable makes the power dissipation contribution to be insignificant compared to the electronics power and is therefore neglected.

### 1.5.4 Thermal Results

The model was run for different tube inner wall temperatures (-35°C to -5°C) and the results of the peak detector temperature are summarised in figure 1.13. The authors investigated subsequent consequences not only at 0.3W per chip but at lower and higher electronics powers such as 0.125W and 0.5W with a self heating of $1mW/mm^2$ at 0°C. Additionally, electronics power of 0.3W per chip together with self silicon heating of $2mW/mm^2$ at 0°C was investigated. For reference, no silicon self heating was investigated.

Figure 1.13 shows that the baseline design of the stave presented does not have a good headroom against thermal runaway when self heating is considered. For 0.3W per chip with self heating at $2mW/mm^2$ at 0°C, thermal runaway begins around -20°C while it begins at around -14°C for self heating at $1mW/mm^2$ at 0°C. These temperature values are measured on the inner wall of the cooling pipe. Driven by the desire to understand the sensitivity of the design in order to improve it by reducing mass, increasing runaway headroom and reducing sensitivity to material change, M. Glichriese et al., performed more studies. The studies were based on the effect of changing the CFRP facing composition, improving thermal performance of the bus cable and replacing the honeycomb with low density carbon foam.

### CFRP Facing Composition variation

Two specimens of K13D2U of different layup and thicknesses were investigated. Their thermal conductivity in the three directions (x/y/z) and their thickness ($\Delta L$) are K13D2U (1.3/294/148), (0.21mm) and K13D2U (1.3/294/148), (0.42mm) respectively. Carbon fibre reinforced polymer K1100 and carbon/carbon (C/C) with higher thermal conductivities were also considered. The results are presented in table 1.3. The thermal analysis is performed with the tube inner wall temperature of 0°C providing enough initial thermal gradient be-

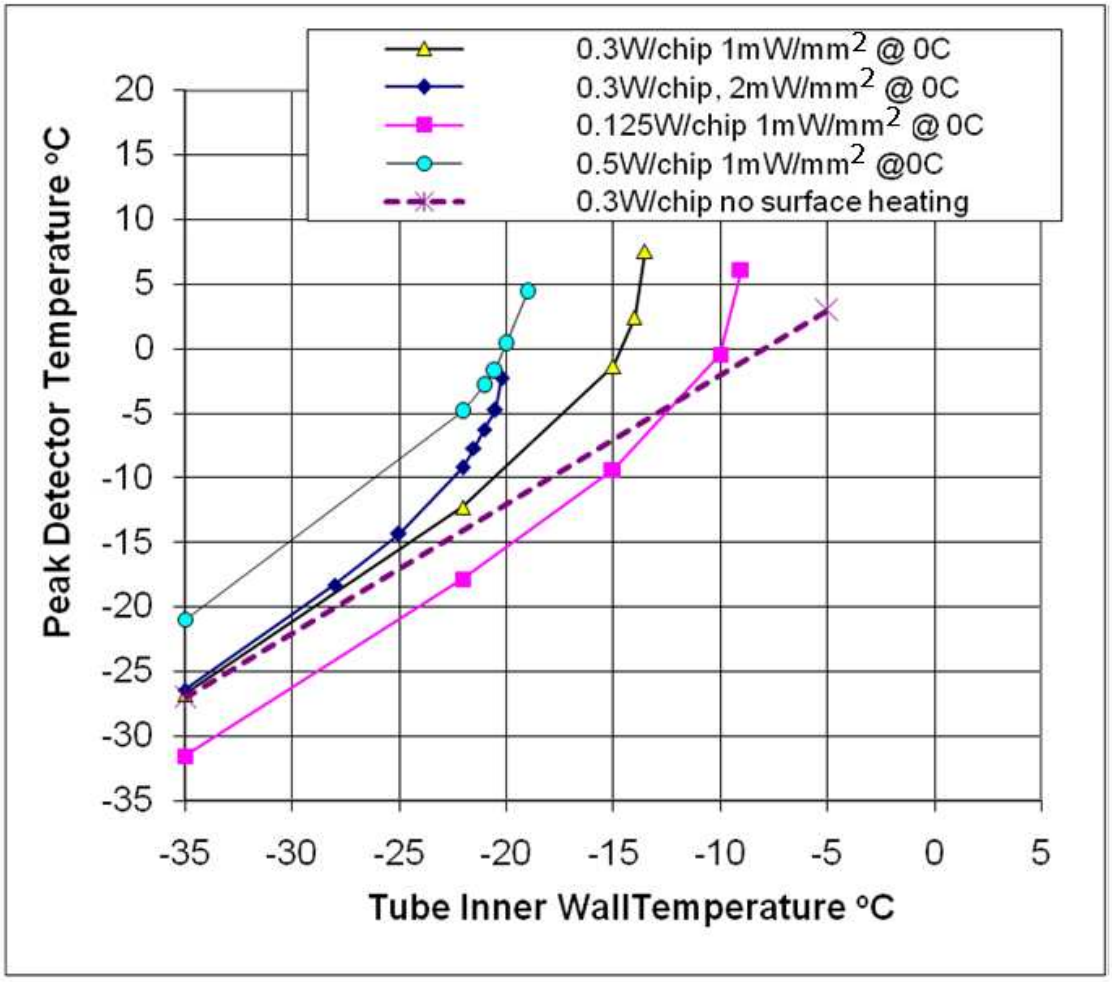


Figure 1.13: Peak detector temperature versus inner wall temperature of cooling tube [21] [22]

tween chip and cooling tube. No detector self heating has been considered. The fibre concentration in the stave longitudinal direction (z) is chosen to provide higher stave stiffness in that direction. '0' is along the stave longitudinal direction.

Table 1.3: Baseline properties used in the finite element model

| Facing conductivity (x/y/z) (W/mK) | Thickness (mm) | Layup | Chip peak $\Delta T$ (°C) | Detector peak $\Delta T$ (°C) |
|---|---|---|---|---|
| K13D2U (1.3/294/148) | 0.21 | 0/90/0 | 8.61 | 7.96 |
| K13D2U (1.3/294/148) | 0.42 | 90/0/0 | 7.93 | 7.24 |
| k1100 (2/367/185) | 0.21 | 0/90/0 | 8.05 | 7.39 |
| C/C (25/367/183) | 0.42 | 90/0/0 | 6.88 | 6.19 |

The use of 0.21 mm thick K1100 as the facing results in 7.71$\%$ less in the detector peak temperature gradient compared to the use of K13D2U of the same thickness. It is worth noting that, despite this performance of K1100 and its significantly higher thermal conductivity than K13D2U, the authors claim that there is no thermal justification to select it, particularly since K13D2U's tensile modulus is within 5$\%$ of K1100. The results show that by doubling the thickness of the K13D2U to 0.42mm, a reduction of the detector peak temperature gradient from 7.96°C to 7.24°C can be achieved. This consequently results in the doubling of the thermal resistance through the stave. A significant improvement of the thermal performance of the stave can been achieved by using 0.42mm thick C/C. The temperature gradient across the stave drops from 7.96°C to 6.19°C by using C/C with a transverse thermal conductivity of 25W/mK.

## Bus cable Variations

The kapton bus cable used in the prototype of the stave is largely covered with layers of copper and aluminium, as shown in figure 1.14.

In the regions having lamination of copper and aluminium both through thickness and in plane conductivities are increased. The authors estimate the through conductivity to be around 0.38W/mK and the in plane conductivity to be up to 80W/mK. In order to be conservative, they use an isotropic value of 0.12W/mK for the bus cable in the FEA with a cable thickness of 125$\mu$m. They claim that changing the thermal conductivity from 0.12W/mK to 0.38W/mK results in reducing the temperature drop across the stave of about 1.5°C.

## Foam versus Honeycomb

The authors also investigate of the possibility of replacing the honeycomb with low density carbon foam (k = 15 W/mK). The low density foam (0.1 - 0.2$g/cm3$) only replaces the honeycomb and the high density foam remains around the cooling pipe. The addition of

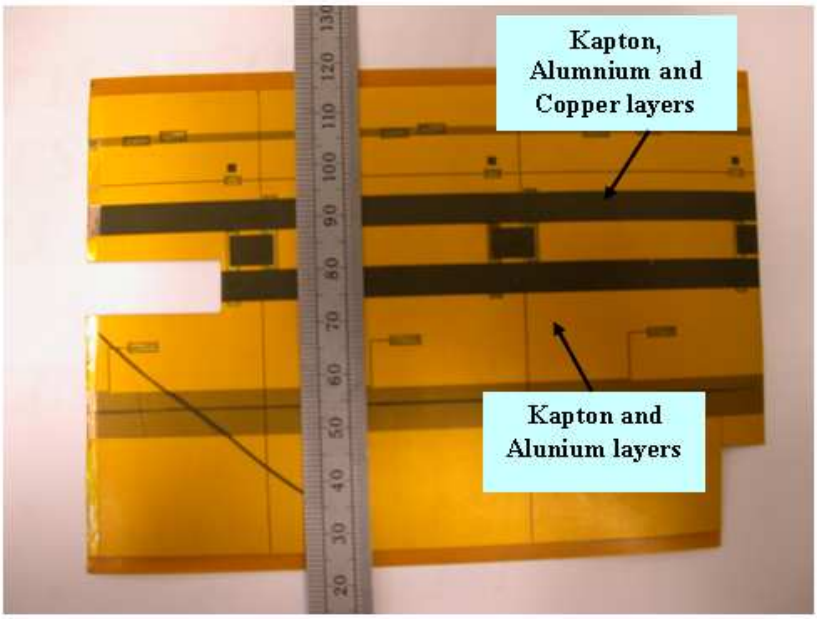


Figure 1.14: Overview of the kapton bus cable

the foam gives substantially better thermal performance since it provides an additional heat conduction path to the coolant tube in addition to the PocoFoam. For the heating assumptions of 0.3W per chip and with self heating at $1mW/mm^2$ at 0°C, the addition of the foam provides about 8 °C more headroom against thermal runaway. It is worth noting that the replacement of the honeycomb by the low density foam does not increase significantly the mass of the stave.

## 1.6 Mechanical Performance

In this section, the concept for the support of the stave is presented together with a brief summary of the work of M. Gilchriese et al. on the mechanical performance of the stave.

The arrangement that supports the stave is a shell like structure, where two layers of staves are supported by a single shell, see figure 1.15. With this design, the facings of the stave can be significantly thin since the stave is supported at several locations. A detailed design of the support of the stave is beyond the scope of this thesis and will not be discussed. After performing an experimental deflection measurement of the stave, M. Gilchriese et al. come to the conclusion that the core shear of the stave is stiff enough and should not be a concern. This high core shear stiffness is due to the honeycomb glued onto the facings, the cooling tube embedded and bonded inside the PocoFoam, which is also glued onto the facings. Because the deflection of the stave is a result of the CFRP facings bent around their neutral axis, M. Gilchriese et al. performed tensile tests on the K13D2U (0/90/0) and obtained a Young's modulus of around 379.2GPa. The Young's modulus is important because it measures the resistance of a material to elastic (recoverable) deformation under load. A stiff material has a high Young's modulus and changes its shape only slightly under elastic loads.

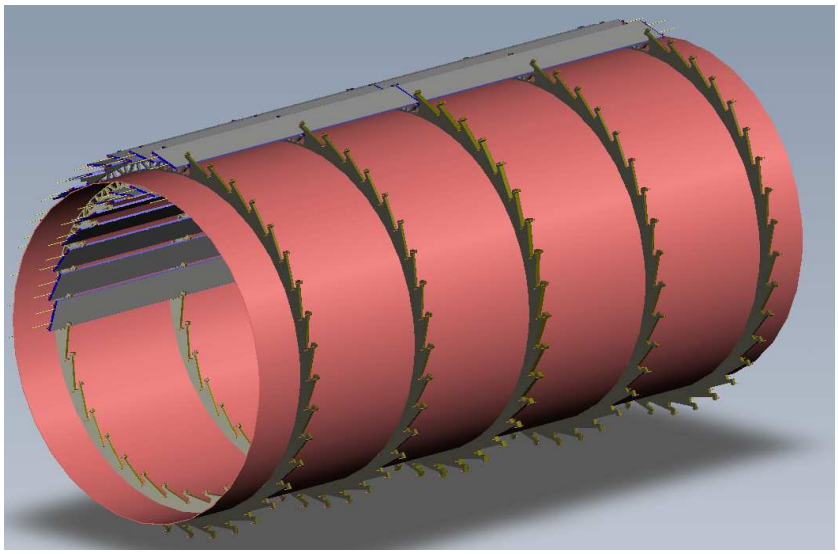

Figure 1.15: Concept for supporting the stave with a thin shell

The Young's modulus value is used in the FEA to mechanically simulate the deflection of the stave. The simulated value of the central deflection is 15% less than the experimentally measured value. The experimental value was performed by performing a four point bend test. A central deflection of 0.118mm was observed for 26.59N load applied at the quarter points.

## 1.7 Aims of the thesis

In the work presented, especially in the CAD thermal performance section, M. Gilchriese et al., makes use of materials that they have not measured the properties of. Material properties such as the Young's modulus and the yield strength. Very often these thermal properties are taken from the available literature. The authors even remark that the conductivities of the stave components are not well understood enough to predict with accuracy the temperatures of the stave components. The FEA results obtained are subsequently not reliable and cannot be trusted for a detailed prediction of the stave's thermal performance. In the mechanical studies, M. Gilchriese et al. make tensile test measurements using the conventional method, which is meant for experiments with high stress and up to failure.

Apart from the aluminium tubes and adhesives, the design of the mechanical core utilises only light carbon based materials. The total mass of the stave is estimated to be between 600g to 800g. The stave is mounted into the barrel such that the total load applied to it consists of its own weight and the force induced by thermal load due to the cooling of the pipe and the heating of the silicon sensors. The magnitude of the force induced by the thermal load is not exactly known, however the maximum stress applied on the stave is estimated by the UK collaborators to be around 30MPa. The cooling of the pipe and the heating of the silicon sensors impose a shear force between the PocoFoam and the cooling pipe. It is therefore essential to understand the mechanical properties of the PocoFoam. The stave will operate at

low stress, <30MPa. It is an imperative to know and understand well the stave mechanical properties at such low stress.

It is clear that to understand well the thermal and mechanical properties of the stave, accurate values have to be used in the finite element analysis model. Accurate values can only be obtained by utilising reliable measurement systems capable of obtaining repeatable results. The aims of this thesis are therefore to design and construct reliable thermal and mechanical measurement systems and apply them to the measurements of the ATLAS upgrade structures. Basic concepts of a direct in-plane thermal conductivity measurement system are presented in chapter 3 together with its detailed operation procedure. The measurement system is used to perform measurements on low density carbon foam, carbon fibre reinforced polymer, Thermal Pyrolytic Graphite and Diamond. In chapter 4, concepts of a transverse thermal conductivity measurement system are presented together with its mode of operation. The measurement system is used to perform measurements on adhesives and solid materials up to a few microns thickness. The measurement system is slightly modified and used to perform measurements on low density foams with thickness up to 25mm. The design concept of a jig for mechanical measurements at low stress is presented in chapter 5. The jig is adapted to a conventional testometer and used to measure Young's moduli of low carbon foams and carbon fibre reinforced polymers. In order to understand the sensitivity of the design, a sandwich arrangement of stainless steel, low density carbon foam and carbon fibre reinforced polymer is constructed in chapter 6 and thermo-mechanical measurements are performed on the sandwich under a shear force. Finally, a simulated model of a low density carbon foam is studied in chapter 7, in order to understand the relationship between density and thermal conductivity of low carbon foams.

# Chapter 2

# Materials & Manufacturing Process

Many materials have been investigated for the design of the mechanical core of the stave, among them Silicon Carbide foam (SiC foam), carbon foams including Allcomp foam and PocoFoam to surround the cooling pipe and Carbon fibre reinforced polymer (CFRP), Thermal Pyrolytic Graphite (TPG) and carbon/carbon as facings. Only PocoFoam or Allcomp foam and carbon fibre reinforced polymer are important for this thesis because they have been selected for the design of the mechanical core of the stave. The selection of PocoFoam and Allcomp foam are motivated by their high thermal performances (high thermal conductivity primarily in the z direction), their low density and radiation hardness. PocoFoam has a vast range of applications including thermal protection systems, thermal management systems, solar radiators, industrial heat exchangers, electronics cooling and noise absorption. The selection of carbon fibre reinforced polymer is due to its light weight, high Young's modulus, high thermal conductivity and radiation hardness. Its application ranges from sporting goods to aircraft structures. Different glues such as Hysol EA9396, Dow Corning SE4445 and Epolite FH-5313 are selected for the assembly of the stave components. The glues are selected for their attractive thermal performance and radiation hardness. In this chapter, carbon graphite foams and CFRP will be introduced followed by their manufacturing processes. The selected glues will be presented.

## 2.1 Foams

Foams are cellular materials and are generally classified by material type (metal, ceramic, polymer or natural) and general structure (open or close cells). Open celled foams have interconnected cells allowing the passage of gas or fluid through the void space from one cell to the next. Whereas, closed celled foams do not have interconnected cell openings. Gas can be trapped inside the cells. Although foams typically consist of one type of cellular structure, it is likely to experience foams with both structures inside a specimen.

Depending on its crystallographic structure, carbon can be thermally insulating or conducting [25]. Carbon is element 6 of the periodic table and has limited long range or-

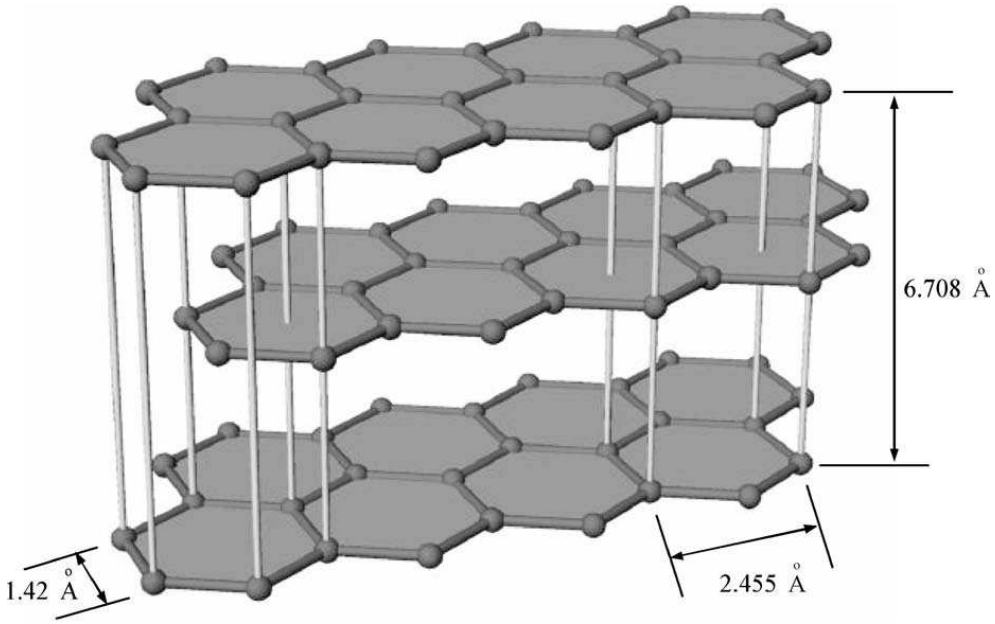


Figure 2.1: Planar structure of ABA stacking sequence [26]

der. Graphite is an allotropic form of carbon consisting of layers of a hexagonal array of carbon atoms which can also exist in a rhombohedral form [25]. In the hexagonal form, graphene layers are arranged parallel to each other in an ABA stacking sequence, see figure 2.1. The layers exhibit long range order which contributes to high thermal conductivity of graphite [26]. The crystallographic nature of graphite makes the thermal conductivity in the planar directions two orders of magnitude higher than in the perpendicular plane.

### 2.1.1 Foam structure

Foams are characterised by several elements. The main components are ligaments (also referred to as struts), cells and nodes, as shown in figure 2.2. The size, shape, direction, anisotropy and uniformity of these elements have significant influence on the bulk properties. The ligaments and nodes establish the framework and structural integrity of the foam, while the cells contribute largely to the porosity and density of the bulk material.

Ligaments of graphite foams may have a highly aligned graphitic structure, see figure 2.3. Graphene layers are typically oriented parallel to the cell structure and can have extremely high thermal conductivity (up to 2300 W/mK), which contributes to the high bulk thermal conductivity of the foams.

Although foams may contain small fractions of both open or closed cells at the same time in a general structure, this thesis focuses exclusively on graphite foams with open celled structures. Cell shapes of graphite foams are typically ellipsoidal or spherical and the cell sizes vary depending primarily on the processing conditions. Because the nodes are the junctions where ligaments come together from different directions, graphite planes get disrupted and the nodes tend to be more isotropic compared to ligaments [28].

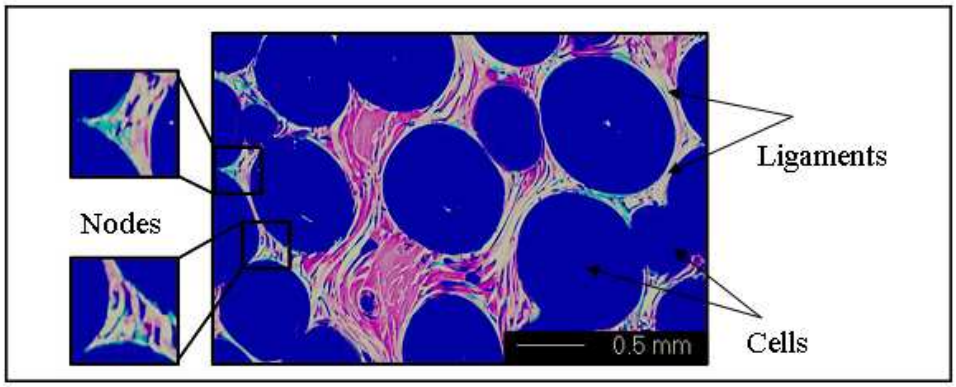


Figure 2.2: Overview of ligaments, cells and nodes inside graphite foam [27]

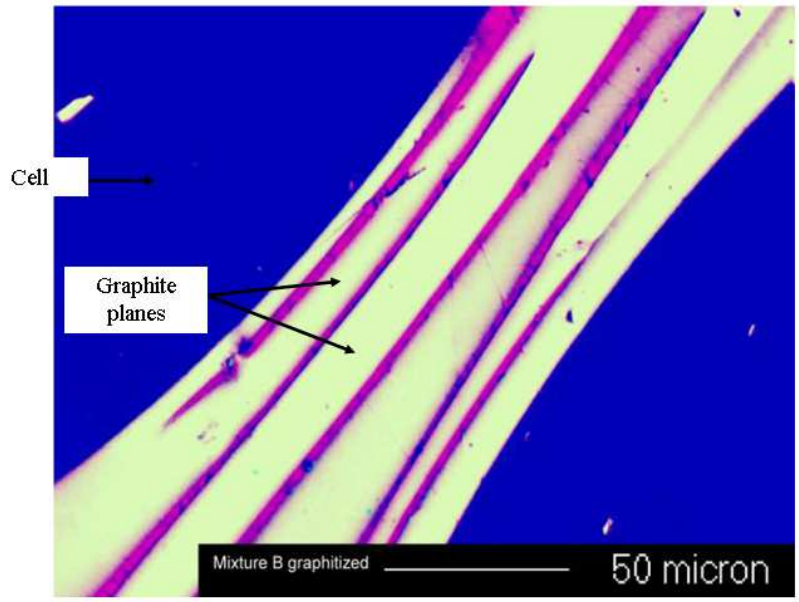


Figure 2.3: Optical view of graphite foam ligament structures [27]

### 2.1.2 Graphite Foam Development

As Klett James reports well [26], reticulated vitreous carbon foams (a network resembling glass), also called glassy carbon foam, were developed in the 1960s to obtain a carbon skeleton but with poor thermal conductivity. Reticulated Vitreous Carbon (RVC) foams are void of graphitic structure and have large openings and linear ligaments, see figure 2.4. They were manufactured by heating a thermosetting organic polymer foam (specially by carbonising polyesters, polyurethanes or phenolics). Ligament surface cracks occur during the heat treatment process when molecular weight changes cause shrinkage. M. D. Sarzynski, K. Lafdi and O. O. Ochoa [29] report that microscopic observations of the ligaments indicate that the surface cracks are filled when the microstructure is coated. They claim that a 10$\mu$m copper coating can significantly increase the thermal conductivity of the carbon foam up to three orders of magnitude. The commonly used method of coating foams is by chemical vapour deposition (CVD). Since the open pore cellular materials are used as heat exchangers they may also require skins to contain the heat exchange media and/or to contain the pressure within the porous core. Attachment of a skin or skins to foam materials was often problematic because the surface of the foam material is composed of a multitude of discreet points or small areas rather than a continuous surface. In order to overcome this challenge, in situ formation of the skins by chemical vapour deposition has been attempted with little success. The results were that either too much of the "coating" entered into the porous material, increasing its weight beyond the usable range; or repeated cycles of deposition and machining were required at great cost. In 2005, Williams et al. [30] invented the thermal spray process to form skins in situ on rigid open and closed-cell materials and claim that the invention overcomes the difficulties encountered by the CVD based process. In principle, it is possible to thermally spray any material with a stable molten phase. Deposition rates are very high in comparison to alternative coating technologies. In the application of the invention, the processing parameters such as viscosity are optimised to control penetration of the "coating" into the foam while still achieving substantially complete bonding throughout the surface of the core of the foam.

A decade after the development of Reticulated Vitreous Carbon foams, production of carbon foams from alternative precursors was achieved. One of the major achievements was production of pitch based foams. Pitch is a residue from the pyrolysis, (decomposition of a chemical by heat), of an organic material or tar distillation and is essentially hydrocarbons and hydrocyclic compounds [26]. Pitch is a thixotropic fluid, which is a gel like substance at rest but fluid when agitated and has high viscosity at its softening point [31]. The first pitch based foams were developed by Bonzom et al., [26] with petroleum derived pitch and in late 1990s Stiller et al. [26] produced the first coal derived pitch foams at West Virginia University.

Mesophase pitch has a complex mixture of hydrocarbons and contains anisotropic liquid crystalline particles [26]. Hager et al. [26] used this precursor to produce graphite foams in the early 1990s at the Wright Patterson Air Force Base Materials Laboratory. Later in 1997, K. James [32] at the Oak Ridge National Laboratory (ORNL) reduced significantly the production steps of the mesophase pitch based graphite foams, eliminating traditional blowing and stabilisation steps, see figure 2.5. They reported graphite foams have bulk

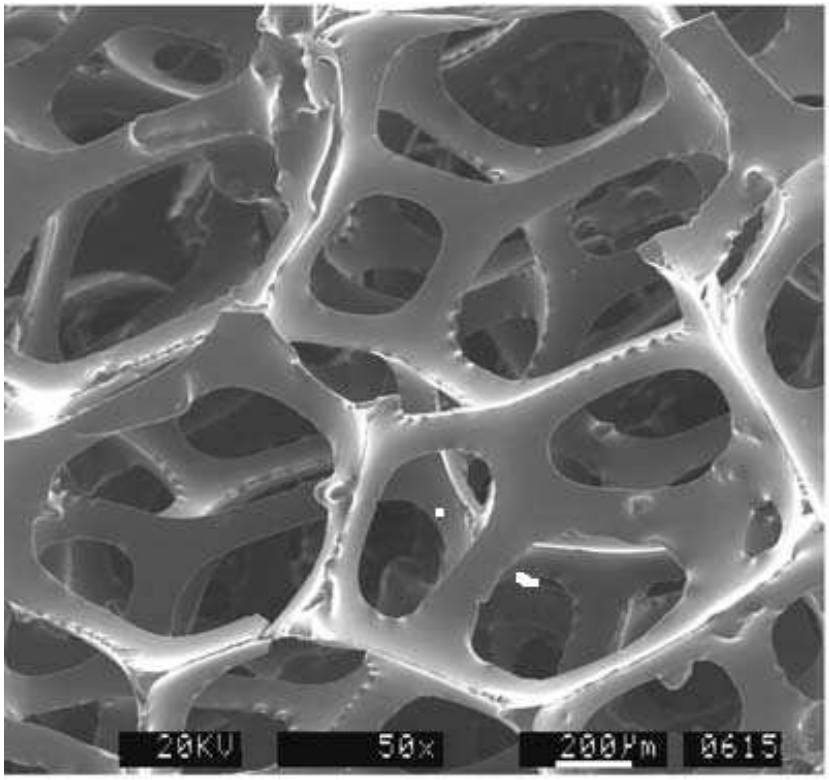


Figure 2.4: Scanning Electron Microscopy (SEM) image of reticulated carbon foam [26]

thermal conductivities greater than 40 W/mK (conductivities up to 180 W/mK have been recently measured).

### 2.1.3 ORNL Graphite Foams Production Method

Manufacturing of ORNL graphite foam is not complex and is performed following three major stages: Foaming, Carbonization and Graphitization heat treatment. The aim of the foaming is to create the general structure of the foam, whereas the objectives of carbonization and graphitization are respectively to remove the residual volatile material and increase the strength of the foam [26].

The foaming process begins with heating a mesophase pitch precursor in an oxygen-free environment to about 50°C above its softening point. When the pitch melts, the pressure and temperature are increased in the furnace at a controlled rate. This increased pressure is called the "processing pressure". During the melting process, the pitch evolves low molecular weight species. The pitch decomposes and begins to release volatile gas bubbles at nucleation sites on the bottom and sides of the crucible and rise to the top, beginning to orient the mesophase crystal in the vertical direction. These bubbles grow upward and with time a significant amount of the mesophase crystals are oriented vertically. At elevated temperatures, the mesophase begins to pyrolyse (polymerise) and creates more volatile species. This pyrolysis weight loss (dependent of the precursor and very rapid sometimes) is accompanied

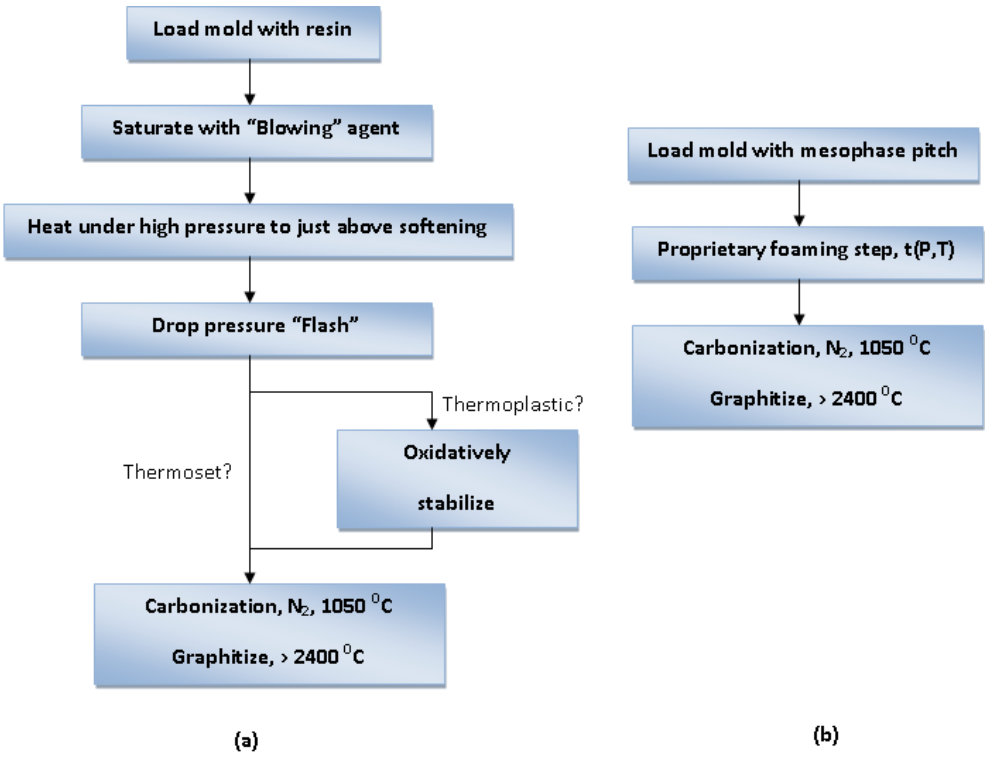


Figure 2.5: Foam producing diagram; (a) Traditional blowing technique; (b) Process developed at ORNL [32]

by an increase in the molecular weight of the precursor and increases the melt viscosity of the liquid mesopahse. With the rapid formation of gases, the increase in viscosity tends to capture the bubbles, forcing the material to foam in the opened direction (called the $z$ direction) of the crucible. The temperature of the furnace is further increased such that the viscosity of the pitch raises until it has enough cross linked ligaments and become infusible (cannot be melted). Typically, the foam presents uniformly shaped bubbles with a normal distribution, see figure 2.6. Properties such as average pore size, orientation and distribution are determined primarily by the pitch viscosity and processing pressure during foaming. It is worth noting that the cells are not spherical but elongated in the $z$ direction for the mesopahse foam, with an accompanying anisotropy of properties in the $z$ direction compared to those in the $x$-$y$ plane.

After formation of the structure, the foam undergoes at a very slow rate a carbonization process performed normally between 600°C and 1000°C to yield a relatively pure carbon foam. Carbonization is the process that increases the carbon content of the foam through transforming organic material in an inert atmosphere [26]. The foam is an excellent insulator at that stage with a bulk thermal conductivity around 1.2 W/mK with a density of 0.5g/cc. With the absence of oxygen during the foaming process, the mesophase crystals of the carbonized foam are not inhibited and can grow to very large sizes.

The final stage of foam production is the graphitization heat treatment process to convert the carbon foam to a highly graphite foam. This operation is normally conducted at temperatures above 2800°C under an argon purge. The resultant graphite crystals are highly aligned

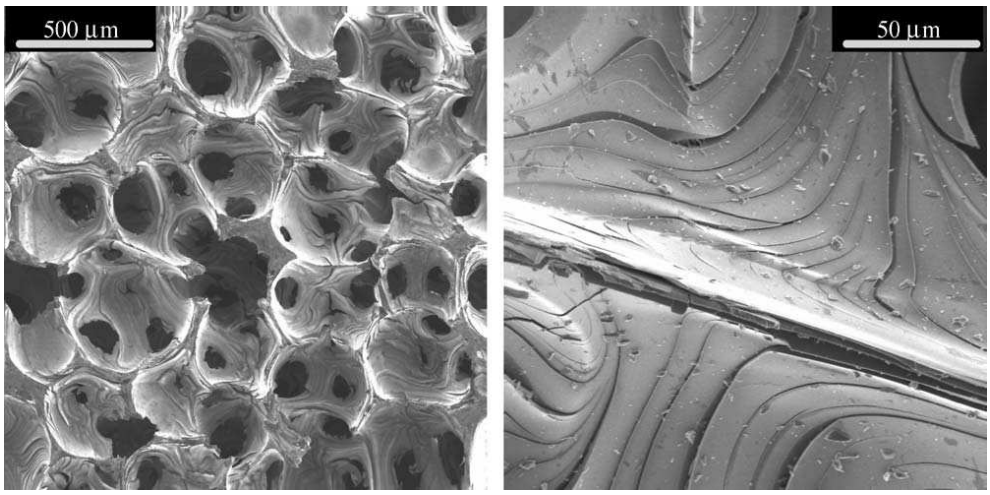


Figure 2.6: SEM images of mesophase pitch based foams [26]

and significantly larger than those found in mesophase derived carbon fibres. Consequently, production of graphite foam with this method yields ligaments which are more thermally conductive than even the best mesophase pitch based graphite fibres.

Presently, the graphite manufacturing process is licensed to Viatherm, Inc. and Poco Graphite, Inc. (manufactured as PocoFoam).

PocoFoam shows an organised structure throughout the junction regions with little folding and all the microcracks running parallel to the graphite planes. Together with little dislocations in the ligaments (dislocation can serve as stress concentration points and initiate cracks [32]), this would lead to improved heat transfer in the PocoFoam. However large pores are evident in the ligaments, see figure 2.7. It is clear that the ligaments will be more conductive than the junctions because of folding, microcracking and dislocations in the junction regions which inhibit heat transfer.

### 2.1.4 Open Celled Foams Properties

Graphite foams are complex in their structure and difficult to model accurately because of the randomness and variety of the cell sizes and configurations; cell size, cells number and shape can vary depending on the analysed location. The bottom portion of graphite foams are reported to have a slightly lower percent porosity compared to the middle or top portion due to gravity during the foaming process [33]. With $x$ and $y$ planes being constrained by the pan (restricting growth), the $z$ direction becomes the foaming direction. The cells appear ellipsoidal when viewed in the $x$ and $y$ planes and spherical in the $z$ plane.

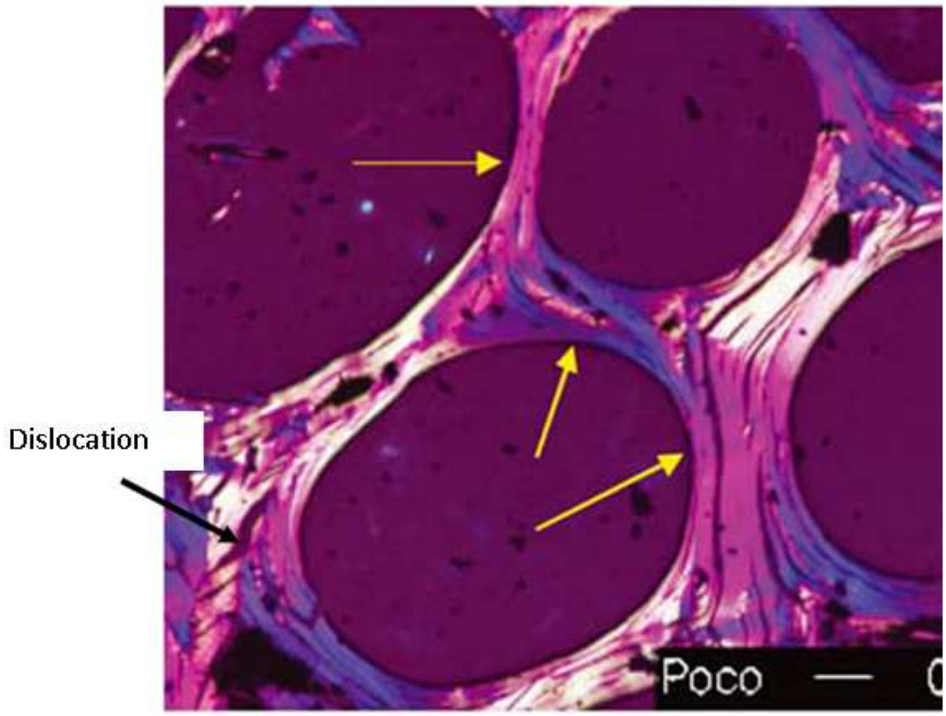


Figure 2.7: Optical micrograph of PocoFoam illustrating high order in the junctions with significant porosity in the ligaments and junctions [27]

#### 2.1.4.1 Thermal Conductivity

The bulk density of graphite foams strongly influence their thermal conductivities. Klett J. W. et al. [27] report after a series of studies on different foam densities, that thermal conductivity increases with the increase of density. This effect can be explained by the presence in the foam of more solid graphite with increase of density, which transfers heat more efficiently than air. Klett J. W. et al. also claim that foam thermal conductivities are very dependent on the process used. They show on figure 2.8 the effects of graphitization rate on thermal conductivity for an ORNL graphitic foam, and defend that the results are valid for all foaming processes.

Thermal conductivities in the $x$ and $y$ directions are considerably lower than in $z$ direction, and are independent of the graphitization rate; whereas the thermal conductivity in z direction decreases with increasing of graphitization rate. It is reported by B. T. Kelly [34], that the strain energies during the graphitization process can be high and result in microcracks, lattice damage and delamination of graphite planes. He claims that graphitization stresses will tend to reduce the thermal properties in the direction parallel to the planes of the graphite, because thermal properties in that direction are much higher than those normal to the planes. However, graphitization will have minimal effect in perpendicular planes where there is strain relief. Knowing that the orientation of the graphitic crystals occurs along the $z$ direction, it is predicted that heat treatment affects the $z$ conductivity with little effect in the $x$-$y$ directions. J. Mueller [35] explains the difference of thermal conductivities between the $z$ and $x$-$y$ directions by the fact that thermal conduction along the graphite planes is

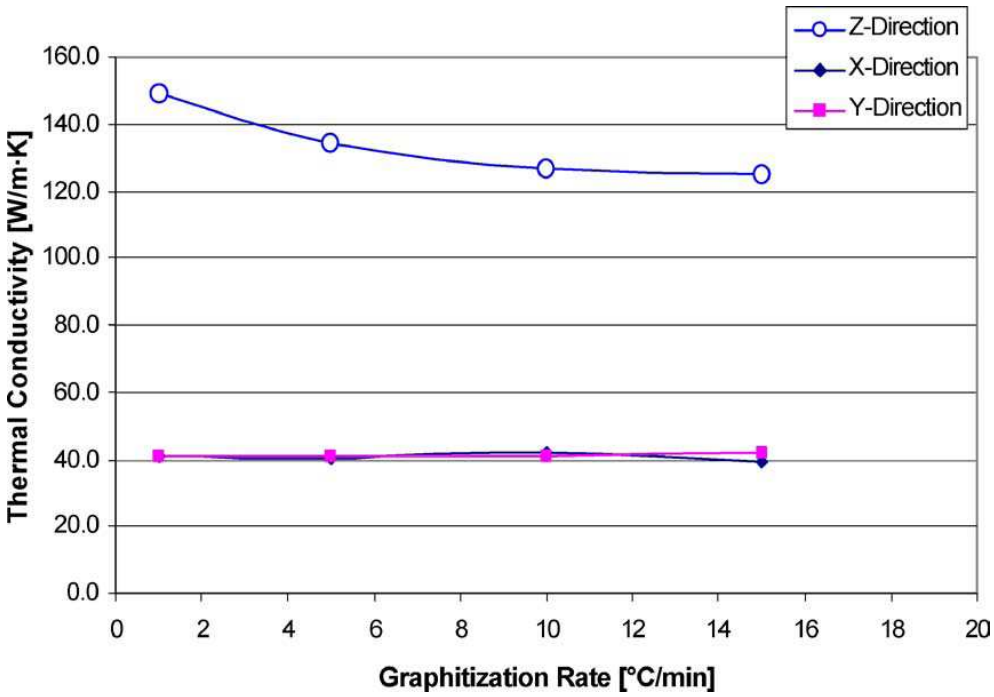


Figure 2.8: Effect of graphitization rate on thermal conductivity

less complicated due to elongation of the ligaments in the $z$ direction. She claims that the path of the heat flowing through the graphite ligaments is less tortuous compared to the $x$-$y$ directions, see figure 2.9.

#### 2.1.4.2 Mechanical Behaviour

P. R. Onck et al. [36] subjected an open cell nickel-chromium foam to micro-structural characterisation and concluded that the failure process of the open cell foam was observed to be ductile. It is clear that metal foams are different from carbon foams. However, the microstructural characterisation of nickel-chromium foam can be used as an important tool to understand the mechanical behaviour of carbon foam. The knowledge acquired through P. R. Onck's et al. study will be used to explain the mechanical behaviour of ORNL foam in chapter 5.

The Ni-Cr foam analysed is a Recemat foam (manufactured by Recemat International BV, The Netherlands) and has a chromium content between 20 and 40 as a percentage of weight with a density of 0.60-0.65$g/cm^3$. Two circular notches were machined in the specimens to ensure that damage development remains localised between the notches. The dimensions of the specimens were 10mm wide, 4mm thick, (giving a cross sectional area of 40 $mm^2$), 20mm high and with a notch radius of 1.5mm. Tests were performed in situ. P. R. Onck et al. report in figure 2.10 the force displacement curves of two tensile fracture tests. The blue curve illustrates a common stress-strain curve of foams and the red curve (the curve with the letters a, b, c and d on) displays the response of the Ni-Cr foam to the tensile test, see figure 2.10.

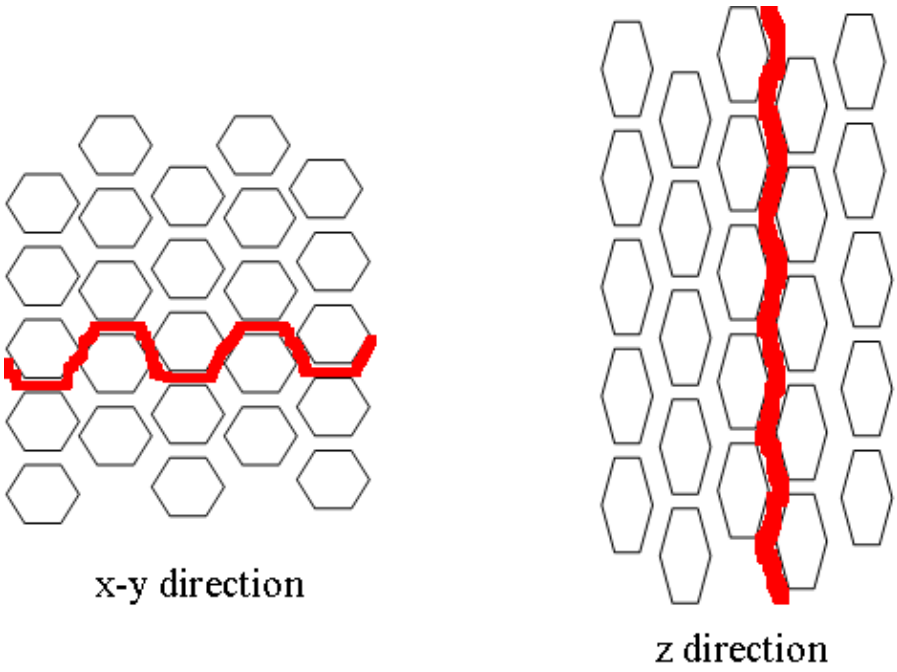


Figure 2.9: Overview of heat paths in different directions

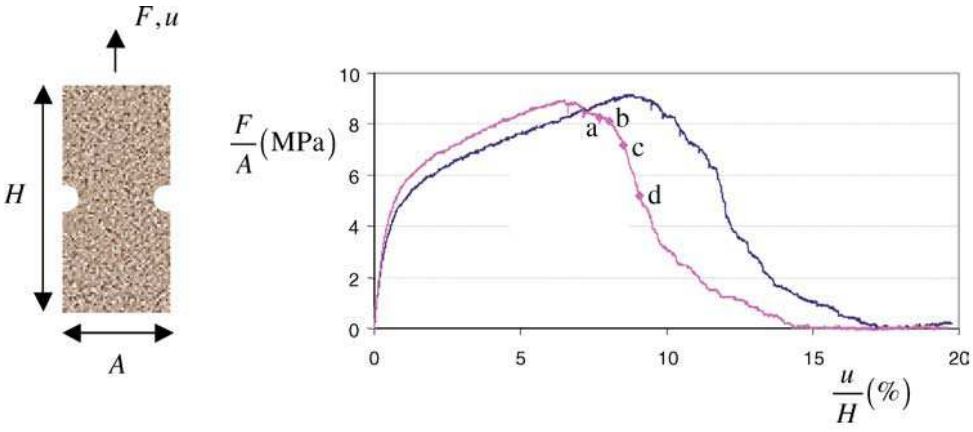


Figure 2.10: Illustration of the linear elastic region obtained at low stress [36]

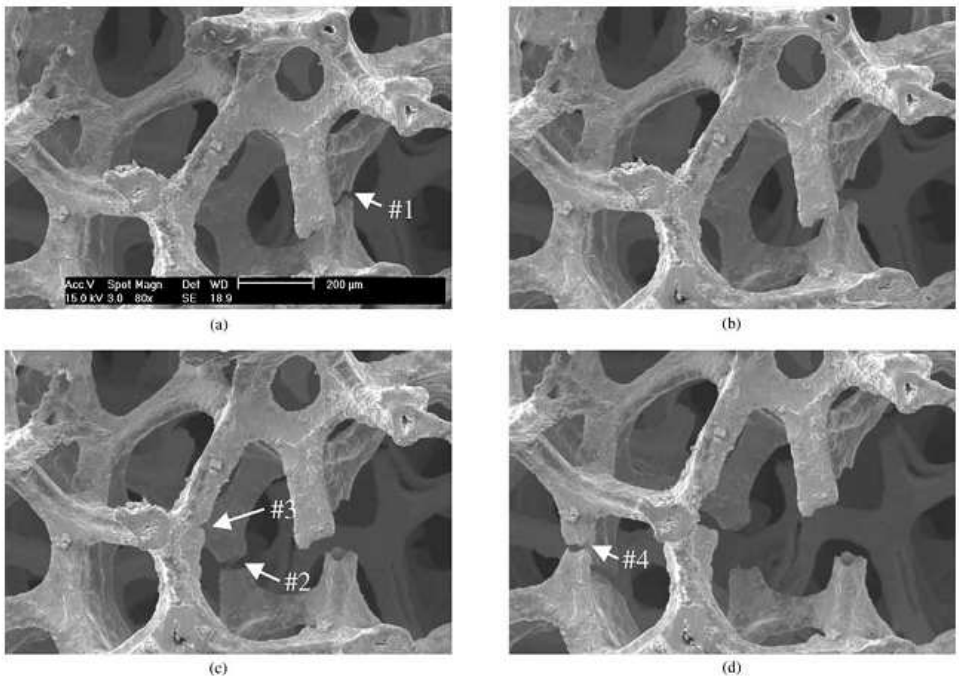


Figure 2.11: In situ snapshots during damage development in the Recemat specimen. The images (a) through (d) correspond to the moments depicted on the stress-strain curve of figure 2.10 [36]

The curves show an elastic region (less than 5 MPa), a linear hardening regime followed by failure at a normalised peak load of approximation 9 MPa. These curves evidence the presence of an Hookean region and the possibility of determining Young's modulus at very low stresses. The four snapshots (denoted a - d) along the unloading region of the red curve (figure 2.10) represents four different stages during the tensile test. (a) shows the moment where the crack begins in a strut (#1) in the vicinity of the right notch, as shown in figure 2.11a. (b) is the moment where the failure in the strut is complete, as shown in figure 2.11b. The gap between the two parts of the strut is increasing till (c), where a second strut (#2) fails, as shown in figure 2.11c. At that point a surface crack appears on a third strut (#3) due to a bending moment that is increasing due to the previous failed struts. On figure 2.11d, struts #3 and #4 fail. It is clear that the failure occurs perpendicular to the tensile direction. One crack forms at the edge and migrates into the foam due to a bending moment imposed by the separation of the parts of the failed strut.

In conclusion, it is worth noting that, it is possible to obtain a linear elastic region for a nickel-chromium foam at low stresses and calculate the Young's modulus. This is supposed to be possible for many types of foams, especially for PocoFoam. Bearing that in mind, in chapter 5 the linear elastic region for PocoFoam will be obtained and the Young's modulus calculated.

### 2.1.5 Allcomp foam

Allcomp foam is manufactured by using a reticulated vitreous carbon (RVC) foam and coating it with carbon by chemical vapour deposition (CVD). The material is annealed until graphite is obtained. The process time is about 4 to 8 weeks depending on specification. The manufacturer claims that the foam is isotropic with densities ranging from 0.09g/c$m^3$ to 0.40g/c$m^3$ with thermal conductivities between 10W/mK and 75W/mK, at room temperature.

## 2.2 Carbon Fibre

A large number of commercial carbon fibres are manufactured by first converting a carbonaceous precursor into fibre form. After that, the precursor is crosslinked in order to render it infusible. In the last process, the crosslinked precursor fibre is heated at temperatures from 1200°C to approximately 3000°C in an inert atmosphere to drive off nearly all of the non-carbon fibre [41]. The carbon fibres final properties are greatly determined by the material, the process and the conditions used to form the precursor. The fibre used in the manufacturing of the CFRP facing that is used in the UK design is a coal tar pitch-based carbon fibre (K13C2U)[1]. The fibre diameter is 10$\mu$m with thermal conductivity equal to 620W/mK.

Almost all commercial fibres are produced using one of the three techniques: melt spinning, wet spinning or dry spinning. In the melt spinning process, the precursor is melted and forced out through a spinneret containing numerous small capillaries. As the precursor exits these capillaries it cools and solidifies into fibre form. The wet spinning process is performed by using a concentrated solution of the precursor and extruding it through a spinneret into a coagulation bath. Because the solvent is more soluble in the coagulation fluid than it is in the precursor, the precursor is precipitated into fibre form as soon as it comes out of the capillaries. In a dry spinning process, a concentrated solution also is forced through a spinneret into a dry chamber. In this case, the solvent evaporates and the precursor precipitates into fibre form. The melt spinning process has the advantage of converting a pure precursor directly into fibre form and does not involve the expense of solvent recycling and recovery. This process is therefore the preferred fibre formation. However, either wet or dry spinning must be employed if the precursor degrades at or near its melting temperature. In this section, only the process used to form the two dominant classes of carbon fibres, polyacrylonitrile-based (PAN-based) and mesophase pitch-based (pitch-based) are detailed.

### 2.2.1 PAN based Fibre

A PAN based carbon fibre is produced by oxidative stabilization of a PAN precursor which is followed by a two-stage carbonization process with an additional ultra high temperature heat

[1] www.mitsubishichemical.com

treatment stage to manufacture a high modulus carbon fibre. In other words, it is the removal as a gas of all elements other than carbon in the PAN based filaments and carbonizing them to form as much graphitic carbon as desired.

#### 2.2.1.1 PAN Precursor

Among the varieties of precursors used for the production of carbon fibres, PAN is one of the most popular. PAN has generally a carbon content of 68% and PAN precursors have a carbon yield of around 55% coupled with the ability to produce high modulus fibres.

#### 2.2.1.2 PAN Homopolymer

The PAN precursor needs to be polymerised for carbon fibre production into PAN homopolymer. Homopolymer is a compound produced by polymerisation and it is constructed of identical monomers or macromolecules consisting of a single type of building unit. The PAN homopolymer is a very difficult polymer to process into carbon, since its oxidisation rate rises very rapidly with temperature and the oxidative stabilization reaction stage becomes difficult to control due to sudden and rapid evolution of heat, coupled with a relatively high initiation temperature. This rapid evolution of heat is undesirable because it can lead to chain breaking resulting in poor fibre properties. This exothermic reaction is controlled by suitable co-monomers such as itaconic acid (ITA), methacrylate (MA), vinyl esters and more. The co-monomers lower the glass transition temperature and affect the reactivity of the polymer structure [37].

#### 2.2.1.3 Spinning of PAN Fibres

The spinning of PAN fibres is made by dissolving PAN copolymer ($\sim 95\%$ PAN homopolymer) in a solvent such as dimethylformamide, dimethylacetamide, sodium thiocyanate or zinc chloride to form a highly concentrated polymeric solution. The solution is thereafter pumped through a spinneret (consisting of many fine capillary holes) into a coagulation bath that extracts the solvent from the fibre [38]. That phase of the process (extraction of the solvent) has a large impact on the morphological structure of the filaments and results in filaments with circular or dog-bone shaped cross-sections (formed due to rapid and incomplete solvent extraction) and some voids in the filaments. D. D. Edie reports [37] that, because of the high concentration of the solvent in the coagulation bath, mass transfer at the fibre/liquid interface is relatively slow in the wet spinning process. The solvent can therefore diffuse radially through the solidifying fibre quicker than it can diffuse away from the fibre surface. This results in a uniform solvent concentration across the fibre's cross section during solidification resulting in uniform shrinking in the radial direction, giving the circular cross section that is characteristic of wetspun PAN. Furthermore, he claims that in case the concentration of the polymer in the spinning solution is low, a relatively rigid fibre skin can also form in this process before the centre of the fibre has solidified, yielding a dogbone-shape fibre.

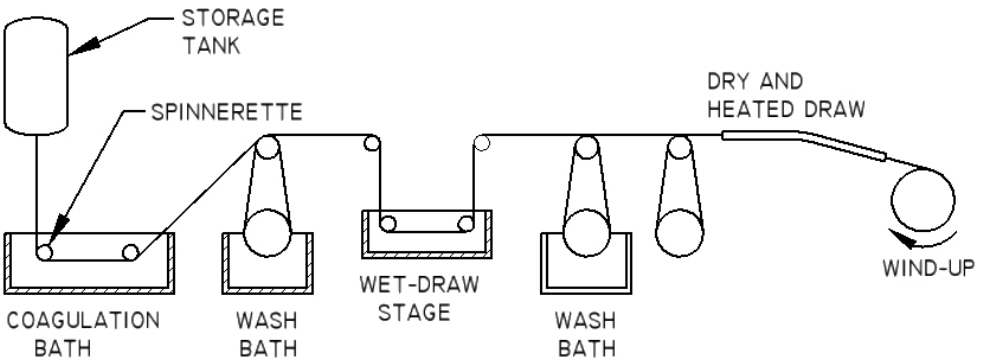


Figure 2.12: Schematic of the wet spinning process used to produce PAN precursor fibres [38]

The adjustment of parameters such as solution concentration, concentration of the coagulation bath, the bath temperature and the rate of extrusion of the filaments control, to an extent, the fibre formation. A wet spinning process is illustrated in figure 2.12.

#### 2.2.1.4 Oxidation/Stabilization

The stabilization process is performed by heating the precursor fibres at low temperature (150°C - 300°C) in air to convert the precursor to a form that can be further heat-treated [39]. The fibres are stabilised mainly to achieve preservation of the molecular structure generated by the spun fibres. The chemical composition of the filament and it's diameter are factors determining the heating rate. The heating rates vary from isothermal to step-wise and have difference consequences. It is worth noting that PAN is a poor conductor of heat and that a run away exotherm is to be avoided during the stabilization process.

#### 2.2.1.5 Carbonization

Tse-Hao, Tzy-Chin Day and Jeng-An Perng [40] report that the carbonization process is performed at a temperature between 800°C and 3000°C in an inert atmosphere. The maximum temperature depends upon the type of carbon fibres required. Increasing the final heat treatment temperature increases tensile strength. Fitzer, E. and Frohs, W. [41] report that, the tensile strength increases with the increase of heat treatment temperature but drops suddenly, when heat treatment temperatures exceed 1600°C. Fitzer, E. [42] claims that the drop is related to the release of nitrogen and that the decrease of the strength can be minimised by applying tension during heat treatment. Despite the drop of the strength, Fitzer, E. and Frohs, W. conclude that the desired orientation within the fibre and thus the modulus of the PAN based carbon fibres increase continually as heat treatment temperature is increased. Because of this reason, there are diverse grades of PAN based carbon fibres on the market with a large range of fibre moduli.

### 2.2.2 Mesophase pitch based carbon fibre

Mustafa Z. Özel and Keith D. Bartle [43] report that synthetic polyvinyl chloride, polyacrylonitriles, naphthene, coal tar pitch and petroleum have been used to prepare carbon fibres. However, coal tar and petroleum appear to be the more promising group of carbon precursors due to their low cost.

Because of its less expensive material, isotropic pitch has enormous potential for the economical production of high performance carbon fibre. Coal tar and petroleum pitches have high molecular weight carbonaceous materials and are residues, respectively of coal tar and crude oil distillation. Due to its lower proportions of undesirable and lighter components, petroleum pitch is preferred to coal tar pitch [43]. T. Y. H. Cheung [44] reports that both pitches have a wide molecular weight distribution with an average ranging from 180 to 600. Basically, these molecules are grouped in four categorises [43]: saturates (low molecular weight aliphatic compounds), naphthene aromatics (made up of low molecular weight aromatics), polar aromatics (contain higher molecular weights and more heterocyclic rings) and asphaltenes (having the lightest average molecular weight).

The initial stage in mesophase production consists of removing the light molecular weight species. This is achieved in conjunction with the free radial reaction of small aromatics to form polyaromatic molecules with molecular weights of around 1200; adequate for the formation of mesophase. It is important to get rid of the volatiles because they interfere with the formation of mesopahse. After the end of this phase, the mesophase reacts well during the purification process. Extraction removes the soluble fraction and the insoluble fraction is used to form mesophase.

#### 2.2.2.1 Heat treatment

T. Y. H Cheung claims that heating the pitch in the temperature range of 300°C to 500°C allows the creation of the polyaromatic mesophase. The processes are the volatilisation of low molecular mass constituents of the pitch and polymerisation and condensation reactions of the hydrocarbons. During this thermal treatment, formation of free radicals is introduced by the thermal cracking of the aliphatic side group at the alpha position in the aromatic molecules. The aromatic free radicals react between each other to give aryl-aryl linkages, building up the polyaromatic molecules to form a carbonaceous mesophase [43].

### 2.2.3 Carbon Fibre Reinforced Polymer

Carbon fibre reinforced polymer is a strong, light and expensive composite material of carbon fibres and a polymer matrix. The polymer usually used is epoxy (a thermosetting polymer formed from reaction of an epoxide “resin” with polyamine “hardener”) but a polymer such as nylon is sometimes used. One method of producing a carbon fibre reinforced polymer is by layering sheets of carbon fibre cloth into a mold in the shape of the final product.

The alignment and weave of the cloth fibres is intentionally selected in order to optimise the strength and stiffness of the final material. The mold is then filled with epoxy and is heated or air cured. The resulting material is corrosion resistant, stiff and strong for its weight. When the material is meant to be used in less critical areas, it can be manufactured by draping cloth fibres over a mold with epoxy pre-impregnated into the fibres (prepreg). Prepreg consists of thin sheets of evenly distributed uni-or multi-directional carbon fibres uniformly impregnated with an exact proportion of epoxy resin, which has been partially cured. When the material is expected to have a high performance, the mold is often vacuum-bagged and/or autoclave-cured, because even small air bubbles in the material can reduce its strength.

The manufacturing process for the high performance carbon fibre reinforced polymer is presented as follows: a carbon fibre mold is polished and a release agent is applied. The fibres and the resin or prepreg are laid down inside the mold and a vacuum is applied. This is set aside to allow the composite to cure. There are two ways used to apply the resin on the carbon fibres in a vacuum mold, the wet layup method and the resin induction system. In the wet layup method, the two-part resin is mixed and applied on the fibres before being laid in the mold and placed in the bag. In the resin induction system, the dry fibres and mold are placed inside the bag, while the vacuum pulls the resin through a small tube into the bag, then through a tube with holes to evenly spread the resin on the carbon fibres.

Another method of manufacturing carbon fibre reinforced polymer is known as dry layup. The carbon fibre is already impregnated with resin, as a prepreg, and applied to the mold. The assembly is then placed in a vacuum to cure. The dry layup method has the least amount of resin waste and can achieve lighter carbon fibre reinforced polymer than wet layup. This is the method used to produce the CFRP studied in this thesis.

## 2.3 Hysol EA9396, Dow Corning SE4445 and Epolite FH-5313

Hysol EA9396 is a low viscosity, room temperature curing adhesive system with excellent strength properties at temperatures from -67°F to 350°F (-55°C to 177°C). Hysol EA 9396 has a shelf life of one year when stored @ 77°F/25°C for separate components[2]. Hysol EA9396 consists of two parts, A and B with colours aqua-blue and light amber red-purple respectively. The mixture has a green to dark purple colour. The mixing ratio by weight is 100:30 (part A:part B). Dow corning SE4445 is a high viscosity, room temperature curing adhesive. It is a thermally conductive gel consisting of two parts (A and B). The two parts are a liquid with a white colour for part A and a charcoal colour for part B. The mix ratio is 50:50 (A:B) by weight. Epolite FH-5313 is a 100% solid, room-temperature curing, optically clear, electrical grade epoxy[3]. The mixing ratio by weight is 100:15 (A:B).

[2] www.aerospace.henkel.com

[3] http://www.lot-oriel.com/files/downloads/andover/en/epolite.pdf?

# Chapter 3

# In-Plane Thermal Conductivity Measurements

The need for the development of advanced materials for design applications requires a more detailed look at their thermal properties. In general, effective conductivities of materials depend on parameters such as density, temperature, moisture content and voids present in their structure. There are tabulated values of thermal properties available in the literature. However, the accuracy of these values is sometimes questionable. The reason is that, manufacturers and researchers use different techniques to obtain these property values. The reliability of a specific method depends on various factors, such as the speed of operation, the required accuracy and execution under various environmental conditions, the physical nature of the material under investigation and the size and shape of the available specimen [45].

The thermal conductivity, k, and the thermal diffusivity, $\alpha$, are heat transport properties of a material (unlike a quantity such as the specific heat, c, which is a property of state). In order to measure k, or $\alpha$, the specimen must be subjected to a heat flow whose pattern is known. The temperature field generated by the heat flow is described by the Fourier heat equation [46]

$$\rho c \frac{\delta T}{\delta t} = \nabla(k \nabla T) \tag{3.1}$$

with the initial boundary conditions appropriate to the experimental situation, where $\rho$ is the material density and $\nabla T$ the temperature gradient. The thermal diffusivity, $\alpha$, is the thermal conductivity divided by the volumetric heat capacity, $\alpha = \frac{k}{\rho c}$.

Thermal techniques are broadly classified under steady state methods and transient methods. D. M. Row [47] reports that, steady state methods provide the most accurate means of measuring thermal conductivity and can be divided into absolute and comparative methods. Absolute methods involve the direct measurement of heat (usually in terms of electrical energy), which passes through the specimen. This method is employed both at low temperatures and at high temperatures. At high temperatures it becomes increasingly difficult to allow for radiation heat losses and comparative methods may be more appropriate. In the comparative methods, the same flow of heat passes through the specimen under test and a

specimen or specimens of similar thermal conductivity placed in series with it. The flow of heat is then calculated from the temperature gradient over the standard specimen(s).

- Steady state methods involve time-independent heat flow generated by a heat source and a heat sink having the temperatures T1 and T2, respectively. Working under steady state conditions, the partial derivative $\frac{\delta T}{\delta t}$ is zero and equation 3.1 is reduced to Laplace's equation 3.2 and therefore steady state methods can determine k only.

$$\nabla(k\nabla T) = 0 \tag{3.2}$$

Among the steady state methods, the guarded hot plate (GHP) is considered as the most commonly used technique for measuring thermal conductivities [48]. This technique works in principle by establishing a steady temperature gradient over a known thickness of a specimen while controlling the heat flow from one side to the other. The advantages of steady state methods are the simplicity of the mathematical processing and the high degree of control of the experimental variables which is reflected in a high precision of results [46], with generally less than $5\%$ of error. However, the GHP and other steady state techniques suffer from major drawbacks. These drawbacks are the long time required to establish a steady state temperature gradient across the specimen (up to several hours), and that this temperature gradient is required to be large. Further, the specimen size also is required to be sufficiently large and that the contact resistance between the thermal sensors (used to record temperatures) and the specimen surface can be considered a non negligible source of error.

- Transient methods are based on subjecting the specimen to time dependent heat flow and monitoring the temperature at one, or more, points within the specimen or on the surface of the specimen. Under transient conditions $\frac{\delta T}{\delta t}$ is not zero and therefore all the properties $\rho$, c and k influence the temperature field. It follows that transient methods can determine both k and the product $\rho$c and therefore also the thermal diffusivity $\alpha$.

The transient techniques measure a response as a signal is sent out to create heat in the specimen. These techniques are therefore distinguished principally by the short time required to obtain the desired results. Among these techniques, the laser flash is mainly used to measure the thermal diffusivity of good conducting solid materials [48].

Other factors associated with the type of property or properties to be measured influence the choice of the measurement method. Some of the relevant factors are:

1. The requirement to measure k only, $\alpha$ only, k and $\alpha$ simultaneously or even to measure all the properties k, $\alpha$ and c in a single experiment.

2. The required accuracy and precision of measurement, e.g. $\leq 2\%$ for basic research and $\leq 10\%$ for calculations in engineering design [46].

This study is based on a steady state method because of the Fourier heat equation which is reduced to a simple mathematical expression, the high degree of control of experimental variables which is reflected in a high precision of results, the requirement of measuring k only, the high degree of accuracy ($\leq$ 2%) due to the purpose of the experiment (basic research) and the range of temperatures of interest (-30 °C to 20 °C). The work presented in this chapter describes the design and construction of an in-plane thermal conductivity measurement system devoted to get reliable thermal parameters for CAD thermal simulation and material characterisation. The basic concepts used to design this measurement system and all the details concerning its operation and implementation are described. Essential considerations about the measurement capabilities and experimental issues are presented together with experimental results on PocoFoam, Allcomp foam, CSiC foam, carbon fibre reinforced polymer, TPG and diamond.

## 3.1 Concept

The utilised method is based on the heat conduction phenomena through solids. If the temperature field (T) and the heat flux (q[$W/m^2$]) are known, the thermal conductivity can be obtained from the Fourier law of heat conduction

$$k\nabla T = -q \tag{3.3}$$

The flux can be determined from the heat supplied by the source or received by the sink. In steady state, the scalar quantity thermal resistance is defined as the difference in temperature $\Delta T$ between two closed isothermal surfaces divided by the heat flowing between them. It is considered that all the heat flowing through one surface also flows through the other one and no heat generation occurs between the surfaces. It is worth noting that these surfaces are not physical solid surfaces but rather imaginary surfaces of constant temperature.

An example with an easy analytical solution of the Fourier's law is the case of a material specimen of area (A), thickness (L) and thermal conductivity (k) being crossed by a steady, homogeneous heat flow density normal to its faces, see figure 3.1

Flat isothermal surfaces are generated parallel to the specimen faces, two of them will coincide with temperatures $T_{hot}$ and $T_{cold}$ respectively, see figure 3.1. Replacing q by the total heat flow expression (Q = Aq), equation 3.3 is simplified to

$$Q = -kA\nabla T \tag{3.4}$$

Knowing that $\nabla T = \frac{\Delta T}{L}$, equation 3.4 can be rearranged as

$$Q = -kA\frac{T_{cold} - T_{hot}}{L} = kA\frac{T_{hot} - T_{cold}}{L} = kA\frac{\Delta T}{L} \tag{3.5}$$

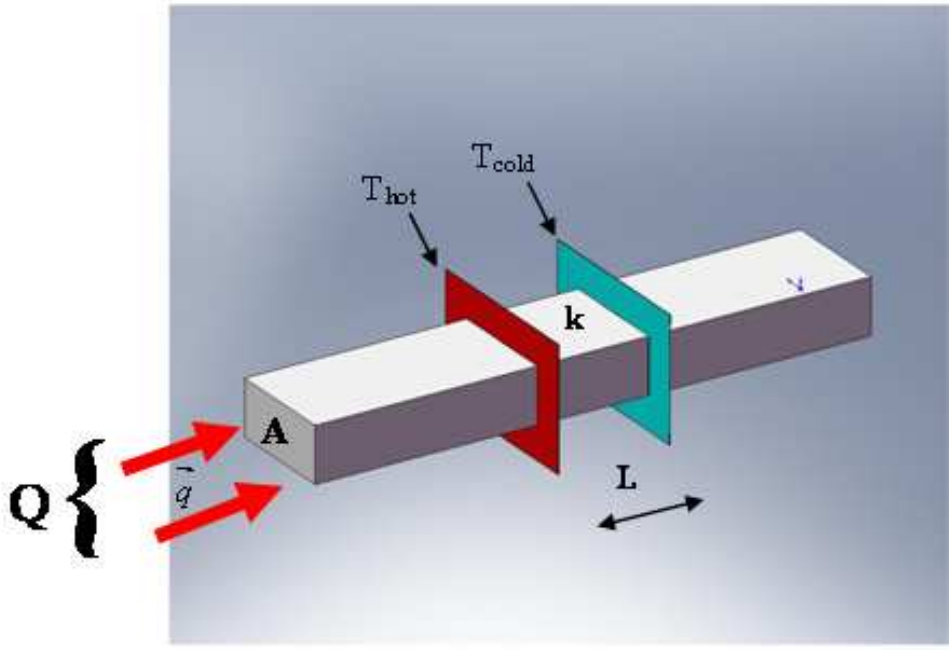


Figure 3.1: Material of area (A), thickness (L) and thermal conductivity (k) crossed by a steady state, homogeneous heat flow density $\vec{q}$ normal to its surfaces (Q being the total heat flow).

## 3.2 Measurement System

The conventional method of measuring the thermal conductivity in a given material is the determination of a temperature profile along the direction of the energy flow under investigation. There is a possibility that the heat be transferred by convection and/or radiation during these measurements. These modes of heat transfer are not accounted for by the Fourier heat equation 3.1 and therefore precautions have to be taken in the methods of measurement to suppress them. In practice it is almost impossible to ensure that all the heat supplied goes through the specimen since heat exchanges occur between the specimen surfaces and its surrounding and along sensor wires [49], see figure 3.2. Furthermore, it can be difficult and time consuming to ensure that measurements are made under equilibrium conditions. Nevertheless, equilibrium conditions must be established as they are vital for the measurements in order to obtain accurate results. G. K. White and S. B. Woods [50] point out that, making measurements under vacuum ensures that any heat losses from the specimen surfaces are radiative and at temperatures below about 100 K careful design will ensure that radiative losses are negligible compared to conduction through the specimen. The same was also emphasised by G. A. Slack [51]. For temperatures from 100K to room temperature, the radiation losses become significant and must be minimised or taken into account. The use of a heated radiation shield around the specimen with a temperature gradient similar to the gradient of the specimen is effective in reducing radiation losses [52].

In this section, a direct measurement system of heat conduction is designed and constructed for measurement of in-plane thermal conductivities, $k_{ab}$. C. A. Heusch, H. G. Moser

and A. Kholodenko measured in-plane thermal conductivities of Thermal Pyrolytic Graphite (TPG) using two sets of boundary conditions with a similar experimental setup [53]. In the first setup, they placed the apparatus in a vacuum vessel and in the second they surround the apparatus with polystyrene and left it at ambient atmosphere. Measurements with both setups were performed without surrounding the sample with radiation shields. The values obtained from the two sets are in good agreement, however they disagree with the manufacturer's values. Although the results are not in agreement with the recommended values, C. A. Heusch, H. G. Moser and A. Kholodenko claim that the discrepancy in the results is not caused by thermal radiation. This is an erroneous conclusion as the convective heat loss in the measurement system could simply equal the radiative heat loss compensated by the polystyrene in the vacuum vessel equipment. The technique used for the direct measurement of in-plane thermal conductivities in this thesis is illustrated on figure 3.2. This technique makes two noteworthy contributions

1. The specimen is surrounded by Aluminium thermal shields and the apparatus is placed in a vacuum with a residual pressure of approximately $10^{-5}$ mbar. The inside-walls of the vacuum vessel are covered with thin multi-layer thermo-reflective insulation with U=$0.19W/m^2K$[1]. The outside vessel temperature is kept constant at the temperature which the specimen is being investigated. The wires from the temperature sensors are anchored to the heat sink in order to reduce heat loss by conduction.

2. The measurement system is accurately verified. It has been calibrated with a well understood material (copper).

In figure 3.2, $Q_{rad}$ is the heat transferred by radiation, $Q_{conv}$ is the heat transferred by convection and $Q_{cond}$ is the heat transferred by conduction. $Q_{cond\_sen}$ is conduction through the wires connected to the Resistance Temperature Detectors (RTD) on the specimen, $Q_{cond\_el}$ is conduction through electrical wires connected to the heater on the specimen, $Q_{cond\_sp}$ is conduction through the specimen and $Q_{cond\_per}$ is conduction through the perspex. The perspex thermal conductivity is equal to 0.2W/mK[2]

### 3.2.1 Design

The apparatus is designed to achieve one-dimensional heat transfer in the axial direction ($x$ direction). In order to achieve that, flat and rectangular specimens with significantly larger length (around 100 mm) compared to the width (around 15 mm) with a very thin thickness (around 500$\mu$m) are used. The heat transfer in the radial directions ($y$ and $z$) are considered negligible. The apparatus consists of a heat sink, radiation shields (to suppress heat transfer by radiation), temperature sensors, thermal compound, long thin wires and heaters. The apparatus is confined inside a copper box, which is placed inside a vacuum vessel. The copper box serves as the first radiation shield to the specimen and reduces the heat transfer between the vessel's environment and the environment in the vicinity of the radiation shields. This is achieved by connecting the copper box to the bottom face of the heat sink, hence

[1] www.insulation-actis.com
[2] www.roymech.co.uk

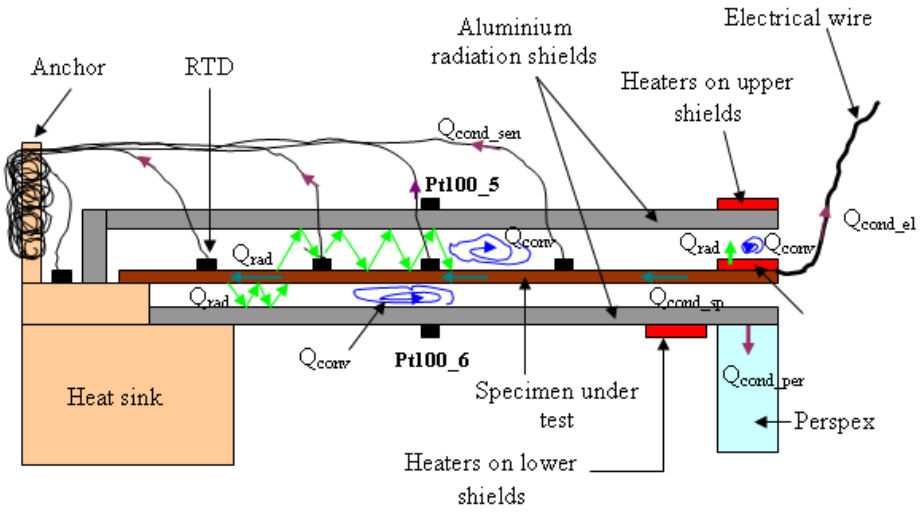


Figure 3.2: Drawing of the in-plane thermal conductivity measurement system

forcing the temperature of the copper box to come near the temperature of the radiation shields. The apparatus together with the copper box are placed inside a vacuum vessel with a vacuum of approximately $10^{-5}$ mbar in order to suppress any heat transfer by convection. Figure 3.3 shows the apparatus out of the box with the specimen surrounded by the radiation shields. Figure 3.4 shows the apparatus without the upper shield making the specimen under investigation visible together with the Resistance Temperature Detectors (RTDs) attached to it. The in-plane thermal conductivty measurement system is shown in detail in Appendix A.

#### 3.2.1.1 Heat sink

A massive heat sink is connected to one end of the specimen in which a coolant circulates. The coolant temperature is regulated by a FP50-MC refrigerated and heating circulator from Julabo. This circulator has a working temperature between -50 °C and 200 °C. The coolant can reduce gradually the heat sink temperature in order to control the heat flow from one side of the specimen to the other. An anchor is built to the heat sink, where all the sensors wires are tightly attached. This is done to reduce the temperature difference $\Delta T$ over the wires in order to achieve a very low amount of heat leak by conduction through the wires.

#### 3.2.1.2 Radiation shields

Aluminium plates are used to surround the entire specimen under investigation. These are used as radiation shields to the specimen. These radiation shields place another resistance in the heat flow path by reducing thermal radiation between the specimen and the copper box environment. The radiation shields are well connected to the heat sink, see figure 3.3 and figure 3.4. The shielding function is achieved by applying controlled heat to the aluminium plates creating a temperature gradient similar to that existing through the specimen.

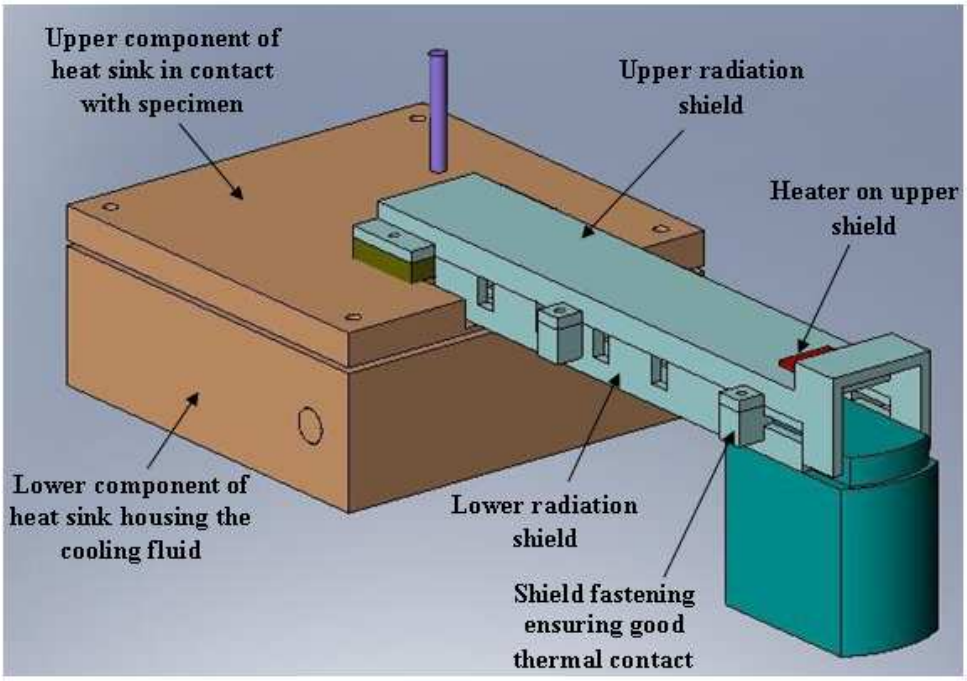


Figure 3.3: Solid Works model of the apparatus with the specimen surrounded by the radiation shields

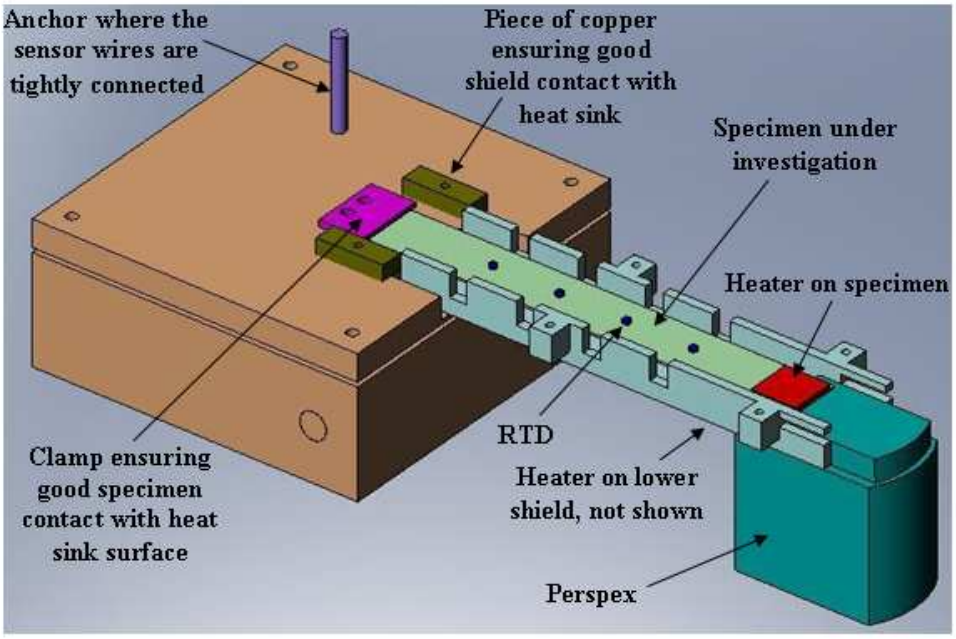


Figure 3.4: Solid Works model of the apparatus with the view of the specimen together with the RTDs attached on it

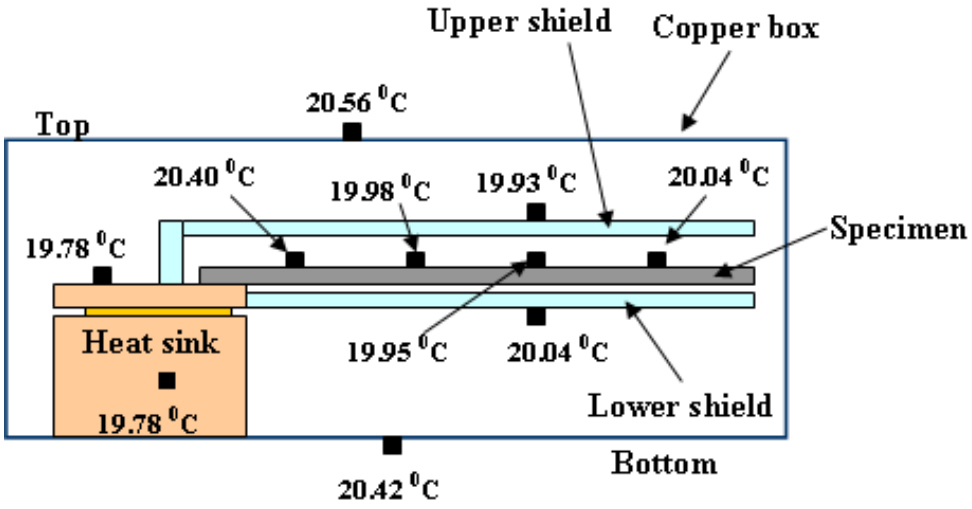


Figure 3.5: Temperatures measured at different locations in the apparatus during the thermal conductivity measurement of CFRP at 20°C, Q = 0W

It is worth noting that, the measurement apparatus is designed so that the gap between the radiation shields and the specimen is minimal. This is done so that the surfaces of the specimen can only exchange radiative heat with the shield surface having the same temperature and directly facing the specimen. A larger gap can allow an additional heat path along the specimen.

The contribution of the aluminium radiation shields is vital in reducing the undesired heat transfer by radiation taking place between the specimen surfaces and the walls of the copper box. The proof is the significant amount of heat that (in the absence of radiation shields) would be directly transferred between the specimen surfaces and the walls of the copper box. This amount of heat is calculated and compared to the heat transferred between the specimen and its environment when the specimen is surrounded with aluminium shields. The temperatures used for the calculations are recorded during thermal conductivity measurements of a CFRP specimen at 20°C. The apparatus is placed inside the copper box before inserting it into the vacuum vessel. The power supply is not switched on, so no intentional heat is applied onto the specimen. Figure 3.5 shows the locations of the RTDs used and the temperatures measured. The bottom of the copper box is in direct contact with the heat sink and the box is covered with a flat copper sheet (top).

The expressions used to calculate the radiative heat are

$$Q(sp/wall) = \sigma A(T_b^4 - T_{sp}^4) \tag{3.6}$$

$$Q(sp/Al) = \sigma A(T_{Al}^4 - T_{sp}^4) \tag{3.7}$$

where $\sigma$ = 5.67x10$^{-8} W/m^2K^4$ is the Stefan-Boltzmann constant, Q(sp/wall) is the amount of heat transferred between the total surface of the specimen and the walls of the copper box, Q(sp/Al) is the amount of heat transferred between the specimen and the aluminium radiation shields, $T_b$(K), $T_{Al}$(K) and $T_{sp}$(K) are the temperature of the box, the aluminium

radiation shields and the specimen, respectively. The total surface of the specimen is equal to $10^{-3}m^2$. In absence of the alumnium radiation shields, 3.49x$10^{-3}$W radiates from the walls of the copper box towards the specimen, while the specimen loses 1.14x$10^{-4}$W with the use of the aluminium shields. The heats applied intentionally on the specimen are 0.1W and 0.2W. Q(sp/wall) represents 3.49% and 1.74% of 0.1W and 0.2W, respectively, while Q(sp/Al) represents 0.11% and 0.06% of 0.1W and 0.2W, respectively. In other words, when other heat transfer sources are neglected, an effective heat of 0.10349W (in the absence of the radiation shields) is flowing through the specimen, while the measurements are thought to be performed at 0.1W. This unexpected amount of heat (0.10349W) will cause inaccuracy in the results. An effective heat of 0.99W (with the use of the radiation shields) is flowing through the specimen, when the measurements are thought to be performed at 0.1W. It is clear that 0.99W$\simeq$1W and does not cause any change in the results. In conclusion, the use of the radiation shields is vital because it serves to reduce by 96.56% the radiative heat between the walls of the copper box and the specimen.

#### 3.2.1.3 Temperature Sensors and wires

Resistance transducers, commonly known as resistance temperature detectors (RTDs) are widely used for the measurement of temperature [54]. The common RTDs are based on copper, nickel and platinum. The resistivity of platinum ($\sim 10\mu\ \Omega$/cm) is six times that of copper. Platinum is relatively nonreactive, has a high melting point (1769°C) and because it has a well-established temperature coefficient of resistance, it is a common choice for the precise measurement of temperatures between -260°C and 1000°C [54]. Platinum resistive elements of thin film type, laid on glass or ceramic, are often used for surface temperature measurements. Their advantages over the wire wound type are their smaller sizes and higher speed of response [55]. Given the accuracy, stability and linearity of the RTDs, they are chosen as the method for the measurement of temperatures in this study. While the cost is relatively high, the long term stability of the RTDs makes them the clear winner for accurate, repeatable temperature measurements [56]. Four RTDs of type PT100[3] are placed on the surface of the specimen along the direction of the energy flow under investigation. They are of the international standard IEC 751.

Long and thin manganin wires are used to connect the RTDs to NI USB-9211A data acquisition modules with integrated signal conditioning that provides plug-and-play connectivity via USB for faster setup and measurements[4]. The USB data acquisition modules are designed to operate with 4 channels of 24-bit thermocouple input, which give good accuracy. They are compatible with Microsoft Windows when using NI-DAQmx driver software. Each NI USB data acquisition module includes a copy of NI LabVIEW SignalExpress LE for Windows, so that data can be quickly acquired, analysed and presented without programming. The modules are linked to a PC with LabVIEW enabling real time temperature reading. The obtained temperatures are transferred to Microsoft Excel for calculation of their average values. The average temperatures of the four RTDs placed on the specimen are exported to a data analysis and technical graphics software (ORIGIN), where graphs of temperatures

[3] www.http://www.omega.co.uk/prodinfo/PT100.html

[4] www.ni.com

versus position of the RTDs is determined. The ORIGIN inbuilt least square fit function is used to extract the corresponding gradients of temperature as a function of distance. These gradients are used to calculate the thermal conductivity coefficients.

The thermal path between the outside environment and the sample is bridged by the wires connecting the RTDs to the data acquisition system. The thermal resistance of this path must be maximized to reduce parasitic heat sources. The choice of long and thin manganin ($\phi$ = 0.122 mm) wires is motivated by their high thermal resistance. The sensor wires are wrapped around an anchor attached to the heat sink which reduces considerably the temperature gradient along the wires. Hence the heat leaks trough the RTD wires, since the specimen is directly connected to the heat sink and therefore at a similar temperature to the heat sink, see figure 3.2.

Long (1 m) AWG 28 wires ($\phi$ = 0.321 mm) are used to connect the heaters to a QL355 TP power supply from Thurlby Thandar Instruments (TTi)[5]. The QL355 TP has two identical outputs which are independent and isolated and measures the voltage (V) and the current (I) with four digits precision. The suffix "P" in QL355 TP indicates that, this "QL-T" model is incorporated with a full bus interface enabling remote control and read-back via a USB. A four-wire measurement system is used for the measurements in this thesis. In such a system, separate wires are used for current supply and voltage measurement. The current supply wires have a resistance, so there is a voltage drop across the wires. The voltage sense wires do not carry any current, so no voltage drop is present across these wires. This fact makes four-wires sensing more accurate than two-wire sensing, where the same wires are used for current supply and voltage sensing. The AWG wires are made of copper and consist of two entangled wires, generally black and white. The maximum temperature difference $\Delta T_{max}$ along the heater wires in this thesis is 13°C, because the maximum temperature measured on the heaters is 33°C and the room temperature is considered to be at 20°C. The maximum heat leak through the heater wires is determined as follows

$$Q = k_{Cu} 4A \frac{T_{heater} - T_{room}}{L} \tag{3.8}$$

where the thermal conductivity $k_{Cu}$ of copper is equal to 380W/mK, A is the cross section area of the wire, L is the length of the wires and 4 corresponds to the number of wires. The maximum heat leak through the heater wires is calculated to 1.6x10$^{-3}$ W/mK, which constitutes 1.6% and 0.8% of the 0.1W and 0.2W intentionally applied power to the specimen. This amount of heat transferred by conduction through the wires is minimal and will be negligible in all the measurements.

#### 3.2.1.4 Thermal compound

The thermal compound Dow Corning 340[6] is used as the interface thermal material in order to fill the gap between surfaces and reduce thermal resistances. Its thermal conductivity has

[5] www.tti-test.com

[6] www.http://www.dowcorning.com

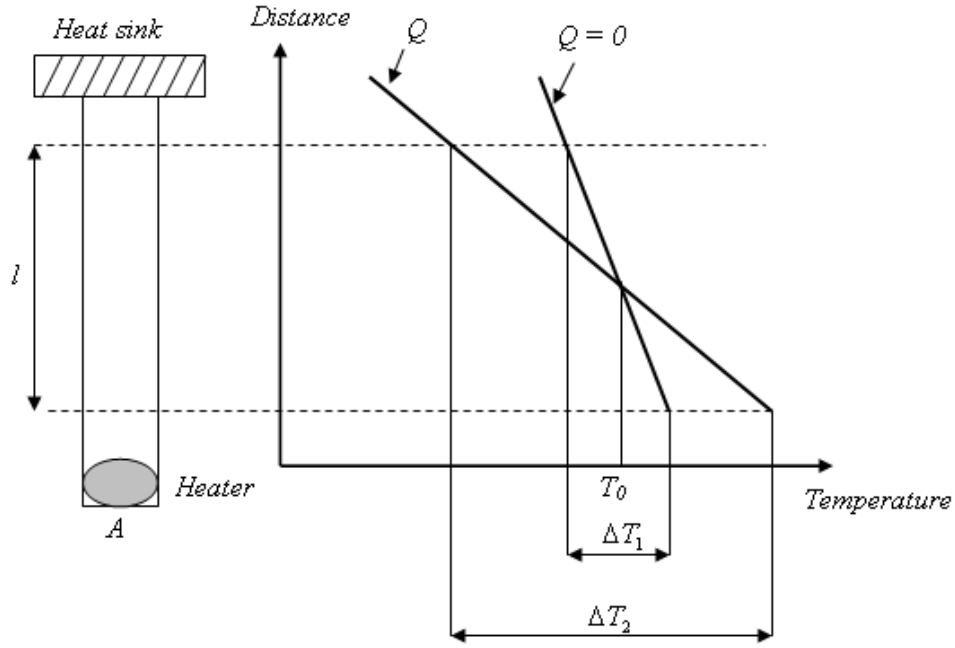


Figure 3.6: Diagrammatic layout of the standard technique for measuring thermal conductivity

been measured in the laboratory and the value is found to be 0.56W/mK. The method of measurement is explained is chapter 4.

#### 3.2.1.5 Heaters

The heaters used on the sample and the aluminium shields are custom built using thick film technology. The heater element has a resistance of approximately 100Ω. The element has a surface area of 10mmx10mm and is deposited onto a 500$\mu$m thick aluminium nitride ceramic to give uniform heat distribution. The back side of the ceramic is attached to the item to be heated.

## 3.3 Measurement Theory

This section describes the technique used for remedy of the effects of parasitic signals present in the measurement system. The measurement technique utilised is based on the double flux technique developed by M. Locatelli, J. Lopez and M. N. Reguiero [57] to remedy parasitic signals from apparatuses similar to that used in this thesis. Remedy of parasitic signals is achieved by performing two different measurements of the conductivity k(T) at an average specimen temperature $T_0$.

The first measurement with no intentional heat applied on the specimen gives a tempera-

ture difference $\Delta T_1$ across the specimen whereas the second measurement with applied heat gives a difference $\Delta T_2$. However, the heat sink is cooled so that the average specimen temperature remains constant, at $T_0$. The method considers the parasitic heat current q(T) to be constant for a given average temperature of the specimen. A is the cross sectional area of the specimen and the measurements with Q = 0W and Q = QW intentionally applied, give the following thermal gradients

$$\bigtriangledown Q_{=0} = \frac{\Delta T_1}{l} = \frac{q(T_0)}{k(T_0)} \frac{1}{A} \tag{3.9}$$

$$\bigtriangledown Q = \frac{\Delta T_2}{l} = \frac{Q + q(T_0)}{k(T_0)} \frac{1}{A} \tag{3.10}$$

Equation 3.9 is used to determine the amount of heat present in the specimen before applying intentional heat. This parasitic heat can originate from different sources such as the electrical heater wires, the sensor wires and the radiation of the specimen with the vacuum vessel environment. Equation 3.10 is used to determine the total amount of the heat present in the specimen after applying intentional heat (the heat applied on the specimen is added to the heat already present). The expression of the thermal conductivity coefficient can be determined as follows

$$k(T_0) = \frac{Q}{A} \frac{1}{\bigtriangledown Q - \bigtriangledown Q_{=0}} \tag{3.11}$$

where $\bigtriangledown Q$ and $\bigtriangledown Q_{=0}$ are the temperature gradients along the specimen, when heat different from zero and heat equal to zero are intentionally applied.

This expression eliminates the effects of any parasitic heat present in the measurement system and prevents the results from being corrupted. The assumption that the parasitic heat load is constant for both measurements has been made. The intentional power is kept low so the temperature change along the specimen is kept low to reduce the parasitic heat in both cases. More over the average temperature of the specimen is constant for both cases.

## 3.4 Measurement Principles

Four PT100 RTDs are placed on the surface of the specimen (labelled PT100_1 to PT100_4) spaced 15mm from each other as shown on figure 3.7. In order to ensure that there is a good contact between the RTDs and the surface of the specimen, pressure is applied on the top of the RTDs by sticking pieces of polystyrene in the inner side of the top radiation shield, directly above the RTDs. The polystyrene pieces are square with a cross section area of 16 mm$^2$ and a height of 2 mm. The amount of heat flowing through this new created heat path is calculated and found insignificant for the measurements. The temperature difference between the specimen and the shields is measured to 0.05°C and the thermal conductivity of polystyrene is 0.03W/mK[7]. The amount of the conductive heat through the polystyrene is calculated to be 1.13x10$^{-5}$W and represents 0.01% and 0.006%, respectively for 0.1W and

[7] www.engineeringtoolbox.com

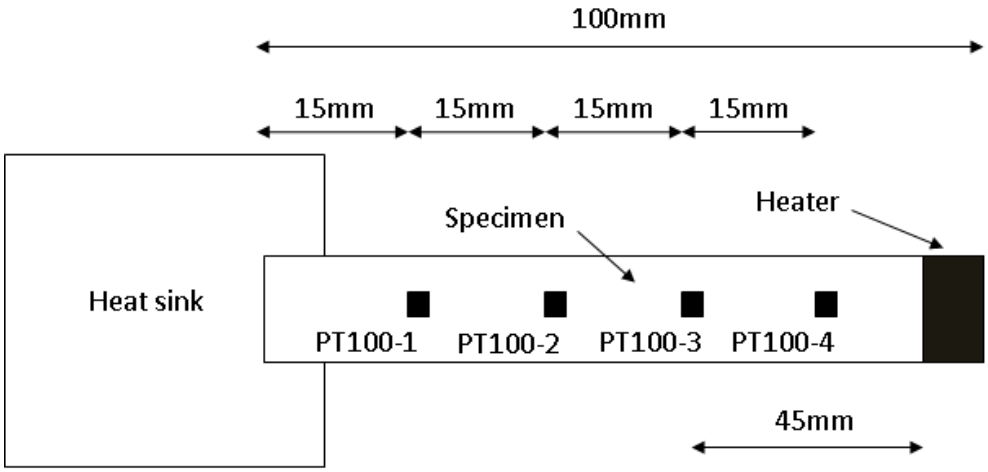


Figure 3.7: Schematic drawing of the measurement system of in-plane thermal conductivity coefficient $k_{ab}$. Dimensions of specimen: length = 100mm, thickness up to 5mm and width $\sim$ 12mm

0.2W intentionally applied on the specimen. The effect of the polystyrene on the measured thermal conductivity is minimal and neglected in all the measurements.

An equal amount of heat is applied to each radiation shield and their temperatures are recorded with a RTD attached to each radiation shield. The RTDs are attached to the radiation shields directly above and below the PT100_3, and the three RTDs form a virtual line perpendicular to the specimen. PT100_3 is located at the centre of the specimen and is considered to be the average temperature of the specimen, see figure 3.7. It is important that the RTDs at the centre of the specimen and those on the shields must be vertically aligned in order to avoid recording offset temperatures.

The desired experimental temperature of the specimen is reached by regulating the temperature of the coolant. Without applying any intentional heat into the system, sufficient time is allocated to reach thermal equilibrium and the first measurement is performed. Thereafter, heat is applied to both the specimen and the thermal shields until they reach the same temperature. The temperature of the coolant is again regulated to bring the temperature of the specimen and the thermal shields down to the desired experimental temperature. Once again sufficient time is allocated to the system to reach thermal equilibrium and then the measurement is performed. It is worth noting that, the intentional heat applied on the specimen can be different from the heat applied on the radiation shields. Several measurements with different amounts of heat applied on the specimen is necessary to obtain reliable results. The values of the conductivities must be equal for a given measurement temperature for each applied heat load to the specimen.

## 3.5 Calibration

In order to validate the measurement method and to demonstrate that the measurement system operates in accordance with the theory described, a number of measurements of thermal conductivity are performed on a copper specimen, whose thermal conductivity is well understood and known. The measurements are performed in the temperature range from -30°C to 20°C. It is known from literature that the thermal conductivity of copper (99.999% pure) is independent of temperature in that temperature range and the value lies between 370W/mK and 400W/mK. It is important to mention that the calibration of the RTDs is necessary to be done before the measurement system is utilised. This ensures that the resistance temperature detectors operate accurately within the conditions that the measurement system is used.

### 3.5.1 Calibration of RTDs

Inside the vacuum chamber, the RTDs are placed closely to each other and attached to the heat sink. Dow Corning 340 is used to ensure good surface contact between the RTDs and the heat sink surface and a chamber is evacuated to a pressure of approximately $10^{-5}$ mbar. The calibration temperature range is taken from -35°C to 25°C to ensure that all the measurement temperature range (-30°C to 20°C) is covered. For a given temperature, enough time is allocated to the process in order to achieve the steady state equilibrium before committing the temperature. The RTDs were calibrated to be equal with each other and a calibrated temperature sensor.

### 3.5.2 Copper measurement

Three sets of measurements are performed on a flat and thin copper specimen, with cross section area around 6.11 $mm^2$. The first measurement is performed with no intentional heat applied on the specimen, the second and third measurements are performed with intentional heat of 0.1W and 0.2W applied on the specimen, respectively.

Plots of average temperature values of the RTDs on the specimen versus distance are presented on figure 3.8 (0.1W intentionally applied) and figure 3.9 (0.2W intentionally applied) together with the obtained gradients. The solid lines represent the linear fits used to extract the gradient of the temperature as a function of distance along the specimen for a given heat intentionally applied. These average temperature values are obtained from thermal measurements of the copper specimen at 0°C. The gradient values obtained in this study, when no intentional heat is applied is -0.003K/mm whereas gradients of 0.04K/mm and 0.08K/mm are obtained, when 0.1W and 0.2W are applied respectively. It is clear that the gradient value doubles by doubling the amount of heat applied on the specimen and that at an average temperature of 0°C the parasitic heat load is less than 0.01W.

The calculated thermal conductivity coefficients are presented in figure 3.10. There is

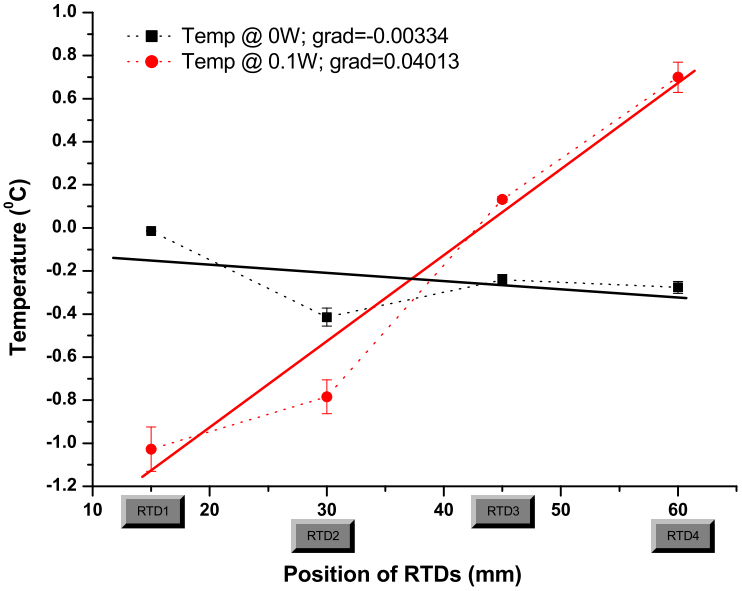


Figure 3.8: The temperature along the surface of the copper specimen at Q = 0W and Q = 0.1W

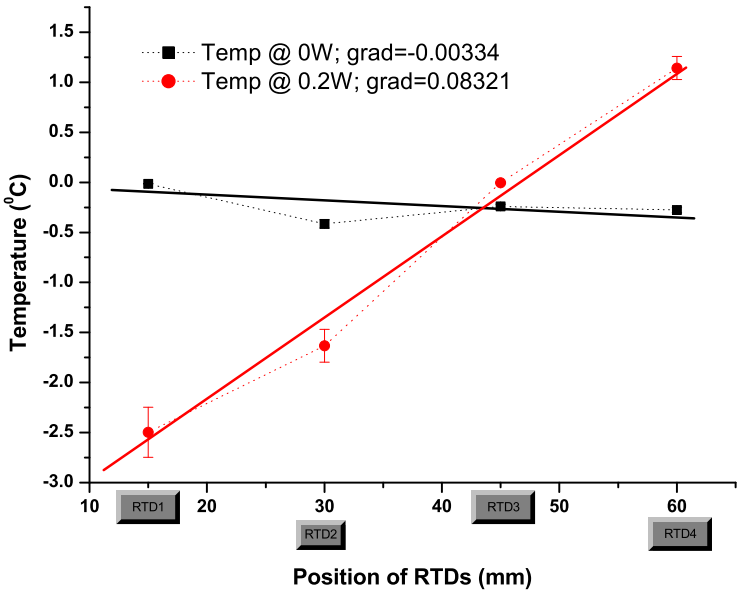


Figure 3.9: The temperature along the surface of the copper specimen at Q = 0W and Q = 0.2W

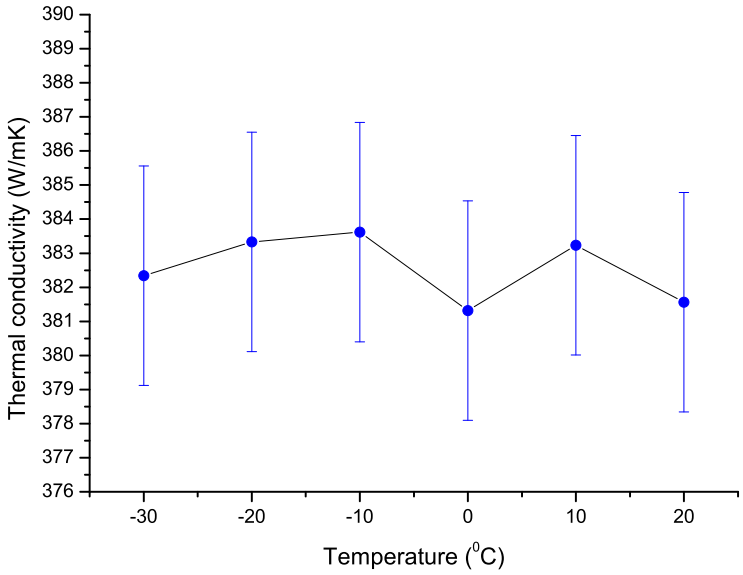


Figure 3.10: Results of in-plane thermal conductivity measurement of copper (99.999% pure)

no temperature dependence of the thermal conductivities in the range from -30°C to 20°C. The values lie between 381W/mK and 383.5W/mK. The results are in good agreement with literature values and 380W/mK is used in this thesis to be the measured thermal conductivity of the copper specimen. In conclusion, the measurement method together with the theory are considered suitable and reliable for in-plane thermal conductivity measurements.

## 3.6 Uncertainties

In this section, a summary of the measuring procedure is addressed together with a study of the uncertainty analysis. Suppose that $u, ..., z$ are measured with small uncertainty $\delta u, ..., \delta$z, and the measured values are used to compute q, given by

$$q = \frac{x \times y \times z}{u \times v \times w}, \tag{3.12}$$

If the uncertainty in $u, ..., z$ are independent, then the fractional uncertainty in q is the sum in quadrature of the original fractional uncertainties,

$$\frac{\delta q}{\mid q \mid} = \sqrt{(\frac{\delta u}{u})^2 + ... + (\frac{\delta z}{z})^2} \tag{3.13}$$

The uncertainty in the coefficient $k$ results from the errors in the measurement of the temperature drop $\Delta T$, the heat flow Q and the reading of the dimensions of the specimens

and positions of the RTDs. The thermal conductivity is calculated with equation 3.11. Using equation 3.13, its uncertainty can be calculated as

$$\frac{\delta k}{\mid k \mid} = \sqrt{(\frac{\delta U}{U})^2 + (\frac{\delta I}{I})^2 + (\frac{\delta A}{A})^2 + (\frac{\delta grad_{Q=0}}{grad_{Q=0}})^2 + (\frac{\delta grad_Q}{grad_Q})^2} \tag{3.14}$$

where Q = U.I, A = d.h (cross section area of the specimen), U is the voltage, I is the current, d and h are the thickness and width of specimen, respectively. The uncertainty in the coefficient $k$ is estimated based on the dimensions of the copper specimen used for the calibration of the measurement system.

The intentional heat applied on the specimen is supplied by QL355TP power supply. The meter accuracies are $\frac{\delta U}{U}$ = $1.1\%$ and $\frac{\delta I}{I}$ = $0.7\%$ for the voltage and the current, respectively.

The specimen thickness and width are measured with a micrometre with a precision of $1\mu$m. The dimensions measured are respectively 0.49mm and 12.6mm for the thickness and the width. The error in the ability of reading the micrometre is found to be around $\theta$=$0.12\%$. The expression of its fractional uncertainty is determined as

$$\frac{\delta A}{A} = \sqrt{(\frac{\delta d}{d})^2 + (\frac{\delta H}{H})^2 + (\theta)^2} \tag{3.15}$$

and the value is deduced at $\frac{\delta A}{A} = \sqrt{(\frac{0.000001}{0.00049})^2 + (\frac{0.000001}{0.0126})^2 + (0.0012)^2} = 0.237\%$

The error in the gradient of the temperature as a function of distance along the specimen is determined from the least square fit to the data. The individual data points have errors in their position and temperature. The distance between two consecutive RTDs is measured as 15mm (0.015 m) and this is determined by the use of a vernier calliper with the following precision $\delta L$ = 20$\mu$m. The vernier calliper is used to measure several times the distance between two RTDs, in order to determine the error in the ability of reading the calliper. This error is found to be around $0.142\%$. The total fractional uncertainty in the distance between two consecutive RTDs is $\frac{\delta L}{L} = \sqrt{(\frac{0.00002}{0.015})^2 + 0.00142^2} = 0.195\%$.

Platinum RTDs (HEL-700) are utilised in the measurement system to measure the temperature drop along the specimen. The functional behavior of these RTDs is

$$R(T) = R(0)(1 + AT + BT^2 - 100CT^3 + CT^4) \tag{3.16}$$

R(T) = resistance ($\Omega$) at temperature T (°C)
R(0) = resistance ($\Omega$) at 0 (°C)
T = temperature in °C
where $A = 3.9083 \times 10^{-3}$, $B = -5.775 \times 10^{-7}$, $C = -4.183 \times 10^{-12}$ (below 0°C), or $C = 0$ (above 0°C). The temperature accuracy is equal to 0.080°C.

The gradient accuracies are calculated to be $\frac{\delta grad_{Q=0}}{grad_{Q=0}}$ = $2.88\%$ and $\frac{\delta grad_Q}{grad_Q}$ = $0.6\%$

The total fractional uncertainty in the coefficient $k$ is determined as
$\frac{\delta k}{|k|} = \sqrt{(\frac{1.1}{100})^2 + (\frac{0.7}{100})^2 + (\frac{0.237}{100})^2 + (\frac{2.88}{100})^2 + (\frac{0.6}{100})^2}$ = $3.22\%$

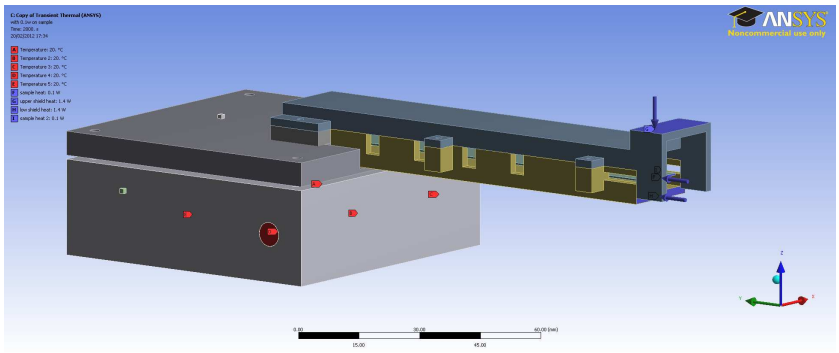


Figure 3.11: FEA model and boundary conditions

## 3.7 Finite Element Analysis (FEA)

This section presents a detailed methodology for the simulation of the copper specimen, used in the calibration of the measurement system. The aim of this section is to cross check the validity of the measurement method and the physics considerations used. A CAD thermal analysis software coupled with engineering data is used to create an environment similar to that of the laboratory. The goal is to determine the temperatures of the resistance temperature detectors placed on the specimen and compare them with the temperatures found experimentally. The measurement system is first modelled in Solid Works[8] and exported to ANSYS Workbench[9] for the finite element analysis. The FEA model and boundary conditions are shown in figure 3.11

### 3.7.1 Analysis Parameters

The materials used to model the measurement system are aluminium (radiation shields), platinum (RTDs), glass (heaters) and copper 99.999% pure (specimen under investigation).

Table 3.1: Properties of the materials used in the analysis

| Materials | Density $kg/mm^3$ | Specific heat $J/kg.K$ | Emissivity | Thermal conductivity $W/m.K$ |
|---|---|---|---|---|
| Aluminium | $2.77\times10^{-6}$ | 875 | 0.07 | 0.235 |
| Copper | $8.9\times10^{-6}$ | 385 | 0.8 | 0.38 |
| Platinum | $2.145\times10^{-5}$ | 25.86 | - | $7.16\times10^{-2}$ |
| Glass | $2.4\times10^{-6}$ | 0.6 | - | 1.05 |

A steady state thermal analysis is performed. Heat transfer by convection around the specimen and heat transfer by conduction through all the wires (sensor and heater wires) are

[8] www.solidworks.com
[9] www.ansys.com

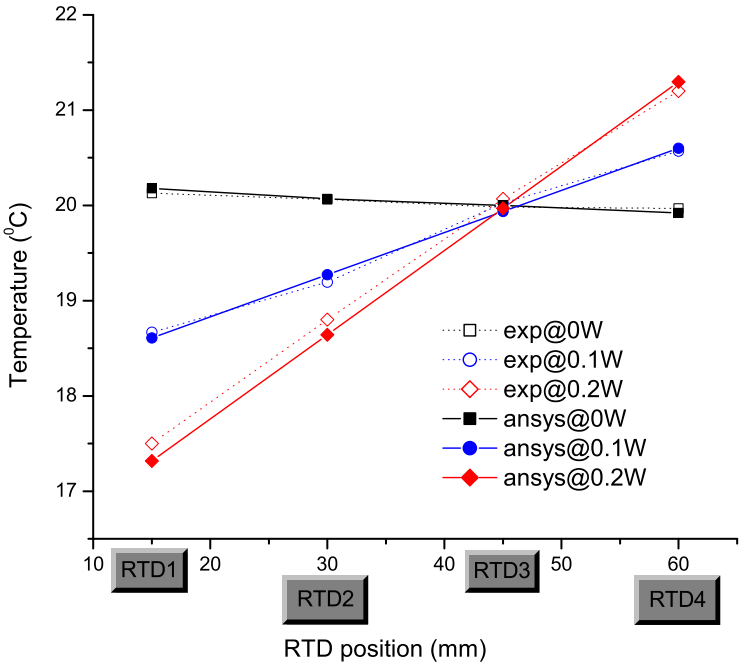


Figure 3.12: Experimental and predicted temperature values of the RTDs on the specimen at 20°C

not considered. The measurement system is run at 20°C in this analysis. The analysis is first performed with no intentional heat applied on the specimen. After that, the analysis is performed with intentional heat flows of 0.1W and 0.2W applied on the specimen, respectively.

### 3.7.2 FEA Results

The experimentally measured temperatures are presented on figure 3.12 and compared to the simulated temperatures. The dashed lines represent the experimental data and the solid lines the Ansys derived data. It is worth noting that the heat flows from RTD1 (nearest to the heat sink) to RTD4 (nearest to the heater) when intentional heat is not applied, which is contrary to the heat flow when intentional heat is applied.

The temperatures (experimental and simulated) agree well within $3\%$ when no intentional heat is applied on the specimen, as shown in table 3.2. The experimental temperatures decrease slightly from 20.18°C (RTD1) to 19.92°C (RTD4) and the simulated temperatures from 20.13°C (RTD1) to 19.97°C (RTD4). For a given amount of intentional heat applied to the specimen there is a good agreement within $3\%$ between the simulated temperatures and the experimental temperatures. It is worth noting that considerations such as neglecting the heat transfer by convection around the specimen, the heat conduction through the electrical wires and the radiation between the specimen and the shields were made. It is assumed for the simulation that the specimen is not exposed to any parasitic heat. The simualtion should

therefore produce values that are considered ideal. The difference observed in the gradients when no heat is intentionally applied indicates that some parasites are still present in the measurement system. The gradients derived from the simulated temperatures differ from the experimental gradients by $7.6\%$ and $3.5\%$, when heat of 0.1 W and 0.2 W is applied, respectively. The thermal conductivities obtained by the simulation are equal to 381W/mK.

Table 3.2: Summary of the derived thermal conductivity from the simulated temperatures

| Power (W) | Gradient Experimental (K/mm) | Gradient Simulated (K/mm) | Conductivity Experimental (W/mK) | Conductivity Simulated (W/mK) |
|---|---|---|---|---|
| 0 | -0.00334 | 0.0003 | | |
| 0.1 | 0.040013 | 0.0433 | 380 | 381 |
| 0.2 | 0.08321 | 0.0862 | 380 | 381 |

## 3.8 Experimental Results

In this section, in-plane thermal conductivities of materials (PocoFoam, CFRP) selected in the design of the stave are presented together with other materials which are Allcomp foam, TPG (candidate materials) and diamond, carbon/carbon (C/C) and carbon silicon carbide foam (CSiC) (materials of interest). The measurements are performed in the temperature range from -30°C to 20°C.

### 3.8.1 PocoFoam

Bulk thermal conductivity of two specimens of PocoFoam with different densities are investigated. The specimens are purchased from Poco Graphite SARL[10]. The densities are 0.56g/c$m^3$ (poco08) and 0.40g/c$m^3$ (poco09). The manufacturer claims a similarity in the two specimens including the manufacturing process. The delivery date is the sole quoted difference and the results are presented in figure 3.13.

The measured thermal conductivities agree well with the companies quoted value which is the range from 25W/mK to 60W/mK for densities between 0.32g/c$m^3$ and 0.68g/c$m^3$. A small temperature dependence of the thermal conductivities with temperature is observed for the y direction. The thermal conductivity of poco08 decreases from 60W/mK at -30°C to 57.5W/mK at 20°C, while that of the poco09 decreases from 57W/mK to 53W/mK. There is no temperature gradient in the $x$ direction. For a given temperature, the thermal conductivity of poco08 is higher than that of poco09 with a maximum difference of $10\%$ ($x$ direction) and $11\%$ ($y$ direction) over the measured temperature range. The increase of $40\%$ of the density of poco09 from 0.40g/c$m^3$ to 0.56g/c$m^3$ results in an increase of the thermal conductivity, however the increase is less than expected and does not increase linearly with density. Of

[10]Poco Graphite SARL, 1 rue des vergers 69760 Limonest FRANCE, POCOEU_sales@entegris.com

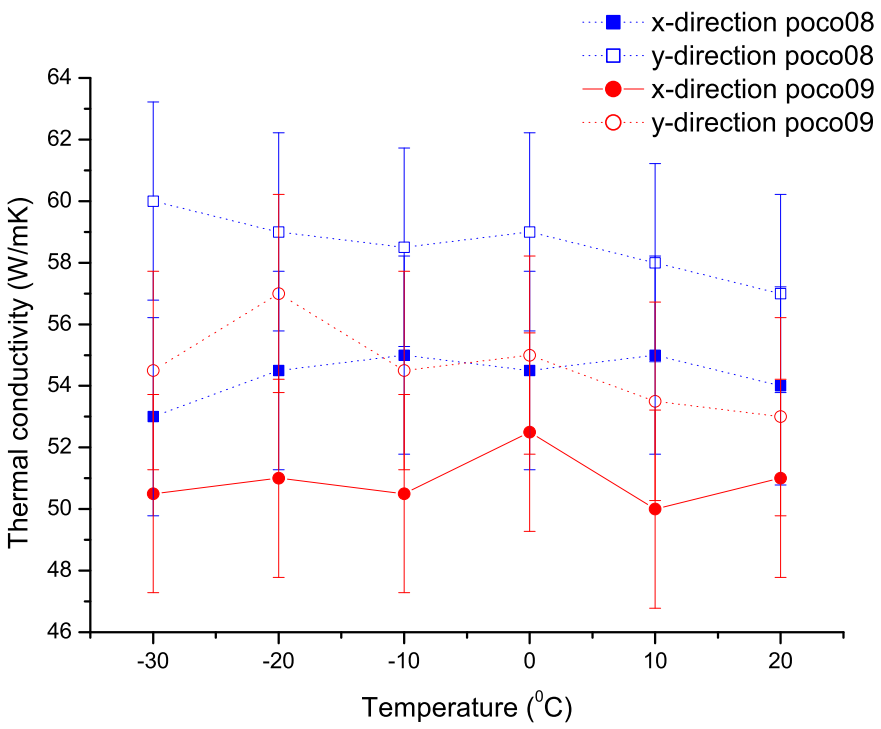


Figure 3.13: In-plane thermal conductivity results of PocoFoam 08 and 09

course, this single result is not able to establish any relationship between density and thermal conductivity. A full understanding of this relationship will be achieved after the study of several PocoFoam densities. Figure 3.14 presents the percentage increase in the conductivity between the two specimens in both the $x$ and $y$ directions for each measured temperature. Over the temperature range of -30°C to 20°C, the average increase of the thermal conductivity in both directions ($x$ and $y$) is the same and is bout $7\%$.

### 3.8.2 Allcomp foam

Bulk thermal conductivities of an Allcomp foam specimen were measured in $x$ and $y$ directions. The specimen was grade K9 foam with a density equal to 0.36g/c$m^3$. A specimen was cut for the in-plane measurement apparatus with a cross-sectional area of 31$mm^2$. The foam was acquired from Allcomp Inc. in USA[11]. A proper observation of the foam made it possible to see several broken ligaments on the surface of the specimen. These broken ligaments resulted from the cutting of the specimen and account for the visual total cross sectional area. This meant that the effective cross section area was less than the measured cross section area that was used to determine the thermal conductivity coefficient. In order to understand the impact of these broken ligaments on the results, two different thicknesses for the $x$ direction (2.46mm and 3.76mm) and three different thicknesses for the $y$ direction

[11] Allcomp Inc., 209 Puente Avenue, vity of industry, CA 91746-2304

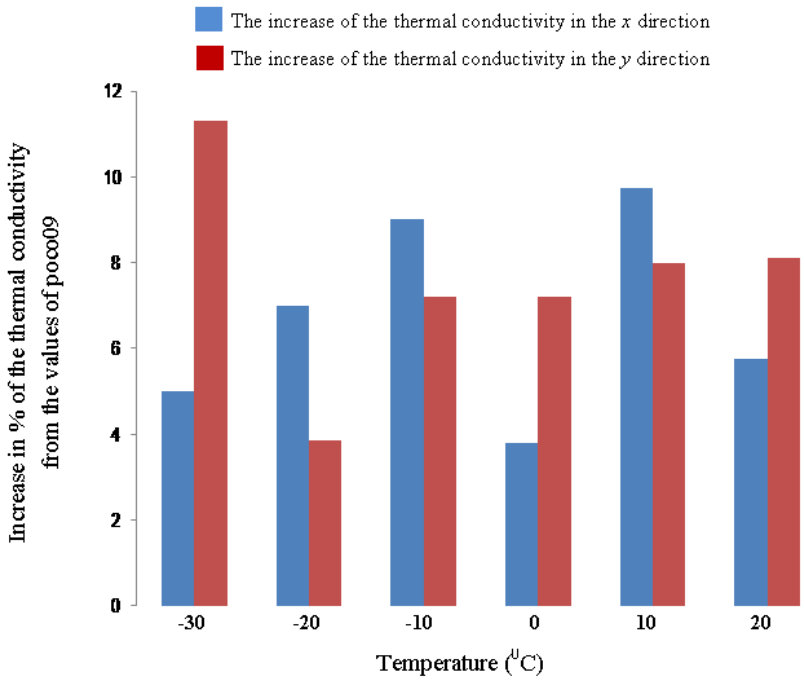


Figure 3.14: The percentage increase of the thermal conductivity at each temperature between two specimens which have $40\%$ difference in density.

specimen (1.47mm, 2.46mm and 3.76mm) were measured. All the measurements results are summarised on figure 3.15.

A small temperature dependence of the thermal conductivities for the specimens with thickness greater than 1.4mm is observed. For these thicknesses, the conductivity reduces with increase of temperature for both the $x$ and $y$ directions. The thermal conductivities decrease from 92W/mK to 86W/mK and 79W/mK to 71W/mK in the x and y direction, respectively. For a given temperature, the thermal conductivity in the $x$ direction is around $17\%$ higher than the conductivity in the $y$ direction. The foam does not appear totally isotropic and the results show that the $x$ direction is more thermally conductive than the $y$ direction. The manufacturer's measured thermal conductivity for Allcomp foam with density of 0.36g/$cm^3$ is around 70W/mK, at room temperature. The thermal conductivity in the $y$ direction agrees well with this value, whereas the conductivity in the $x$ direction is $14\%$ above this value. In order to understand the difference in the results, Allcomp has been approached. They will perform more studies to understand the disagreement in the results. It is worth noting that the manufacturer uses a measurement technique different from that used in this thesis. The manufacturer measures first the thermal diffusivity using the flash laser method on a 1" thick specimen and then converts it to a thermal conductivity. The measured thermal conductivity values of the two thicknesses in the y direction agree well with each other, though the values of the thinner specimen generally lie slightly above those of the thicker specimen.

No temperature dependence is observed for the Allcomp foam for the specimens with thickness equal to 1.4mm. For a given direction, the thermal conductivity value measured with such a thin thickness is greater than the value obtained with thicker specimens. At 20°C, the thermal conductivity of the thin specimen is $12.79\%$ and $16.9\%$ greater than thicker spec-

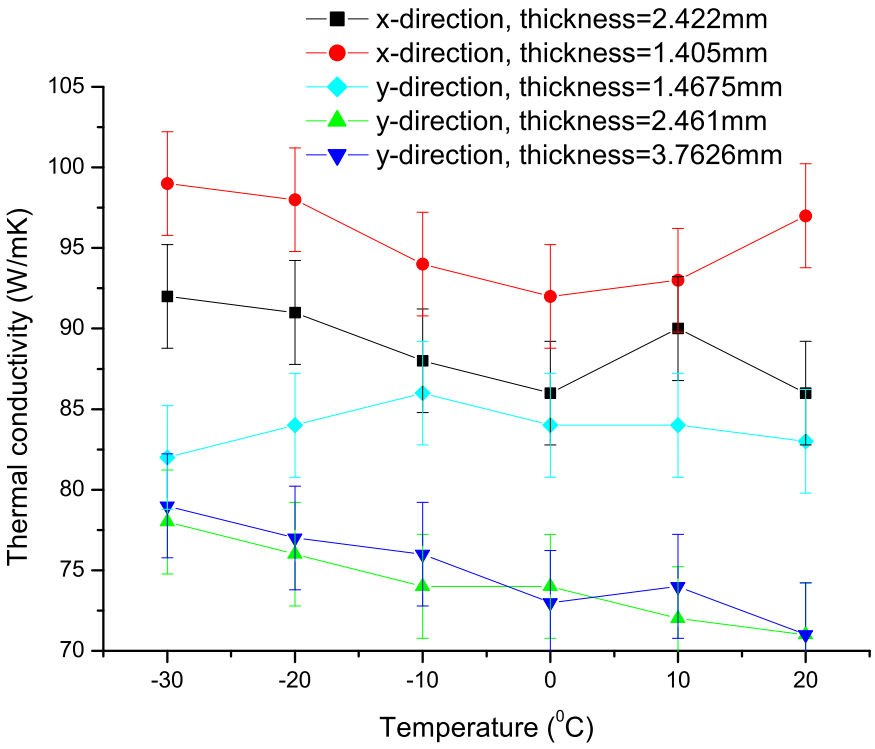


Figure 3.15: In-plane thermal conductivity results of Allcomp with density $\rho$=0.36g/c$m^3$

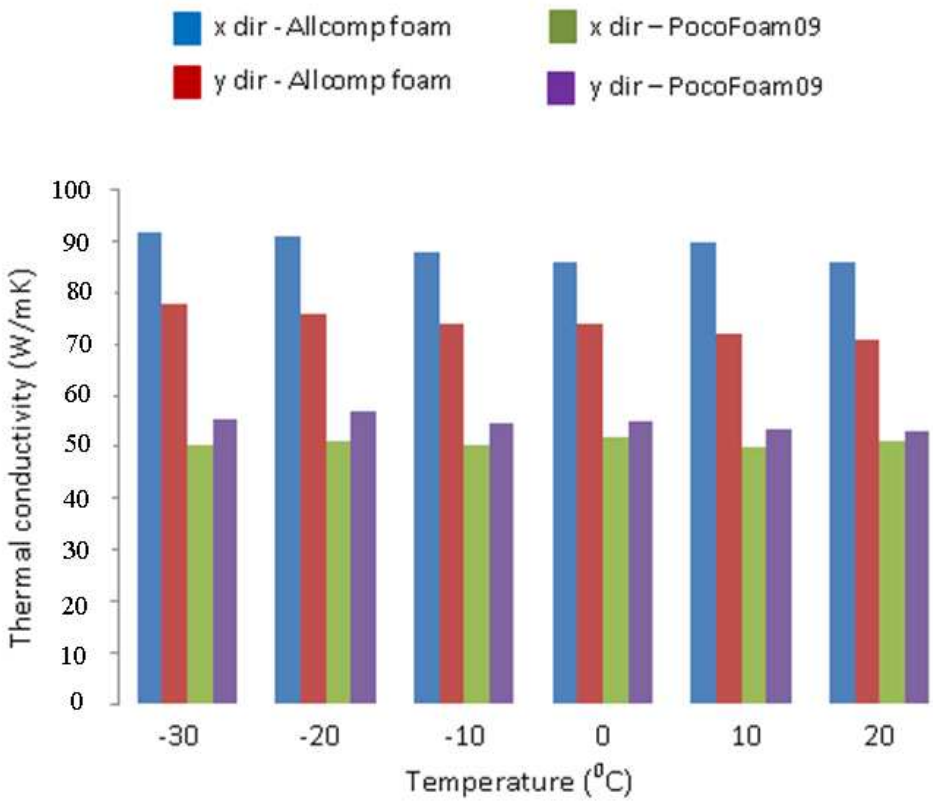


Figure 3.16: Comparison of the thermal conductivity values of poco09 and allcomp foam in the $x$ and $y$ directions

imens in the $x$ and $y$ directions, respectively. It is not understood why the thinner specimens have a higher measured value of thermal conductivity. However, the thin specimens are more affected by broken ligaments near the surface compared to the thicker specimens. For the thicker specimens, the broken ligaments constitute a small percentage of the total cross sectional area than for the thin specimens. This is confirmed by the similar thermal conductivity values in the $y$ direction of the specimens with thicknesses 2.461mm and 3.7626mm. It is therefore concluded that the thermal conductivity values of Allcomp obtained with specimens of thickness greater than 1.4mm are considered accurate and reliable.

The thermal conductivity values of the Allcomp foam appear to be more conductive than the poco09, from $65.4\%$ to $82.2\%$ in the $x$ direction and from $33.33\%$ to $40.54\%$ in the $y$ direction. The comparison is preented in figure3.16.

### 3.8.3 CSiC Foam and carbon carbon

Bulk thermal conductivity measuerements of two carbon silicon carbide foams and carbon/carbon (C/C) specimens are performed at $20°$C in this subsection. CSiC foam is fabricated by depositing, via the CVD process, silicon onto a carbon matrix. This undergoes thermal treatment to form carbon-silicon carbide. The first foam specimen has a density of

$4\%$ of solid SiC and was cut to have a cross sectional area of around $48mm^2$ and the second specimen of density of $8\%$ of carbon silicon carbide was cut to have a cross sectional area of $16mm^2$. Both foam samples were acquired from ERG[12]. The manufacturer measured thermal conductivity is 5.28W/mK at $250°$C. The C/C specimen was purchased from Dunlop and cut to a sample with a cross sectional area of $9.984mm^2$. The results of the measurements are summarised in table 3.3. The thermal conductivity of pure SiC is 120W/mK[13]. Therefore the conductivity of $4\%$ and $8\%$ SiC foam should be as shown in table 3.3.

Table 3.3: Results of CSiC and C/C measurements

| Material | Thermal Conductivity (W/mK) |
|---|---|
| CSiC foam $4\%$ | 43 |
| CSiC foam $8\%$ | 52 |
| C/C | 300 |

The results show that the measured value for $8\%$ CSiC foam is ten times higher than the recommended value for CSiC at $250°$C. Though the measurements in this study are performed at $20°$C (a temperature ten times lower than the temperature quoted by the manufacturer), it is considered that the difference between the measured and recommended values is large. In order to understand the causes of the disagreement in the results, meetings with ERG were organised. The explanation given by ERG is that a graphite core remains (from the fabrication process) in the foam. This graphite core has a higher thermal conductivity than SiC, which causes this significant increase of the thermal conductivity.

### 3.8.4 CFRP

Thermal conductivity of a carbon fibre reinforced polymer specimen was also investigated. The carbon fibre used in this study is a 0-90-0 K13D2U from Mitsubishi Dialead in a unidirectional preimpregnated (prepreg), and the epoxy is the cyanate ester RS3 from Tencate. The specimen has been autoclave cured at the University of Liverpool at a temperature around $177°$C. The specimen has a thickness about 0.222mm with a cross section area equal to $2.74mm^2$. The results are presented in figure 3.17.

It is observed that the thermal conductivity decreases with the increase of the temperature in the temperature range from $-20°$C to $20°$C. At $-20°$C, the thermal conductivity is around 324W/mK and decreases to 310W/mK at $20°$C. The thermal conductivity value is about 315W/mK at $-30°$C. In the temperature range between $-30°$C to $20°$C, it appears that the thermal conductivity of the CFRP increases, reaches a peak and decreases. The results conform with predictions based upon current CAD simulation models analysed with ANSYS.

[12] www.ergaerospace.com
[13] http://accuratus.com/silicar.html

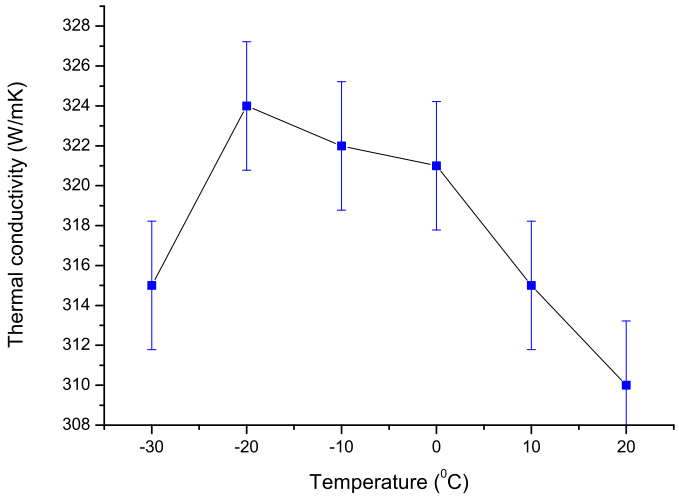


Figure 3.17: In-plane thermal conductivity results of CFRP in the 0-direction. The error in the measurements is $5\%$.

### 3.8.5 TPG

Thermal conductivity measurements of a thermal pyrolytic graphite specimen were also performed. TPG is a unique form of pyrolytic graphite. Pyrolytic graphite can be manufactured by decomposing a carbonaceous gas which builds up a layer of pyrolytic graphite on a hot preformed mandrel [58], [59]. It is characterised by a strong anisotropy in its thermal properties. Pyrolytic graphite is a good conductor in its crystallographic direction and less so in the other direction. The pyrolytic graphite used in this study is supplied by Momentive[14]. The investigated specimen has a thickness of 435$\mu$m and a cross section area of 5.032$mm^2$. Thin layers of TPG are generally difficult to handle because of frequent bends that occur in the specimens during handling. In order to understand the impact of these bends in the specimen on the thermal performance, an intentional bend is made on the specimen and measurements are performed. The bend is placed between pt100_3 and pt100_4, see figure 3.18. Figure 3.19 summaries the results obtained together with the recommended values by Momentive.

Similarly to the values obtained by Momentive, the thermal conductivity decreases with the increase of the temperature. The thermal conductivity measured at $-30$°C and $20$°C are 1920W/mK and 1510W/mK, respectively against 1930W/mk and 1565W/mK recommended by Momentive. The measured thermal conductivity values in this study agree well with the recommended values within $3.5\%$.

The thermal conductivity measurement of the TPG with a bend is performed at $20$°C and it is observed that the thermal conductivity is increased. As unexpected, the introduction of the intentional bend has a contrary effect on the thermal conductivity. The thermal conductivity over the bend, from PT100_4 to PT100_3, is measured to 1641 W/mK. This is an increase of $13.27\%$ over the value of the TPG specimen with no bend. The causes of the

[14] www.momentive.com

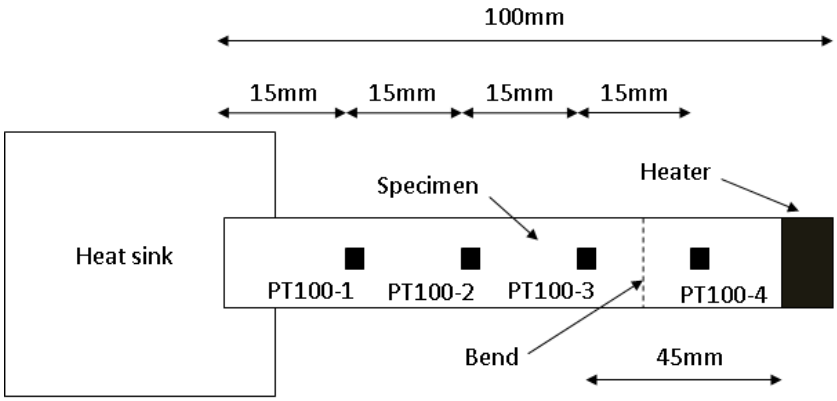


Figure 3.18: View of TPG under investigation with bend placed between PT100_3 and PT100_4

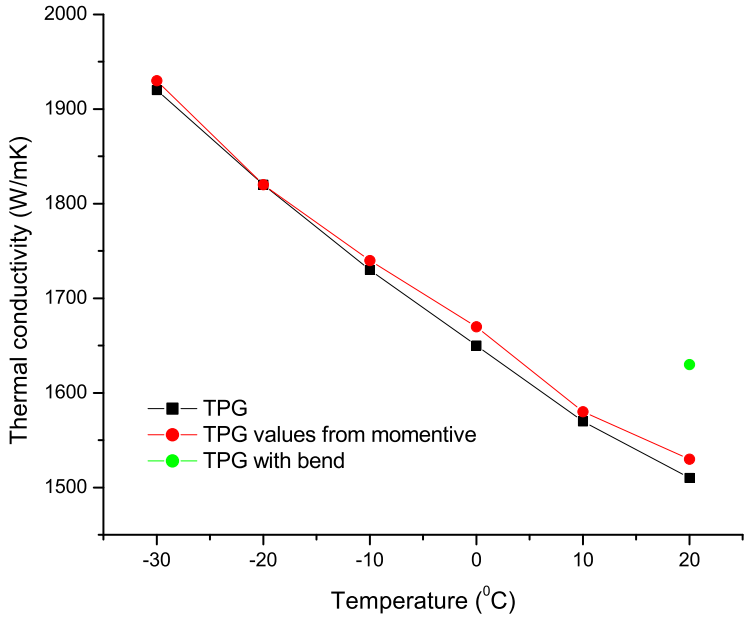


Figure 3.19: View of the TPG measurement results together with the values recommended by Momentive

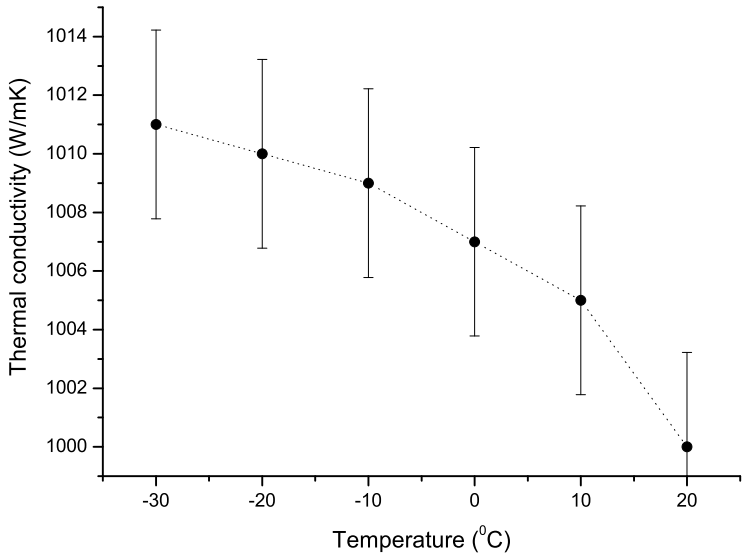


Figure 3.20: Results of the thermal conductivity measurements performed on a e2v diamond specimen

increase of the thermal conductivity are unknown and not understood, therefore more studies are required.

### 3.8.6 Diamond

Thermal conductivity measurements of a diamond specimen from e2v[15] Technologies were also performed. The specimen has a thickness of 0.282mm with a cross sectional area of $2.87mm^2$. The results are summarised on figure 3.20.

It is observed that the thermal conductivity of e2v diamond is dependent on temperature. The thermal conductivity decreases from 1011W/mK at $-30°$C to 1000W/mK at $20°$C. As expected, the thermal conductivity of diamond is high and more than 2.5 times that of copper.

In conclusion, it is observed that the measured thermal conductivities generally decrease with the increase of temperature. The thermal conductivity measurements were performed on non-metal specimens in this chapter. In non-metals, heat conduction occurs mainly by lattice vibrations[16]. Lattice vibration is the phenonmenon taking place in a solid that is heated, and where atoms in the hotter region vibrate vigorously and collide with the neighbouring atoms (the colder atoms). Energy is transferred to these colder atoms and also vibrate vigorously. The process is repeated in every part of the solid, resulting in a transfer of heat energy from the hotter end to the colder end of the solid. This phenomenon in solids resembles the passage of waves and it is called phonon. In crystals that are free from detects and impurities, lattice

[15] www.e2v.com

[16] www.http://www.mtm-inc.com/reduce_project_risk/thermal_conductivity_at_low_temperatures_part_1_theory/

vibrations can travel over long distances in solids and effectively transport heat. Lattice vibrations scatter in collisions with other lattice vibrations.

The decrease of the thermal conductivities can be explained by the fact that the increase of the temperature in the specimens increases the number of lattice vibrations, combined with the impurities and the defects of the solid hinder the lattice vibrations to travel far. This reduces the thermal conductivity.

## 3.9 Summary

An in-plane thermal conductivity measurement system has been designed and built and reported in this chapter. Heat transfer by radiation, convection and conduction have been considered during the design process and solutions to reduce the undesired effects have been applied. The measurement system has been calibrated with a 99.999% pure copper specimen of well known and understood material properties. Measurements of materials such as CRFP, PocoFoam, Allcomp foam, TPG, diamond, CSiC foam and carbon carbon have been performed with the system and the measured results agree well with the materials having documented literature values. ANSYS analysis of the measurement system has been performed and the heat transfer by convection around the specimen, the conductive heat trough the electrical wires and the radiation between the surfaces of the specimen and the surfaces of the shield were neglected. At 20°C, the measured gradients differ from the gradients obtained with ANSYS by up to 11%.

# Chapter 4

# Transverse Thermal Conductivity Measurements

During the use of the upgrade tracker a considerable amount of heat will be generated in the silicon modules (ASIC and silicon detector) and the electrical cables in the heavily irradiated silicon tracker. This heat will establish heat transfer paths through the silicon sensors and their support structures towards the cooling fluid. These paths consist of various materials and the interfaces between them that resist the transport of thermal energy and lead to an increase temperature throughout the thermal circuit. Efficient dissipation of the heat necessitates a reduction of the contact resistances. J. P. Gwinn and R. L. Webb [60] report that for solids of high thermal conductivity, the contact resistance can be reduced by the following two methods:

(1) Increasing the area of the contact spots. This can be achieved by an increase of the contact pressure which "flattens" the peaks of the micro-roughness and deflects the mating surfaces to reduce any non-flatness. The increase of the contact spots can also be achieved by reducing the roughness of the surface before the interface is formed by grinding the surfaces to remove any non-flatness and buffing the surface to reduce any micro-roughness.

(2) Using a Thermal Interface Material (TIM) of high thermal conductivity that can conform to the imperfect surface features of the mating surfaces.

Load constraints on electronic components make it unfeasible to use high contact pressure. Manufacturing of highly finished surfaces is not practical due to the high cost involved. Hence, the best alternative is to use a TIM applied at a moderate contact pressure. The properties of the TIMs need to be well understood in order to achieve a satisfactory heat management inside the design of the stave. The study of TIMs requires a reliable test method capable of achieving accurate and repeatable values. In this chapter, the design and construction of a transverse thermal conductivity measurement system are performed according to the ASTM D-5470 test method. The study is based on 1-D steady state heat conduction at room temperature. The one dimensional heat flow assumption was investigated by Gwinn J., Saini M. and Webb R. [61] with models and it was concluded that the 1-D heat flow can be

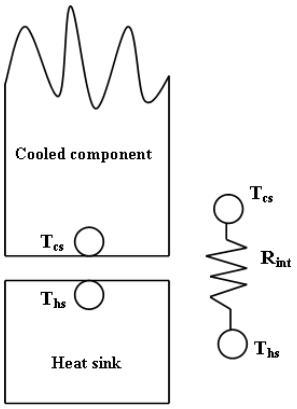


Figure 4.1: Schematic representation of interface resistance

achieved by using long bars, distanced temperature sensing with accurate knowledge of the position of these sensors.

The ASTM D-5470 test method is a standard method to measure thermal impedance for TIMs such as elastomers, tapes, greases and phase change materials (PCM) [62]. ASTM D-5470 describes a method to measure interface resistance ($R_{int}$). The apparatus consists of two metal bars, across which heat is transferred. The TIM is inserted at the interface between the two bars. The standard test is useful with either homogeneous or composite thermally conductive materials ranging from 0.02mm to 10mm in thickness. Electric heat is applied at the end of one bar and the end of the other bar is connected to a heat sink. Two or more temperature sensors are installed on each metal bar. The surface temperature of each bar is obtained from the temperature gradient in each bar together with the location of the temperature sensors. This test method will be also be used in this study to measure thin and solid materials with thickness up to 1mm.

## 4.1 Background

Thermal interface resistance is a measure of how well heat is transferred across the interface of two mating rigid surfaces. A schematic representation of interface resistance is shown in figure 4.1. Referring to figure 4.1, the interface resistance (per unit area) is defined as follows

$$R_{int} = \frac{T_{cs} - T_{hs}}{\dot{Q}} \tag{4.1}$$

where T(cs) is the cooled surface temperature, T(hs) is the heat sink baseplate temperature and $\dot{Q}$ is the power per unit area of the heat-emitting component. The R(int) is commonly presented with units of K/W. It is clear that from equation 4.1, the lowest possible interface resistance is reached when the heat sink temperature approaches that of the cooled surface. The junction of the cooled component and the heat sink contains generally a combination of surface roughness and surface non-flatness as shown on figure 4.2. The micro-roughness is superimposed on a macroscopic non-planar surface in the form of a concave, convex or


Figure 4.2: (a) Heat sink and cooled component roughness, (b) poor heat sink and cooled component flatness [62]

wavy surface which can result in as much as 99% of the interface surface area being by air gaps (see figure 4.3) unless a TIM is used [62].

J.P. Gwinn and R.L. Webb report that, the contacting surfaces will contact each other only at discrete points and the number of contact points will increase with the increase of pressure on the interface. Air is a very poor thermal conductor, with $k_{air}$ equal to 0.026W/mK at room temperature and acts as thermal barrier and hinders efficient heat transfer through the interface. As seen in figure 4.3, the contact resistance ($R_{contact}$) consists of the conduction resistance at the points where the mating surfaces touch each other and the conduction and/or radiative resistance across the gaps of non-contacting area. Any substance (with thermal conductivity exceeding that of air) that fills the gap will decrease the contact resistance [63], see figure 4.4.

The ideal TIM (figure 4.4) is expected to have high thermal conductivity, be easily deformed by small contact pressure and have minimal thickness. Further, the TIM should not leak out of the interface, should maintain performance indefinitely and be manufacturing friendly (easy to apply and remove). To date, no TIM on the market can meet the expectation of an ideal TIM. Available TIMs will not completely fill the cavities and small air pockets will remain on both sides of the interface material and the TIM will not have minimal thickness, see figure 4.5

As presented in figure 4.5, $R_{contact1}$ is the contact resistance between the TIM and the electronic component's surface, $R_{cond}$ is the conduction across the thickness of the TIM and $R_{contact2}$ is the contact resistance between the TIM and the heat sink base plate. The interface resistance $R_{int}$ is the sum of the three resistances and it is expressed as follows

$$R_{int} = R_{contact1} + R_{cond} + R_{contact2} \tag{4.2}$$

with

$$R_{cond} = \frac{\Delta L}{k_{TIM}} \tag{4.3}$$

where $\Delta L$ and $K_{TIM}$ are the effective thickness of the thermal interface material and its thermal conductivity, respectively. $R_{cond}$ is the conductivity of the material.

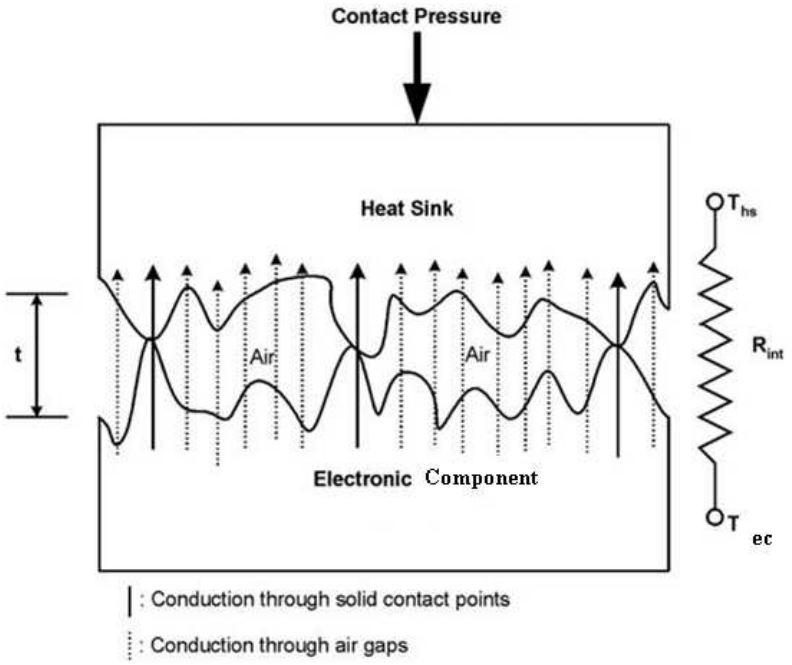


Figure 4.3: Exploded view of thermal interface when no TIM is used [62]. R(int) is composed only of contact resistance

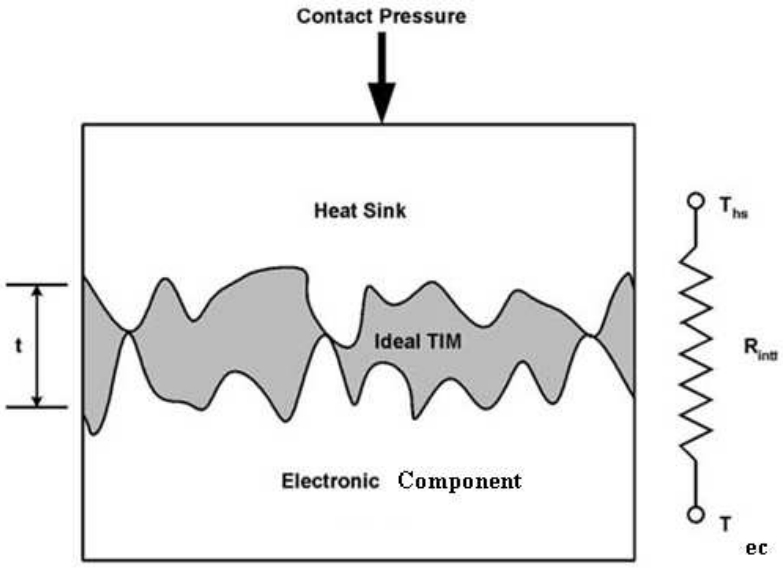


Figure 4.4: Exploded view of thermal interface when an ideal TIM is used [62]

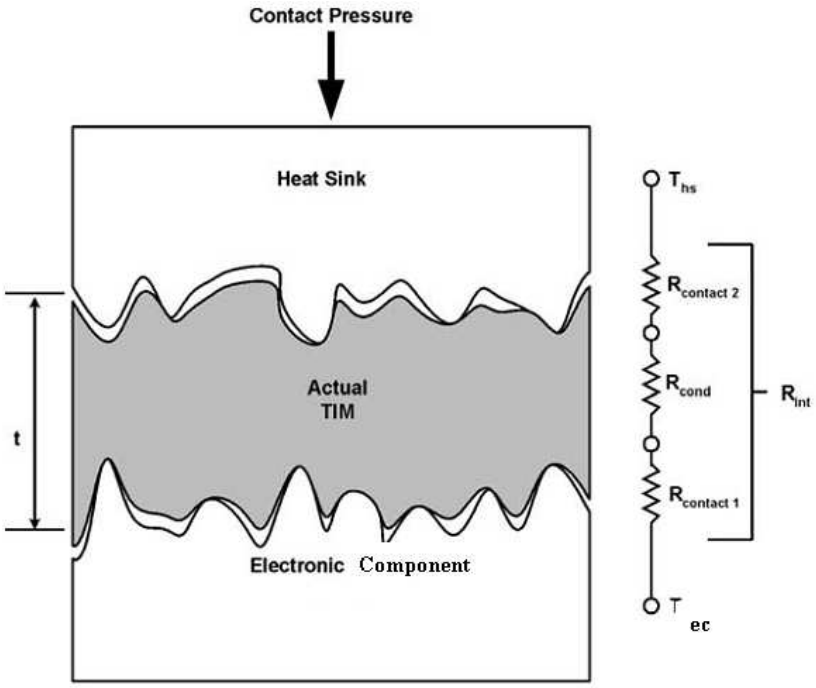


Figure 4.5: Exploded view of thermal interface with actual TIM [62]

## 4.2 Setup

Figure 4.6 shows the experimental setup for the measurement of interfacial contact conductance based on 1-D steady state conduction used in this study. The setup consists of a heater placed high on the upper copper bar and a liquid-cooled heat sink maintaining a constant heat flux in the test column which consists of two copper bars with the material under investigation sandwiched between. The copper bars have a uniform cross section area of $100mm^2$. The copper used to machine the bars is heavily oxidised with emissivity equal to 0.8. The end surfaces of the copper bars are polished to a surface roughness of around $R_a{\sim}1\mu$m. The temperature distribution is measured along the heat path by RTDs stuck with tape on the copper bars on each side of the material under investigation. Thermal grease is used as a thermal interface material between the RTDs and the copper bar surfaces to ensure good contact. The RTDs are placed on two coinciding copper bar surfaces and their positions form a virtual vertical line equidistant from the vertical edges of the bars. The distance $\Delta L$ from the RTDs to the material under investigation is accurately measured with a caliper. The distance between the upper RTD and the heater is more than two and half times the length of the heater, allowing the heat flow to be well developed and steady. A load cell is used to apply controlled pressure on the material under investigation.

The measurements are performed at room temperature and the average temperature of the RTDs is kept similar to the environment temperature. This is done in order to reduce the heat transfer by radiation between the copper bars and the environment temperature. The amount of heat flowing by conduction through the copper bars is large compared to the radiation loss to the environment because of the large cross sectional area of the bars. Therefore, it

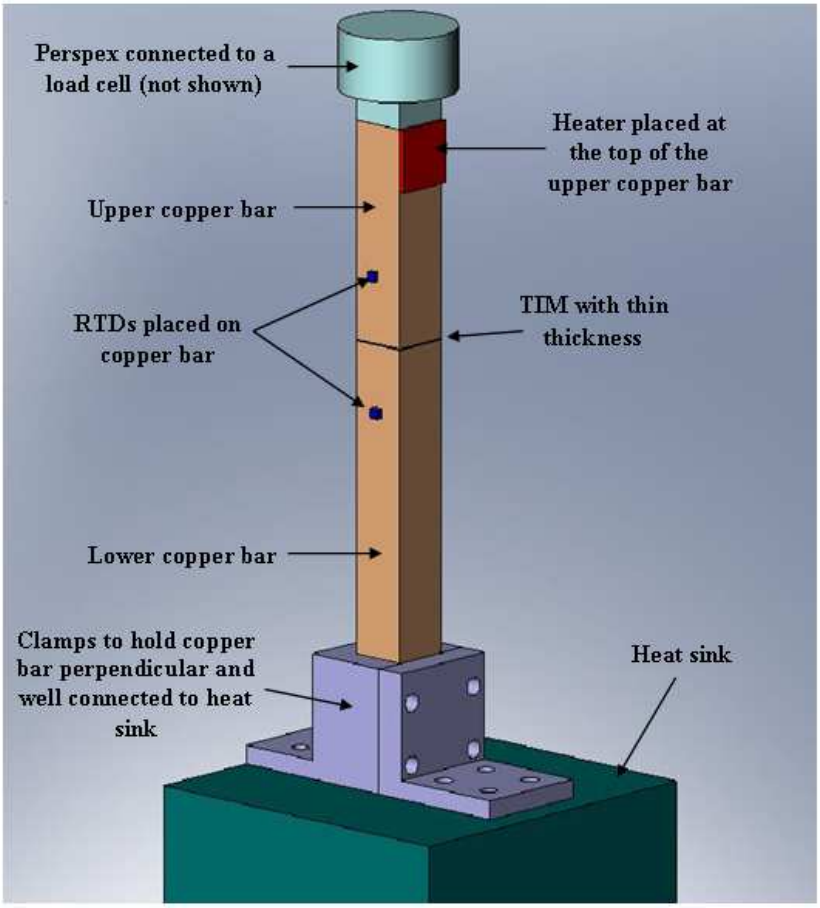


Figure 4.6: Solid Works model of the transverse thermal conductivity measurement system

is assumed that achievement of satisfactory measured results can be obtained without using any radiation shield. The measurement system used in the laboratory is shown in appendix B.

The measurements are performed in the laboratory at a location where the air surrounding the setup is stationary. There are no external means such as fans, pumps and suction devices switched on in the vicinity of the measurement system to provoke the flow of the air. The application of heat on the upper copper bar establishes a temperature difference between the surfaces of the bar and the stationary air. The adjacent air to the upper copper bar will move upward. This mode of heat transfer is referred to as natural convection. The location of the heater (high up on the upper copper) constrains the bulk of the air to move above the copper bars, reducing considerably the amount of heat transfer by convection along the copper bars. The remaining heat transfer by convection along the copper bars is considered insignificant compared to the amount of the heat transfer by conduction and is therefore not considered in this study.

Thermal resistances and conductivities of thermal interface materials such as Dow Corning 340, Dow Corning SE4445, Hysol EA9396, Araldite 2011 and Epolite FH-5313 epoxy were measured in this study. Measurements of solid materials such as CFRP and kapton films was also be performed. The setup was also modified in order to allow measurements of the thermal properties of blocks of PocoFoams and Allcomp foams.

## 4.3 Determination of the thermal resistance

Generally, the total contact resistance, per unit area, ($R_{contact}$ = $R_{contact1}$ + $R_{contact2}$ ) is determined experimentally by measuring thermal resistance data for a range of TIM thicknesses and plotting $R_{int}$, per unit area, versus thickness. The resulting graph exhibits a linear relationship expressed as follows

$$R_{int}(\Delta L) = R_{contact} + \frac{\Delta L}{k_{TIM}} \tag{4.4}$$

The slope is equal to the inverse of $k_{TIM}$ and the intercept of the straight line with the $R_{int}$ axis is equal to $R_{contact}$ [64]. It is worth noting that the $R_{contact1}$ (surface between the electronic component and the TIM) and $R_{contact2}$ (surface between heat sink base and the TIM) resistances can be different because each of the two contact surafces may differ in roughness or flatness.

The actual thermal conductivity of the TIM can also be determined by measuring thermal resistance data and plotting $R_{int}$ versus pressure. It is observed using this method that the resistance decreases with the increase of the pressure until $R_{int}$ reaches a constant value. This constant value is equal to twice the thermal resistance at the contact between the TIM and sandwishing surface. This method is usually used when the surfaces sandwiching the TIM have similar flatness and roughness. This causes $R_{contact1}$ to be equal to $R_{contact2}$ and

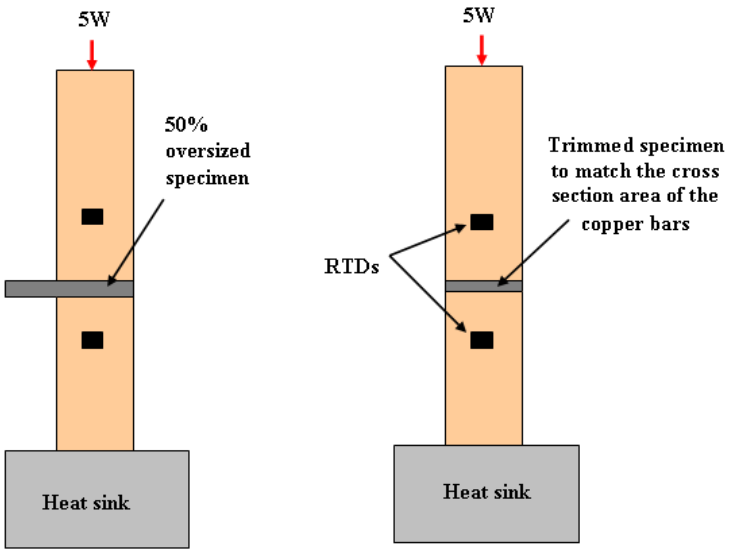


Figure 4.7: Overview of the specimens with different cross section areas used the ANSYS analysis. $Q_{rad}$ and $Q_{conv}$ are the radiative and convective heats transferred between the non sandwiched part of the oversized specimen and the room temperature.

simplifies the expression of the total resistance to

$$R_{contact} = 2R_{contact1} \tag{4.5}$$

The two methods mentioned above will be used in this study to determine the thermal conductivity of Dow Corning 340[1]. However, the method using $R_{int}$ vs pressure will be utilised for the determination of the transverse thermal conductivity values presented in this thesis.

## 4.4 Measurement Optimisation - FEA

A thermal analysis of a solid TIM was performed in ANSYS in order to understand whether the dimensions of the cross section area of the specimen sandwiched between the copper bars influences the results. The analysis consists of reproducing a laboratory measurement of two specimens of the same material and of the same thickness (500$\mu$m), measuring the thermal conductivities and determining the corresponding thermal resistances. One specimen is trimmed to match the cross sectional area of the copper bars ($1cm^2$) and the other specimen is 50% oversized, as shown figure 4.7.

[1] www.dowcorning.com

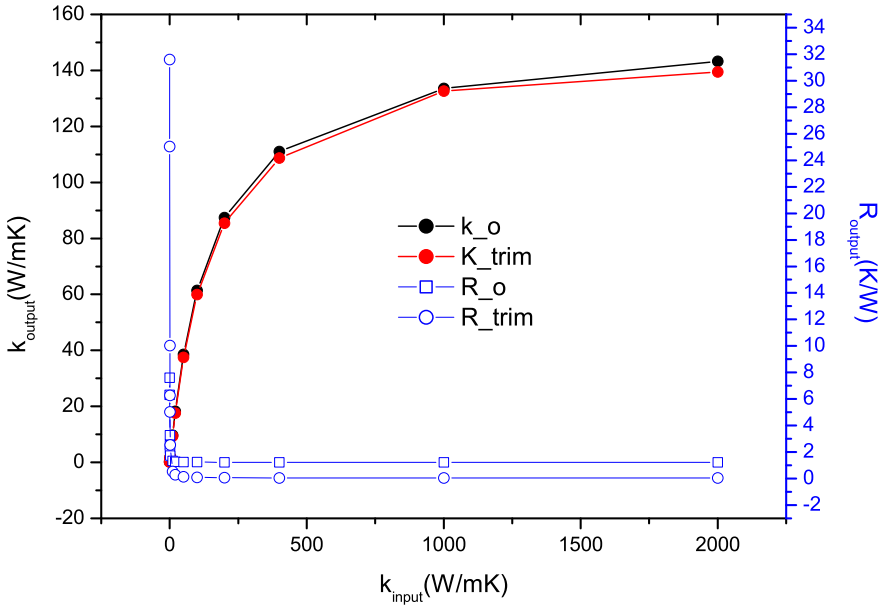


Figure 4.8: Graphical representation of the calculated thermal resistance and thermal conductivity versus the input thermal conductivity. $R_o$ and $k_o$ are the resistance and conductivity of the oversized specimen; $R_{trim}$ and $k_{trim}$ are the resistance and conductivity of the trimmed specimen

### 4.4.1 Basic Simulation

The components of the CAD assembly have the same material properties as the components used in the laboratory. A constant heat flow of 5W is applied on the top surface of the upper copper bar and a fixed temeprature of -10°C is applied on the heat sink. Two points are accurately located on the copper bars, one on each side of the specimen under investigation. These points represent two RTDs with well known distances to the surfaces of the specimen. For a given value of the input thermal conductivity, temperatures are measured at the two points and used to calculate the corresponding output thermal conductivity. Heat transfer by radiation and convection are not considered in this analysis.

### 4.4.2 Results and Discussion

Thermal conductivity values ranging from 0.16W/mK to 2000W/mK are taken as the input into ANSYS and the corresponding output thermal conductivities are determined. It is worth noting that the output thermal conductivities are the conductivity values calculated by using the temperature measured with the RTDs. The results of the whole range of the calculated conductivities together with the calculated resistances are presented on figure 4.8. The calculated thermal conductivity values of the specimens (oversized and trimmed) increase from 0.16W/mK to around 140W/mK when the input conductivity values increase

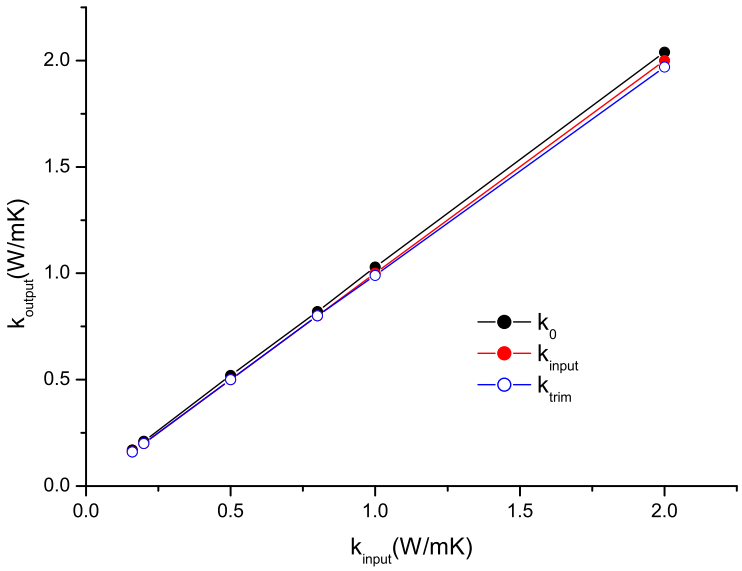


Figure 4.9: Graphical representation of the calculated thermal conductivities compared to the expected conductivity. $k_{input}$ is the expected thermal conductivity, $k_0$ is the thermal conductivity of the oversized specimen and $k_{trim}$ is the thermal conductivity of the trimmed specimen.

from 0.16W/mK to 2000W/mK. The calculated thermal resistance values of the specimens decrease rapidly from 33K/W and "flattens" to a constant value of 0.03K/W with the increase of the input conductivity values from 0.16W/mK to 2000W/mK.

The results of the calculated conductivity values together with the input thermal conductivity values are presented on figure 4.9, for the input thermal conductivity values increasing from 0.16W/mK to 2W/mK. The calculated conductivity values obtained from the trimmed specimen are equal to the input values until the input conductivity values reach 1W/mK, where they begin to differ progressively. The calculated conductivity is lower than the input conductivity for an input value equal or greater than 1W/mK. The calculated conductivity values obtained from the oversized specimen differ from the input values over the whole range of the input thermal conductivity values. However, for a given input value between 0.1W/mK and 2W/mK the thermal conductivity values of the oversized specimen agree within 3%. Within this input value range, the oversized and trimmed specimen values agree within 4%, while the thermal conductivity values of the trimmed specimen agree well with the input values within 1.5%. The value of the trimmed specimen agrees better with the expected value for a given input conductivity value less than 2W/mK. It is worth noting that for a given input value between 2W/mK and 10W/mK, the calculated conductivity values of the oversized and the trimmed specimens differ by up to 6.1%.

For a given input thermal conductivity ranging from 0.16W/mK to 2W/mK, the calculated thermal resistance of the oversized specimen decreases from 30.20K/W to 2.45K/W, see figure 4.10, and of the trimmed specimen from 31.59K/W to 2.53K/W. When the input thermal conductivity is above 2W/mK, the calculated thermal resistance of the specimens is

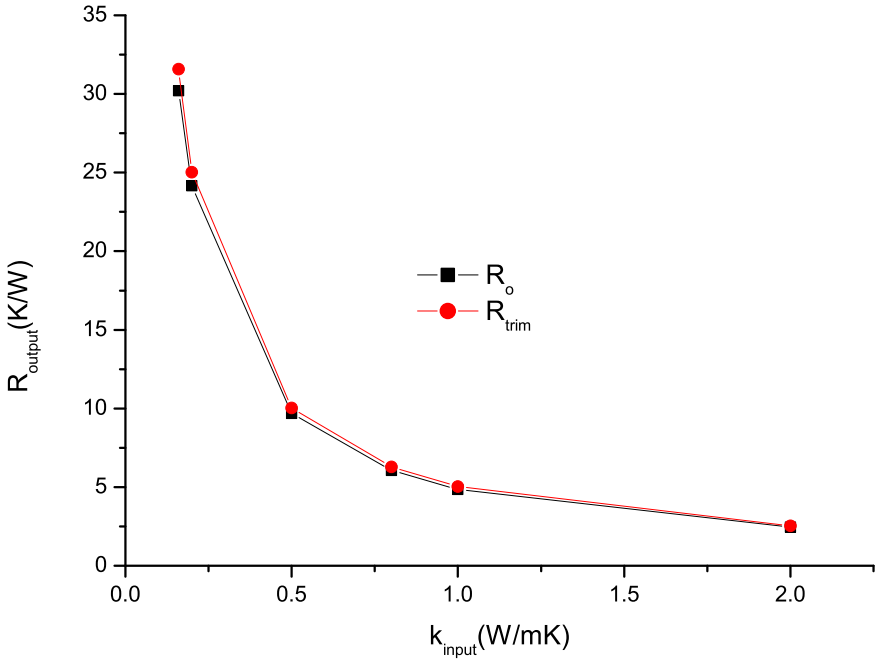


Figure 4.10: Graphical representation of the calculated thermal resistances versus the input thermal conductivity

less than 2K/W and their values agree well with each other within 0.25%.

In conclusion, it is considered that measurements of solid materials with thickness around 500$\mu$m and a thermal resistance less than 2K/W are not suitable to measure with the present measurement system. Measurements appear more accurate with specimens with cross section area matching the cross section area of the copper bars. Specimens larger than the cross section area of the copper bars cause additional heat paths which contribute to the small difference observed from the specimen having the cross section area matching that of the copper bars.

## 4.5 Uncertainties

In this section, the error in the thermal conductivity of the specimen under investigation is presented. This error is due to the experimental uncertainties in the measured data such as the positions of the RTDs on the copper bars, the thermal conductivity of the copper bar, the temperature drop and the heat flow along the copper bars, the cross section area of the copper bars and the heat loss along the copper bars.

The total error in the position of the RTDs, including the error in the ability of reading the calliper was found in chapter 3 to be around 0.195%. The uncertainty in the temperature

drop is about 1.8% and is associated with the platinum (HEL-700) type RTD error data acquisition (0.08°C) together with the uncertainty in the position of the RTDs (0.155%). The uncertainty in the heat flow is introduced by the uncertainty of the reading of the voltage (0.1%) and the current (0.2%). The uncertainty in the thermal conductivity of the copper bars is determined by performing conductivity measurements of the copper bars several times under the same conditions. The uncertainty in the cross sectional area of the copper bars is due to the ability of reading the micrometer that was used to measure the dimensions of the bars. This uncertainty was found to be equal to 0.14%. The uncetainty in the heat loss by radiation along the copper bars is determined by calculating this heat value several times under the same conditions. The uncertainty of the heat loss was found to be 0.30%. Based upon the standard uncertainty analysis technique [65], the uncertainty is found be equal to 2.64%.

## 4.6 Thermal Properties of Thermal Interface Materials

For the stave design materialss of interest, Dow Corning 340, Hysol EA 9396, Epolite and Dow Corning SE4445 are selected as thermal interface materials. These substances are investigated for their thermal properties, particularly their resistances and their thermal conductivities. Preparations and curing processes of the aforementioned thermal interface materials are presented together with a detailed explanation of the methodology used to mesure their thermal properties.

### 4.6.1 Methodology of surface area of copper bars at interface ($\approx$ (1$cm^2$)

Figure 4.11 shows the terms used in the calculations to determine the thermal resistance and conductivities. $T_1'$ and $T_2'$ are respectively the temperatures at the bottom of the copper and at the top of the lower copper bars. $T_1$ and $T_2$ are the temperatures of RTD1 and RTD2, placed on each side of the TIM on the copper bars. The average temperature of $T_1$ and $T_2$ are kept equal to the room temperature constraining the temperature of the TIM to be near the room temperature. This is done in order to reduce heat transfer by radiation between the TIM and the environment. $T_{Cu}$ and $T_{heater}$ are placed at the top of the upper copper bar and on the heater respectively. The temperatures of these RTDs are used to determine the heat loss from the heater and the exact amount of heat moving through the upper copper bar from the heater.

The heat loss by conduction through the AWG 28 electrical wires ($\phi$ = 0.321mm) used to power the heater was investigated by removing the wire's electrical insulation and placing two RTDs directly on the surface of the copper wire near the heater. By supplying 1W, it was found that the heat loss by conduction through the wires was 2.05%. The surface area of the heater is equal to 2.5x$10^{-5}m^2$. The heat losses by radiation from the heater and the surfaces of the copper bars depend on the room temperature and they are calculated for each measurement. The total radiative heat loss is typically around 3.60% of the heat applied. The

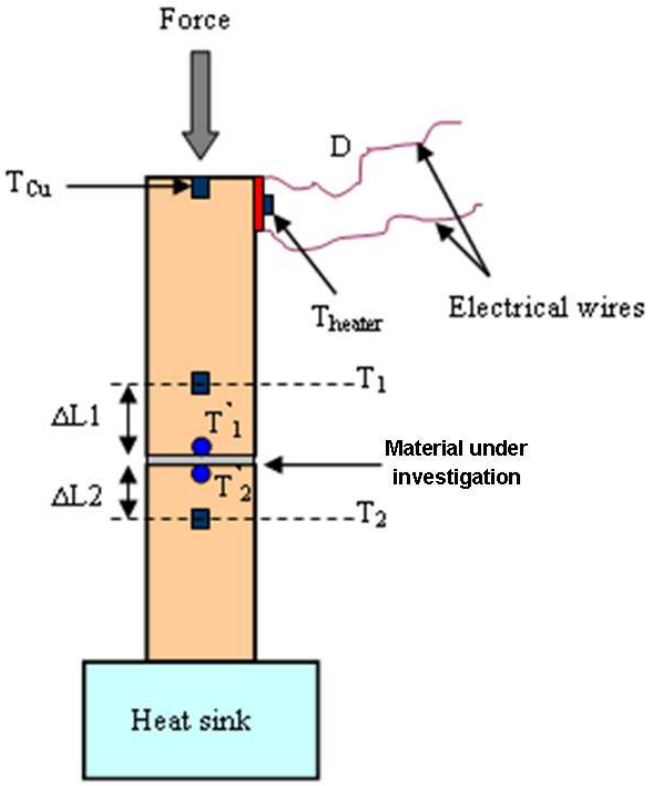


Figure 4.11: Drawing of the thermal interface measurement system

sum of the heat losses by conduction and radiation is considered high and non-negligible, therefore the measurement system is corrected accordingly.

The locations of RTD1 and RTD2 from the edges of the copper bars are accurately known and denoted ($\Delta$L1) and ($\Delta$L2). These distances are measured with callipers. The $T_1'$ and $T_2'$ are the temperatures at these edges and are calculated with the following expressions:

$$T_1' = T_1 - \frac{Q - Q_{heat} - Q_{Cu} - Q_{(RTD1-edge)}}{k_{Cu}A_{Cu}}\Delta L1 + K_0 \tag{4.6}$$

$$T_2' = T_2 + \frac{Q - Q_{heat} - Q_{Cu} - Q_{(RTD1-edge)} - Q_{(edge-RTD2)}}{k_{Cu}A_{Cu}}\Delta L2 + K_0 \tag{4.7}$$

where Q is the amount of heat intentionally applied by the heater, $Q_{heat}$ is the heat loss by radiation from the heater, $Q_{Cu}$ is the heat loss by radiation by the portion of the upper copper bar between the top of the bar and RTD1, $Q_{(RTD1-edge)}$ is the heat loss by radiation between RTD1 and the bottom of the upper copper bar, $Q_{(edge-RTD2)}$ is the heat loss by radiation between the edge of the lower copper bar and RTD2 and $K_0$ = 273.16K. The radiative heat loss by the portion of the copper bar below RTD2 does not influence the results. This heat loss is therefore not considered in the calculations.

In this study, $R_{contact1}$ and $R_{contact2}$ are considered equal by ensuring that the roughness

and flatness of the copper bars are similar. Hence, equation 4.2 is simplified in this study as

$$R_{int} = R_{cond} + 2R_{contact1} = \frac{T_1' - T_2'}{Q'} \tag{4.8}$$

where Q' = Q - $Q_{heat}$ - $Q_{Cu}$ - $Q_{RTD1-edge}$ is the corrected heat and is considered the exact amount of heat going through the TIM. Finally, the actual resistance of the TIM ($R_{cond}$) is determined by the following expression

$$R_{cond} = R_{int} - 2R_{contact1} \tag{4.9}$$

### 4.6.2 Dow Corning 340

Dow Corning 340 is the thermal grease used in all the measurements in this thesis. It is an odourless white paste that is easy to apply and remove from surfaces. Its thermal resistance is measured with two different ways in order to cross check the reliability of the methods.

The determination of the thermal interface resistance of Dow Corning 340 is firstly achieved by performing measurements on different thicknesses of a solid composite consisting of Hysol EA9396 and 23.1% Boron Nitride . The preparation of this composite is explained later in this chapter. The composite is placed inside the copper bars and a thin layer of Dow Corning 340 is applied between its surfaces and the copper cross section. A pressure of 0.47MPa and a power of 1W are applied on the composite and resistance measurements are performed on the composite with following thicknesses: 85$\mu$m, 164$\mu$m, 207$\mu$m, 257$\mu$m and 438$\mu$m. Table 4.1 presents the results of the measured thermal interface resistances together with the temperature difference $T_1'$-$T_2'$.

Table 4.1: Summary of the thermal resistance results measured on different thicknesses of Hysol EA9396 + 23.1% Boron Nitride of cross sectional area equal to $1cm^2$

| Thickness ($\mu$m) | $R_{int}$ (K/W) | $T'_1$-$T'_2$ (K) |
|---|---|---|
| 85 | 1.90 | 1.79 |
| 164 | 3.91 | 3.62 |
| 207 | 4.13 | 3.91 |
| 257 | 5.05 | 4.68 |
| 438 | 8.42 | 7.65 |

These results are plotted on figure 4.12 where they exhibit a linear graph intersecting the $R_{int}$ axis. At that intersecting point, $R_{int}$ = $2R_{Cu/DC340}$ = 0.55. The resistance at the interface of copper/Dow Corning 340 is therefore determined in this study as

$$R_{Cu/DC340} = 0.27 \pm 0.066 K/W \tag{4.10}$$

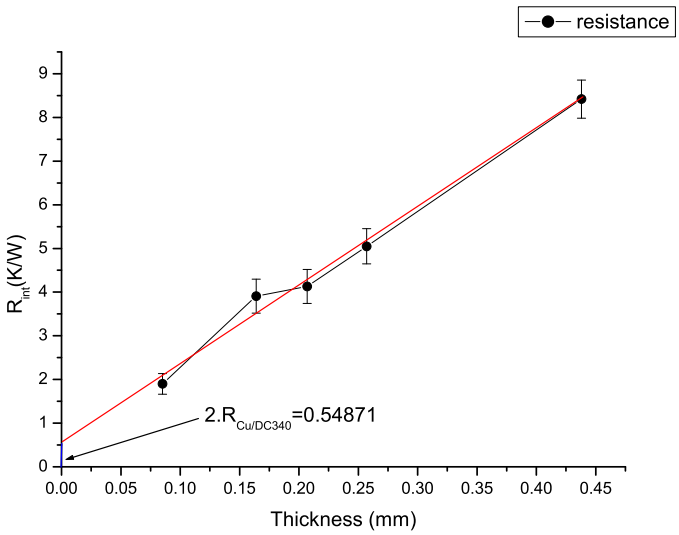


Figure 4.12: DC 340 Thermal Interface Resistance vs thickness

The second method consists of measuring the interface resistance of DC 340 and plotting $R_{int}$ vs pressure, as shown in figure 4.13. The interface resistance decreases with the increase of pressure until it reaches a constant value of 0.27K/W from 0.43 MPa. A similar result is observed when the measurement is performed on a layer of DC 340 sandwiched inside two pieces of carbon/carbon of measured thermal conductivity 287W/mK and roughness $R_a \sim 1.5 \mu$m. The interface resistance decreases until it reaches a constant value of 0.30K/W. This value differs slightly from 0.27K/W because of the difference in the materials surface properties.

It is clear that the values obtained from the two methods to determine the contact resistance agree well. The value of the thermal interface resistance of Dow Corning 340 is considered to be 0.27K/W. This value will be used for the calculation of transverse thermal resistances in this thesis. The pressure applied on the interface materials during all of the following measurements is 0.47MPa.

### 4.6.3 Araldite 2011

Araldite 2011[2] epoxy adhesive is a multi-purpose, viscous material that is suitable for bonding a variety of materials, including metal, ceramic, wood, foams and plastic. Araldite consists of two parts A and B, with mixing ratio 1:1. One of the recommended schedule for curing the epoxy is 10 min @ 100°C. It is easy to apply and has a good resistance to static and dynamic loads. At the beginning of this thesis, araldite 2011 was the epoxy that was under investigation to be used for the design of the stave. Thermal conductivity studies have been therefore carried out. Other epoxies were later preferred for the stave design and araldite

[2] www.ebpltd.com

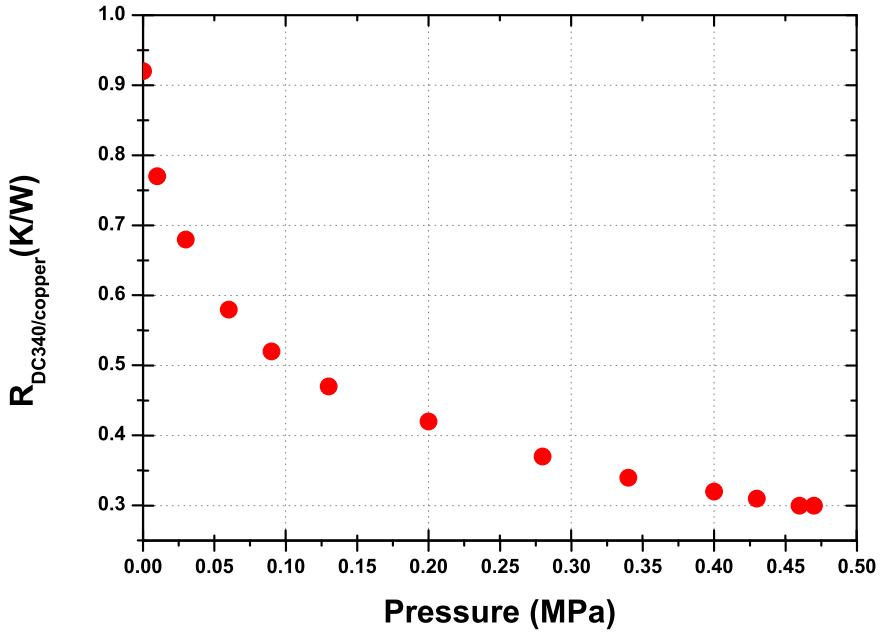


Figure 4.13: DC 340 Thermal Interface Resistance vs Pressure and Thermal conductivity

2011 was dropped. The measurements were performed using two copper bars to sandwich the araldite at room temperature with a power of 1W applied on the copper. The thermal conductivity was measured as 0.22W/mK and agrees well with recommended values.

### 4.6.4 Hysol EA9396, Dow Corning SE4445 and Epolite FH-5313 epoxy

Hysol EA9396, DC SE4445 and Epolite FH-5313 are proposed for the manufacture of the stave of the ATLAS inner tracker. Figure 4.14 shows a schematic view of the cross section of the proposed stave design showing the different glue layers.

The preparation of the glue specimens is performed by mixing thouroughly the two components according to the defined mixing ratio. The mixture is poured onto a flat teflon sheet between two stainless steel shims. These shims define the eventual specimen thickness. Teflon is used due to non-stick property which allows easy specimen removal after the cure process.A flat edge pressed hard onto the two shims is drawn over the glue specimen to define the glue thickness. The finished specimens are flat, solid sheets that are easy to cut with a blade, as shown in figure 4.15.

Measurements of these solid specimens were performed by using Dow Corning 340 between the surfaces of the specimens and the copper bars. The meausrements were made at room temperature with a pressure of 0.47 MPa applied on the specimens. The contact resistance was assumed equal to that found for the two copper bars with DC 340. The tem-

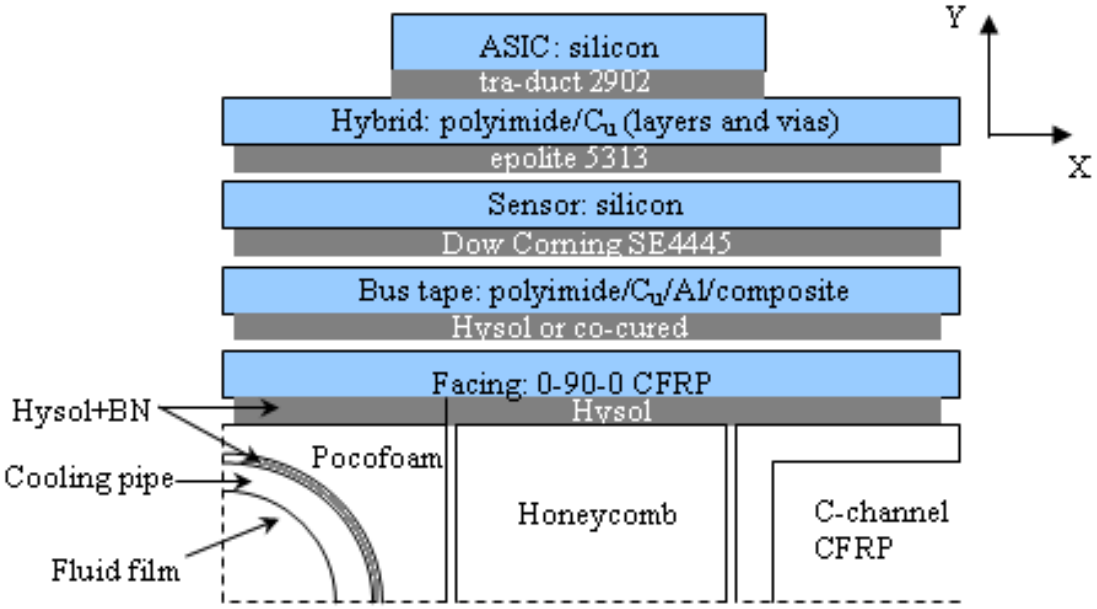


Figure 4.14: Schematic view of the cross-section of the stave with the different glue layers applied

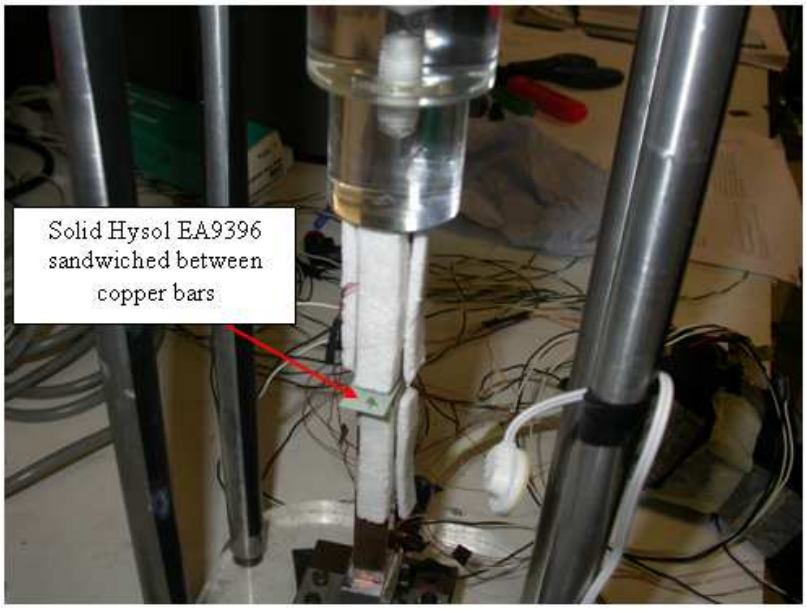


Figure 4.15: View of a solid TIM sandwiched between the copper bars

perature difference between the surfaces of the specimens were measured to be $12.71°$C and $12.76°$C for the epolite and the Hysol specimens, respectively. After the subtraction of the contact resistances, the epolite specimen with a thickness of 390$\mu$m exhibited an actual resistance equal to 13.85K/W and the thermal conductivity was found to be 0.28W/mK. The Hysol EA9396, with a thickness of 415$\mu$m exhibited an actual resistance equal to 14.02K/W and the thermal conductivity to be 0.28W/mK. The resistance of the Dow Corning 340 represents 15.51$\%$ and 26.68$\%$ of the actual resistance of the epolite and the Hysol EA9396, respectively.

The Dow Corning SE4445 is rubber like and cannot be measured using the method utilised for the epolite or the Hysol. The thickness of the DC SE4445 reduces considerably when a pressure of 0.47 MPa is applied. Therefore, another method is used for the measurement of its thermal conductivity. The method consists of producing the DC SE4445 specimen by bonding two copper bars together with the epoxy under modest pressure. Two fishing lines of diameter (500$\mu$m) were placed inside the DC SE4445 during the curing process (overnight at room temperature) to define the thickness of the specimen to equal that of the fishing lines. Therefore, when a pressure of 0.47 MPa is applied, the fishing lines keep the thickness of the DC SE4445 at 500$\mu$m preventing the DC SE4445 from deforming. After the subtraction of the contact resistances, the Dow Corning SE4445 exhibits an actual resistance equal to 8.47K/W, a temperature difference between the surfaces of $8.17°$C and a thermal conductivity equal to 2$\pm$0.2 W/mK. The resistance of the Dow Corning 340 represents 8.97$\%$ of the total resistance. Table 4.2 summarises the results.

Table 4.2: Summary of the thermal conductivity results of Epolite FH-5313, Hysol EA9396 and Dow corning SE4445

| Adhesives | Thickness ($\mu$m) | Power applied (W) | $\Delta T$ (°C) | Resistance (K/W) | Thermal conductivity (W/mK) |
|---|---|---|---|---|---|
| Epolite FH-5313 | 517 | 1 | 15.83 | 17.41 | 0.28$\pm$0.01 |
| Hysol EA9396 | 415 | 1 | 12.76 | 14.02 | 0.28$\pm$0.01 |
| DC SE4445 | 214 | 1 | 8.17 | 8.47 | 2$\pm$0.2 |

## 4.7 Thermal behaviour of epoxy resin filled with high thermal conductivity micropowders

Hysol EA9396 and Araldite 2011 are strong candidates to glue the CFRP facings to the PocoFoam. Their application in the stave design is limited by their low thermal conductivities causing an increase of the thermal resistance between the CFRP facing and the PocoFoam and therefore a temperature rise in the CFRP over the foam temperature. In order to improve these conductivities, thermally conducting but electrically insulating filler (Boron Nitride) is used to dope the matrices and obtain polymer-based composites. Boron Nitride is attractive because it has a low atomic number and therefore a high radiation length. The high thermal

conductivity of Boron Nitride in the bulk state can be attributed to the simplicity of the crystal structure, the low atomic mass, the existence of strong covalent bonding between the atoms and the low disorder within the crystal lattice [66]. The theoretical limit of thermal conductivity for a single crystal of Boron Nitride at room temperature is 1300W/mK. However, the experimental thermal conductivity of the powder is significantly lower than its crystalline counterpart (200 to 500W/mK), because of the interface between powder particles [67].

### 4.7.1 Different models

Berman R. [68] reports that the thermal resistance in a solid is caused by phonon scattering, therefore the phonon scattering has to be minimized in order to increase the thermal conductivity. Winco Yung [69] concludes, after his studies on different particle sizes of Boron Nitride, that more and larger Boron Nitride particle sizes help to shorten the low thermal conductivity path in the epoxy matrix and establish a high thermal conductivity network (Boron Nitride) for heat conduction. Larger size means lower surface to volume ratio[3], thereby, lower interfacial phonon scattering for a given weight of the filler [70]. In consequence, a higher percentage and larger particle sizes of Boron Nitride yields a higher thermal conductivity. In this study, the effective thermal conductivity of Hysol filled with Boron Nitride is determined experimentally as a function of Boron Nitride concentration. The obtained values are compared with existing theoretical and empirical models. The existing theoretical and empirical models are discussed below followed by the experimental results.

#### 4.7.1.1 Lewis and Nielsen

The Halpin-Tsai theoretical model [71], considered as the best and most versatile to calculate the elastic moduli of all kinds of composite materials, has been modified by Lewis and Nielsen [72] to include the effect of the shape orientation and type of packing of the particle filler in a two-phase system. The modified equations [73] for the two-phase systems are

$$\frac{k_c}{k_m} = \frac{1 + AB\phi}{1 - B\phi\psi} \tag{4.11}$$

$$A = k_E - 1 \tag{4.12}$$

$$B = \frac{\frac{k_f}{k_m} - 1}{\frac{k_f}{k_m} + A} \tag{4.13}$$

[3]The surface to volume ratio and variously denoted SA:V is the amount of surface area per unit volume of an object. The surface area to volume ratio is measured in units of inverse distance. For a given shape, SA:V decreases linearly with increasing volume

$$\psi = 1 + (\frac{1-\phi_m}{\phi_m^2})\phi \tag{4.14}$$

The properties $k_c$, $k_f$, $k_m$ are the thermal conductivities of the composite, filler material and polymer matrix, respectively and $\phi$ is the volume fraction of the filler. The constant A depends primarily upon the shape of the dispersed particles and how they are oriented with respect to the direction of flow of thermal currents. The constant A is related to the generalised Einstein coefficient $k_E$. The factor B is a constant which takes into account the relative conductivity of the two components. The factor $\psi$ is determined by the maximum packing fraction $\phi_m$ of the dispersed particles. The maximum packing fraction $\phi_m$ is defined as the true volume of the particles divided by the volume they to occupy when packed to their maximum extent. For fillers which are aggregates of spheres, the constant A is equal to $\frac{2.5}{\phi_m}$-1 [74]

#### 4.7.1.2 Agari and Uno

Agari and Uno propose a semi-empirical thermal conduction model (fundamentally based on the generalisation of parallel and series conduction models of a composite) for filled polymer with particles [75]. The expression governing the thermal conductivity in this model is given as follows

$$logk_c = \phi C_2 logk_f + (1-\phi)log(C_1 k_m) \tag{4.15}$$

where $C_1$ and $C_2$ are experimentally determined constants of order unity. Dilek Kumlutas and Ismail H. Tavman [76] report that, $C_1$ is a measure of the effect of the particles on the polymer, like crystallinity and the crystal size of the polymer. $C_2$ (smaller than 1 and larger than 0) shows how easy the particles can form conductive paths inside the polymer. In other words, the easier the particles are gathered to form conductive chains, the more the thermal conductivity of the particles contributes to the thermal conductivity of the composite and $C_2$ tends towards 1. The coefficients $C_1$ and $C_2$ are determined by using the linear regression equation of the plot of the logarithm of the thermal conductivities of the experimental data against volume contents of the particles.

#### 4.7.1.3 Maxwell

Maxwell [77] uses potential theory and obtains an exact solution for the conductivity of randomly distributed and non-interacting homogeneous spheres in a homogeneous medium. The governing equation is expressed as follows

$$k_c = k_m \frac{k_f + 2k_m + 2\phi(k_f - k_m)}{k_f + 2k_m - \phi(k_f - k_m)} \tag{4.16}$$

This Maxwell model is expected to predict the thermal conductivity of composites for low filler concentrations when filler particles do not touch each other.

#### 4.7.1.4 Russell

With the assumption that the particles are cubic with the same size, Russell [78] proposed the following model using a series parallel network.

$$k_c = k_m \frac{\phi^{2/3} + \frac{k_m}{k_f}(1-\phi^{2/3})}{\phi^{2/3} - \phi + \frac{k_m}{k_f}(1+\phi-\phi^{2/3})} \tag{4.17}$$

#### 4.7.1.5 Cheng and Vachon

Tsao [79] obtained a model relating the two phase solid mixture thermal conductivity of the individual components and to two parameters, which describe the spatial distribution of the two phases. Assuming a parabolic distribution of the discontinuous phase in the continuous phase, Cheng and Vachon breakthrough and propose a solution to Tsao's model. The new proposed model does not require knowledge of additional parameters. The determination of the constants of the parabolic distribution are obtained experimentally and presented as a function of the discontinuous phase volume fraction. The equivalent thermal conductivity of the mixture is derived in terms of the distribution function and the thermal conductivity of the constituents. For $k_f > k_m$, the expression gorverning the model is given as follows

$$\frac{1}{k_c} = \frac{1}{\sqrt{C(k_f-k_m)[k_m+B(k_f-k_m)]}} \ln \frac{\sqrt{k_m+B(k_f-k_m)} + \frac{B}{2}\sqrt{C(k_f-k_m)}}{\sqrt{k_m+B(k_f-k_m)} - \frac{B}{2}\sqrt{C(k_f-k_m)}} + \frac{1-B}{k_m} \tag{4.18}$$

where

B = $\sqrt{3\frac{\phi}{2}}$ and C = -4 $\sqrt{\frac{2}{3\phi}}$

Cheng and Vachon claim that, for two phase materials with the thermal conductivity of the continuous phase being much smaller than the thermal conductivity of the discrete phase ($k_m \ll k_f$ and as long as $\phi < 0.667$), effective thermal conductivity of the composite can be expressed as follows

$$k_c \approx \frac{k_m}{1-B} \tag{4.19}$$

#### 4.7.1.6 Geometric mean

In the case of the geometric mean model, the effective thermal conductivity of the composite is given by [71]

$$k_c = k_f^{\phi}.k_m^{1-\phi} \tag{4.20}$$

### 4.7.2 Hysol EA9396 filled with Boron Nitride (BN)

The Hysol based composite is prepared by mixing the epoxy resin, hardener and Boron Nitride particles and cured at room temperature over a period of three days. Boron Nitride is non-toxic and transparent to microwaves. Two types of Boron Nitride powders (Japanese and Goodfellow[4]) are used to fill the Hysol matrix. The goodfellow Boron Nitride has a density of 1.9g/$cm^3$ and a maximum particle size of 10$\mu$m in diameter. The goodfellow Boron Nitride has a hexagonal structure[5] and is sometimes called white graphite, due to its lubricity, anisotropic properties, heat resistance and high thermal conductivity. This latter property, combined with a low thermal expansion, leads to excellent resistance to thermal shock. The Japanese Boron Nitride is from the previous ATLAS SCT build.

The Hysol filled with Boron Nitride is prepared with concentrations of 5, 10, 15, 20, 25, 30 and 35$\%$ by weight. The quantity, by weight, of Hysol used is 2.6g (part A=2g and part B=0.6g). Table 4.3 summarises the filler amount in the composite. The following expression is used to calculate the volume fraction of the filler for a given weight fraction

$$\phi = \frac{W}{W + (1 - W)\frac{\rho_f}{\rho_m}} \tag{4.21}$$

where $\phi$ is the volume fraction of the filler additives, W is the weight fraction, $\rho_f$ and $\rho_m$ are the densities of the filler (Boron Nitride) and polymer matrix, respectively.

### 4.7.3 Results and Discussion

Thermal conductivity measurements are performed on Hysol EA9396 filled with Boron Nitride of two different origins (Japanese and Goodfellow) up to a volume fraction of 24$\%$. In accordance with litterature values, the addition of the Boron Nitride raises the thermal conductivity of the Hysol with increasing loading. The experimental values of thermal conductivity at room temperature are compared to calculated values from Maxwell, Cheng and Vachon, Lewis and Nielsen, Russell and the geometric mean models on figure 4.16 and figure 4.17. The density of Hysol is 1.14$g/cm^3$[6]. It is known from literature that Boron Nitride has a density value between 1.9$g/cm^3$ and 2.2$g/cm^3$. Two similar measuring jars, filled

[4]www.goodfellow.com
[5]www.azom.com
[6]www.aerospace.henkel.com

Table 4.3: Summary of the filler amount in the mixture

| Boron Nitride weight (%) | Boron Nitride mass (g) | Hysol EA9396 + BN mass (g) | %BN by volume |
|---|---|---|---|
| 0 | 0 | 2.6 | 0 |
| 4.8 | 0.13 | 2.73 | 0.03 |
| 9.1 | 0.26 | 2.86 | 0.06 |
| 13 | 0.39 | 2.99 | 0.08 |
| 16.7 | 0.52 | 3.12 | 0.11 |
| 20 | 0.65 | 3.25 | 0.13 |
| 23.1 | 0.78 | 3.38 | 0.15 |
| 25.9 | 0.91 | 3.51 | 0.17 |
| 29.7 | 1.1 | 3.7 | 0.20 |
| 35 | 1.4 | 4 | 0.24 |

with the Japanese and the Goodfellow Boron Nitride were measured with a weight scale. It is observed that the density of the Japanese Boron Nitride is less than the density of the Goodfellow's. As the exact values of the densities are unknown, $1.9 g/cm^3$ and $2.1 g/cm^3$ are assumed as the densities of the Japanese and the Goodfellow, respectively. The Goodfellow Boron Nitride has a maximum particle size around $10\mu$m. The bulk thermal conductivity of the Boron Nitride is unknown, and a lowest value of 200W/mK is used for the calculations. The thermal conductivity of the Hysol EA9396 is experimentally measured and found to be equal 0.28W/mK, see table 4.2. As the maximum packing fraction is unknown, a value of $\phi_m$ = 0.637 is used is the calculations to determine the thermal conductivity values in the Lewis-Nielsen model.

For the Japanese Boron Nitride at low volume content ($\phi$ <8%), particles are dispersed in the Hysol EA 9396 matrix and they are not interacting with one other. The equations of the geometric mean and that of Cheng and Vachon predict the best values for the thermal conductivity of the Hysol EA9396 in this region. The deviation from the experimental data is maximum 9.5% and 4% for the geometric mean equation and Cheng and Vachon equations, respectively. The Maxwell and both of the Lewis and Nielsen model predictions are lower than the experimental results in the whole range. However, at higher Boron Nitride content, as aggregates of particles are formed, Lewis and Nielsen with A = 3 (the particles are of irregular shapes approximating roughened spheres) and $\phi_m$ = 0.637 gives better prediction than their model using A = 1.5 (the particles are spherical) and $\phi_m$ = 0.637. For particle content greater than 10% by volume, conductive chains of the particles are formed giving rise to a large increase in effective thermal conductivity of the Hysol EA9396. The Russell model prediction of thermal conductivity is fairly accurate in that region. With a loading of 8% Boron Nitride (by volume), the thermal conductivity of the Hysol EA9396 reaches 0.51W/mK, which is an increase of 57% compared to pure Hysol EA9396 with a thermal conductivity of 0.28W/mK.

The Hysol EA9396 was filled with 16% and 23% volume of the Goodfellow Boron Nitride in this study. The results agree well within 5% with the corresponding thermal conduc-

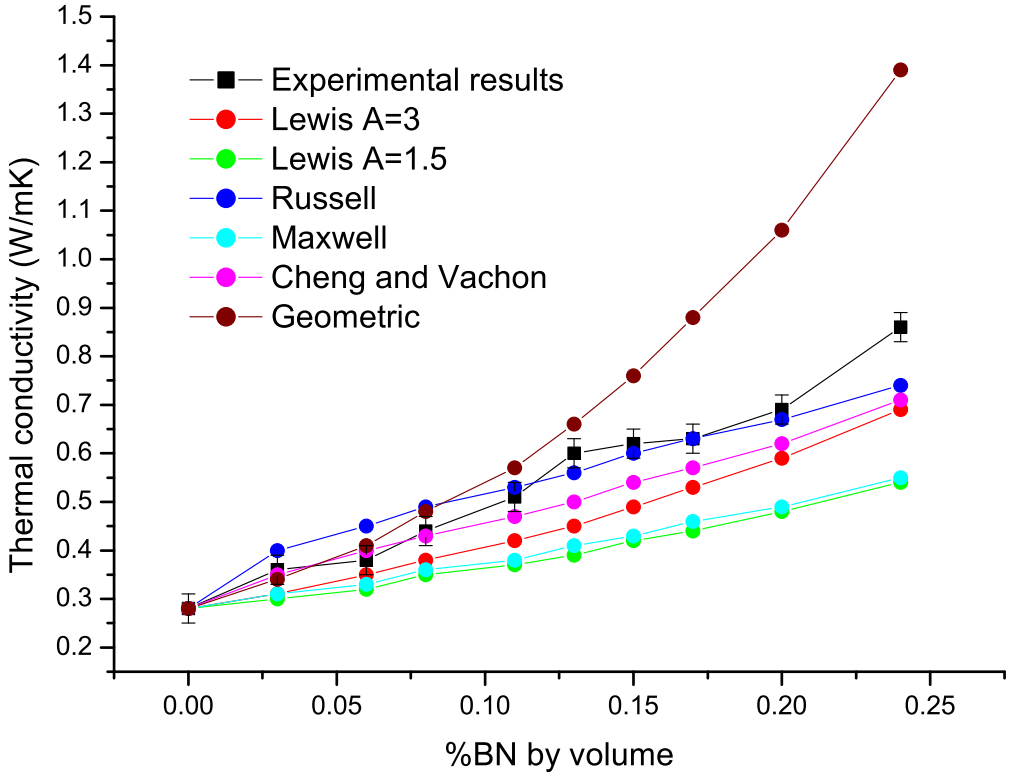


Figure 4.16: Thermal conductivity results of Hysol filled with Boron Nitride (Japanese) and compared with different models

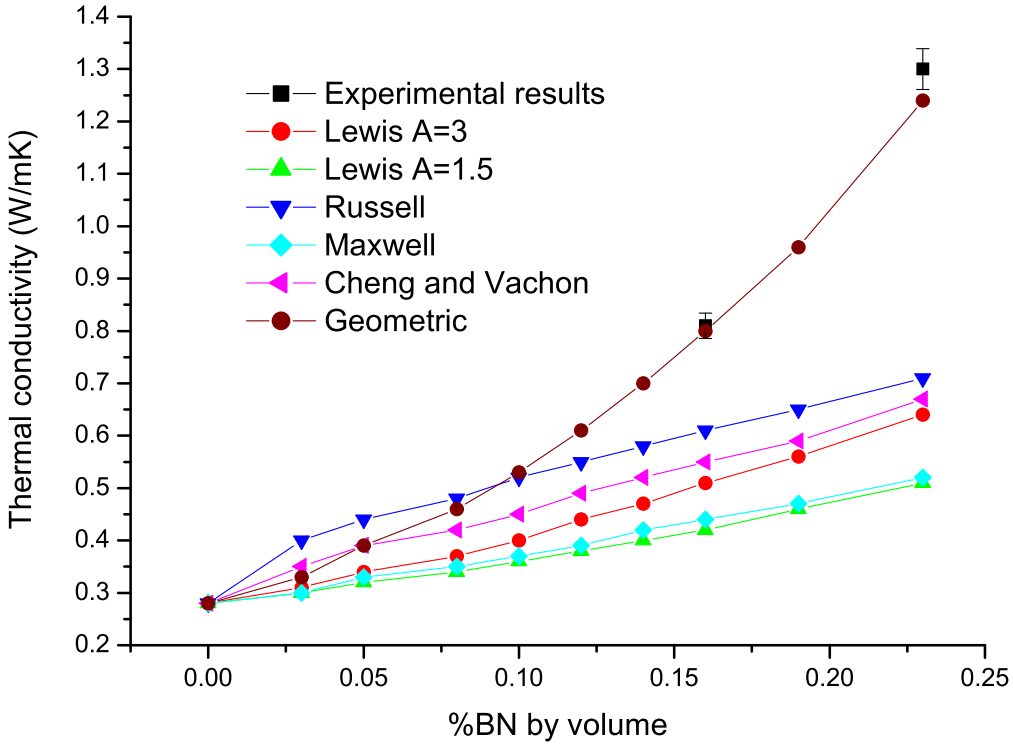


Figure 4.17: Thermal conductivity results of Hysol filled with Boron Nitride (Goodfellow) and compared with different models

tivity values derived from the Geometric model. It is observed that none of the other models is useful for the prediction of the experimental results. Loading the Hysol EA9396 with the Goodfellow boron Nitride, the thermal conductivity of the Hysol increases from 0.28 W/mK to 0.81 W/mK and 1.3 W/mK for 16% BN and 23%BN, respectively. This is an increase of the thermal conductivity by 65.4% and 78.5% compared to pure Hysol EA9396 with a thermal conductivity of 0.28 W/mK.

### 4.7.4 Araldite and Boron Nitride

Thermal conductivity measurements of Araldite 2011 filled with the Japanese Boron Nitride were also performed. The mixture proportion by weight is resin 38.5%, hardener 30.75% and Boron Nitride 30.75%. The curing time at room temperature was three days. The measurements are performed at room temperature with a pressure of 0.47MPa and 1W applied on the composite and Dow Corning 340 grease was used at the copper specimen interfaces. The measured thermal conductivity is found to be 0.77W/mK. This is an increase of 250% compared to the pure Araldite 2011 thermal conductivity value.

## 4.8 Kapton Bus

The basic function of the kapton bus in the stave is to deliver power and signals to and from the front-end electronics. The bus is not uniform but made with layers of different materials shown in table 4.4. On the surface of the kapton bus, black traces are observable. These traces consist of kapton, aluminium and copper. The copper serves as the conductors to drive the twelve (12) modules mounted on the stave. The aluminium layer serves as a shield to isolate the modules from noise pick up from the signals in the traces. Figure 4.18 shows a portion of the kapton bus with the black trace.

Table 4.4: Summary of the different materials present in the assembly of the kapton bus

| components | thickness $\mu$m | manufacturer |
|---|---|---|
| kapton | 25 | Shin-Etsu CA333 |
| adhesive | 25 | Shin-Etsu CA333 |
| aluminium shield | 25 | foil |
| adhesive | 25 | DuPont LF0100 |
| kapton | 25 | Shin-Etsu CA333 |
| adhesive | 25 | Shin-Etsu CA333 |
| copper | 18 | (Espanex) MC 18-25-00 |
| kapton | 25 | (Espanex) MC 18-25-00 |

In the design of the stave, the kapton bus, also called the bus cable, is mounted between the hybrids and the carbon fibre plate, see figure 4.14. The kapton bus crosses the heat path

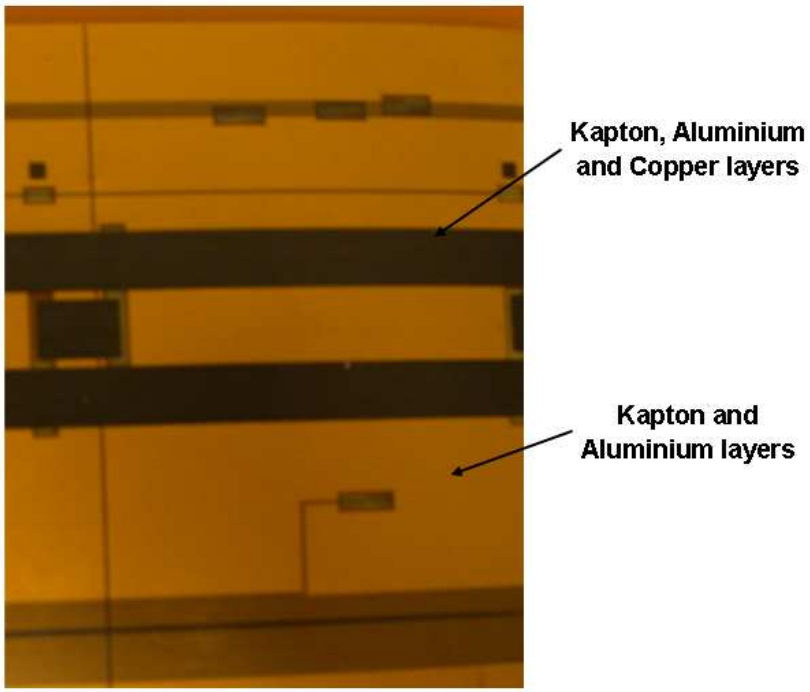


Figure 4.18: Overview of the kapton bus used for the prototype of the stave

from the silicon sensors to the cooling pipes. Due to its location, there is a need to understand the thermal properties of the kapton bus in order to understand the thermal performances of the stave. This section focuses on the measurement of the transverse thermal conductivities of the kapton, assembly of (kapton - glue - aluminium shield) and assembly of (kapton - glue - aluminium shield - glue - copper layer - kapton). It is worth noting that measurements are not performed on the adhesives alone because this is out of the scope of this study. The measurements are performed in the TIM apparatus at room temperature with a pressure of 0.47 MPa applied on the copper bars and Dow Corning 340 is used as the thermal grease between the copper bars and the specimen.

After substraction of the contact resistances, the kapton has a resistance of 1.31K/W with a temperature difference of $1.74°C$ and a resulting thermal conductivity equal to 0.22 W/mK. The assembly of the kapton and the aluminium has a resistance of 6.41K/W with a temperature difference between the two surfaces of $14.3°C$ and a resulting thermal conductivity equal to 0.26 W/mK. The assembly of kapton, aluminium, copper and kapton exhibits a temperature difference of $15.6°C$ between its two surfaces with a resistance of 7.05K/W and a resulting thermal conductivity equal to 0.24W/mK. Table 4.5 summarises the results.

## 4.9 Foams

In this section transverse thermal conductivity measurements of PocoFoam and Allcomp foam are performed at room temperature. The technique used for the measurements is shown in figure 4.19; where the foam specimen is placed vertically on a copper bar connected to a

Table 4.5: Summary of the thermal conductivity results of the kapton bus

| Layer | Thickness ($\mu$m) | Power applied (W) | $\Delta T$ (°C) | Resistance (K/W) | Thermal conductivity (W/mK) |
|---|---|---|---|---|---|
| Kapton Shin-Etsu | 29.8 | 1 | 1.74±0.05 | 1.31±0.02 | 0.22±0.01 |
| Assembly(kapton-Al) | 170 | 2 | 14.30±0.05 | 6.41±0.02 | 0.26±0.01 |
| Assembly(kapton-Al-Cu) | 189 | 2 | 15.60±0.05 | 7.05±0.02 | 0.24±0.01 |

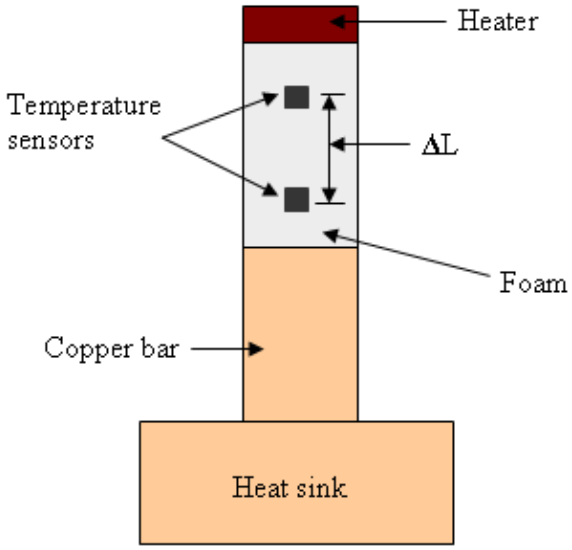


Figure 4.19: Overview of a foam specimen under investigation

heat sink. The foam is 10 mm wide, 10 mm long and 20 mm deep. It is heated at the top by a ceramic heater and cooled at the other end by the heat sink. Two RTD sensors are attached on the foam for the reading of the temperature through the foam. The distance ($\Delta L$) between the sensors is accurately measured with callipers and the heat sink is adjusted so that the average temperature of the sensors is similar to the environment temperature. This is done to ensure the temperature of the foam is as near as possible to the environment temperature in order to reduce heat transfer by radiation between the surfaces of the foam and the environment. When the average temperature is adjusted and equal to the environment temperature, sufficient time is given for the system to reach equilibrium before performing measurements. Convection is considered negligible in this study due to the location of the heater on the top of the foam. As a consequence, only heat conduction is assumed to be important in this study. It is worth noting that the blocks of foam have the following dimensions (250mm x 250mm x 30mm), when purchased. These dimensions allows measurements to be performed in all the three directions ($x$, $y$ and $z$), where $z$ is the deep direction.

### 4.9.1 PocoFoam

Transverse thermal conductivity measurements of two PocoFoam specimens with different densities ($\rho$=0.40$g/cm^3$ and $\rho$=0.56$g/cm^3$) are performed. PocoFoam is expected to be anisotropic with conductivity in the z direction ($k_z$) ranging from 50W/mK to 160W/mK. The difference in conductivity values between the $x$, $y$ and $z$ directions is due to the manufacturing process. The elongation of pores in the $z$ direction effectively increases the ligament length in the $z$ direction. This reduces the number of low conductivity junctions and therefore increases the overall foam thermal conductivity in the z direction. Table 4.6 shows the results of the transverse thermal conductivity results together with the PocoFoam values measured at room temperature with the in-plane measurement system.

Table 4.6: Summary of the In-plane and Transverse thermal conductivity results of PocoFoam

| Density (g/c$m^3$) | $k_x$ (W/mK) | $k_y$ (W/mK) | $k_z$ (W/mK) | Measurement method |
|---|---|---|---|---|
| 0.56 | - | - | 135±2 | Transverse |
| 0.40 | 43±2 | 43±2 | 55±2 | Transverse |
| 0.56 | 54.5±3 | 57.5±3 | - | In-plane |
| 0.40 | 51±3 | 53.5±3 | - | In-plane |

As expected, the conductivities measured are higher in the z direction (135W/mK and 55W/mK, for $\rho$=0.56$g/cm^3$ and $\rho$=0.40g/c$m^3$, respectively) than the other directions ($x$ and $y$) and lie in the range quoted by the manufacturer. Transverse measurements for $\rho$=0.40$g/cm^3$ performed in the three directions show that $k_z$ is 28% higher than $k_x$/$k_y$.

Comparing the transverse values with the in-plane values, it was observed that for $\rho$=0.40$g/cm^3$, $k_z$ was 7.8% and 2.8% higher than $k_x$ and $k_y$, respectively. For $\rho$=0.56$g/cm^3$, $k_z$ is 47.7% and 34.8% higher than $k_x$ and $k_y$, respectively. Due to the lack of specimens, no measurement was performed in $x$ and $y$ directions for $\rho$=0.56$g/cm^3$. However, the results obtained with $\rho$=0.40$g/cm^3$ indicate that there was a considerable difference between the values obtained by the two methods. The values obtained with the in plane method were higher (18.6% and 24.4% for $k_x$ and $k_y$, respectively) than the values obtained with the transverse method.

### 4.9.2 Allcomp foam

Transverse thermal conductivity measurements of two Allccomp foam specimens with different densities ($\rho$=0.22$g/cm^3$ and $\rho$=0.36$g/cm^3$) were performed. Allcomp foam was expected to be isotropic with conductivities, at room temperature, ranging from 10W/mK to 75W/mK for density ranging from 0.09$g/cm^3$ to 0.40$g/cm^3$. The transverse thermal con-

ductivity measurements were performed in all the three directions ($x$, $y$ and $z$) and the results were shown in table 4.7.

Table 4.7: Summary of the Transverse thermal conductivity results for Allcomp foam

| Density (g/c$m^3$) | $k_x$ (W/mK) | $k_y$ (W/mK) | $k_z$ (W/mK) |
|---|---|---|---|
| 0.22 | 33.5±2 | 38±2 | 33.5±2 |
| 0.36 | 61±2 | 62±2 | 75±2 |

Contrary to the expected, the thermal conductivities are not isotropic for a given density. However, the obtained values lie within the thermal conductivity range measured by the manufacturer. Differences are observed between the measured values of the thermal conductivities. For a specimen with a density of 0.22g/c$m^3$, $k_y$ is 13.5% higher than $k_x$ = $k_z$ = 33.5W/mK. For a specimen with a density of 0.36g/c$m^3$, $k_z$ is 23% and 21% higher than $k_x$ and $k_y$, respectively. It is observed that, with an increase of around 64% of density (0.22g/c$m^3$ to 0.36g/c$m^3$), the thermal conductivity increases by more than 100%.

The measured conductivity values of Allcomp foam with density equal to 0.36g/c$m^3$ obtained at 20°C in the x and y directions by the use of the in-plane thermal conductivity measurement system is shown in table 4.8.

Table 4.8: In-plane conductivity of Allcomp foam in the x and y directions measured at 20°C

| Density (g/c$m^3$) | $k_x$ (W/mK) | $k_y$ (W/mK) | $k_z$ (W/mK) |
|---|---|---|---|
| 0.36 | 83±3 | 72±3 | - |

Comparing the results obtained from the transverse measurement system and the in-plane measurement system, it is observed that there is a significant difference between the results of the two methods. The values obtained by the in-plane system are higher than those obtained with the transverse system as observed for the PocoFoam. $k_x$ and $k_y$ are 36% and 16.13% higher than the values obtained by the transverse conductivity system at room temperature.

The high values obtained by the in-plane thermal conductivity system compared to the transverse system can be explained by the presence of radiation shields that add undesired heat paths to the system and increase the thermal conductivity. It has also been shown that thermal conductivity measurements performed on PocoFoam specimens thinner than 1.4 mm of PocoFoam result in inaccurate results. Based on these reasons, the transverse thermal conductivity system is considered more accurate and the measured values are considered reliable.

## 4.10 CFRP

The transverse thermal conductivity of the K13D2U specimen studied in the previous chapter, was investigated. The thickness of the specimen was 217$\mu$m and a cross section area of $1cm^2$. The measurements were performed at room temperature with a power of 1W applied on the CFRP. Dow Croning 340 was used as thermal interface material and a pressure of 0.47 MPa was applied between the copper bar and the CFRP surfaces.

After the subtraction of the contact resistances, the CFRP exhibits a resistance of 1.78K/W with a temperature difference of $2.22°$C between its surfaces what results in a thermal conductivity equal to 1.20$\pm$.02W/mK. The filament thermal conductivity of this CFRP is 800 W/mK with a density equal to $2.19g/cm^3$. A prediction based on FEA analysis performed in the collaboration does not conform with the measured value because of unknown factors, such as the transverse thermal conductivity of the filament. The filament transverse conductivity is important to know in order to determine the bulk transverse thermal conductivity of the CFRP.

## 4.11 Summary

A 1-D steady state heat conduction system at room temperature has been designed, built and reported in this chapter. Heat loss by radiation has been corrected and convection has been neglected. Measurements of epoxies such as Hysol EA9396, Dow Corning SE4445 and Epolite FH-5313 have been performed and the results agree well with literature values. The measurement system has been used to measure the thermal resistances and conductivities of PocoFoam and Allcomp foam. The thermal conductivities obtained by the transverse system are generally lower than those obtained by the in-plane system at room temperature. As expected, the thermal conductivities of PocoFoam are not isotropic for a given temperature. An anisotropy in the thermal conductivities has also been observed for Allcomp foam that was expected to be isotropic. A measurement was performed on a K13D2U specimen and the result was found to be equal to 1.20$\pm$0.02 W/mK.

# Chapter 5

# Mechanical Measurements

After investigation of the thermal properties of the silicon module's support structures, it is important to ensure that these structures are dimensionally and structurally stable in order to enable accurate track reconstruction. As seen in figure 4.14, apart from the aluminium cooling pipe, (US design), the core of the stave consists of PocoFoam, honeycomb and carbon fibre reinforced polymer. The bulk of the materials used in the stave design are of low mass and the total mass of the stave is evaluated to be between 600g and 800g. The mounting of the stave inside the barrel is designed in a way that the total load applied on the stave consists of the stave's own load coupled with the thermal force created by the cooling of the pipe and the heating of the silicon sensors. Due to the stave's low mass combined with the thermal induced force, it is estimated that the maximum stress applied on the stave is around 30MPa. Furthermore, this maximum stress is expected to occur at the pipe to foam interface.

The CFRP skins provide bending stiffness modules to a face to attach the stave to the macro-support structure of the tracker barrel. The fixture points are attached to "C-channels" which run along the long edge of the stave. The C-channel design is beyond the scope of this thesis and will not be discussed in this study. The CFRP skins are subject to tension and/or compression and are largely responsible for the strength of the stave. The function of the honeycomb is to support the skins so that they do not buckle (deform) and stay fixed relative to each other. The honeycomb will experience mostly shear stresses (sliding) as well as some degree of vertical tension and compression. There will not be any investigation of the honeycomb in this thesis. PocoFoam is important because of its good thermal performances, i.e high thermal conductivity. Like the honeycomb, the PocoFoam will experience shear stresses as it is located between the CFRP skins. PocoFoam also suffers large shear stress due to the differential thermal expansion between the CFRP skins and the cooling pipe, both of which the foam is glued to.

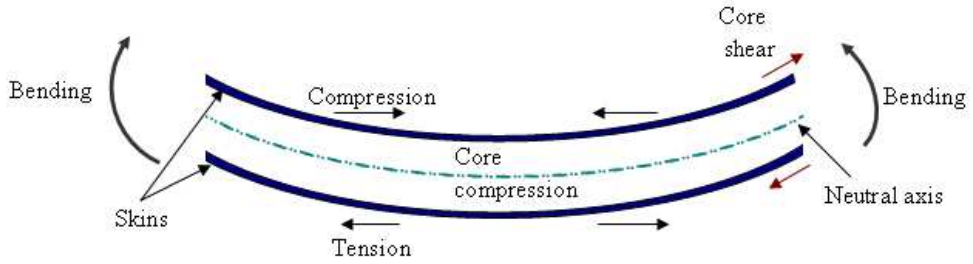


Figure 5.1: Overview of the bending of the stave along its longitudinal axis, the PocoFoam is not shown

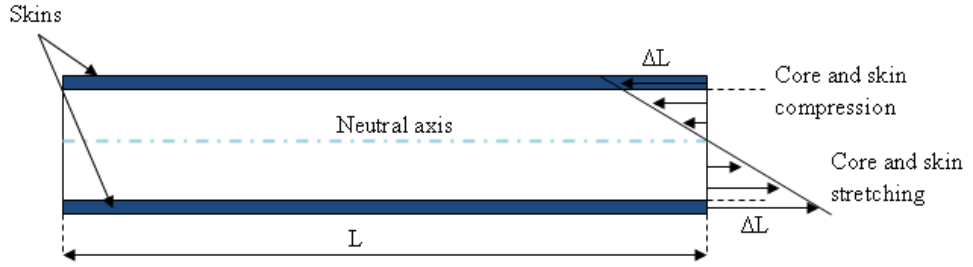


Figure 5.2: Detailed view of the forces involved in the bending of the stave shown in figure 5.1

## 5.1 Motivations

The mass of the stave will create a self deflection of the stave resulting several forces including bending forces at the ends of the stave. The self deflection causes tension and compression stresses in the CFRP skins and the creation of shear stress in the honeycomb and PocoFoam, see figure 5.1. The induced thermal force will create an additional shear stress between the PocoFoam and the pipe.

The bending forces cause the stave to stretch below the neutral axis and to compress above the axis as illustrated on figure 5.2. The neutral axis experiences zero stress and strain. As the stave bends, both the core and the skin elongate and shrink linearly from the neutral axis. The "black" solid line represents the new section of the stave after bending. Because the CFRP skins are firmly glued to the honeycomb and the PocoFoam, both the core and the CFRP skins stretch similarly at the glued junction. It is worth noting that, although the CFRP skins and the core stretch equally at the skin/core boundary. The honeycomb, PocoFoam and carbon fibre reinforced polymer have different physical properties and therefore will react differently to the created elongation.

In engineering terms, the ratio of the elongation ($\Delta L$) to the original length ($L_0$) is called

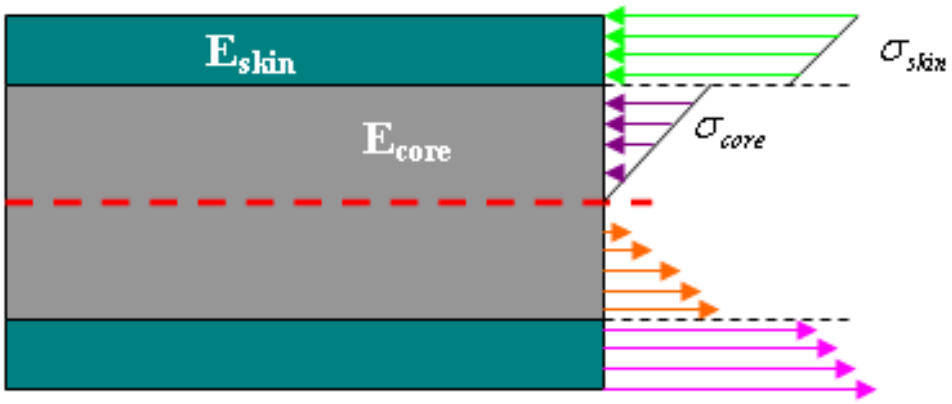


Figure 5.3: Overview of the stress distribution along the cross section of the stave

"strain", $\epsilon$, and expressed as

$$\epsilon = \frac{\Delta L}{L_0} \tag{5.1}$$

Knowing the strain, the stress in both the core and the skins can be determined. The stress is expressed by equation 5.2, where E is the material's modulus of elasticity (Young's modulus). Young's modulus describes the material's response to linear strain and it is a measure of the stiffness[1] of a material.

$$\sigma = E\epsilon \tag{5.2}$$

It is known from the available literature that CFRP has larger modulus than the honeycomb and the PocoFoam. Therefore, given an equal strain at the glued junction in the different materials, it is clear that a larger stress will be created in the CFRP skins. The discontinuity of the stress at the skin/core boundary is an indication that the carbon fibre skins absorb far more tension and compression than the honeycomb and PocoFoam, see figure 5.3.

A preliminary finite analysis of the UK stave performed with ANSYS shows that the self deflection is small and can be neglected when the stave is supported with five points along one edge and two points on the other edge[2]. Additionally, the analysis shows that the cooling pipe detaches itself from the PocoFoam due to the induced thermal force. Figure 5.4 shows the cooling pipe embedded and glued into the PocoFoam. It is worth noting that the material properties, such as Young's Modulus, shear modulus and yield stress, used in the analysis are taken from the available literature. These values are generally obtained from measurements at high stress up to failure. In order to understand well and be able to interpret the outcome of the Finite Element Analysis performed on the stave, it is necessary to use in the simulation the material properties obtained at the expected low stresses.

The aims of this chapter are to:

[1] Stiffness is the resistance of an elastic body to deflection or deformation by an applied force. It is an extensive material property.

[2] https://twiki.cern.ch/twiki/bin/view/Sandbox/TrackerExchange?topic=TrackerExchange - 18th August 2008


Figure 5.4: Overview of the cooling pipe embedded and glued into the PocoFoam

- design and construct a mechanical jig that can be adapted to a conventional testometer to achieve accurate measurements of pure mechanical properties, such as Young's modulus, at low stress. The function of the jig is to reduce significantly the parasitic effects present in the measurement
- measure pure compressive and tensile Young's moduli and yield strengths of materials such PocoFoam and CFRP
- measure the shear modulus, (G), of PocoFoam

The measurements were performed at room temperature and at low stress, up to 30MPa. The values obtained from the measurements will be compared to text book values and the yield stress will be compared to the stress values simulated for the stave. The stave design will be concluded dimensional stable only when the stresses applied on the materials of the stave are less than the corresponding yield strength.

In this chapter, the important aspects of stress and linear elastic regions are first introduced. This is followed by a detailed explanation of the origin of the parasitic effects present in the measurement system which are the causes of the non-achievement of the elastic region, when measurements are performed at low stress. Additionally, detailed explanations of the design of the jig that was used to reduce significantly these parasitic effects are given, together with experimental results of CFRP and PocoFaom. Finally, a method for measuring the shear modulus of PocoFoam is presented together with experimental results.

## 5.2 Conventional Measurement of Young's modulus

Tensile measurement is probably the most important test of a material's mechanical response and it is used to determine the Hookean region of elastic bodies[3]. Tensile and compressive

[3]In a Hooke body, stress is directly proportional to strain. The relationship is known as the Hooke's law and the behaviour is referred to as Hookean behaviour

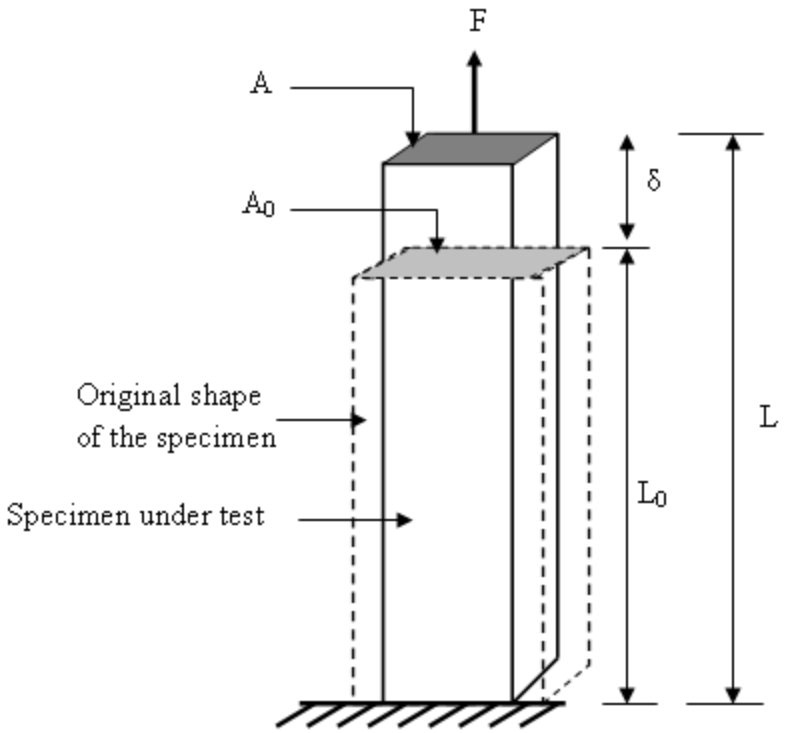


Figure 5.5: Schematic illustration of tensile tests

properties indicate how the material reacts to an applied force. Compression tests are relatively less complex to perform than tensile measurements. These measurements are carried out to determine mechanical properties including Young's modulus and yield strength.

Tensile measurements were performed by placing a carefully prepared specimen inside a conventional testometer. The specimen is thereafter submitted to a force in tension in a controlled way. The applied force and the elongation of the specimen are recorded simultaneously. Figure 5.5 presents a simplification of the measurement process and shows the dimensional changes of the specimen. $A_0$ and $L_0$ are the original cross section area and the original length of the specimen, A and L are the actual corresponding dimensions under the force, F, applied to the specimen and $\delta$ is the elongation of the specimen.

The main derivation of a tensile measurement is a force versus elongation curve, which is converted into a stress versus strain curve. The engineering stress, $\sigma(e)$, is the applied force F divided by the original cross section area $A_0$;

$$\sigma(e) = \frac{F}{A_0} \tag{5.3}$$

When true stresses based on the actual cross sectional area of the specimen are used, the stress-strain curve increases continuously until fracture. The stress-strain curve relates the applied stress to the resulting strain and each material has its own unique stress-strain curve. Figure 5.6 shows a stress-strain curve of a Hooke's body.

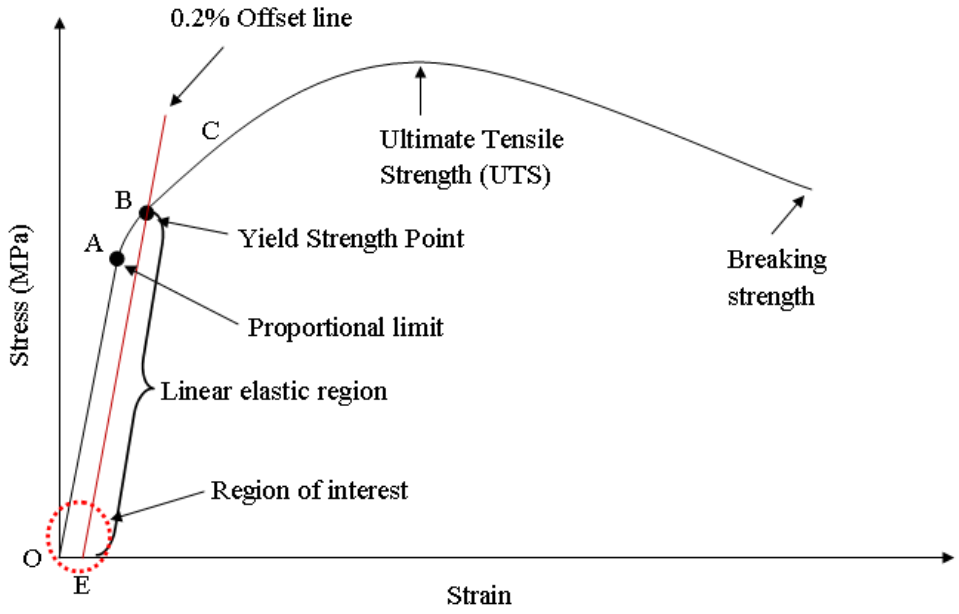


Figure 5.6: Schematic illustration of common stress-strain of Hooke's bodies [81]

### 5.2.1 Hookean Region

The Hookean region is characterised by a linear relationship between the stress and strain indicating that no plastic deformation is occurring. When the applied force is reduced, the specimen returns to its original shape and dimensions. This region is commonly called the linear-elastic region.

### 5.2.2 Yield Strength

If the loading of a test specimen is discontinued below point A, in figure 5.6 and the load is removed, the stress and strain retraces line OA back to the origin. The proportional limit is the highest stress at which stress is directly proportional to strain. Above the proportional limit, both elastic and plastic strains occur as indicated by the curve segment AB. When the point B is reached and the load is gradually removed, the stress and strain now follow the line BE. Once the stress reaches zero, the elastic strain disappears and the plastic strain (OE) remains. The reloading of the specimen now follows the line EBC. In other words, a small amount of plastic strain raises the proportional limit from A to B and is followed by an increase of the yield strength. The yield strength is the smallest stress required to produce plastic deformation. The yield strength obtained by offsetting the line OA by 0.2% is commonly used for engineering purposes because it avoids the practical difficulties of measuring the proportional limit.

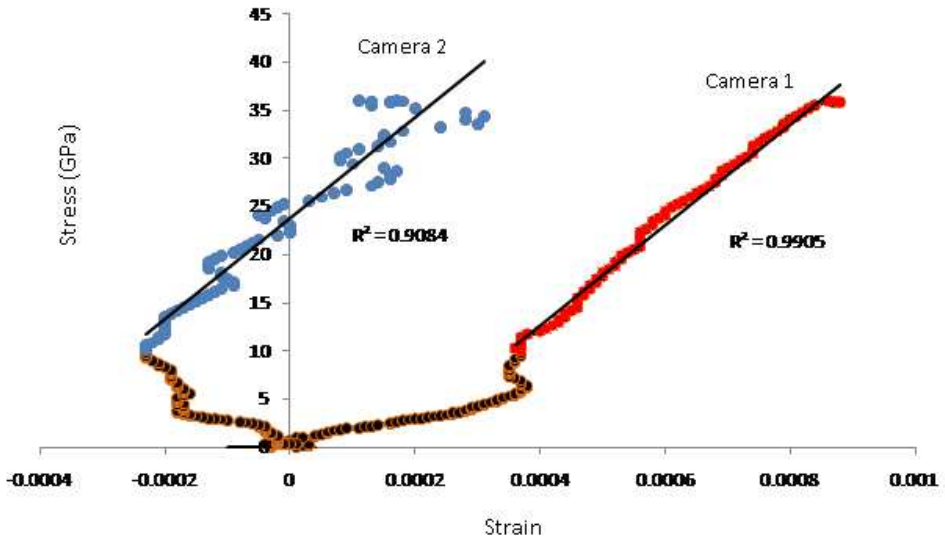


Figure 5.7: An example of stress-strain graphs obtained from the two cameras after a low stress tensile test. The test was performed on an aluminium specimen using a universal testometer

## 5.3 Parasitic effects in the measurement of stress-strain

At low stress, the determination of the linear-elastic region of Hookean bodies for the calculation of Young's modulus has proven to be difficult to obtain with a universal testometer. In order to understand the factors working against the determination of the linear-elastic region, a video extensometer system[4] was used to record strains inside a specimen during the measurements. The system consists of two cameras positioned to face each surface of the specimen. A flat specimen is placed inside a universal testometer and a tensile test is performed. The data recorded from each camera were used to establish a stress-strain curve for each surface of the specimen.

It is clear that the stress-strain graphs shown in figure 5.7 are not similar, which explains that the specimen surafces behave differently, especially at stress below 10MPa. The surface faced by the camera 1 exhibits a tensile behaviour while the other surface exhibits a compressive behaviour. Above 10MPa, both surafces display a similar tensile behaviour. The Young's moduli obtained from the two surfaces are 54GPa and 49GPa for surface 1 and 2, respectively. These Young's moduli are below the well known average value of 70GPa for aluminium available in literature.

The reasons for the different responses of the surfaces in the beginning of the test were found to be caused by two major factors:

- Misalignment between the force applied and the centre line of the specimen

[4]Operation procedure is explained in section 5.5

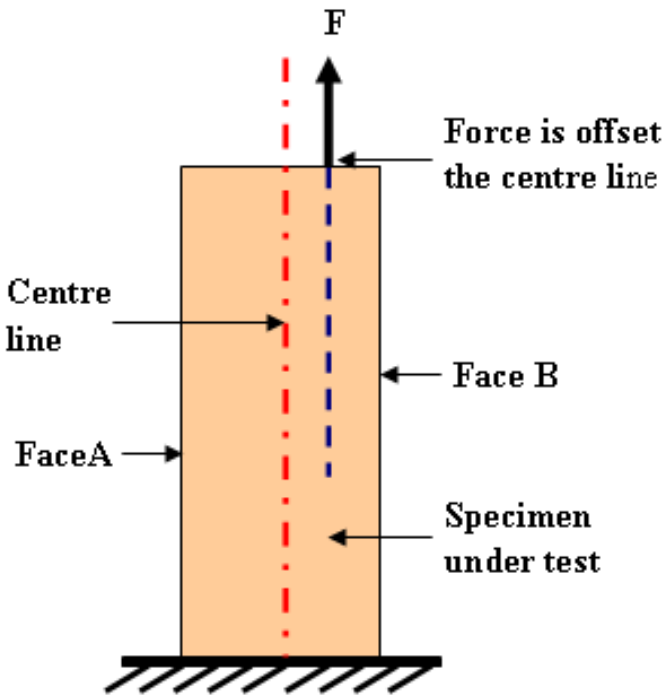


Figure 5.8: Illustration of misalignment between the centre line and the applied force

- Twisting of the specimen caused by the manner the specimen is gripped by the testometer

### 5.3.1 Misalignment

Tensile measurements during which the applied force is offset from the centre line, as shown in figure 5.8, result in compression of one face of the specimen (A) and tension of the other (B). As a consequence, the values obtained from these tensile measurements do not reflect the pure "tensile" properties.

### 5.3.2 Twist

Conventional testometers are designed in a way that the ends of the specimens are clamped tightly in order to position them ready for measurement. These applied forces on the ends of the specimens cause considerable twist in the specimens.

It is worth noting that misalignment and twist are insignificant during conventional tensile measurements. Conventional measurements, designed to be performed with relatively high stress until failure of the materials occur, use large forces such that the effect of misalignment and twist are negligible. However, misalignment and twist effect significantly measurements

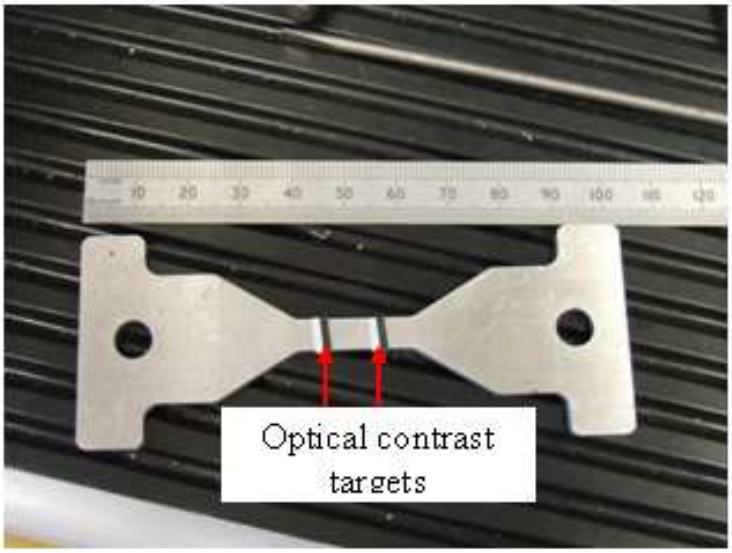


Figure 5.9: View of a specimen used in the jig

performed at low stress and appear as parasitics that corrupt the results. There is therefore a need to get the parasitics remedied. This was achieved by designing a jig and adapting it to a conventional testometer.

## 5.4 Jig Description

A jig was designed (by me) to correct the misalignment between the applied force and the centre line of the specimens under investigation. The clamping mechanism to hold the specimens ready for measurements was also improved in order to achieve tensile measurements with no twist in the specimens. The jig was mounted into a conventional testometer and becomes a vital component of the measurement system. Unlike in conventional techniques, specimens are placed directly inside the jig. Figure 5.9 shows a specimen that will be used inside the jig together with optical contrast targets used with the video extensometer system.

The jig consists of, see figure 5.10:

- two shafts containing four linear bearings each that constrain the specimens to pure vertical movements. Two cylindrical pins are fixed on each shaft in such away that they constrain the specimens in the desired vertical position inside the jig. A cylindrical threaded tube is mounted on each shaft and constrains the applied force to be aligned with the centre line of the specimen. In addition, the cylindrical threaded tube contributes to obtain the desired vertical position of the specimen by pressing the specimen against the inner vertical walls of the jig. The lower shaft is fixed onto the bottom of the jig, whereas the upper shaft moves upward and stretches the specimens when force is applied.

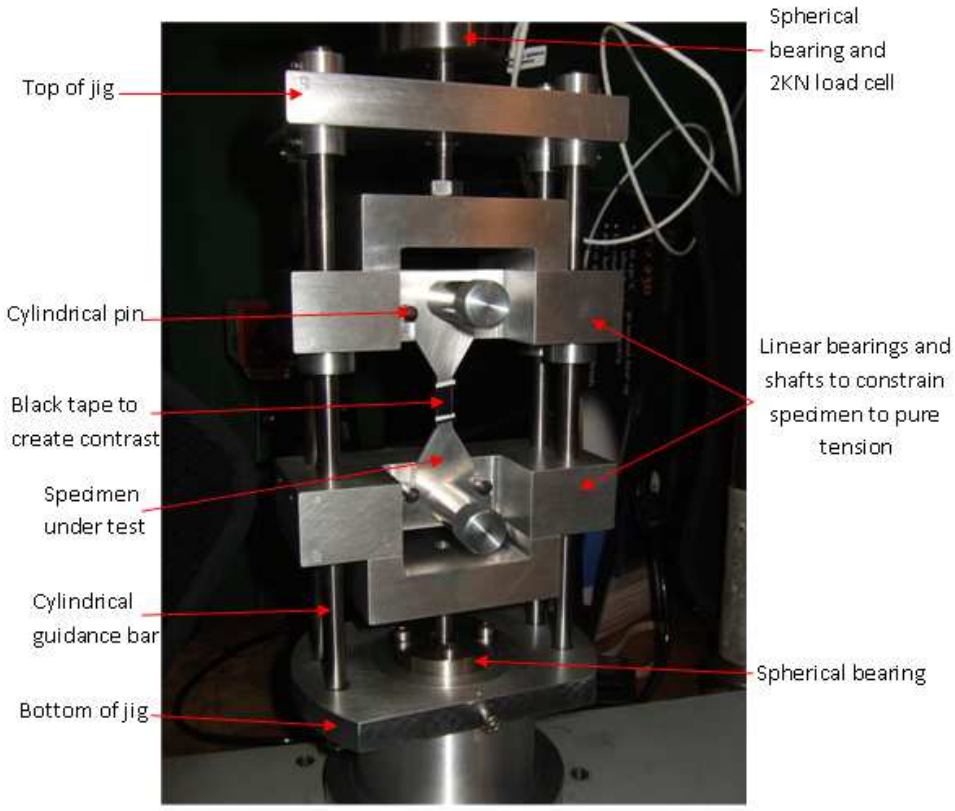


Figure 5.10: Overview of the jig

- four parallel cylindrical bars that constrain the upper shaft to vertical movements.
- top and bottom plates of the jig assure that the four cylindrical bars stand parallel. Additionally, the top plate constrains the applied force to be parallel to the specimen.

## 5.5 Measurement Procedure

For rigid materials, the strain can be measured by using conventional "clip-on" mechanical extensometers or foil strain gauges bonded to the specimen. However, these devices are not usually suitable for the measurement of materials such as fibres and foams as their weight and method of attachment can influence the results.

Various non-contacting systems such as mechanical driven optical followers and laser extensometers are available[5], but these systems do not possess the necessary resolution for the accurate determination of material properties at low strain levels. A video Extensometer System was used for the strain measurement in this thesis. This system has numerous advantages including:

[5] www.sensorland.com

- No influence on the measured specimen
- Directly measures strain
- Can measure strain up to failure
- Arbitrary choice of gauge length and operating range (Specimens can be any length from millimetres to metres)
- Allows simultaneous measurement of transverse strain
- Allows measurement of materials such as cables, thin foils, fibres, foams and composites
- No moving parts to wear out
- No errors due to inertia of moving parts

### 5.5.1 Video Extensometer

The system consists of two cameras that allow the in-built features to be easily adjusted in order to obtain the best images. The cameras are placed on opposite sides of the specimen at an equal distance from the specimen's face, see figure 5.11. The cameras are connected to a "frame-grabber" interface card, controlled by PC Windows 9x/2000/NT based software. The video extensometer PC is directly connected to the tensile testing machine's analogue load signal, so that load and strain values are saved simultaneously. In addition, the analogue input signal is scaled so that the monitor also provides a real time digital display of applied load. The extensometer can be controlled automatically from the measuring system computer or manually with the Windows 9x/2000/NT based software using the extensometer PC. In the case that the operation is done manually, both the start and end measurement load values are input and the data in between are automatically saved in a tab ASCII format[6].

### 5.5.2 Principles of operation

The jig is mounted into a extensometer together with two load cells. One S type load cell, IP67 tension/compression, indicates the amount of force applied by the testometer. The other load cell (Universal load cell, Miniature metric, 25 to 35 mm diameter) displays the actual load on the specimen responsible for the strain recorded by the video extensometer system. The load cells require to be well calibrated to each other in order to achieve satisfactory results. The cameras are rigidly fixed on a support and focused on a target of high contrast (for example black tape) mounted on the specimen under test, see figure 5.11. It is worth noting that the distance between each camera and the specimen must remain constant during the measurement because any movement will alter the image size. This will erroneously be interpreted by the software as a change in the specimen size. In the case that the cameras

[6]https://www.nottingham.ac.uk

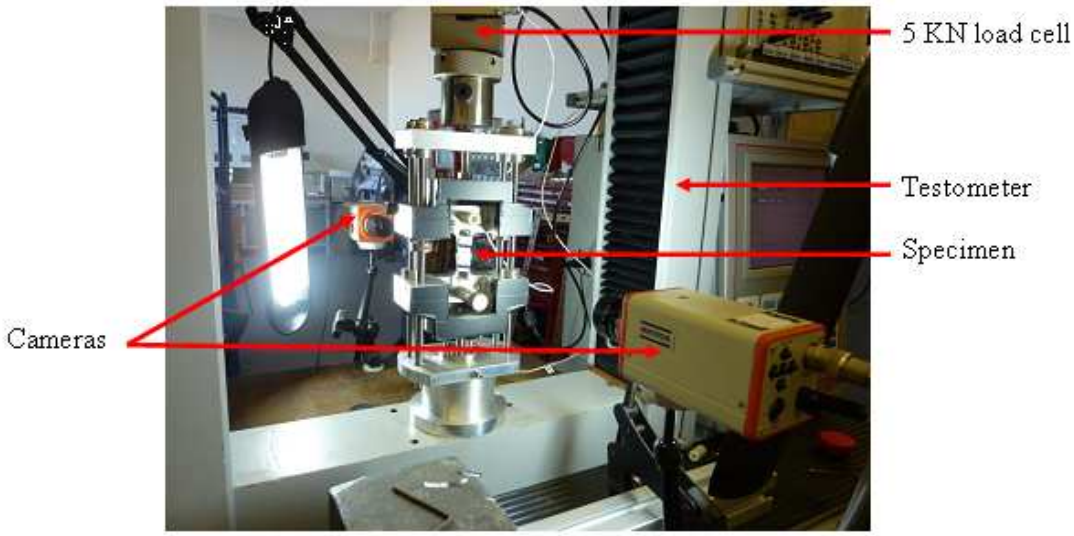


Figure 5.11: Overview of the jig adapted to a conventional testometer

and the surfaces of the specimen are not placed orthogonal, the software will misinterpret eventual angles between the focus and the contrast targets as elongation. The specimen is illuminated on both sides with a constant and similar luminosity lights during the measurements and this is achieved by using separate and similar external lights. Self adhesive targets are placed on the specimen, see figure 5.9. It is important that the targets create a sharp and as great a contrast difference as possible to ensure correct automatic target recognition and tracking. The target position is detected at the edge of a contrast transition. It is therefore not affected by the changes in target width.

The video extensometer used in this study employs a strain sensitivity of the order of $10^{-5}$ and operates by capturing video images. The video system finds the edges of the contrast transition (gauge marks) and calculates the distance between them before the measurement begins (original length). During the measurement, a real time processing algorithm runs and calculates the actual distance between the gauge marks. The video system subtracts the original length from the actual distance of the gauge marks to find the elongation. Finally, it calculates the strain by dividing the elongation with the original length. It is worth noting that the rate of cross-head movement for all the measurements in this study is 0.5mm/minute. Appendix C shows the specimen and the jig mounted into a conventional testometer and ready for measurements.

## 5.6 Calibration

The measurement system described in this study was first used to determine the Hookean region of a specimen made of aluminium to calculate its tensile Young's modulus. Aluminium being a material with well understood mechanical properties, it serves to demonstrate that the measurement system operates well and achieves satisfactory results. The measurement is performed at room temperature and on a specimen with cross section area of $17.73mm^2$

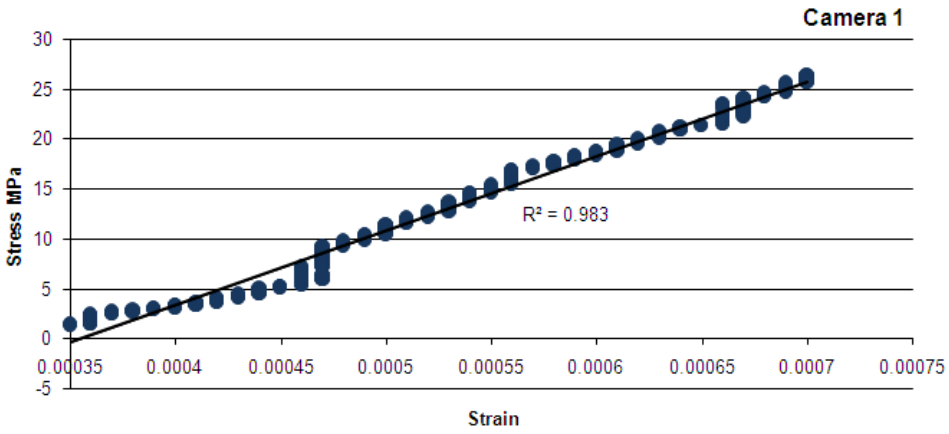


Figure 5.12: Stress strain graph for aluminium captured by camera 1. The linear fit to calculate the Young's modulus is shown.

between the optical contrast targets. Schmid E. and Boas W. [82] report that the Young's modulus of aluminium ranges between 62.7GN/$m^2$ and 75.4GN/$m^2$.

The tensile measurement of aluminium shows a good degree of similarity for results obtained by both cameras, see figure 5.12 and figure 5.13. This means that both surfaces of the specimen response equally to the tensile force applied on the specimen which implies that only pure tensile forces act. This confirms that the jig has removed the bending and twisting forces applied in the specimen during the measurements, which caused a disagreement of the first set of results reported by the cameras.

The Young's moduli calculated from camera 1 and camera 2 are 74$\pm$0.25GPa and 71$\pm$0.25GPa, respectively. The results obtained from the surfaces of the aluminium specimen agree well within 4$\%$ with each other. The average Young's modulus value measured is 72.5$\pm$GPa and agrees well with literature values.

It is worth noting that the lights used during the measurements are two portable table lamps that can be sometimes difficult to position satisfactorily in order to achieve the same illumination intensity on both surfaces of the flat specimen. The small change in strains between the two cameras indicates that the lightnings on the surfaces of the specimen are not constant.

The jig is considered as an accurate and reliable tensile measurement system component that achieves satisfactory Young's modulus values at low stress. It will therefore be used in this study to determine the Young's moduli of carbon fibre reinforced polymer and PocoFoam.

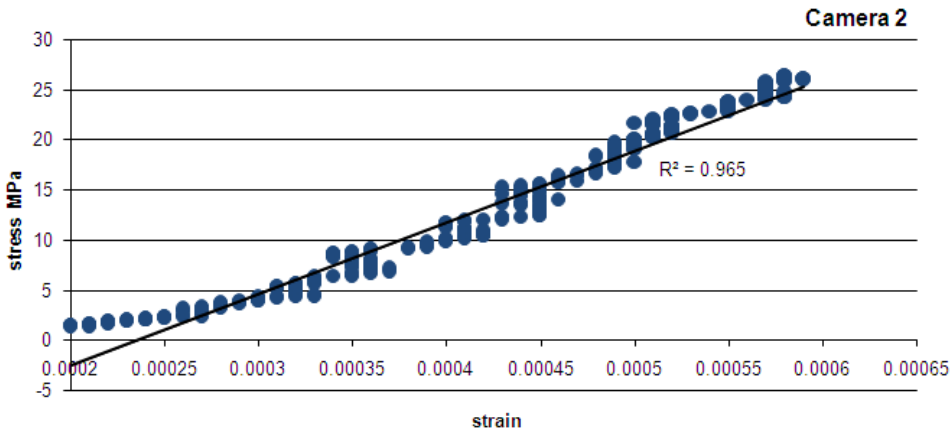


Figure 5.13: Stress strain graph for aluminium captured by camera 2. The linear fit to calculate the Young's modulus is shown.

## 5.7 Young's Modulus of CFRP and PocoFoam

Tensile measurements of PocoFoam and CFRP specimens are performed in this section. The PocoFoam specimen has a density of $0.56 g/cm^3$ and it is manufactured by Poco Graphite in France. The measurements of the CFRP are performed on two carbon fibre reinforced polymers with different fibre orientations. One CFRP specimen is a uni-directional prepreg with a 3 layer lay up structure with fibres running along directions 90/0/90. It uses K13C2U pitch carbon fibres with RS-3C cyanate ester/resin and has 168 grams per square meter areal weight with $32\%$ resin content. The other CFRP is a quasi isotropic skin 0/60/-60 and it was used in the design of the wing of the current ATLAS SCT end cap support structure.

### 5.7.1 Carbon Fibres

During the R&D stage for the design of the current ATLAS SCT end cap, tensile measurements of the isotropic -60/60/0/0/60/-60 CFRP were performed at the Engineering Research Laboratory (MERL)[7] and Young's modulus values between 109GPa and 116GPa were measured. It was reported that these measured values were aligned with the recommended value, which is around 114GPa. Both the recommended Young's modulus value and the Young's modulus value measured at the Engineering Research Laboratory were certainly obtained by performing tensile measurements with conventional testometers, since there was no mention of low stress measurements. The current ATLAS SCT End cap was designed with the Young's modulus value for CFRP of 114GPa. This Young's modulus value is acceptable because of the magnitude of stress involved in the current design. Because of the low stress that the stave of the ATLAS upgrade will be submitted to, measurements of the Young's modulus of the CFRP at corresponding low stress values were made. The obtained values, if different

[7] https://www.usbr.gov/pmts/materials-lab

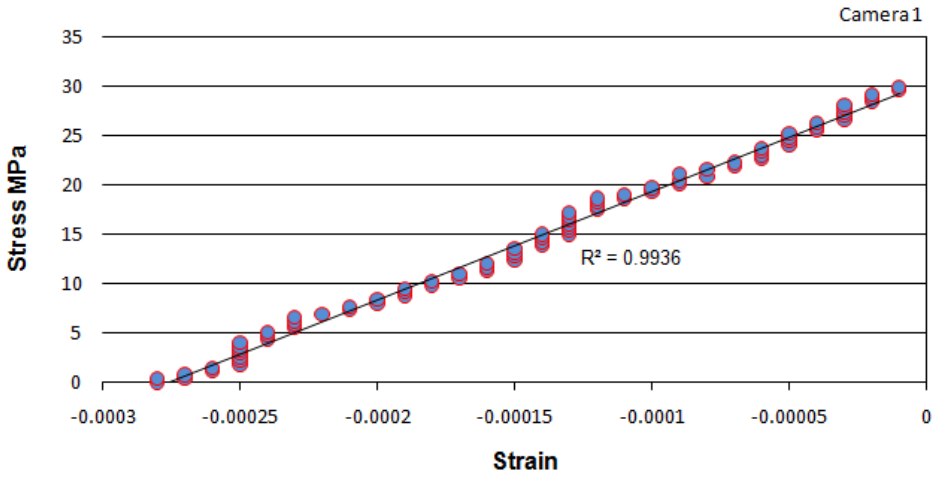


Figure 5.14: Linear-elastic region of carbon fibre specimen (-60/60/0/0/60/-60) calculated by camera1

from the value obtained at high stress, will contribute to a better understanding of the stave mechanical behaviour. In case the values are similar it will be established that there is no difference between the Young's moduli of CFRP obtained at low and high stress.

#### 5.7.1.1 Experimental Results

Figure 5.14 and figure 5.15 show the stress-strain curves recorded by the two cameras for the 0/60/-60 CFRP specimen. The values of the Young's modulus extracted from a linear fit to the data are 110$\pm$1GPa and 108$\pm$2GPa for camera 1 and camera 2, respectively. The CFRP specimens measured in this study have a constant cross section area of 2.737$mm^2$ between the optical contrasts targets. The results of the tensile measurements of CFRP -60/60/0/0/60/-60 and 90/0/90 are presented in table 5.1.

Charles W. Marschall and Robert E. Maringer [**?**] report also that the elastic modulus of structural materials diminishes gradually with the increase of temperature inside the specimen. This reduction of the elastic modulus is an expected consequence of the small increase in atom spacing associated with the greater atom vibration that accompanies heating. They claim that for elastic strains, tension produces a decrease of temperature and compression produces an increase of temperature in the measured specimen. This implies that the compressive elastic modulus is less than the tensile elastic modulus for a given material. The forces applied on the specimen at low stress are so small that the temperature inside the specimen does not decrease appreciably during the tensile measurements. Based on this knowledge, elasticity moduli values measured at low stress are expected to be slightly lower or equal to the elasticity moduli obtained with conventional methods.

The Young's modulus values for -60/60/0/0/60/-60 and 90/0/90 that are used and assumed

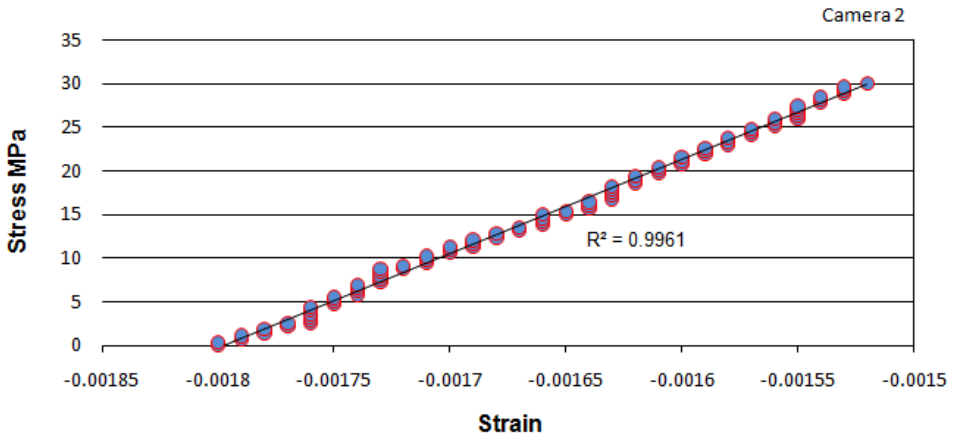


Figure 5.15: Linear-elastic region of carbon fibre specimen (-60/60/0/0/60/-60) calculated by camera2

correct at the Brookhaven National Laboratory (BNL) in the USA are 114GPa and 125GPa, respectively. These values were obtained at high stress. The corresponding measured values are 109GPa and 126GPa, respectively. There is good agreement between these values. In conclusion, the Young's modulus value of CFRP at low stress is equal to the Young's modulus value obtained with high stress. In consequence, the CFRP's Young's modulus measured at high stress can be used to undertake precision design of the stave.

### 5.7.2 PocoFoam

PocoFoam is a low density carbon graphite foam with mechanical properties that are not well understood. The majority of the research performed on PocoFoam is oriented towards its thermal properties, which have great performances. There are no documented recommended PocoFoam's mechanical properties that can be used as a reference. However, having achieved good agreements using the jig between the recommended and the measured values of the Young's moduli of CFRP and aluminium, it is believed that accurate and reliable Young's modulus values of PocoFoam can be obtained. The measurements are performed on PocoFoam specimens with a density of $0.56 g/cm^3$.

PocoFoam is fragile and does not require much force applied on it before fracture occurs. It is impossible to measure PocoFoam directly inside the jig by machining and shaping the specimen as shown in figure 5.9 and obtain accurate results. Another technique is therefore used to prepare and make the PocoFoam specimen ready for measurements. Rectangular PocoFoam specimens were cut according to the direction that was investigated and glued onto two aluminium pieces, as shown in figure 5.16. Measurements were performed in $x$, $y$ and $z$ directions. The aluminium pieces have equal dimensions with the ends of the specimen shown in figure 5.9. The thickness of the PocoFoam specimens investigated in this study is around 4mm and the glue used is Araldite 2011. The PocoFoam specimen is glued onto

Table 5.1: Young's modulus values of CFRP -60/60/0/0/60/-60 and 90/0/90. 97MPa(∗) is not taken into consideration in the calculation of the average value because this value was measured when the portable table lamp slipped from its position

| CFRP | Measured tensile modulus (GPa) | Average tensile modulus (GPa) | BNL values (GPa) | Values used in current simulation (GPa) |
|---|---|---|---|---|
| 0° tensile modulus 0/60/-60 | 110<br>97(∗)<br>110<br>108 | 109 | 114 | 112 |
| 0° tensile modulus 90/0/90 | 124<br>124<br>124<br>132 | 126 | 125 | |

the aluminium ends and the assembly is put into an oven for 30 minutes at a temperature of 100°C. The optical contrast targets are placed directly on the PocoFoam away from its ends. This constrains the cameras to capture the displacement occurring only in the PocoFoam and not in the glued region.

#### 5.7.2.1 Experimental Results

The stress-strain results, shown in figures 5.17 and 5.18 show that the surfaces of the PocoFoam specimen faced by the cameras do not behave similarly below 0.3MPa. This is not yet understood.

It appears that PocoFoam behaves non-elastically in the region up to 0.3MPa. The Young's moduli values obtained by the cameras in this region do not agree with each other. This phenomenon is observed during the tensile measurements of all the three directions of the PocoFoam specimen. It can be explained by the spacing out of the highest cell layer that is directly in contact with the tensile force applied on the specimen. This is followed almost immediately by the spacing out of the next cell layer and the phenomenon propagates through the specimen to the lowest cell layer. All the successive cell spacings take place until all the layers are individually spaced out to a certain level. This is achieved with a stress of 0.3MPa. Below that stress level, Young's modulus values of two specimens are not similar due to the random bubble's creation during the PocoFoam foaming process. From 0.3MPa to 0.6MPa, the cells elongate uniformly and together. Measurements of the Young's modulus of two specimens are similar and repeatable in that stress range. Above the stress of 0.6MPa, the slopes of the curves of two specimens are different, hence different Young's modulus values. This is an indication that permanent deformation occurs immediately after 0.6MPa. The ultimate yield strength is observed at around 0.8MPa followed shortly by failure at around

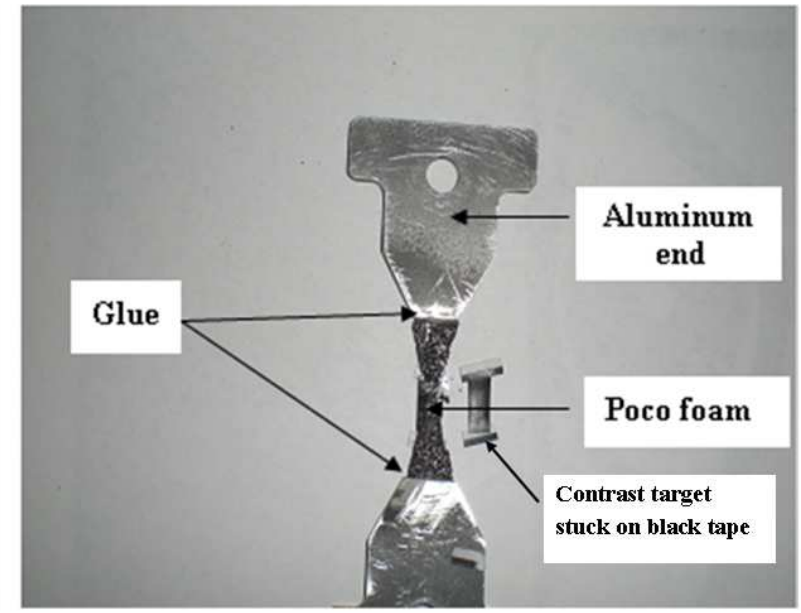


Figure 5.16: Overview of pocoFoam glued to aluminium ends

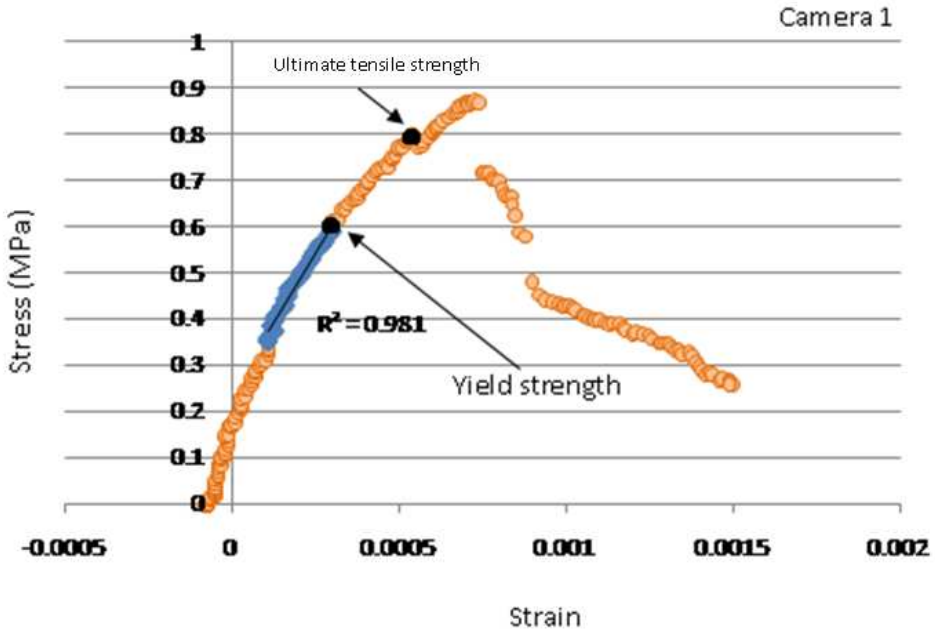


Figure 5.17: Stress-strain curve for PocoFoam captured by camera 1. The linear fit to calculate the Young's modulus was performed over the blue region of the graph.

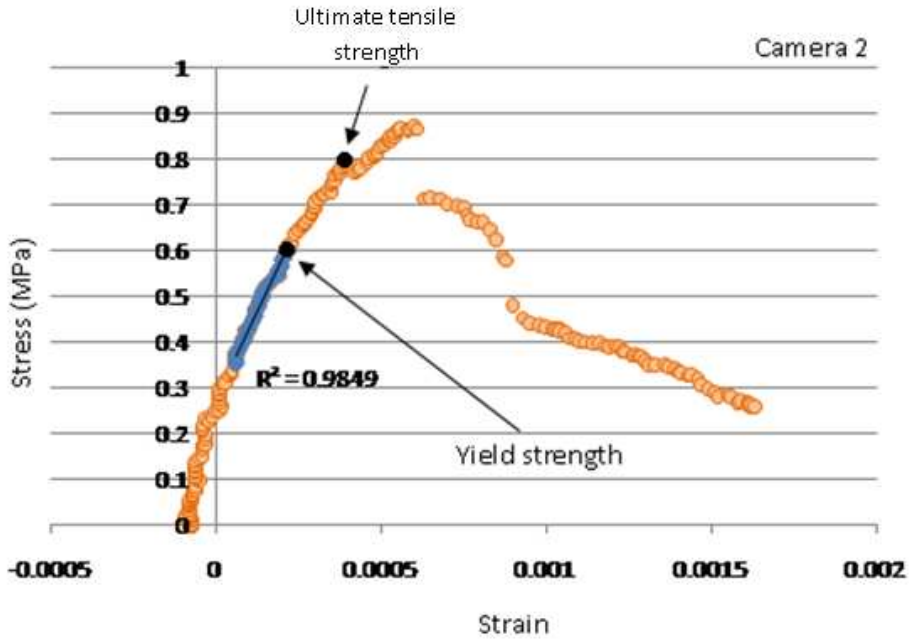


Figure 5.18: Stress-strain curve for PocoFoam captured by camera 2. The linear fit to calculate the Young's modulus was performed over the blue region of the graph.

0.85MPa. Table 5.2 present the results of the tensile and compressive measurement performed on PocoFoam specimens. The obtained values agree well with the values reported by Delsen Testing Laboratory, Inc[8]. Delsen Inc. is the testing Laboratory that investigates the materials involved in the US stave design.

The tensile Young's modulus value in the $z$ direction appears to be three times higher than the Young's moduli value obtained in the $x$ and $y$ directions. The compressive Young's modulus is twice the value of the modulus measured for the y direction. The considerable difference between the moduli in the z direction and the other directions were expected because of the elongation of the foam in that direction. As shown in table 4.6, the elongation of the foam in the z direction causes the thermal conductivity to be almost two and half times higher than the thermal conductivities in the other directions.

## 5.8 Shear Modulus of PocoFoam

The shear modulus is a measure of the ability of a material to resist transverse deformations. It describes the material's response to shearing strains. The shear modulus is the elastic modulus used in the calculations during deformations caused by an applied force parallel to one surface of an object when the opposite surface is held fixed by another equal force. In the case where an object of height L, with cross sectional area A, experiences a force F parallel to one surface and is held at the lower surface, the surface subjected to the force F (sheared

[8] www.delsen.com

Table 5.2: Summary of results of tensile and compressive measurements performed on a PocoFoam specimen of density equal to 0.56g/$cm^3$

| Test | Direction | Measured YM (MPa) | Average measured YM (GPa) | Yield strength (MPa) | Ultimate yield strength (MPa) | YM used for modeling (GPa) |
|---|---|---|---|---|---|---|
| Tension | x | 1122<br>1070<br>1102<br>1142 | 1.1±0.27 | 0.6±0.03 | 0.8±0.03 | 1 |
| | y | 1212<br>1440 | 1.3±0.27 | 0.6±0.03 | 0.8±0.03 | 1 |
| | z | 4115<br>3488<br>4071<br>3470 | 3.8±0.27 | 1±0.03 | 2±0.03 | 4 |
| Compression | y | 983<br>991<br>1188<br>1111 | 1.07±0.08 | - | - | - |
| | z | 2130<br>2140<br>2190<br>2140 | 2.15±0.02 | - | - | |

surface) will move a distance $\Delta X$, see figure 5.19. The created shear stress ($\tau$) is defined as the magnitude of the force per unit cross sectional area of the surface being sheared (F/A). $\tau$ is applied parallel or tangential to the surface being sheared, as opposed to a normal stress which is applied perpendicularly. The created shear strain is defined as $\Delta X$/L.

The shear modulus is mathematically defined as the ratio of the stress to the strain and expressed as follows

$$G = \frac{shearstress}{shearstrain} = \frac{F}{A}\frac{L}{\Delta X} \tag{5.4}$$

It is clear from equation 5.4 that, the bigger the shear modulus the more rigid is the material since for the same change in horizontal distance (strain) a bigger force (stress) is needed. That is the reason why the shear modulus is sometimes called the modulus of rigidity. There is no change in volume of the material during the deformation. The planes of atoms merely slide sideways over one another. The block is fixed and does not move from its position at the base. This implies that an equal force F that is not shown on figure 5.19 is

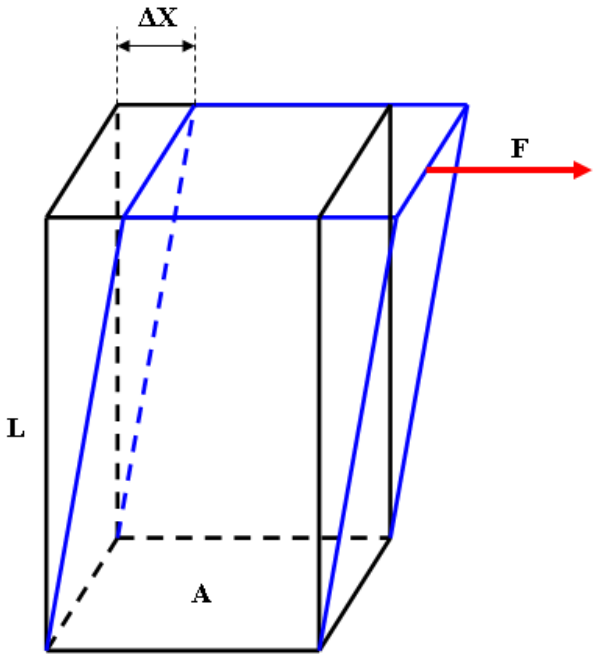


Figure 5.19: Schematic illustration of a shear test

applied at the lowest surface.

The coolant temperature of the stave during the operation of the inner tracker is around -27°C [94]. The considerable amount of heat generated from the silicon modules during the operation of the ATLAS inner tracker will create a significant temperature gradient between the cooling fluid and the silicon modules. M. Gilchriese et al. reported after an ANSYS analysis that this temperature difference will affect the stave design by causing the cooling pipe to detach itself from the PocoFoam. The separation is not caused by failure of the glue layer applied between the PocoFoam and the pipe but by breaking the PocoFoam ligaments. This implies that the thermal induced stress in the PocoFoam is greater than the PocoFoam's shear modulus. It is worth noting that the shear values used in this analysis are obtained from the available literature. It is therefore necessary to determine the shear moduli of the PocoFoam at low stress and use them as ANSYS input values in order to interpret well the analysis. Knowledge of the accurate shear modulus of the PocoFoam will also improve the stave design by keeping the thermal induced shear stress lower than the allowable shear stress value.

## 5.9 Measurement Technique

Many shear testing methods exist and can be used for the measurement of shear modulus of different materials. Nevertheless, the shear measurements of PocoFoam exhibit some restrictions such as thickness and size, therefore a suitable measurement technique must be

utilised. Methods such as ISO 11003-2[9], ISO 1922[10] and ISO 1827:2007[11] are investigated in order to use the most suitable one for the measurement of the shear modulus of PocoFoam. These methods are assumed to be the most suitable available.

### 5.9.1 ISO 11003-2 Shear behaviour of structural adhesives

This method requires that the maximum thickness of the structural adhesive under investigation lies around 0.8 mm. The machining of PocoFoam with a thickness less than 1mm can be achieved, however concern is raised about the state of the ligaments, hence the stiffness of the specimen. It is considered that the specimen will be very fragile and it will be easy to damage further the ligaments during the handling of the specimen. Due to this reason, the ISO 11003-2 method is considered not suitable for the shear measurement of PocoFoam.

### 5.9.2 ISO 1922 Shear modulus of cellular plastics

PocoFoam is usually manufactured in the form of sheets with dimensions approximating 250mm x 250mm x 25mm. The measurements of the shear modulus can only be performed in the $x$ and $y$ directions and not in $z$ direction. The actual cost of PocoFoam is around 3000USD per sheet. This method requires the use of PocoFoam pieces that are 250mm long. The measurement of one specimen in each of the $x$ and $y$ directions requires the purchase of at least two sheets. Considering the high cost involved in using this shear testing method, the measurement system described in ISO 1922 is considered unsuitable for the shear measurement of PocoFoam.

### 5.9.3 ISO 1827:2007 Shear modulus of rubbers

This method tolerates no rotation of the rubber pieces under investigation and requires four elements with dimension around 25mmx25mmx4mm. It is important for the PocoFoam pieces under investigations not to rotate in order to achieve pure shear properties. The availability of PocoFoam pieces at the dimensions mentioned earlier, makes the test piece arrangement shown on figure 5.20 to be considered suitable for the shear measurement of PocoFoam.

The technique used to measure the shear modulus of rubbers is utilised in this study to measure the shear modulus of PocoFoam. The measurements are preceded by carefully preparing the test specimens. This includes the machining of the PocoFoam pieces according to required dimensions, gluing the pieces with Araldite 2011 inside the test arrangement and

[9] ISO 11003-2:1993, Determination of shear behaviour of structural bonds

[10] ISO 1922:2001, Rigid Cellular plastics - Determination of shear strength

[11] BS ISO 1827:2007, Rubber, vulcanized or thermoplastic - determination of shear modulus and adhesion to rigid plates, quadruple-shear methods

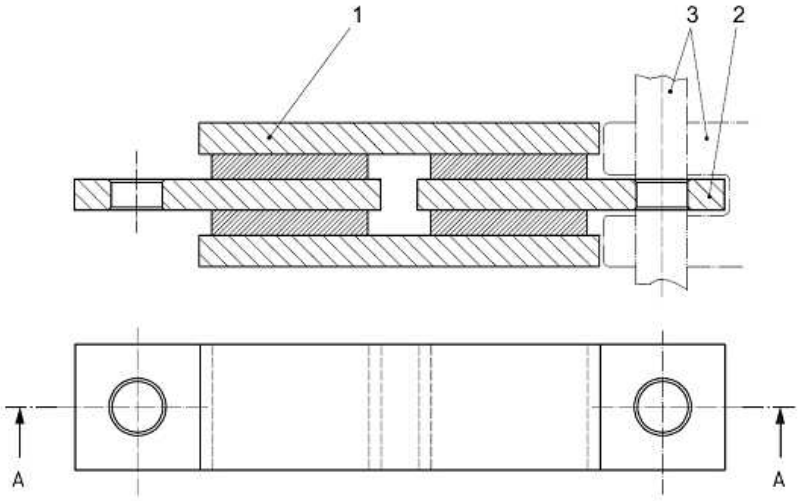


Figure 5.20: Schematic illustration of the test piece arrangement for the measurement of the shear modulus of rubbers. (1) Two external plates, (2) two internal pulling devices and (3) pin and fixture for tensile loading

curing the whole arrangement in an oven at 80°C for 30 minutes. Figure 5.21 shows a ready PocoFoam arrangement for the measurement of shear modulus.

## 5.10 Calculation of the Shear Modulus

The determination of the shear modulus is obtained by acquiring the shear strain $\gamma$ and the shear stress $\tau$. The units are in $N/cm^2$. In this section ISO 1827:2007 is used as reference to the mathematical expressions.

The shear strain is calculated from the following expression

$$\gamma = \frac{d}{2c} \tag{5.5}$$

where

$d$ is the deformation, in millimetres, of the test piece. $c$ is the thickness, in millimetres, of one PocoFoam element.

The calculation of the shear stress is performed by the following expression

$$\tau = \frac{F}{2A} \tag{5.6}$$

where

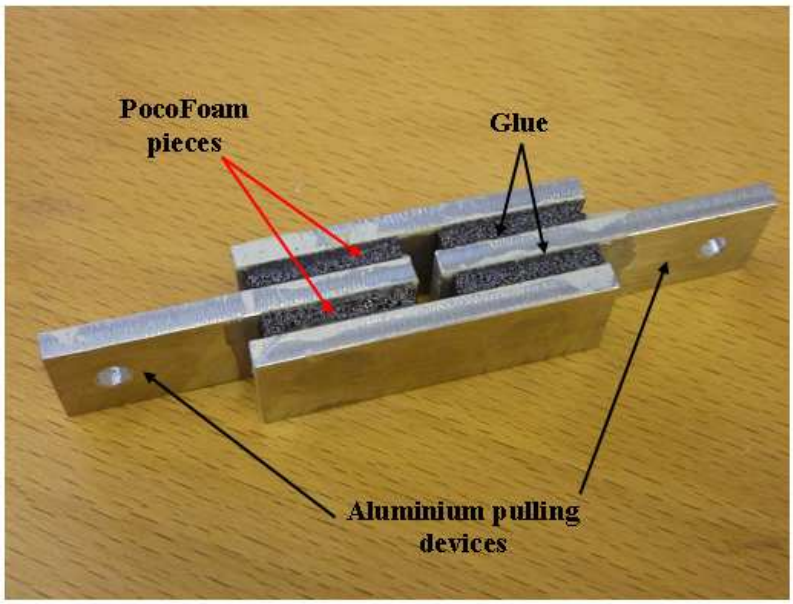


Figure 5.21: Overview of the PocoFoam arrangement for measurement of the shear modulus

$F$ is the force, in newtons where $A$ is the glued area, in square millimetres, of one face of one PocoFoam element.

Finally, the value of the shear modulus is calculated by dividing the shear stress by the shear strain,

$$G = \frac{\tau}{\gamma} \tag{5.7}$$

## 5.11 Measurements

The measurement of the shear modulus of PocoFoam is performed by utilising the conventional testometer and the video extensometer system mentioned earlier and shown in figure 5.11. The optical contrast targets are attached one each on the two aluminium pulling device. This constrains the cameras to measure only the strains appearing in the PocoFoam ligaments caused by the upward movement of the upper aluminium pulling device. Misalignment between the force applied and the centre line of the PocoFoam arrangement together with twist have been identified and remedied by the design of the arrangement, see figure 5.22.

### 5.11.1 Experimental Results

The measurements of the shear modulus were performed on PocoFoam pieces that have a density of 0.56g/$cm^3$. Measurements were performed at room temperature with a maximum force of 450N applied to the PocoFoam arrangement. The results obtained for one of the

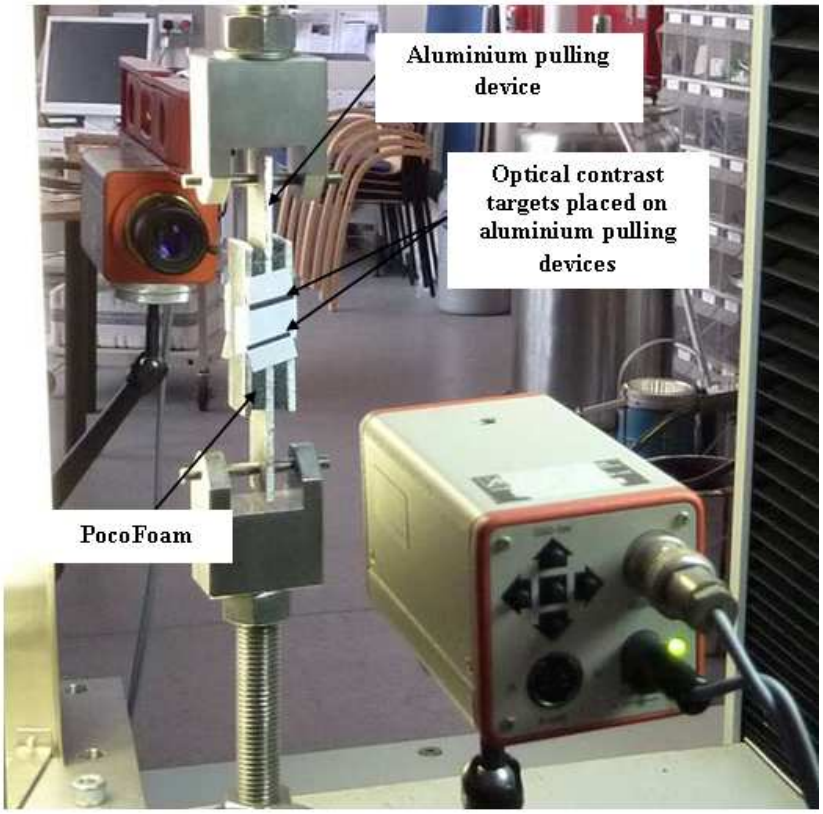


Figure 5.22: Overview of the PocoFoam arrangement mounted into a conventional testometer

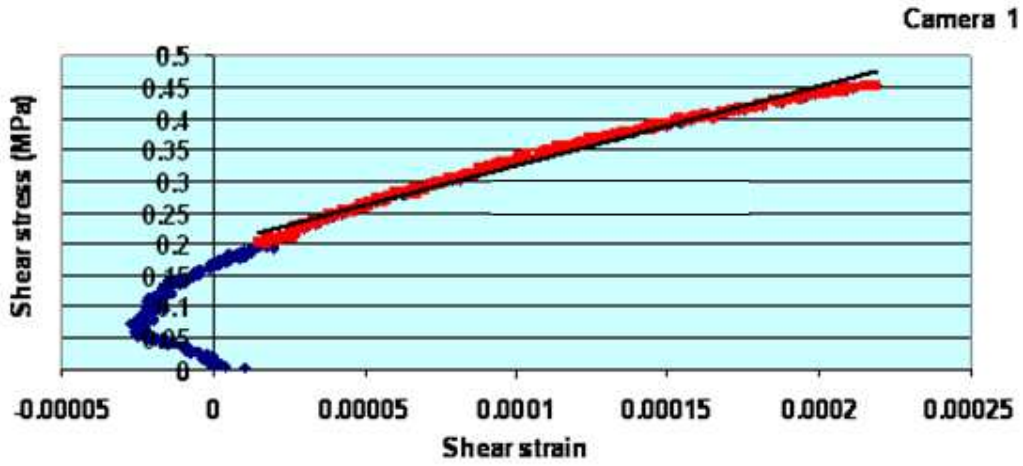


Figure 5.23: Shear linear-elastic region of PocoFoam captured by camera1. The linear fit used to calculate the Young's modulus is performed over the region shown by the red data points.

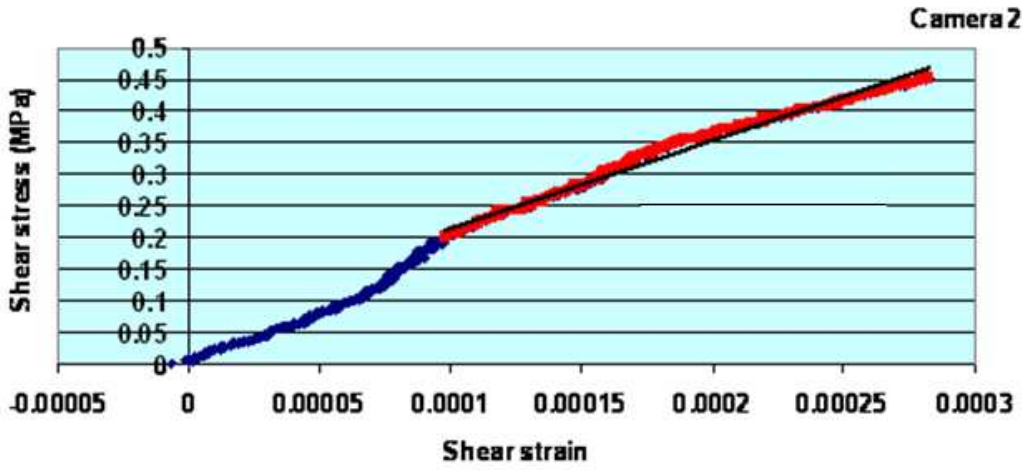


Figure 5.24: Shear linear-elastic region of PocoFoam captured by camera2. The linear fit used to calculate the Young's modulus is performed over the region shown by the red data points.

shear measurements of Pocofoam in the $y$ direction is shown in figure 5.23 and figure 5.24. On these figures, it is observed that the shear stress-shear strain curves are not linear at the beginning of the measurements until the shear stress reaches the value of 0.2MPa. This phenomenon is observed during the shear measurements of PocoFoam in the $x$, $y$ and $z$ directions. It appears that the shear force applied onto the PocoFoam causes the outer cell layers to slide first. The increase of the shear force increases progressively the number of sliding cell layers. All the cells get slid sideways to a certain level when the stress applied on the PocoFoam pieces is around 0.2MPa. Above this stress value, the shear stress and the shear strain exhibit a linear relationship. The measured shear moduli are repeatable for shear stress values between 0.2MPa and 0.45MPa, and agree well with each other within $8\%$. A summary of the PocoFoam shear modulus measurements is presented in table 5.3.

## 5.12 Summary

Young's modulus measurements of CFRP (0/60/-60) and CFRP (90/0/90) together with PocoFoam have been performed at low stress and at room temperature using a jig designed to remedy the misalignment and twist occurring during the measurements. The jig is adapted to a conventional testometer and has successfully contributed to the achievement of the elastic linear region in the stress-strain curves. The measured Young's modulus value of CFRP (0/60/-60) agrees well with the previously reported value measured at high stress to within $4.6\%$ . However, as expected the value is slightly lower than the manufacturer's value [89]. The results obtained at low stress show that the Young's modulus value of a given CFRP is constant and independent of the magnitude of stress applied during the measurements.

Table 5.3: Summary of the PocoFoam shear modulus measurements performed on PocoFoam of density 0.56g/$cm^3$

| Test | Direction | Measured modulus (MPa) | Average modulus (GPa) |
|---|---|---|---|
| Shear | x | 1331.1<br>973.07<br>1012.6<br>861.73 | 1.04±0.16 |
| | y | 1261.5<br>1369.5<br>988.92<br>1014.3 | 1.16±0.16 |
| | z | 1840.3<br>1817.1<br>1613.5<br>1724.7 | 1.75±0.16 |

The results obtained from the measurements performed on the PocoFoam specimens show that PocoFoam is mechanically anisotropic. As already observed in the thermal conductivities, this mechanical anisotropy is expected due to the foaming process of PocoFoam. The tensile and compressive Young's modulus values are around 1.1GPa in the x and y directions. In the z direction, the tensile and compressive Young's modulus values are around 3.8GPa and 2.15GPa, respectively.

Shear modulus measurements of PocoFoam have also been performed at low stress and at room temperature. The measurement method normally used to measure rubbers has been used for the measurement of PocoFoam. The results obtained show that the shear modulus values are equal in the x and y directions but differ for the value in the z direction. The values obtained in x and y directions are similar to the tensile/compressive values at 1GPa but the value in the z direction is around 1.75GPa.

# Chapter 6

# Thermo-Mechanical Measurements

In previous chapters, thermal and mechanical material characterisations have been performed. Pure thermal material properties such as thermal conductivities and thermal resistances have been measured. Measurements of pure mechanical material properties such as yield strength, shear and Young's moduli have also been performed. During the operation of the inner tracker, both heat and mechanical forces will act simultaneously on the stave components which effect the stave design. An example of this combination of forces is the cooling of the pipe and the heating of the silicon sensors that create a force along the length of the pipe inside the PocoFoam. The thermally induced force can act as a shear force to the PocoFoam and distort its structure including breaking its ligaments. This will result in a change of the PocoFoam thermal properties including an increase of its thermal resistance. The transverse thermal response of the stave design can be changed significantly with a change of the actual resistance of the PocoFoam.

The objective of this chapter is to acquire a detailed understanding of the impact that the damaged PocoFoam ligaments can cause to the thermal performance of the stave. In order to achieve this objective, measurements of an assembly called a sandwich, is performed. The sandwich is shown on figure 6.1. It is important to reproduce in the laboratory conditions similar to that present in the PocoFoam during the use of the inner tracker in order to achieve accurate understanding of the behaviour of the thermal performance of the stave. The sandwich is therefore designed with stainless steel, PocoFoam and carbon fibre reinforced polymer in order to reproduce the core materials of the UK stave design. The glues used in the design of the sandwich such as Hysol EA9396 and Hysol EA9396 + 35$\%$BN are strong candidates to be used in the stave design.

The sandwich consists of a PocoFoam piece of cross sectional area close to $1cm^2$ that is glued with Hysol EA9396 on one side to a stainless steel piece and on the other side to CFRP sheet with Hysol EA9396 + 35$\%$BN. The CFRP is 200$\mu$m thick with a 30mmx30mm area. A 2mm thick piece of Tufnol is attached to the CFRP, see figure 6.1, to aid mechanical attachment to the measurement apparatus. The thermal measurement system used in chapter 4 for the transverse thermal conductivity measurements is used in this study. The sandwich is placed inside a wooden base that is machined in a way that the bottom surface of the sand-

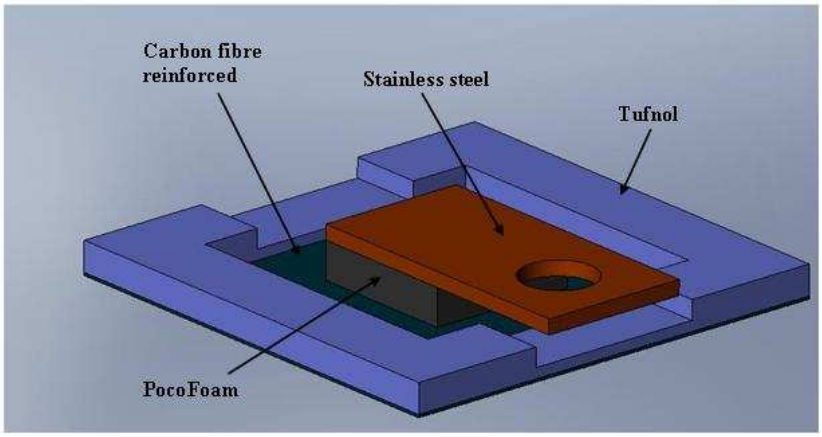


Figure 6.1: Solid Works model of the sandwich

wich (CFRP) is directly in contact to the lower copper bar. The CFRP and stainless steel are glued with Hysol EA9396 on the lower copper bar and the upper copper bar, respectively. A summary of the components involved in the design of the sandwich is presented in table 6.1.

Table 6.1: Summary of the components used in the design of the sandwich

| Component | Thickness ($\mu$m) | Thermal conductivity (W/mK) |
|---|---|---|
| Solid components | | |
| Stainless steel | 500 | 16 |
| PocoFoam | 2500 | 54 |
| CFRP | 200 | 1.2 |
| Copper | | 370 |
| Adhesives | | |
| Hysol + 35%BN (PocoFoam to CFRP) | 100 | 1.24 |
| Hysol EA9396 (Poco to s/s, s/s to Cu, CFRP to Cu) | 20 | 0.28 |

## 6.1 Measurement Principles

Resistance Temperature Detectors are used to record the temperature drop along the copper bars. Two RTDs are attached on the copper bars, one on each side of the sandwich. Figures 6.2 and 6.3 show the position of the sandwich in the wooden base together with the RTDs attached to the copper bars. The copper bars have the same cross sectional area as the Poco-

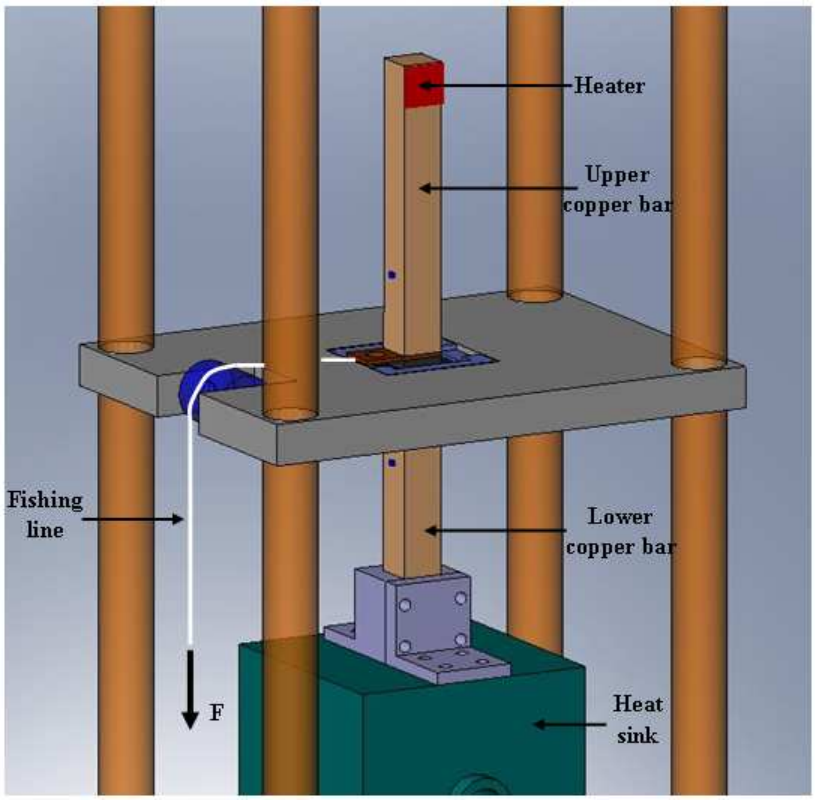


Figure 6.2: Solid Works model of the sandwich placed inside the wooden base

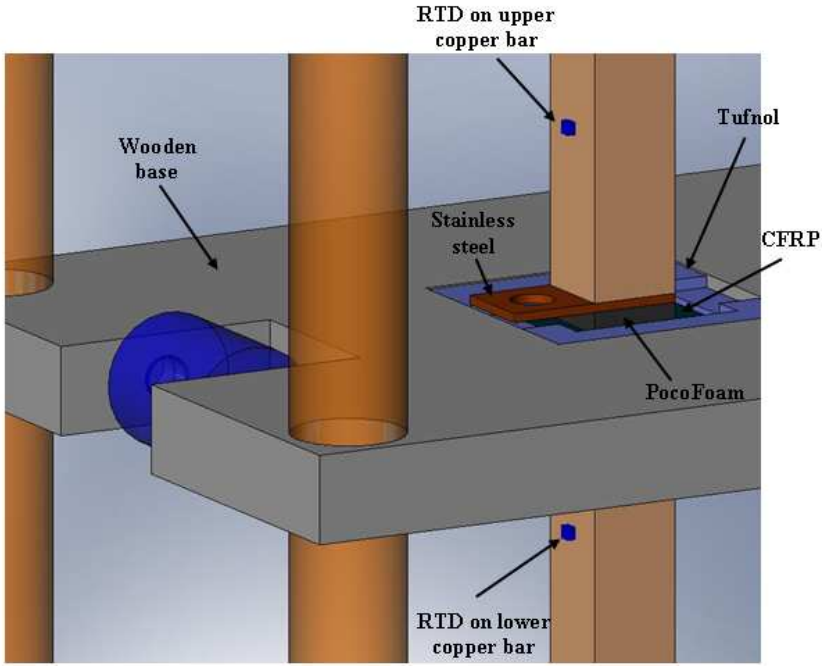


Figure 6.3: Zoomed Solid Works model of the sandwich showing the RTDs on the copper bars

Foam specimen, of $1cm^2$. The PocoFoam specimen is placed in the measurement system in a way that the vertical surfaces of the copper bars coincide with that of the PocoFoam specimen. This ensures a perfect alignment of the copper bars with the PocoFoam specimen. The measurements are performed at room temperature with 1W applied on the heater. A fishing line with a diameter of 500$\mu$m and maximum bearing load of 13.6kg is used to create a shear force acting on the PocoFoam specimen. This is achieved by tying the stainless steel piece to one end of the fishing line and a mass to the other end. The fishing line slides on a teflon rod in order to hang the mass, see figure 6.2. To prevent the sandwich from being pulled out of the wooden base due to a torque between the force on the fishing line and the reaction between the sandwich and the base, the Tufnol was clamped to the base at the opposite side of the fishing line attachment.

The measurements are performed in situ, meaning that the power is switched on and the mass is increased and remains hung on the fishing line during the measurements. Sufficient time is given to the heat flow to fully develop and reach thermal equilibrium before temperatures are recorded. The average temperature of the two RTDs is kept as close as possible to room temperature in order to maintain a sandwich temperature similar to the room. This is done in order to minimise heat transfer by radiation between the sandwich and the room temperature. As with previous measurements using the transverse measurement system, heat transfer by convection is not considered because of the high position of the heater on the upper copper bar.

## 6.2 Results

The resistances presented in this section are calculated and measured from the Hysol EA9396 gluing the upper copper bar onto the stainless steel piece to the Hysol EA9396 gluing the CFRP to the lower copper bar.

### 6.2.1 Theoretically Expected Values

Equations 6.1 and 6.2 are used to calculate the individual resistances and the total resistance, respectively, of the sandwich glued between the copper bars. $\Delta L$ is the thickness of the component, k is the thermal conductivity of the component and A is the cross section area equal to $1cm^2$. $R_{Hysol}$ is the resistance of the Hysol, $R_{s/s}$ is the resistance of the stainless steel, $R_{poco}$ is the resistance of the PocoFoam, $R_{Hysol+BN}$ is the resistance of the Hysol filled with 35$\%$BN and $R_{CFRP}$ is the resistance of the CFRP.

$$R_{total} = \frac{\Delta L}{kA} \tag{6.1}$$

$$R_{total} = R_{Hysol} + R_{s/s} + R_{Hysol} + R_{Poco} + R_{Hysol+BN} + R_{CFRP} + R_{Hysol} \tag{6.2}$$

A summary of the expected resistances is given in table 6.2 and shows that the resistance of the Pocofoam constitutes 12.29% of the total resistance of the sandwich.

Table 6.2: Summary of the expected resistances of the componenets involved in the sandwich design

| Component | Expected Resistance (K/W) |
|---|---|
| Hysol EA9396 (Cu to s/s) | 0.65 |
| Stainless steel | 0.28 |
| Hysol EA9396 (s/s to Poco) | 0.65 |
| PocoFoam | 0.60 |
| Hysol EA9396+BN (PocoFoam to CFRP) | 0.56 |
| CFRP | 1.51 |
| Hysol EA9396 (CFRP to Cu) | 0.65 |
| Total Resistance | 4.88 |
| Percentage of PocoFoam (%) | 12.29 |

### 6.2.2 Experimental Values

Measurements are first performed with no pulling force applied to the PocoFoam in order to measure the resistance across the sandwich and compare it to the theoretical expected resistance value. After correcting the heat for the radiation loss, the sandwich exhibits a resistance equal to 4.90K/W with a $\Delta T$ equal to 4.62°C. The measured total resistance value agrees well with the expected value (4.88K/W). Thereafter, the pulling force acting on the PocoFoam is increased progressively by adding more mass to the fishing line. This increases the shear stress and further measurements are performed. However, the resistance remains unchanged until the shear stress reaches 0.5MPa and the sandwich resistance changes to 4.97K/W. Theoretically, this means that the resistance of PocoFoam increases by 15%, from 0.60K/W to 0.69K/W. Practically, this implies that no PocoFoam ligament breaks below the shear stress value of 0.5MPa. This value is considered the yield shear strength of PocoFoam above which plastic deformation of ligaments occurs. This yield shear value agrees reasonably well with the tensile yield strength measured in chapter 5. The yield shear value is 16.7% less than the obtained tensile yield strength (0.6MPa).

The resistance remains again unchanged at 4.97K/W with the increase of the mass until the shear stress reaches 0.78MPa and the sandwich resistance changes to 5.06K/W. This

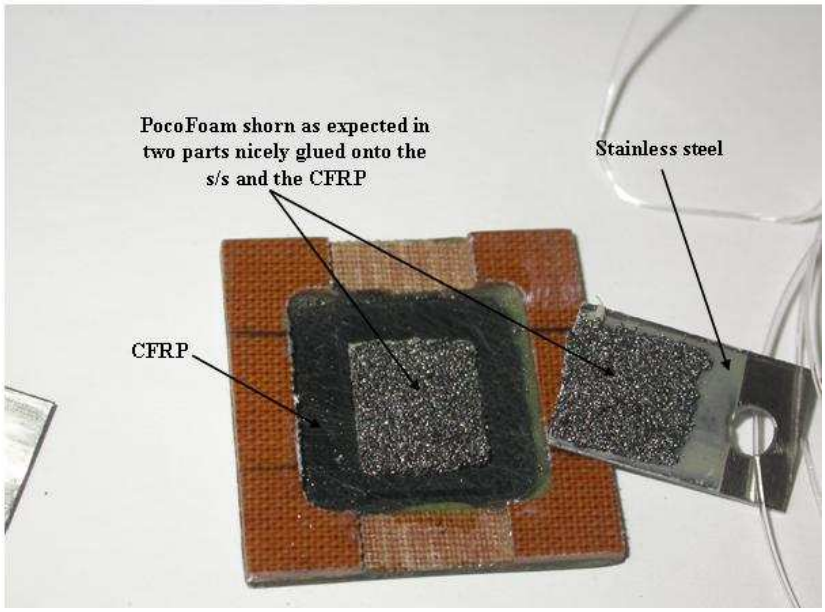


Figure 6.4: Overview of a broken PocoFoam specimen in two parts. As expected the parts are still glued onto the stainless steel and the CFRP

implies that the PocoFoam resistance has increased to 0.83K/W which is a 28% increase above 0.6K/W. This implies that the broken ligaments has to reach a certain number before their combined contribution can increase the resistance. All the ligaments breaks shortly after, at 0.88MPa, implying that after a certain number of broken ligaments, the rate at which the remaining ligaments break increase rapidly and failure occurs shortly after. Stresses of 0.78MPa and 0.88MPa are therefore considered as the ultimate shear strength and the breaking shear strength, respectively. Figure 6.4 shows the PocoFoam as expected broken in two parts through the ligaments.

The measured shear stress values agree well with the tensile stress measured values. This shows that the tensile yield strength, the ultimate tensile strength and tensile breaking strength are practically equal to the shear yield strength, the ultimate shear strength and the breaking shear strength, respectively. A summary of the shear measurement results is presented in table 6.3 together with the tensile values obtained from figures 5.17 and 5.18

Table 6.3: Summary of the tensile and shear mechanical properties

| Mechanical Property | Tensile (MPa) | Shear (MPa) |
|---|---|---|
| Yield strength | 0.6 | 0.5 |
| Ultimate strength | 0.8 | 0.78 |
| Breaking strength | 0.86 | 0.88 |

The error associated with the repeatability of the measurements is about 2%. This is obtained by repeating the same measurements several times under similar conditions.

The total resistance of the sandwich increases on average by 3.2% from 4.9±0.02K/W to 5.06±0.02K/W shortly before failure occurs. Knowing the error experienced in the repeatability of the measurements, it is considered that the sandwich total resistance only increases by 0.14K/W. This implies that the thermal conductivity of the PocoFoam decreases from 54W/mK to 38W/mK, a reduction of around 33%, if only the foam conductivity changes.

An ANSYS simulation[1] performed on the full length of the cooling pipe (1200mm) with end closeout piece and constrained at one end shows that the maximum stress in the PocoFoam is around 0.47MPa. This maximum value is very close to the shear yield stress but far below the ultimate shear stress and the breaking shear stress. This implies that small plastic deformations of the ligaments can occur inside the PocoFoam during the use of the stave. However, failure will not occur in the PocoFoam. In conclusion, the PocoFoam thermal conductivity is not expected to be reduced to 38W/mK due to thermally induced shear stress in the stave.

[1] https://twiki.cern.ch/twiki/pub/Sandbox/TrackerExchange/thermal effects of a Stave with SS pipes

# Chapter 7

# CAD Modeling of Carbon Foam

In this chapter, a 3D geometry of micro-cellular carbon foam is modelled. Matlab is used to write a 2D digital foam algorithm and convert it into a 3D model. The solid model is transferred to Solid Works for void creation in order to obtain a micro-cellular carbon foam model. The primary objective of this model is to develop a predictive capability toward establishing a process-property relationship of carbon foams. In order to capture the effect of processing parameters that affect the foam micro-structure and hence the foam properties, it is necessary that detailed micro-structural characteristics are included in the model [82]. 3D models of carbon foams can contribute to better understanding and therefore prediction and manipulation of its mechanical and thermal properties. Models can also reduce significantly the cost and time associated with experimental measurements. However, 3D modeling of carbon foams is complex due to the foam's heterogeneous and anisotropic structure. The non-uniformity of bubble sizes and pore sizes, average porosity and randomness of bubble placement are the factors that must be considered.

In 2006, Qijun Yu, Brian E. Thompson and Anthony G. Straatman [83] proposed a CAD model of carbon foams. The model was based on a unit-cube geometry characterising the internal foam structure. The model consists of stacked interconnected sphere-centred cubes that constitute a regularly packed array of spheres. The proposed model predicts well the foam thermal conductivity as a function of pore size but makes erroneous assumptions such as single uniform pore diameter of the foam, the centre location inside the unit-cubes of all the pores and intersection of each pore with six adjacent pores on the six surfaces of the unit-cube. These assumptions do not conform to the real foam topology.

Mesut Kirca et al., [84] developed in early 2007 a CAD based algorithm to generate carbon foam models. The method consists of computer programs that generate random bubble sizes and locations which become an input to a CATIA CAD script that produces a solid foam model. The only assumption that Mesut Kirca et al., make is that the cells are exactly spherical. The authors claim that this assumption is mostly valid for mesophase pitch based carbon foams that are heated up to 300°C during the production process. This assumption is also made by A.M. Druma, A.K. Alam and C. Druma [85] in their analysis study of thermal conduction in carbon foams. Moreover, the spherical cell assumption arises from

the assumption of spherical bubble growth mechanisms studied in literature [86], [87]. The Young's modulus and Poisson's ratio obtained with this model agree well with that of the actual subject foam. These results are the proof that physical parameter based modeling techniques can produce CAD foams which are able to represent real foams in a simulation.

In this thesis, the digital foam algorithm developed by Lamontie James et al., [88] is used to model Poco carbon foams. The model is not complex, easy to understand and seems accurate in simulating PocoFoam. Great interest was shown for the model and the authors were contacted in order to use the algorithm for further studies such as mechanical and thermal analysis of PocoFoam. The model is considered the most accurate of the models actually available because the assumptions made conform to the topology of PocoFoam. Randomness of cell locations is achieved by randomly distributing the coordinates of the centre points of the spheres that represent the bubbles. The porosity value, which indicates the pore volume of the foam model, and properties of microstructural topology such as minimum and maximum cell diameters and mean pore diameter values are other characterisation parameters used as variables in the determination of geometrical data. The cells are assumed to be spherical. The model makes two noteworthy contributions:

- The algorithm is fast. It is written in Matlab and does not require a CAD package whose performance can be significantly degraded when rendering large numbers of bubbles. Creation of bubbles is explained later in this chapter.
- The model's void fraction is accurately verified using an image processing technique also performed without the use of a CAD package.

The reason for generating a PocoFoam model is to import the model to ANSYS and predict the thermal and mechanical properties of the foam. These properties will be compared to those measured experimentally in the laboratory.

## 7.1 2D Foam algorithm

Lamontie James et al., report that careful observation of various specimens of Poco carbon foam reveals a repeated pattern of the way the spherical bubbles intersect. The sizes of the bubbles and pores are not uniform, see figure 7.1. Considering a 2D cross section of the PocoFoam specimen, it appears that each bubble has a circular shape and a pore is created at the intersection of the bubbles, see figure 7.2. It is clearly seen that the bubbles are not randomly positioned since each bubble intersects with another one. Moreover, the intersection looks so close so that it allows a particular pore length.

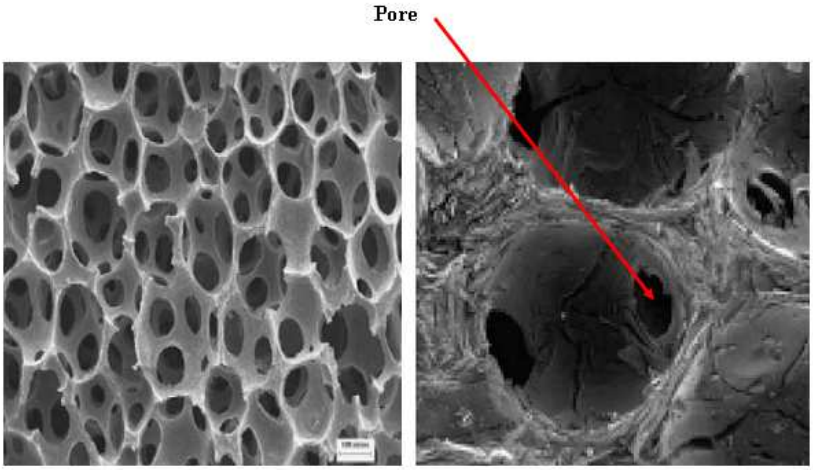


Figure 7.1: Scanning electron microscope (SEM) image of PocoFoam [88]

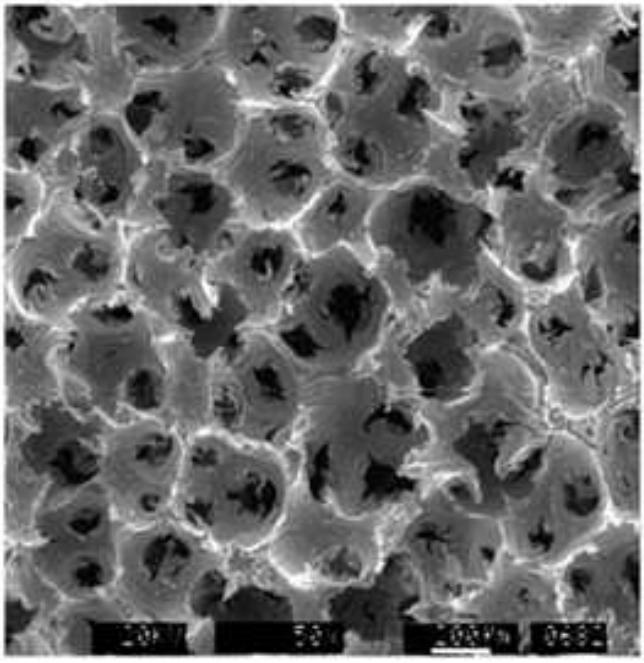

Figure 7.2: 2D view of a PocoFoam specimen [88]

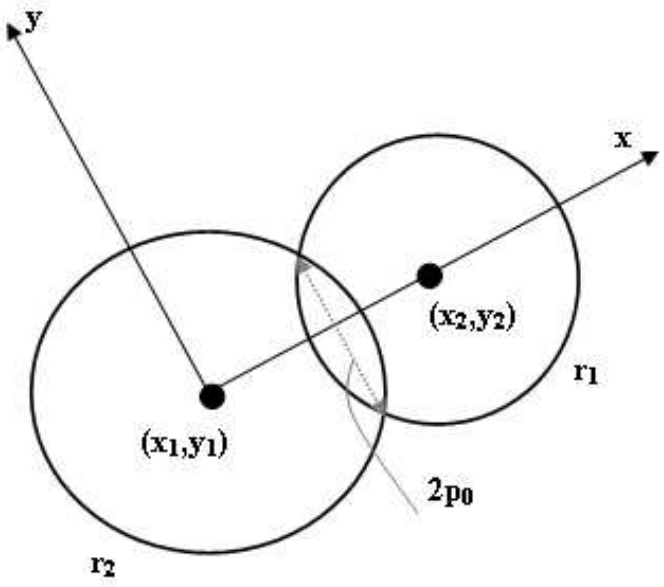


Figure 7.3: Placement of the second bubble as a function of the desired pore diameter what is randomly chosen. $r_1$ and $r_2$ are the radii of the first and second circles, respectively. ($x_1$,$y_1$) and ($x_2$,$y_2$) are the coordinates of the first and second circles, respectively

The 2D digital foam algorithm was developed based on these observations in order for the model to approximate the real PocoFoam topology. The bubbles are selected randomly from a distribution of diameters equal to that observed for PocoFoam. The position of the first bubble is fixed at the origin of the algorithm's inbuilt coordinate system. The position of the second bubble relative to the first is chosen in a way that the diameter of their pore is equal to $2p_0$, see figure 7.3. This value is randomly selected from a data collection of pores with a distribution equal to that measured for a PocoFoam specimen. The algorithm makes sure that the centre of the next bubble is not occupied before allocating the position to be the centre of a bubble. The PocoFoam bubble size is between 350$\mu$m and 400$\mu$m and the pore size is between 150$\mu$m and 200$\mu$m [88].

As seen on the 2D view of the PocoFoam specimen, the intersection of two bubbles offers the possibility to create two more bubbles. The newly created bubble intersects with the previous two intersected bubbles. Given a desired radius of the new bubble, Lamontie James et al., establish a strong relationship between the position of this bubble and the radii of the previous two intersecting bubbles, the distance between the centre points of the bubbles and the pore diameters. In the present example, given the radius $r_3$ of the third bubble its position is conditioned by the radii $r_1$ and $r_2$, the distance $d_{13}$ and $d_{23}$, the pore radii $p_1$ and $p_2$, see figure 7.4. The mathematical expressions used to calculate the positions are the following

$$d_{12} = \sqrt{(x_2 - x_1)^2 + (y_2 - y_1)^2} \tag{7.1}$$

$$d_{13} = \sqrt{(r_1^2 - p_1^2)^{1/2} + (r_3^2 - p_1^2)^{1/2}} \tag{7.2}$$

$$d_{23} = \sqrt{(r_2^2 - p_2^2)^{1/2} + (r_3^2 - p_2^2)^{1/2}} \tag{7.3}$$

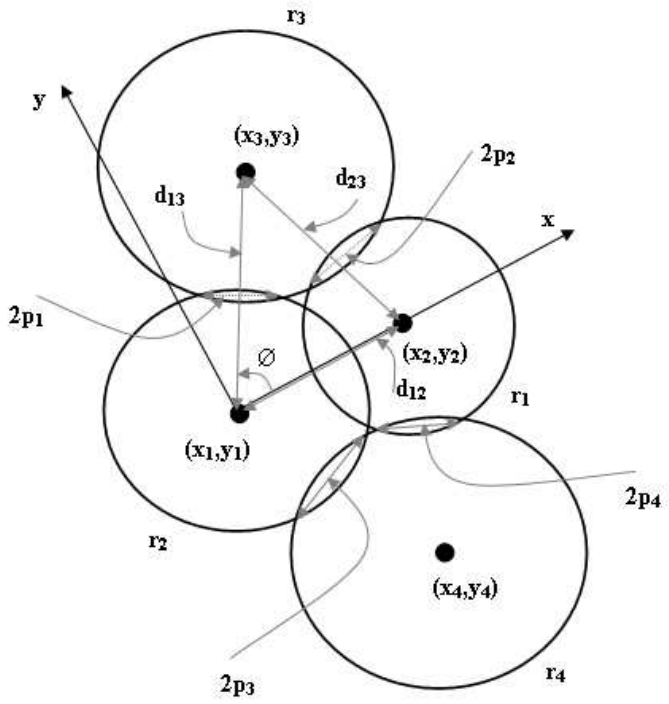


Figure 7.4: Placement of two other bubbles adjacent to the previous intersecting bubbles

$$\phi = \pm cos^{-1}\left(\frac{d_{23}^2 - d_{13}^2 - d_{12}^2}{-2d_{12}d_{13}}\right) \tag{7.4}$$

$$(x_3, y_3) = (x_1, y_1) + (d_{13}cos\phi, d_{13}sin\phi) \tag{7.5}$$

The centre point of the fourth bubble is determined by rotating the centre point of the third bubble by $180°$ using random values of the bubble radius ($r_4$) and pore diameters ($p_3$,$p_4$). By using the equations 7.1 to 7.5, the algorithm follows a precise order in generating the bubbles. The algorithm first selects randomly the radius of the new bubble from the radius range, selects the pore diameters from the pore range and calculates the position of the bubble. The algorithm verifies that the calculated position is not already occupied and places the bubble there before finding other possible bubble intersections and processes the same calculations.

## 7.2 3D digital foam algorithm

After the creation and the positions of the circles in 2D is completed, the algorithm undergoes a further step converting the circles into bubbles. The intersection lines between bubbles become planes. The algorithm works by creating an intersection plane between two bubbles. The creation of this plane is constrained to contain the centres of the intersecting bubbles. Equations 7.1 to 7.5 are used to position a third bubble on that new created plane, see figure 7.5.

In the 2D digital foam algorithm, the fourth circle is created at that stage by rotating the

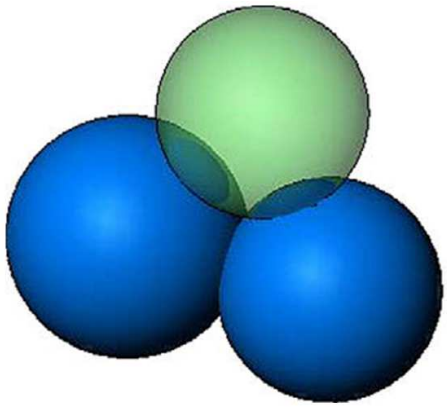

Figure 7.5: placement of third bubble on top of the first two [88]

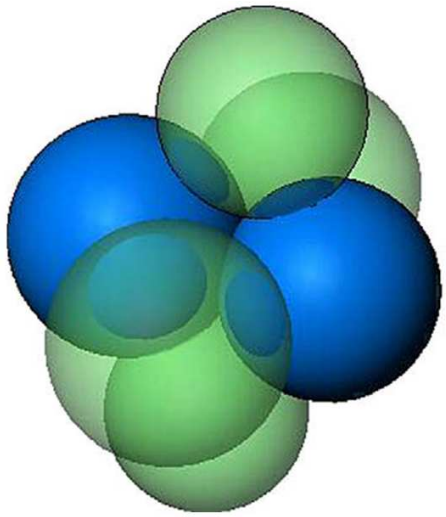

Figure 7.6: Four bubbles placed at $90^\circ$ intervals about an axis [88]

coordinates of the third circle by $180^\circ$ about an axis passing through the centres of the first two circles. The 3D digital foam algorithm instead places three bubbles at $90^\circ$ about that axis creating a total of six bubbles and eight pores, see figure 7.6. Similarly to the 2D digital foam algorithm, equations 7.1 to 7.5 are recalculated using a randomly chosen bubble radius and two randomly chosen pore diameters for each new bubble.

Equations 7.1 to 7.5 are continually used until the circle and bubble creation process is completed with the desired number of bubbles created. An example of a completed 3D bubble generation algorithm is shown in figure 7.7, with 581 bubbles. This solid 3D model is exported to a CAD package where it is extruded. In this study, Solid Works[1] is the CAD package used to extrude the created 3D model. This is done by writing a macro in visual basic that converts the Matlab created bubbles into a solid works model. Figure 7.8 shows the 3D solid works model ready to be transferred to ANSYS.

The porosity of the foam is an important parameter to know in order to establish a rela-

[1] www.solidworks.com

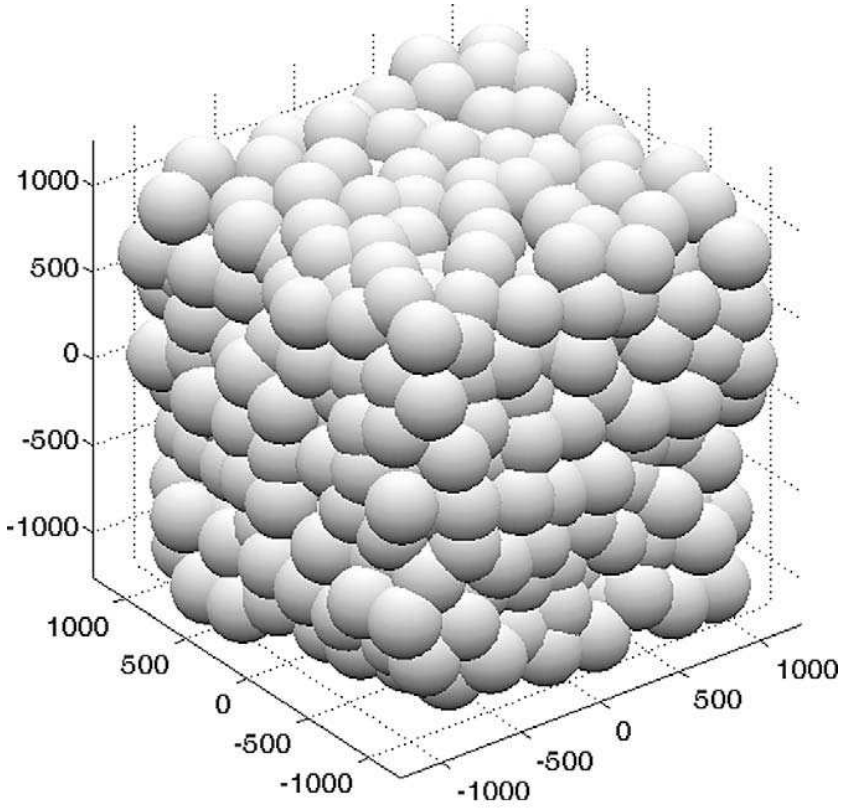


Figure 7.7: overview of 581 bubbles created with the algorithm [88]

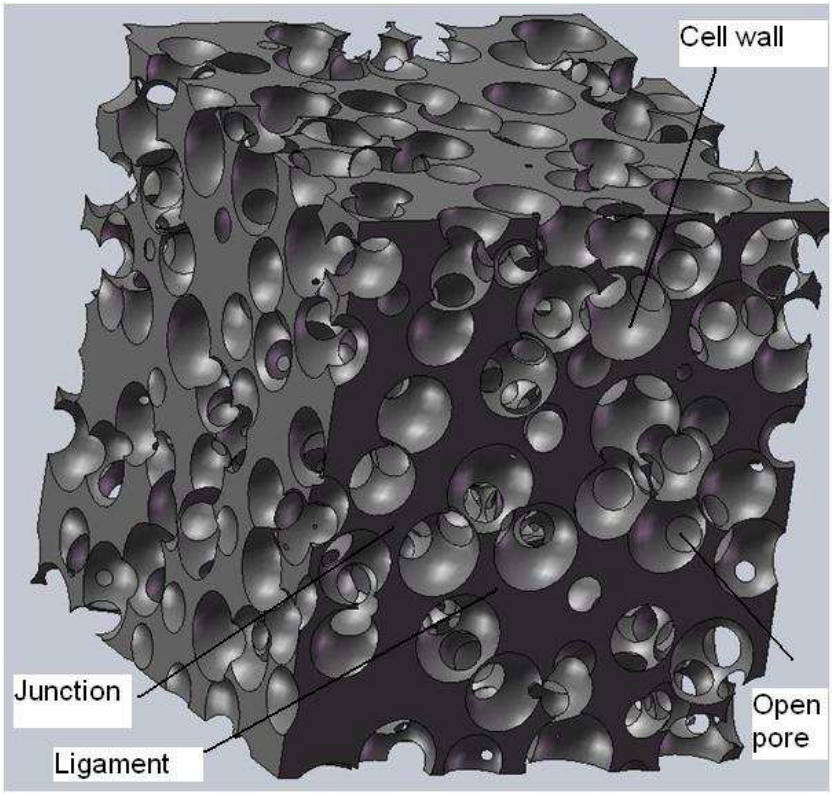


Figure 7.8: CAD rendering of digital carbon foam with a porosity of 0.65

tionship between the density and the physical properties of the foam. The porosity, P, or the void content of the foam is determined as follows

$$P = 100\frac{V_{void}}{V_{total}} \tag{7.6}$$

where $V_{void}$ is the volume occupied by the pores and $V_{total}$ is the total volume of the foam.

The relative density (R) is expressed by

$$R = \frac{\rho(b)}{\rho_s} = 1 - \frac{P}{100} \tag{7.7}$$

where $\rho(b)$ is the bulk foam density and $\rho_s$ is the intrinsic density of the solid in the foam.

## 7.3 Finite Element Method

In this study, the focus is on developing a finite element model (FEM) of conduction transport in PocoFoam. The effect of convection and radiation within the pores are not considered. The FEM is used to determine the bulk thermal conductivity of PocoFoam. This is achieved by establishing a thermal gradient through the PocoFoam specimen.

For the analysis of the thermal field in the PocoFoam specimen, the governing differential equation of steady state heat conduction without internal heat generation in the foam is considered. The PocoFoam specimen is sandwiched between two slabs of non-porous solid as shown in figure 7.9. The steady state heat conduction equation applied to the specimen is given by:

$$\nabla.(k\nabla T) = 0 \tag{7.8}$$

with the boundary conditions:
$x$ = 0, power at the top surface of the slab
$x = L$, $T = T_2$ at the bottom surface of the slab
$x \neq 0$ and $x \neq L$, no heat transfer through all other surfaces

The heat flux through the specimen is identical to the flux at the top and bottom surfaces because there is no internal heat generation in the specimen. The bulk thermal conductivity can therefore be calculated as follows:

$$k_{bulk} = q\frac{\Delta L}{\Delta T} \tag{7.9}$$

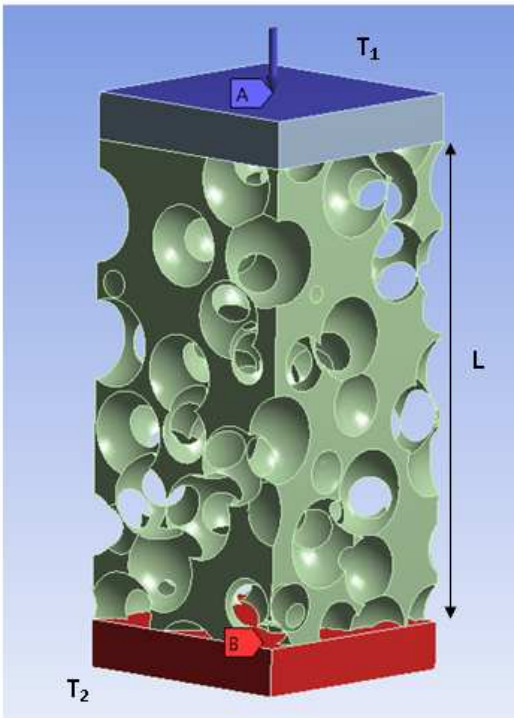


Figure 7.9: Overview of the boundary conditions and loads in the thermal analysis

The 3D PocoFoam geometry shown in figure 7.8 is exported to ANSYS. The software provides an automatic mesh generator that allows surface building and solid meshes that are either uniform or concentrated around critical regions. The size of the mesh can be specified either as relative to the dimensions of the model (percentage of the smallest characteristic dimension of the model) or as a absolute value (absolute dimension of the edge length). In this study, the PocoFoam geometry is meshed with the uniform meshing option. In order for the PocoFoam geometry to be mesh satisfactorily, the geometry was trimmed to the following dimensions: 1mm x 1mm x 2mm. The PocoFoam block obtained with these dimensions is considered large enough to predict both the thermal and mechanical properties of PocoFoam.

## 7.4 Results and discussion

In this study, the simulated PocoFoam has a density equal to $0.60 g/cm^3$. The properties obtained from the simulation will be compared to the properties of the PocoFoam with density equals to $0.56 g/cm^3$ presented in chapters 5 and 6. Due to the random process of the bubble's creation, it is sometimes difficult to generate a PocoFoam model with the exact density that is desired. This is the reason why the density of the simulated PocoFoam in the present study differs from the density of the PocoFoam compared with. The simulated results will only be compared to the PocoFoam properties in the x and y directions. This is done because the PocoFoam topology shows spherical bubbles in these two directions [33]. The study is ongoing and aims to establish a relationship between PocoFoam density and thermal conductivity.

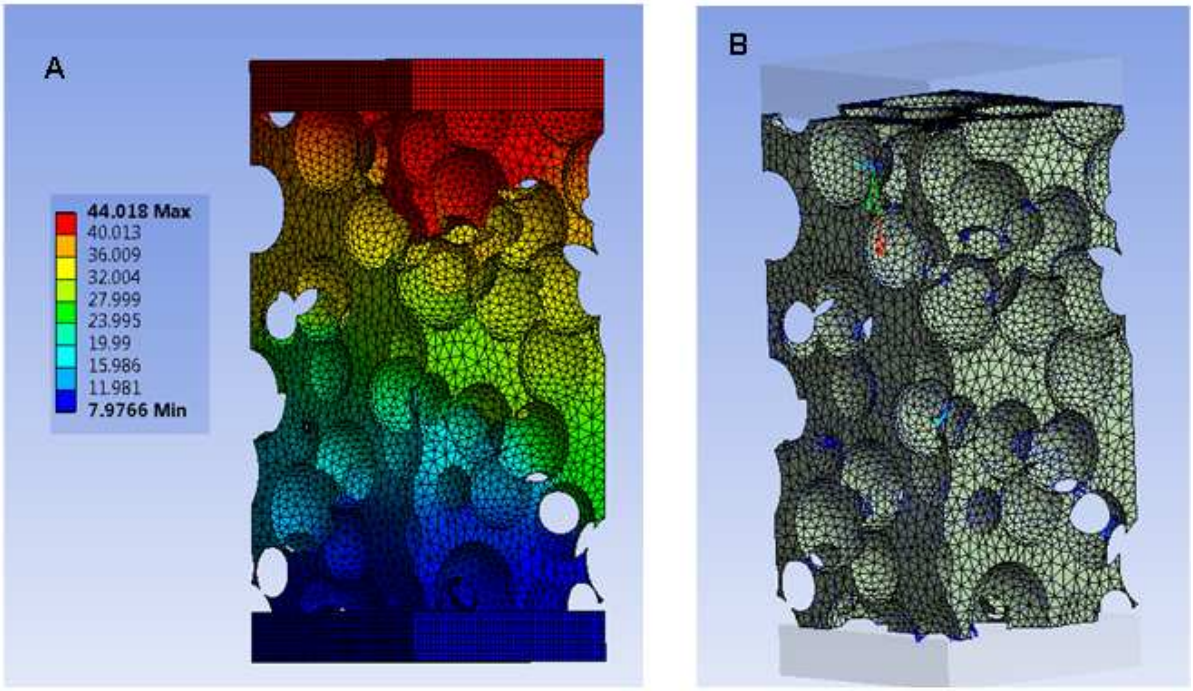


Figure 7.10: Thermal analysis finite element model showing temperature (°C) distribution (A) and heat flux variation in cell walls (B)

### 7.4.1 Thermal conductivity

The temperature and heat flux distribution of a simulated PocoFoam are presented in figure 7.10A and figure 7.10B, respectively. It is observed that the temperature distribution is mostly one-dimensional in most of the PocoFoam specimen except near the pores. The heat flux varies in the walls of the PocoFoam specimen because greater heat flux occurs in thinner cell walls.

A heat flow of 1W is applied on the top slab and the bottom slab is cooled at $8°$C in order to calculate the bulk thermal conductivity of the PocoFoam specimen. The bulk material of PocoFoam is taken as carbon graphite and is assumed to be isotropic. From the available literature, the density is defined as 1.7 g/c$m^3$, the thermal conductivity is 390 W/mK and the specific heat capacity is 710 J/KgK. The temperature gradient through the specimen is observed to be around $36°$C and the calculated thermal conductivity around 55.49 W/mK. The conductivities measured with the in-plane system at $20°$C are 54.5 W/mK and 57.5 W/mK in x and y directions, respectively, see chapter 3. The density of the simulated PocoFoam specimen is $7\%$ greater than the density of the measured specimen. However, a corresponding $7\%$ increase in the conductivity is not observed. The calculated thermal conductivity agrees well with the conductivity values measured in the x and y directions. Of course, this single result is not able to establish any relationship between density and thermal conductivity. A full understanding of this relationship will be achieved after the study of several PocoFoam densities.

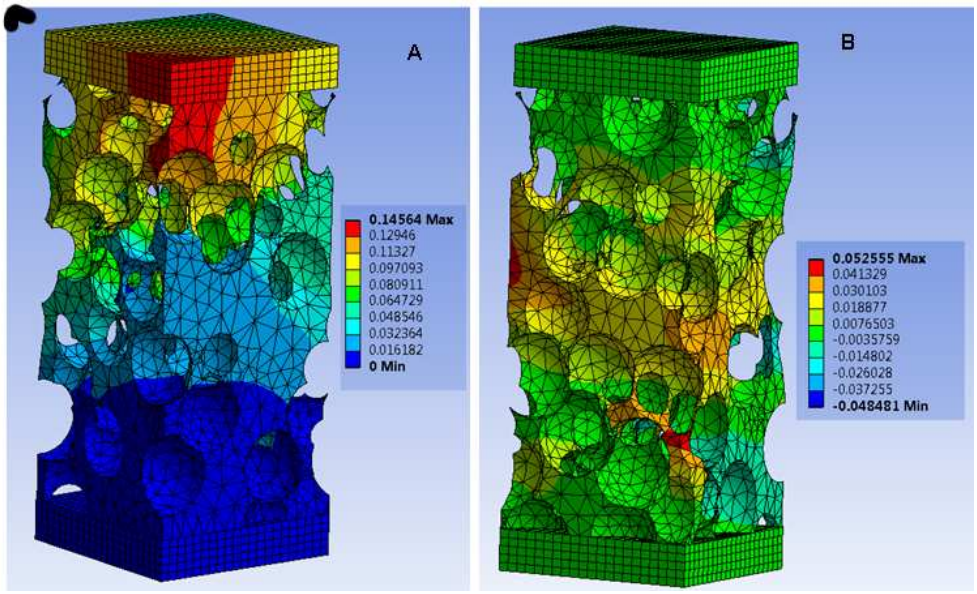


Figure 7.11: Stress analysis of the PocoFoam specimen assuming the material properties are isotropic

### 7.4.2 Young's modulus

The surface contacts between the foam and the slabs are bonded to prevent separation. The Young's modulus and the Poisson's ratio of the bulk material (graphite) of the PocoFoam are taken to be 15.61GPa and 0.33 [84].The bottom slab is a fixed support and a pulling force of 40N is applied on the top slab. The results of the longitudinal and transverse displacements are shown in figure 7.11A and figure 7.11B, respectively.

The average longitudinal displacement is simulated to be around 0.81mm and the average transverse displacement is around 0.03mm. The bulk Young's modulus is calculated to be 0.98GPa and the Poisson's ration is 0.04. The experimentally obtained Young's moduli are 1.1GPa and 1.3GPa in x and y directions, respectively. These experimental values are 12% and 33% higher than the calculated value, in the x and y directions, respectively. Unexpectedly, the calculated Young's modulus is slightly lower than the measured value. Being 7% denser than the measured specimen, the simulated PocoFoam specimen was expected to have a higher Young's modulus value, hence stiffer.

# Chapter 8

# Conclusions and Summary

The work described in this thesis centred upon the thermo-mechanical characterisation of carbon foams and composite materials for the stave design of the ATLAS inner tracker upgrade. The work focused on the design and construction of measurement systems capable of accurately measuring the thermal and mechanical properties of these materials. The thermal material characterisation was performed at the University of Glasgow and the mechanical material characterisation at the Rutherford Appleton Laboratory (RAL). The results obtained agree well with the manufacturer measured values for the materials having well understood properties and new results were obtained for the other materials. The work undertook contributed to understand better the manufacturing process of CSiC foam by discovering that the thermal conductivity of the foam, recommended by the manufacturer, was inaccurate. The value measured for the $8\%$ foam is 52 W/mK instead of the 0.52 W/mK published by the manufacturer. Additionally, this work establishes that the Young's modulus value of Carbon fibre reinforced polymer (CFRP) at low stress ($<30MPa$) is equal to its corresponding value at high stress. The work also achieves to determine the mechanical properties of Poco-Foam of 0.56g/c$m^3$ at low stress, which were unknown until now, and concludes a similarity between its tensile Young's modulus and shear modulus values.

The results achieved by the studies undertaken made a considerable contribution to the R&D of the design of the ATLAS inner tracker upgrade. The values measured were used to understand and optimize the actual inner tracker stave design and explore new design options.

Three main measurement systems were designed and used to determine thermal and mechanical material properties in this thesis

- In-Plane thermal conductivity measurement system
- Transverse thermal conductivity measurement system
- Jig for mechanical measurements at low stress

Thermo-mechanical measurements were also performed on a sandwich device composed

of stainless steel, PocoFoam and CFRP. The transverse thermal conductivity measurement system was used to performed these measurements. Finally, a modelling of PocoFoam of density 0.60 g/c$m^3$ was performed in Solid works and its thermal and mechanical properties were predicted in ANSYS. The simulation work of PocoFoam is ongoing and aims to establish a relationship between its density and its thermal and mechanical properties.

The conclusions and summaries drawn for each of the above mentioned measurements and results are discussed in sections 8.1 to 8.3. The immediate Post PhD work plan is detailed in section 8.4.

## 8.1 In-plane thermal conductivity measurement system

An in-plane thermal conductivity measurement system was designed and reported in this thesis and used to measure in-plane thermal conductivity values of PocoFoam, Allcomp foam and CFRP which are all materials used in the stave design of the ATLAS inner tracker upgrade. In-plane thermal conductivity values of materials of interest such as TPG, diamond, CSiC foam and carbon carbon were also determined. The method used for these measurements is the steady state direct measurement method. The system is designed to measure flat and thin specimens of length equal to 100mm, width approximately equal to 12mm and thickness up to 5mm. The specimen under investigation is heated at one end and cooled at the other end with a massive heat sink. The specimen is surrounded with aluminium radiation shields and all the RTDs wires are anchored on the heat sink. The temperature of the radiation shields are kept equal to the specimen temperature during the measurements. The measurements are performed by recording temperatures with RTDs placed on the specimen along the path of the heat flow. The residual undesired parasitics present in the measurement system are remedied by the double flux technique. Measurements are performed in the temperature range from -30°C to 20°C inside a vacuum vessel with an air pressure of approximately $10^{-5}$ mbar. The total fractional uncertainty in the measured thermal conductivity values is around 1.5$\%$. The thermal conductivity values measured for carbon carbon, diamond, CFRP, TPG, Allcomp foam and PocoFoam agree well with the available literature values. However, measurements of thermal conductivity of Allcomp foam specimens with thickness equal to or less than 1.4mm result in inaccurate values. The thermal conductivity value of the CSiC foam 8$\%$ measured is greater than the expected value. This is likely due to graphite core which was left from the manufacturing process of the foam.

## 8.2 Transverse thermal conductivity measurement system

The transverse thermal conductivity measurement system designed in this thesis was used to measure thermal resistances and thermal conductivities of materials such as Dow Corning 340, Dow Corning SE4445, Hysol EA9396, Hysol EA9396 + Boron Nitride, Araldite 2011, Epolite FH-5313 epoxy, CFRP and kapton films. The measurement system was also used to investigate PocoFoam and Allcomp foam specimens. The material under investigation was

sandwiched between two copper bars. The system was heated by a heater that was placed high on the upper copper bar and cooled by a massive heat sink connected to the lower copper bar. Two RTDs were placed on the copper bars along the path of the heat flow. One RTD on each side of the material under investigation. The measurements were performed at room temperature. The average temperature of the RTDs were kept similar to the environment temperature. Measurements of the thermal conductivity values of Dow Corning 340, Hysol EA9396, Araldite 2011, Epolite FH-5313 epoxy, CFRP and kapton films agree well with book values and the measurement of Hysol EA9396 + Boron Nitride was compared to theoretical models of powders in a matrix. The thermal conductivity measurement of Dow Corning SE4445 results in $2\pm0.2$W/mK, which is different from the value published by the manufacturer (1.26W/mK[1]).

Measurements of PocoFoam and Allcomp foam specimens were performed by placing two RTDs directly on the specimens. The average temperature of these RTDs average temperature was kept similar to the room temperature. The measured transverse thermal conductivity of the PocoFoam specimen with density equal to 0.56g/c$m^3$ agrees very well with the expected value. The measured value is around three times greater than the values obtained for the other two directions. This confirms the expected anisotropic conductivity of PocoFoam. The transverse measurement of Allcomp foam with density equal to 0.22g/c$m^3$ results in a value similar to that found for the other two directions. This confirms the expected isotropic conductivity of Allcomp foam.

## 8.3 Jig for mechanical measurements at low stress

A jig was designed in this thesis and adapted to a conventional testomer to eliminate twisting and bending of the specimen, which appear to influence negatively the results during tensile measurements at low stress. This mechanical system was used together with a video extensometer system to measure mechanical properties of CFRP and PocoFoam of density 0.56g/c$m^3$. The measurements were performed at room temperature. The results of the Young's moduli of the CFRP specimens measured (0/60/-60 and 90/0/90) agree well with the values obtained at the Engineering Research Laboratory (MERL) for 0/60/-60 and at the Brookhaven National Laboratory for 90/0/90 at higher stress values. The results of the PocoFoam measurements show that it is possible to determine its elastic region at low stress and determine graphically the yield strength and the ultimate tensile strength.

## 8.4 Post PhD work

The simualtion work of PocoFoam is expected to be completed by establishing a relationship between its density and its thermal and mechanical properties. However, due to the discontinuity of the production of PocoFoam, it is more likely that Allcomp foam will be used in

[1] http://www.ellsworth.com/display/productdetail.html?productid=2491

the design of the inner tracker of the ATLAS upgrade. Therefore, the immediate work will be focused on the simulation of the Allcomp foam.

# Bibliography


[1] http://www.interactions.org.

[2] M. Bongi et al. Astroparticle physics at LHC: The LHCf experiment ready for data taking. *Nucl. Instr. and Meth. A*, 612(3):451–454, 2010.

[3] The TOTEM Collaboration. "TOTEM technical design report". *CERN-LHCC-2004-002; addendum CERN-LHCC-2004-020*, 612(3), 2004.

[4] L. Bonechi. a LHC detector for astroparticle physics. *Nucl. Phys. B*, 177(4):263–264, 2008.

[5] A. Tricomi et al. The LHCf experiment at the LHC: Physics goals and status. *Nucl. Phys. B (Proc. Suppl.)*, 196(3):30–35, 2009.

[6] A. Augusto Alves Jr. et al. The LHCb collaboration. *I. INST*, S08005(4), 2008.

[7] The ALICE Collaboration. ALICE technical proposal. *CERN/LHCC/95-71*, 95(3), 1995.

[8] The ALICE Collaboration. ALICE collaboration. *J. Phys. G: Nucl. Part.*, 30(4), 2004.

[9] The CMS Collaboration. CMS collaboration. *J. INST*, 3(4), 2008.

[10] G. Aad et al. The ATLAS experiment at the CERN large hadron collider. *J. INST*, 3(4):S08003, 2008.

[11] P. Lengo. Status and performance of the ATLAS experiment. *Nuc. Phys. (Proc. Suppl.)*, 3(4), 2010.

[12] C. Roda. Jet production in proton-proton collision at s = 49 Tev with the ATLAS experiment. *Nucl.Phys. (Proc.Suppl.)*, 9(4):207–208, 2010.

[13] F. Martin. The ATLAS transition radiation tracker (TRT) from construction to installation. *Nucl. Instr. and Meth. A*, 581(4):535–537, 2007.

[14] T. Kohiriki et al. Hybrid and module designs for ATLAS silicon tracker upgrade for super LHC. *Nucl. Phys. Inst.*, 579(4):806–811, 2007.

[15] P. Sicho. SLHC upgrade plans for the ATLAS pixel detector. *Nucl. Instr. and Meth. A*, 607(4):31–34, 2009.

[16] A. Di Ciaccio. Status and commissioning of the ATLAS experiment at the LHC. *Nucl. Instr. and Meth. A*, 602(4):682–686, 2009.

[17] The ATLAS Collaboration. The ATLAS inner detector: technical design report. 1, CERN-LHCC-97-016, http://cdsweb.cern.ch/record/331063; ATLAS inner detector: technical design report. 2, CERN-LHCC-97-017, http://cdsweb.cern.ch/record/331064.

[18] The ATLAS Collaboration. ATLAS pixel detector: technical design report, CERN-LHHC-98-013, http:cdsweb.cern.ch/record/381263.

[19] G. Aad et al. ATLAS pixel detector electronics and sensors. *J. INST*, 3(4):07007, 2008.

[20] Y. Unno. Silicon sensor development for the ATLAS upgrade for SLHC. *Nucl. Instr. and Meth. A*, 569(1):41–47, 2006.

[21] M. Gilchriese et al. Mechanical and cooling design studies for an integrated stave concept for silicon strip detectors for the super LHC. *ATL-UPGRADE-PUB-2008-001*, 1(4), 2008.

[22] P. P. Allport et al. The ATLAS collaboration. *Nucl. Instr. and Meth. A, DOI:10.1016/j.nima.2010.04.091*, 3(4), 2010.

[23] http://www.aitechnology.com.

[24] http://www.poco.com.

[25] H. Marsh. Activated carbon. *ISBN 10: 0-08-044463-6, ISBN 13: 978-0-08-044463-5*, 554, 2006.

[26] K. James. Cellular ceramics: Structure, manufacturing, properties and application. *DOI: 10.1002/3527606696.ch2f*, 2006.

[27] K.James et al. The role of structure on the thermal properties of graphite foams. *JMTSAS*, 39(11):3659–3676, 2004.

[28] K. Alam et al. Thermal transport in graphitic carbon foams. *J. Comp. Mat doi: 10.1177/0021998304044772*, 38(22):1993–2006, 2004.

[29] M. D. Sarzynski et al. Multifunctional hybrid carbon foams: Integrating processing and performance. *J. Comp. Mat, DOI: 10.1177/0021998309347805*, 44(5), 2010.

[30] Williams et al. United states patent, us 6, 929, 866 b1.

[31] X. Wang et al. The study on the formation of graphite foam. *doi:10.1016/j.matlet.2006.05.052*, 61(3):741–746, 2007.

[32] N. C. Gallego and K.W. James. Carbon foams for thermal management. *DOI:10.1016/S0008-6223(03)00091-5*, 41(7):1461–1466, 2003.

[33] A. G. Straatman et al. Thermal characterization of porous carbon foam-convection in parallel flow. *JHMT*, 49:1991–1996, 2006.

[34] B. T. Kelly. Physics of graphite. *JNM, DOI: 10.1016/0022-3115(83)90088-0*, 114(1):116, 1981.

[35] J. E. Mueller. Determining the role of porosity on the thermal properties of graphite foam, Thesis at virginia polytechnic institute and state university. 2008.

[36] P. R. Onck et al. Fracture of open and closed cell metal foams. *JMS*, 40(1):5821–5828, 2005.

[37] D. D. Edie. The effect of processing on the structure and properties of carbon fibres. *DOI: 10.1016/S0008-6223(97)00185-1*, 36(4):345–362, 1998.

[38] G. J. Capone. Wet spinning technology, acrylic fibre technology and applications, Marcel Dekker Inc.,. pages 71–78, 1995.

[39] www.harperintl.com/pan-based-carbon fiber.htm.

[40] T. H. Ko et al. The characterization of pan-based carbon fibres developed by two-stage continuous carbonization. *DOI:10.1016/0008-6223(93)90013-Z*, 31(5):765–771, 1993.

[41] W. Frohs E. Fitzer and M. Heine. Optimization of stabilization and carbonization treatment of pan and structural characterization of the resulting carbon fibres. *DOI:10.1016/0008-6223(86)90257-5*, 24(4):387–395, 1986.

[42] E. Fitzer. Pan-based carbon fibres-present state and trend of the technology from the viewpoint of possibilities and limits to influence and to control the fibre properties by the process parameters. *DOI:10.1016/0008-6223(89)90197-8*, 27(5):621–645, 1989.

[43] Z. O. Mustafa. Production of mesophase pitch from coal tar and petroleum pitches using supercritical fluid extraction. *Turk J Chem*, 26(1):417–424, 2001.

[44] T. Y. H. Cheung. PhD thesis, Leeds university, uk, 1993.

[45] A. Franco. An apparatus for the routine measurement of thermal conductivity of materials for building application based on a transient hot-wire method. *DOI:10.1016/j.applthermaleng.2007.02.008*, 27(14):2495–2504, 2007.

[46] P. Nesvadba. Methods for the measurement of thermal conductivity and diffusivity of foodstuffs. *DOI:10.1016/0260-8774(82)90003-6*, 1(2):93–113, 1982.

[47] D. M. Rowe and C. M. Bhandari. Preparation and thermal conductivity of doped semiconductors. *DOI:10.1016/0146-3535(86)90028-6*, 13(4):233–289, 1986.

[48] S. A. Al-Ajlan. Measurements of thermal properties of insulation materials by using transient plane source technique. *DOI:10.1016/j.applthermaleng.2006.04.006*, 26(3):2184–2191, 2006.

[49] A. I. Vahanyan. A method for the thermal conductivity measurement of semiconductors. *DOI:10.1016/j.measurement.2005.11.022*, 39(5):447–450, 2006.

[50] G. K. White and S. B. Woods. Electrical and thermal resistivity of the transition elements at low temperatures. *DOI:10.1098/rsta.1959.0004*, 251(2):273–302, 1959.

[51] G. A. Slack. Effect of isotopes on low temperature thermal conductivity. *DOI:10.1103/PhysRev.105.829*, 105(2):829–831, 1957.

[52] G. A. Slack. Thermal conductivity of CaF2, MnF2, CoF2 and ZnF2 crystals. *DOI:10.1103/PhysRev.122.1451*, 122(2):1451–1464, 1961.

[53] C. A. Heusch et al. Direct measurements of the thermal conductivity of various pyrolytic graphite samples (PG, TPG) used as thermal dissipation agents in detector applications. *Nucl. Instr. and Meth. A*, 480(3):463–469, 2002.

[54] P. R. N. Childs. Resistance temperature detectors, DOI:10.1016/b978-075065080-9/50006-x. pages 145–193, 2001.

[55] S. K. Sen. An improved lead wire compensation technique for conventional two wire resistance temperature detectors (RTDs), DOI:10.1016/j.measurement.2006.01.002. 39(5):477–480, 2006.

[56] J. R. Culham et al. Assembly and commissioning of a test apparatus for characterizing thermal interface materials. *ITHERM*, 45(2):128–134, 2002.

[57] M. Locatelli et al. Thermal radiation effects in thermal conductivity measurements. *J. Phys. D:Appl. Phys. DOI:10.1088/0022-3727/16/4/009*, 16(4):479, 1983.

[58] J. Pappis and S. L. Blunn. Properties of pyrolytic graphite. *DOI:10.1111/j.1151-2916.1961.tb11664.x*, 44(12):592–597, 2006.

[59] A. Q. D. Faisal. Preparation of pyrolytic graphite (PG) shell using CVD technique. *Eng. Tech. Journal*, 27(5):868–879, 2009.

[60] J. P. Gwinn et al. Performance and testing of thermal interface materials. *DOI:10.1016/S0026-2692(02)00191-X*, 34(3):215–222, 2003.

[61] J. P. Gwinn et al. Apparatus for accurate measurement of interface resistance of high performance thermal interface materials. *10.1109/ITHERM*, 9(3):379–391, 2009.

[62] C. T. Murray et al. Rumination on design and build of an ASTM D-5470 thermal interface test instrument. *THERM*, 28(3):309–318, 2006.

[63] F. P. Incropera. Fundamentals of heat and mass transfer. *OSTI ID: 6008324*, page 832, 2008.

[64] C. P. Chu et al. Thermal modeling of grease-type interface material in PPGA application. *10.1109/STHERM.1997.566783*, pages 57–63, 2002.

[65] R. Taylor. An introduction to error analysis. *ISBN-10: 093570275X*, pages 273–291, 1997.

[66] S. L. Shinde. High thermal conductivity materials. *ISBN: 0387220216*, pages 168–179, 2005.

[67] R. Kochetov et al. Thermal conductivity of nano-filled epoxy systems. *10.1109/CEIDP.2009.5377801*, pages 658–661, 2010.

[68] R. Berman. Some experiments on thermal contact at low temperatures. *DOI: 10.1063/1.1722369*, 27(4):318–323, 1956.

[69] W. Yung. A cost effective advanced thermal material for metal-core printed circuit board (MCPCB). *HKPCA*, (24), 2007.

[70] H. Ishida and S. Rimdusit. Very high thermal conductivity obtained by Boron filled polybenzoxazine. *ISSN 0040-6031*, 320(2):177–186, 1998.

[71] R. C. Progelhof. Methods for predicting the thermal conductivity of composite systems. *DOI: 10.1002/pen.760160905 Polymer Engineering & Science*, 16(9):615–625, 2004.

[72] T. B. Lewis and L. E. Nielsen. Dynamic mechanical properties of particulate filled polymers. *DOI: 10.1002/app.1970.070140604 Journal of Applied Polymer Science*, 14(6):1449–1471, 2003.

[73] The thermal and electrical conductivity of two-phase systems. Ind eng chem fundam. *DOI: 10.1002/app.1970.070140604*, 13:17–20, 1974.

[74] R. Pal. New models for thermal conductivity of particulate composites. *J Reinf Plast Compos*, 26:643651, 2007.

[75] Y. Agari and T. Uno. Estimation on thermal conductivities of filled polymers. *DOI: 10.1002/app.1986.070320702 Journal of Applied Polymer Science*, 32(7):5705–5712, 2003.

[76] I. H. Tavman and D. Kumlutas. A numerical and experimental study on thermal conductivity of particle filled polymer composites. *DOI: 10.1177/0892705706062203 Journal of Thermoplastic Composite Materials*, 19(4):441–455, 2006.

[77] J. C. Maxwell. A treatise on electricity and magnetism. *ark:/13960/t9s17v886, http://www.archive.org/details/electricandmagne01maxwrich*, 2006.

[78] H. W. Russell. Principles of heat flow in porous insulators. *DOI: 10.1111/j.1151-2916.1935.tb19340.x Journal of the American Ceramic Society*, 18(12):1–5, 2006.

[79] T. N. G. Tsao. Thermal conductivity of two-phase materials. *Ind. Engng Chem.*, 53(5):395 – 397, 1961.

[80] Charles W. Marschall and Robert E. Maringer. Dimensional Instability, an introduction. *ISBN 0-08-021305-7*, First edition 1977.

[81] E. Schmid and W. Boas. Plasticity of crystals: With special reference to metals. *ISBN 13: 9780412091308*, page 277286, 1968.

[82] S. Sihn and A. K. Roy. Modeling and prediction of bulk properties of open-cell carbon foam. *DOI:10.1016/S0022-5096(03)00072-3 Journal of the Mechanics and Physics of Solids*, 52(1):167191, 2004.

[83] E. B. Thompson Q. Yu and A. G. Straatman. A unit cube-based model for heat transfer and fluid flow in porous carbon foam. *DOI:10.1115/1.2165203, J. Heat Transfer*, 128(4):352361, 2006.

[84] M. Kirca et al. Computational modeling of micro-cellular carbon foams. *DOI:10.1016/j.finel.2007.08.008 Finite Elements in Analysis and Design*, 44(2):4552, 2007.

[85] M. K. Alam A. M. Drunna and C. Druma. Analysis of thermal conduction in carbon foams. *DOIdoi:10.1016/j.ijthermalsci.2003.12.004*, 43(7):689695, 2004.

[86] K. Lafdi T. Beechem and A. Elgafy. Bubble growth mechanism in carbon foams. *DOI:10.1016/j.carbon.2004.11.046*, 43(5):10551064, 2005.

[87] G. Rosebrock et al. Study of the growth and motion of graphitic foam bubbles. *DOI:10.1016/j.carbon.2005.06.044*, 43(15):30753087, 2005.

[88] L. James et al. Modeling the principle physical parameters of graphite carbon foam. *DOI:10.1016/j.carbon.2010.02.043*, 48(9):24182424, 2010.

# Appendix A

# Detailed view of the in-plane thermal conductivity measurement system

The in-plane thermal conductivity measurements are performed by recording temperatures with four RTDs placed on the specimen along the path of the heat flow, see figure A.1. The specimen is surrounded with aluminium radiation shields in order to minimise heat transfer by radiation between the specimen and the environment around the measurement system, see figure A.2. The measurement system is placed inside a copper box that serves as radiation shield between the vacuum chamber environment and the measurement system, see figure A.3. The entire assembly is placed inside the vacuum chamber whose inside walls are covered with a thin multi-layer thermo-reflective insulation, see figure A.4.

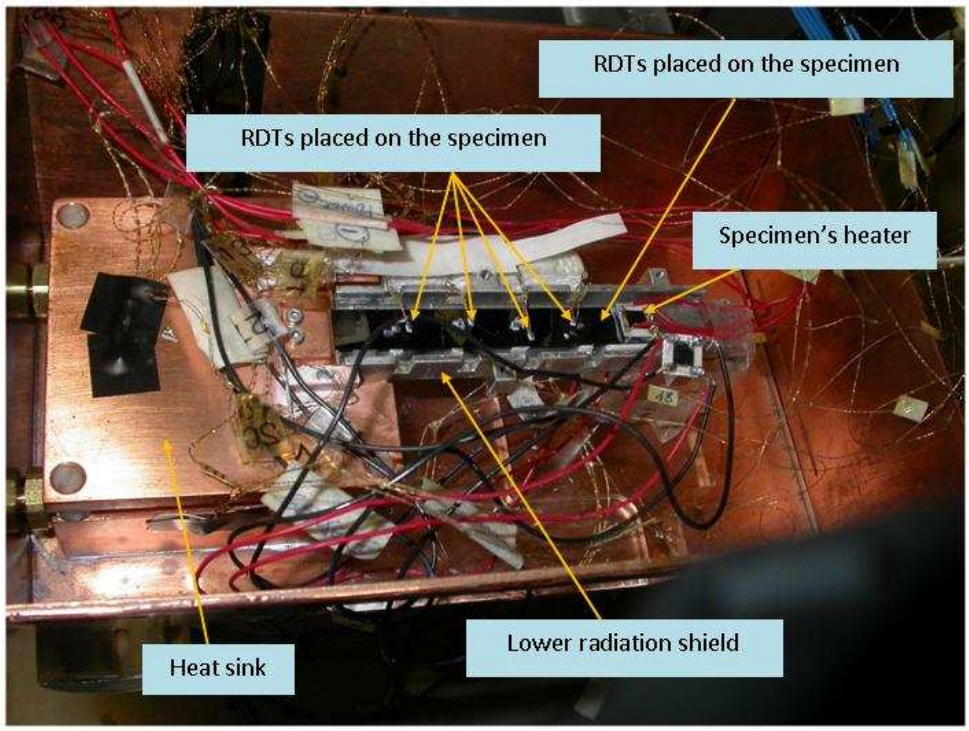


Figure A.1: Overview of the specimen placed inside the measurement system. Four RTDs are placed on the specimen along the heat path. The specimen heater and the upper shield heater are shown

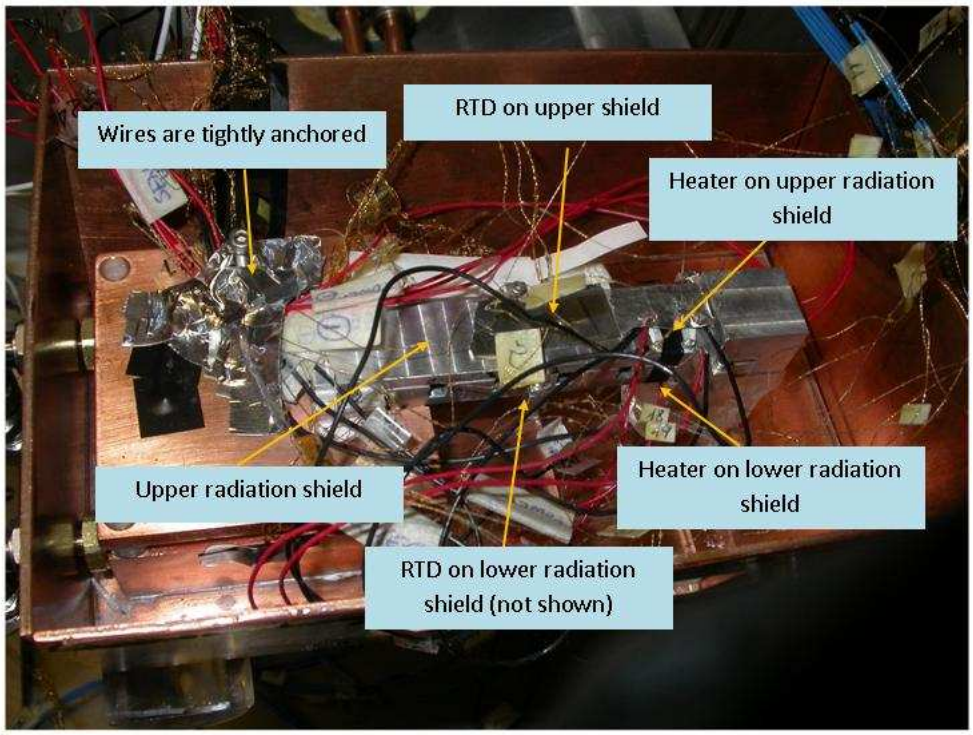


Figure A.2: Overview of the measurement system with radiation shields around the specimen. The upper heater and a RTD are placed on the upper shield, the wires anchored on the copper block. The measurement system is ready to be covered inside the copper box

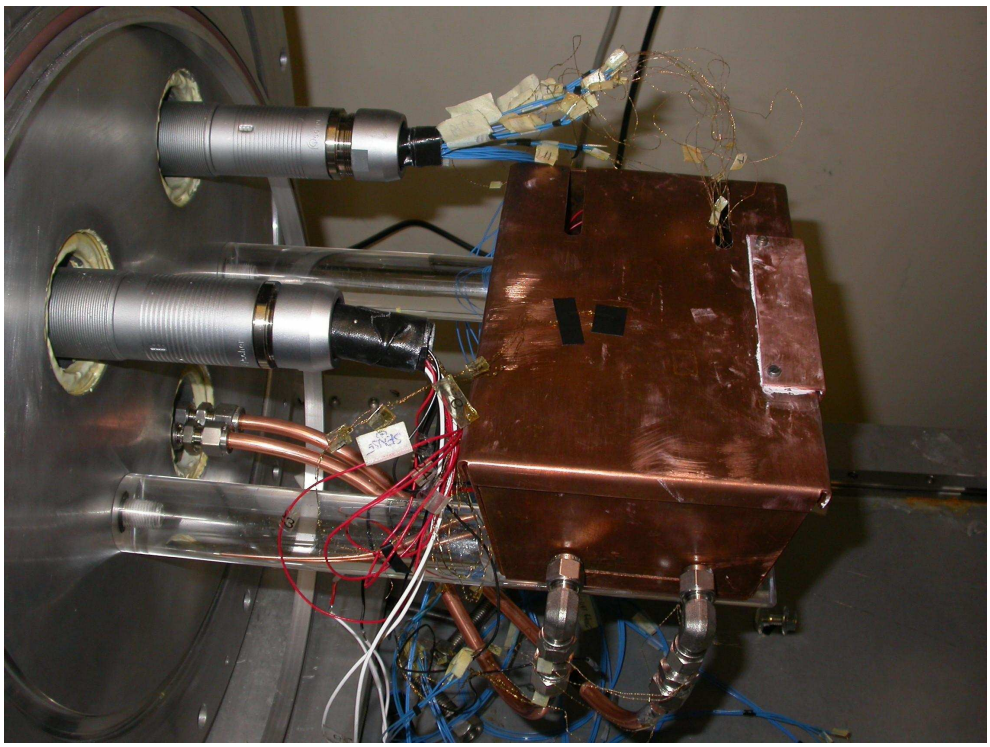

Figure A.3: Overview of the box containing the measurement system together with the cooling fluid pipes. The box is ready to be placed inside the vacuum chamber for measurements

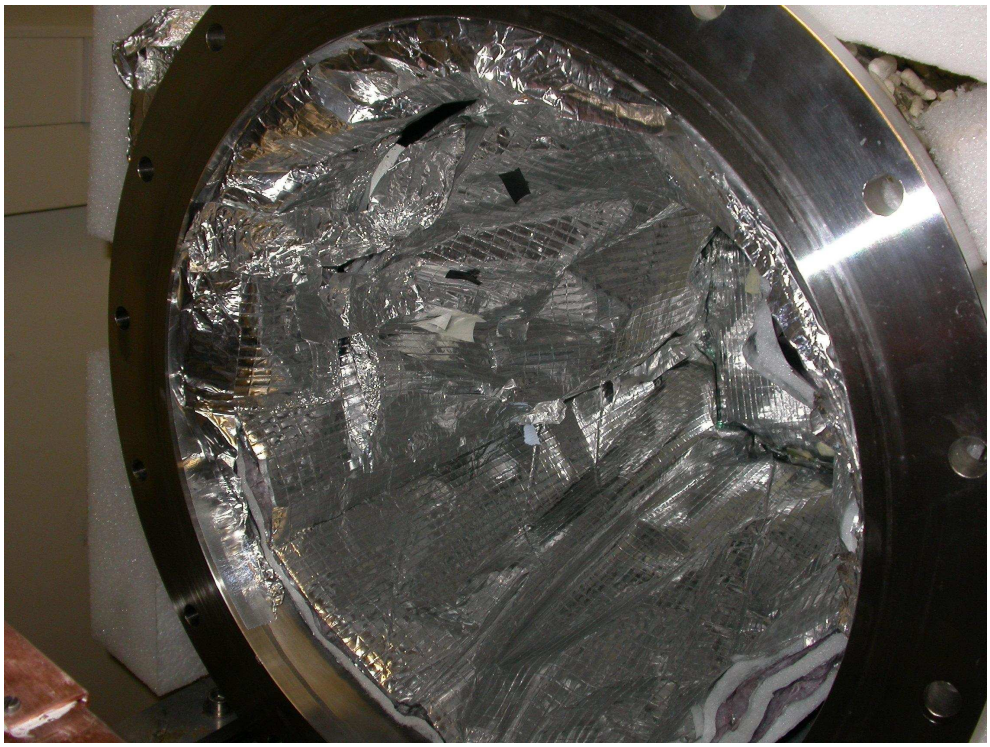

Figure A.4: Overview of the inside walls of the vacuum chamber covered with a thin multilayer thermo-reflective insulation

# Appendix B

# View of the transverse thermal conductivity measurement system

The transverse thermal conductivity measurements are performed by recording temperatures with RTDs placed on the copper bars along the path of the heat flow, see figure B.1. One RTD is placed at the top of the upper copper bar and another one on the heater. These RTDs are used to calculate the heat loss during the measurements in order to determine the actual heat going through the specimen under investigation. A load cell is used in order to calculate the pressure applied on the specimen.

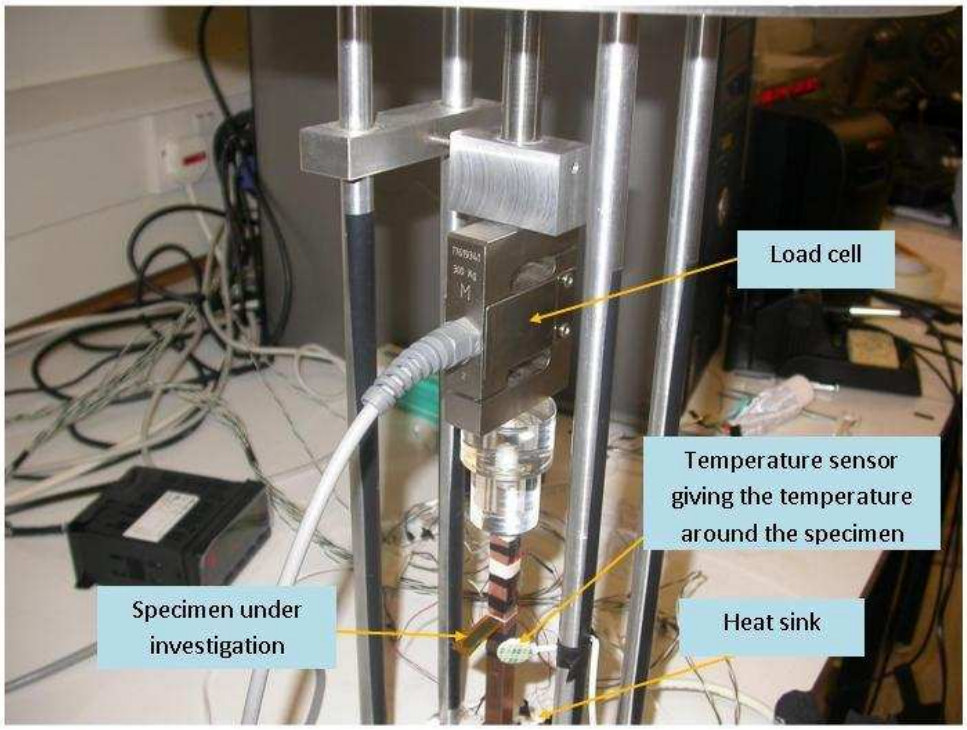


Figure B.1: Overview of a specimen placed inside the transverse thermal conductivity measurement system. Two RTDs are placed on the copper bars along the heat path. One RTD is placed above the specimen and the other one below the specimen.

# Appendix C

# Overview of the jig mounted into a conventional testometer

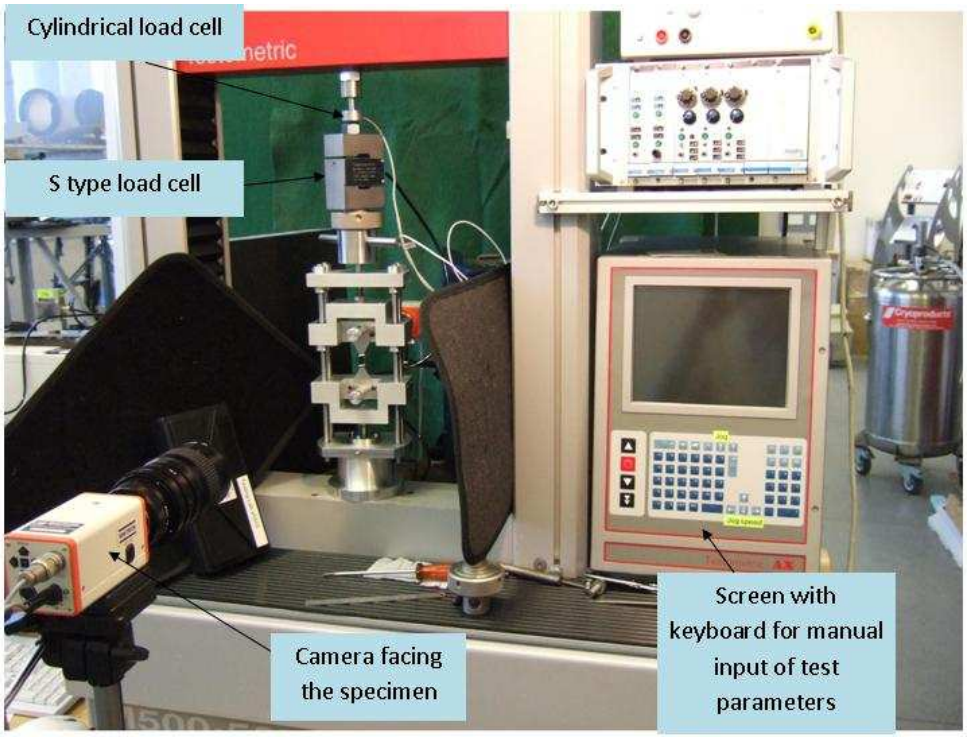


Figure C.1: Overview of the jig mounted into a conventional testometer. The specimen is ready to be measured